

NORTHWESTERN UNIVERSITY

Molecular Junctions: Control and Dynamics at the Single Molecule Limit

A DISSERTATION

SUBMITTED TO THE GRADUATE SCHOOL
IN PARTIAL FULFILLMENT OF THE REQUIREMENTS

for the degree

DOCTOR OF PHILOSOPHY

Field of Chemistry

By

David Quigley Andrews

EVANSTON, ILLINOIS

December 2008

© Copyright by David Q. Andrews 2008

All Rights Reserved

Abstract

Molecular Junctions: Control and Dynamics at the Single Molecule Limit

David Quigley Andrews

The overarching goal of this work is to understand nanometer scale junctions and electron transport through molecules in these junctions. Calculations detailing quantum interference in the electron transport through molecules, and the control of these features, show great potential for use as discrete electronic elements. Concurrent work on the fabrication of an ultra high vacuum scanning tunneling microscope, designed to enable Raman spectroscopy, is presented.

Scanning tunneling microscopy is required to image spatially molecules and surfaces at the sub-angstrom length scale. The imaging of a number of surfaces, utilizing scanning tunneling microscopy, as well as attempts at measuring single molecule conductance, are presented. The experimental measurements of transport through single molecules strongly coupled to both electrodes entail a large uncertainty in the localized structure of the junction and consequently there is a large distribution of conductance values. Calculations addressing the variability of conductance due to small geometric changes show the sensitivity of the localized structure. Molecular dynamics and charge transport calculations are coupled to model the effects of thermal motion on conductance. Our new microscope aims to overcome the uncertainties in experimental measurements by measuring spectroscopic and electrical properties at the same time.

Transport calculations on limited classes of molecules show a very large dynamic range in electron transmission probability. The large dynamic range is attributed to quantum interference between orthogonal molecular states. The dynamic range in these systems, and the synthetically common chemical motif, makes them promising candidates for further studies and future electronic devices. Quantum interference and the breakdown in the traditional 'rules of thumb' for charge transport open a new window of possibility into the design of molecular devices with switching speed and dynamic range that rival solid state devices. In an example of a single molecule transistor, we calculate a change in conductance of 8 orders of magnitude with an applied gate voltage. In designing a molecule with multiple interference features, we propose and calculate the current/voltage behavior of a molecular rectifier with a rectification ratio of $> 150,000$. Unexplored chemical space should yield new and promising candidates for future electronic devices.

Prof. Mark A. Ratner

Prof. Richard P. Van Duyne

Research Advisors

Acknowledgements

I would like to thank Professor Mark Ratner and Professor Richard Van Duyne for creating and fostering an academic environment that has broadened and developed my intellectual curiosity. It is not just course material but, more importantly, the colleagues and teachers around you who make learning happen. The chemistry program here at Northwestern University has exceeded my expectations.

I need to thank both advisors for giving me a large amount of academic freedom. Working between multiple professors in a new research direction can be an enormous challenge. I cannot imagine working on a theory-experiment project with two more helpful and understanding advisors.

The path by which I have traveled to make it this far has been marked with encouragement and support of my scientific education. The path starts with my parents, Elin and Charlie, and the numerous family trips spent looking at geology books attempting to find minerals and fossils. For my first introduction to scientific research, I would like to thank Nahid Tayebi and Ellen Sidransky at NIH. This was the first place where I was given experimental freedom and the ability to utilize expensive equipment. The time spent in their lab also introduced me to the difficulty in genotype-phenotype relationship, specifically, the difficulty in correlating genetic mutations in a patient's DNA with disease severity. I would like to thank my advisors at Wesleyan University, chemistry professors David Beveridge and Wallace Pringle. I should also acknowledge Anne Greene for the great course on nonfiction writing, and the Wesleyan swim team, which provided enough physical exercise to last a lifetime.

I would like to thank the back row in its two incarnations (1. Julia, Kallie, Paul, 2. Julia, Sam, Kristin) for being there daily and providing a humorous respite from the lab atmosphere. I would like to thank all the group members who have made my time at Northwestern enjoyable; The Van Duyne Group: Kevin Biggs, Julia Bingham, Prof. Jon Camden, Jon Dieringer, Kathryn Kosuda, Olga Lyandres, Dr. Adam McFarland, Nilam Shah, Dr. Leif Sherry, Dr. Jiha Sung, Dr. Alyson Whitney, Prof. Kallie Willets, Dr. Matt Young, and Dr. Xiaoyu Zhang; The Ratner Group: Dr. Revital Cohen, Dr. Misha Galperin, Dr. Chad Risko, Dr. Alex Xue, Dr. Zach Dance, Dr. Randy Goldsmith, Dr. Joe Letizia, Qixi Mi, Dr. Gemma Solomon (thanks for quantum interference and proof-reading most of this), Sina Yeganeh, and Prof. Emily Weiss; and the Hersam Group: Dr. Eddie Foley, Dr. Nathan Yoder, Qing Hua Wang, and Mike Walsh.

I need to thank all of my siblings: Steven, who has recently proven that with a little statistics you can quickly prove a big point and make it an even bigger point when you go to the media before peer-review (do be wary of the Fleishman effect); Paul, who quickly recognized the benefits of multiple computer monitors, Dan, who seems to be doing well doing his own thing; Katie, good work for running the Burrito Mile this year; and Sarah, being last I have no doubt that you will surely upstage everyone.

Science research can be all consuming but it is my varied experiences from travel to art that have kept me focused. I would like to thank my friend, the snowy Van Gogh painting in the Art Institute, and my many friends in the Isabella Stewart Gardner Museum. I also need to thank John Singer Sargent, an internationally famous and successful portrait painter, who, once financially secure, became able to travel and do the landscape painting he enjoyed. As stated

by Sargent in one of his letters (as quoted in a *New York Times* book review of *John Singer Sargent: His Portrait* by Stanley Olson), "I have vowed a vow not to do any more portraits...it is to me positive bliss to think that I shall soon be a free man."¹ I hope that he does not mind that the new theory computer was given his name.

Most importantly, I need to thank my wife, Lena. It is with her support that I have been able to stay in a mental daze for weeks, waking up at crazy hours, trying to figure out how to come up with some new idea, or fix old broken ones. Lena keeps me grounded and reminds me that she has the harder task of teaching those who struggle to be taught. It is her teaching that constantly reminds me that doing the science may be hard but conveying what has been done and teaching others is at least as important. Thank you for everything, including the commas.

And, finally, I would like to thank the referees of our recently submitted manuscript. I find that in certain instances, negative and unhelpful comments go far in providing motivation. Calling our recent work "usual, expected, obvious, lacking significant novelty, and unuseful [work] on an idea that has been floating around for years" has provided the necessary motivation to push through and continue.

-DQ, May 2008

List of Acronyms

AFM	Atomic force microscope (microscopy)
APD	Avalanche photodiode
ATK	Atomistix ToolKit
DFT	Density function theory
HOMO	Highest occupied molecular orbital
HOPG	Highly ordered pyrolytic graphite
IETS	Inelastic electron tunneling spectroscopy
LCTF	Liquid crystal tunable filter
LUMO	Lowest unoccupied molecular orbital
SERS	Surface enhanced Raman spectroscopy
SMSERS	Single molecule surface enhanced Raman spectroscopy
STM	Scanning tunneling microscope (microscopy)
TERS	Tip enhanced Raman spectroscopy
UHV	Ultra high vacuum

to the advancement of science education

Table of Contents

ABSTRACT.....	3
ACKNOWLEDGEMENTS.....	5
LIST OF ACRONYMS	7
TABLE OF CONTENTS	10
LIST OF ILLUSTRATIONS	13
LIST OF TABLES	22
CHAPTER 1. ADDRESSING INDIVIDUAL MOLECULES.....	23
1.1 ELECTRICAL MEASUREMENTS.....	25
1.2 SPECTROSCOPIC MEASUREMENTS.....	27
1.2.1 <i>Surface enhanced Raman spectroscopy</i>	27
1.2.2 <i>Single molecule surface enhanced Raman spectroscopy</i>	27
1.2.3 <i>Tip enhanced Raman spectroscopy</i>	30
1.2.4 <i>Fluorescence</i>	30
1.3 CALCULATING SINGLE MOLECULE BEHAVIOR	31
1.3.1 <i>Computational methods</i>	31
1.4 SINGLE MOLECULE JUNCTIONS	31
1.5 SCANNING PROBE BREAK JUNCTIONS.....	32
1.5.1 <i>Measured conductance</i>	32
1.5.2 <i>Single molecule inelastic electron tunneling spectroscopy</i>	34
1.5.3 <i>Force spectroscopy and other single molecule techniques</i>	35
1.6 MOTIVATION	36
1.7 NOTE ON PUBLISHED WORK	37
CHAPTER 2. STM IMAGING	38
2.1 HIGHLY ORDERED PYROLYTIC GRAPHITE	39
2.1.1 <i>HOPG on the microscope</i>	41
2.1.2 <i>Adsorbed molecules</i>	42
2.1.3 <i>Au <111> surface</i>	44
2.1.4 <i>Monolayers on Au</i>	47
2.2 AG NANOWELLS	51
CHAPTER 3. STM BREAK JUNCTIONS.....	53
3.1 EXPERIMENTAL SETUP.....	54

		11
3.2	DERIVATION OF QUANTIZED CONDUCTANCE	54
3.3	EXPERIMENTAL QUANTIZED CONDUCTANCE.....	57
3.4	INITIAL TESTS ON SINGLE MOLECULE JUNCTIONS	58
3.5	CALIBRATION OF A LOG AMPLIFIER.....	59
3.6	TESTS ON BENZENEDIAMINE.....	61
3.7	CONCLUSIONS ON BREAK JUNCTIONS	65
CHAPTER 4.	TWO PROBE CALCULATIONS.....	67
4.1	INTRODUCTION	68
4.2	CONTACT COUPLING.....	68
4.3	COMPUTATIONAL METHODS	69
4.4	AU WIRE CONDUCTANCE	71
4.5	HÜCKEL-IV.....	73
4.6	ATK.....	78
4.7	DISCUSSION OF CONTACT STRUCTURE	85
4.8	MOLECULAR DYNAMICS	86
4.9	CONCLUSIONS ON MOLECULAR DYNAMICS	108
CHAPTER 5.	CONSTRUCTION OF A UHV-STM	111
5.1	MOTIVATION	112
5.2	DESIGN.....	112
5.3	CONSTRUCTION DETAILS	116
5.3.1	<i>Polishing the rails</i>	117
5.4	SILICON PASSIVATED SURFACE	119
5.5	COMPETING DESIGNS	121
CHAPTER 6.	QUANTUM INTERFERENCE	125
6.1	MOTIVATION AND OVERVIEW OF MOLECULAR ELECTRONICS RESEARCH	128
6.1.1	<i>The Simmons model</i>	131
6.1.2	<i>Quantum-interference transistors and quantum dots</i>	133
6.1.3	<i>Interference in model systems</i>	134
6.1.4	<i>Single molecules</i>	134
6.2	CONTROLLING ELECTRON FLOW	135
6.2.1	<i>Switch design</i>	136
6.2.2	<i>Voltage switch</i>	138
6.2.3	<i>Switching a molecule</i>	140
6.3	METHODS	143
6.4	TRANSMISSION AND COUPLING.....	144

	12
6.5	MODEL SYSTEMS CALCULATIONS..... 147
6.5.1	<i>Two site model</i> 147
6.5.2	<i>Four site model</i> 159
6.5.3	<i>Six site ring</i> 161
6.6	COMPARING MODEL SYSTEMS WITH REAL MOLECULES..... 169
6.6.1	<i>Meta & para connected benzene</i> 169
6.6.2	<i>Interference in fulvene</i> 171
6.7	INITIAL INTERFERENCE WORK..... 180
6.7.1	<i>Current from 0V transmission plots</i> 186
6.7.2	<i>Directionality of transport: a breakthrough molecule</i> 190
6.8	CROSS-CONJUGATION..... 192
6.8.1	<i>Bond length analysis</i> 196
6.8.2	<i>Transport through cross-conjugated molecules</i> 198
6.8.3	<i>Cross-conjugation: breaking the rules</i> 202
6.8.4	<i>Bigger cross-conjugated molecules</i> 207
6.9	ELECTRONIC DEPHASING 213
6.10	MOLECULAR DYNAMICS 215
6.11	CONTROLLING INTERFERENCE FEATURES 218
6.12	TRANSISTOR DESIGN 224
6.12.1	<i>Tuning the interference location: Simulated gate control and switching</i> 224
6.12.2	<i>Interference depth and the relative position of the Fermi level</i> 226
6.12.3	<i>A molecular transistor</i> 229
6.13	A MOLECULAR RECTIFIER 234
6.14	NEGATIVE DIFFERENTIAL RESISTANCE 243
6.15	CONCLUSION 244
CHAPTER 7.	OUTLOOK & PERSPECTIVE 247
REFERENCES 250
APPENDIX A. COMPUTER CODE 272
APPENDIX B. TRANSMISSION PLOTS CALCULATED IN HÜCKEL-IV 3.0 277
APPENDIX C. VITA 351

List of Illustrations

FIGURE 1-1. TWO SINGLE MOLECULE JUNCTIONS SHOWN FROM A RAMAN SPECTROSCOPY PERSPECTIVE AND A MOLECULAR ELECTRONICS PERSPECTIVE.	25
FIGURE 1-2. AN EXAMPLE OF A NANO-PARTICLE AGGREGATE THAT PRODUCED SINGLE MOLECULE SERS. ¹⁴	29
FIGURE 2-1. STM IMAGES OF HOPG	40
FIGURE 2-2. IMAGES OF HOPG IN AN ISOLATION CHAMBER AND IN OPEN AIR ON A MICROSCOPE.	41
FIGURE 2-3. STERIC ACID ADSORBED ON HOPG. THE STERIC ACID MOLECULE HAS A CHAIN LENGTH OF $\approx 2.5\text{nm}$	43
FIGURE 2-4. COMPARISON STM IMAGES OF TRIACONTANOL IN PHENYLOCTANE ON GRAPHITE. ¹⁰¹	43
FIGURE 2-5. Au(111) ON MICA SUBSTRATES. THE RECONSTRUCTION AND UNIAXIAL COMPRESSION OF THE SURFACE CAN BE SEEN.	45
FIGURE 2-6. HIGH RESOLUTION IMAGING OF THE Au(111) SURFACE IN 0.1 M H ₂ SO ₄	46
FIGURE 2-7. THE FIRST COLLECTION OF HIGH RESOLUTION UHV-STM IMAGES DETAILING THE STRUCTURE OF THE Au(111)	46
FIGURE 2-8. Au(111) HERRINGBONE RECONSTRUCTION IMAGES RECORDED IN UHV AT 4K. ¹⁰⁶	47
FIGURE 2-9. OCTANETHIOL MONOLAYER ON Au(111) ON MICA SUBSTRATE.....	48
FIGURE 2-10. DECANTHIOL MONOLAYER ON Au(111) ON MICA SUBSTRATE.	49
FIGURE 2-11. TWO STM IMAGES OF ORGANSULFUR MONOLAYERS ON Au.....	50
FIGURE 2-12. TWO UHV-STM IMAGES OF UNDECANETHIOL ON Au(111).....	50
FIGURE 2-13. AN STM IMAGE OF NANOWELL SURFACE COATED IN SILVER.	52

	14
FIGURE 3-1. MEASURING AU QUANTIZED CONDUCTANCE USING AN STM.	58
FIGURE 3-2. SCHEMATIC CIRCUIT DIAGRAM OF THE CURRENT-VOLTAGE CONVERTERS USED. (A) SHOWS A LINEAR PREAMPLIFIER AND (B) SHOWS THE QUASILOGARITHMIC PREAMPLIFIER. ¹²⁶	60
FIGURE 3-3. CALIBRATION OF THE LOGARITHMIC PREAMPLIFIER.	61
FIGURE 3-4. SIX EXAMPLE TRACES OF THE CONDUCTANCE AS A FUNCTION OF DISTANCE FOR SEPARATING A AU TIP FROM A AU SUBSTRATE IN THE PRESENCE OF 1,4-DIAMINO BENZENE.....	62
FIGURE 3-5. A HISTOGRAM OF 3000 CONDUCTANCE-DISTANCE TRACES OF 1,4-DIAMINO BENZENE ON A AU(111) ON A MICA SURFACE IN 1,2,4- TRICHLOROBENZNE.	64
FIGURE 3-6. A ZOOMED IN IMAGE OF FIGURE 3-5 SHOWING THE HISTOGRAM VALUES BELOW $1G_0$	65
FIGURE 4-1. AU WIRE CONDUCTANCE	72
FIGURE 4-2. THE CURRENT WITH INCREASING AU-S BOND LENGTH	75
FIGURE 4-3 TRANSMISSION COEFFICIENTS CALCULATED USING NEGF-DFT FOR BDT IN THE THREE FOLD FCC SITE.....	80
FIGURE 4-4. (A) AND (B) ILLUSTRATE THE HOMO AND THE LUMO LEVELS FOR THE BDT MOLECULE	81
FIGURE 4-5. TRANSMISSION COEFFICIENTS FROM NEGF-DFT UPON SYMMETRIC BREAKING OF THE AU-S BOND	83
FIGURE 4-6. MOLECULAR STATES AROUND THE FERMI ENERGY OBTAINED USING TRANSIESTA-C	84
FIGURE 4-7. THE IMAGE SHOWS MULTIPLE TIMESHOTS TAKEN FROM A 1NS TRAJECTORY OF A DITHIOL TERMINATED MOLECULE FREE TO MOVE BETWEEN TWO AU ELECTRODES.....	89
FIGURE 4-8. THE AU-SURFACE POTENTIAL DESCRIBED BY AN EXPONENTIAL-6 TYPE FUNCTION.	92

	15
FIGURE 4-9. THE P-BENZENEDIAMINE JUNCTION SHOWN WITH THE AU ADATOMS ATTACHED. IN THE HÜCKEL CALCULATIONS ONLY THE AU ADATOM AND ITS 3 NEAREST AU ATOMS ARE INCLUDED IN THE CALCULATION.....	94
FIGURE 4-10. (A) THE CONDUCTANCE OF A CHEMISORBED P-BENZENEDITHIOL MOLECULE BETWEEN AU ELECTRODES.....	97
FIGURE 4-11. THE VARIATION IN CONDUCTANCE AS A FUNCTION OF ENERGY	98
FIGURE 4-12. COMPARISON OF A GAUSSIAN AND LORENTZ FIT TO HISTOGRAM OF CONDUCTANCE DATA.	100
FIGURE 4-13. GAUSSIAN CURVES FIT TO 500 GEOMETRIES FOR A CHEMISORBED P-BENZENDITHIOL MOLECULE.....	101
FIGURE 4-14. TEMPERATURE DEPENDENCE FOR A AU- CHEMISORBED P-BENZENDITHIOL-AU JUNCTION	102
FIGURE 4-15. A CHEMISORBED P-BENZENEDIAMINE MOLECULE BETWEEN AU ELECTRODES AT A FIXED SEPARATION DISTANCE OF 11 ANGSTROMS.....	104
FIGURE 4-16. A CHEMISORBED P-BENZENEDIAMINE MOLECULE BETWEEN AU ELECTRODES AT A VARIED AU ELECTRODE DISTANCE.....	106
FIGURE 4-17. (A) CONDUCTANCE VERSUS ELECTRODE-ELECTRODE DISTANCE FOR BOTH THE CHEMISORBED P-BENZENEDITHIOL AND THE CHEMISORBED P-BENZENEDIAMINE MOLECULES	107
FIGURE 5-1. A SCHEMATIC SHOWING THE INTEGRATION OF THE UHV-STM WITH BROAD LASER TUNABLIITY FROM 233-1600NM.	114
FIGURE 5-2. DETAIL OF UHV CHAMBER EXTERIOR HARDWARE.....	115
FIGURE 5-3. DETAIL OF UHV CHAMBER INTERIORS AS VIEWED THROUGH THE FRONT WOBBLSTICK FLANGE VIEWPORTS.....	116
FIGURE 5-4 . A FULLY POLISHED BERYLLIUM COPPER RAIL.	118

	16
FIGURE 5-5. FAILED COATING OF THE BERYLLIUM COPPER RAILS WITH TITANIUM NITRIDE.	119
FIGURE 5-6. SCANNING TUNNELING MICROSCOPE IMAGES OF A HYDROGEN PASSIVATED <100> SILICON SURFACE. ¹⁷¹	120
FIGURE 5-7. TWO Si(100) IMAGES FROM PUBLISHED MANUSCRIPTS.....	121
FIGURE 6-1. THE TRANSMISSION PROBABILITY IS A SUM OF THE ORIENTATION-DEPENDENT TRANSPORT CHANNELS BETWEEN SOURCE/DONOR- MOLECULAR ORBITALS – DRAIN/ACCEPTOR. THE ELECTRON “SEES” ALL AVAILABLE MOLECULAR ORBITAL PATHWAYS IN ENERGY SPACE.	132
FIGURE 6-2. IN AN IDEAL SWITCH THE OFF STATE WOULD BE A PERFECT INSULATOR (BLUE LINE AT 0 G Ω) AND THE ON STATE WOULD BE A PERFECT CONDUCTOR (RED LINE AT 1 G Ω)	137
FIGURE 6-3. THE TRANSMISSION AND CURRENT/VOLTAGE BEHAVIOR OF A PERFECT VOLTAGE SWITCH IS SHOWN SCHEMATICALLY, WHERE THE CONDUCTANCE GOES FROM 0 TO ~1G Ω AS A FUNCTION OF VOLTAGE	139
FIGURE 6-4. SWITCHING SHOWN IN TRANSMISSION PLOTS	142
FIGURE 6-5. THE COUPLING, T _{DA} , FOR THE LINEAR (SHOWN IN BLACK) AND PERPENDICULAR (SHOWN IN RED) TWO SITE MODELS.....	151
FIGURE 6-6. TRANSMISSION THROUGH A TWO SITE MODEL	152
FIGURE 6-7. THE CONTRIBUTIONS TO THE COUPLING FROM EACH MOLECULAR CONDUCTANCE ORBITAL OF THE TWO 2-SITE SYSTEMS	155
FIGURE 6-8. THE PHASE OF THE TRANSMISSION THROUGH EACH MOLECULAR CONDUCTANCE ORBITAL (TOP) AND THE TOTAL PHASE OF THE TRANSMISSION (BOTTOM) FOR THE TWO 2-SITE SYSTEMS.	156
FIGURE 6-9. PARAMETRIC PLOTS FOR THE TRANSMISSION THROUGH BOTH TWO SITE SYSTEMS.	158

FIGURE 6-10. 4 SITE MODEL SYSTEM WITH SIX POSSIBLE DONOR-ACCEPTOR COUPLINGS. IN ALL MODEL SYSTEMS WITH A SIDE GROUP THERE IS AN ANTIRESONANCE FEATURE, ALTHOUGH NOT NECESSARY AT $E=0$.	160
FIGURE 6-11. THE 6-MEMBERED RING MODELS. ALL MODELS INCLUDE THE BLACK ELECTRODE, THE 6-MEMBERED RING AND ONE OF THE OTHER ELECTRODES, SPECIFICALLY THE ORTHO, META AND PARA CONNECTIONS USE THE BLUE, RED AND GREEN CONNECTIONS RESPECTIVELY. ²¹⁴	161
FIGURE 6-12. THE 6-MEMBERED RING MODELS. ALL MODELS INCLUDE THE BLACK ELECTRODE, THE 6-MEMBERED RING AND ONE OF THE OTHER ELECTRODES, SPECIFICALLY THE ORTHO, META AND PARA CONNECTIONS USE THE BLUE, RED AND GREEN CONNECTIONS RESPECTIVELY. ²¹⁴	162
FIGURE 6-13. THE CONTRIBUTIONS TO THE COUPLING FOR THE THREE 6-MEMBERED RING SYSTEMS WITH ORTHO, META AND PARA CONNECTIONS TO THE ELECTRODES	164
FIGURE 6-14. COUPLING CALCULATIONS WITH A SINGLE SITE ENERGY CHANGE IN A META-CONNECTED SIX SITE MODEL.	166
FIGURE 6-15. COUPLING CALCULATIONS THROUGH A META CONNECTED SIX SITE MODEL WITH A CHANGING SITE ENERGY.	168
FIGURE 6-16. THE TRANSMISSION THROUGH META AND PARA BENZENE	170
FIGURE 6-17. A FULVENE MOLECULE CAN BE CONNECTED TO ELECTRODES IN 6 DIFFERENT CONFIGURATIONS	172
FIGURE 6-18. TRANSMISSION CALCULATED THROUGH FULVENE MODEL SYSTEMS D1A3 AND D1A4.	172
FIGURE 6-19. TRANSMISSION CALCULATED THROUGH FULVENE MODEL SYSTEMS D3A4 AND D3A5.	174
FIGURE 6-20. TRANSMISSION CALCULATED THROUGH FULVENE MODEL SYSTEMS D3A6 AND D4A5.	175
FIGURE 6-21. FULVENE TRANSPORT CALCULATIONS USING HÜCKEL-IV.	177

	18
FIGURE 6-22. COUPLING AND TRANSMISSION COMPARED FOR 6 DIFFERENT POSSIBLE CONFIGURATIONS	179
FIGURE 6-23. PUBLISHED FANO RESONANCES IN TRANSMISSION PLOTS.....	180
FIGURE 6-24. INITIAL CALCULATIONS ON FANO RESONANCE CALCULATED USING ATK.....	181
FIGURE 6-25. THE TRANSMISSION THROUGH A META AND A PARA CONNECTED BENZENE CALCULATED USING HÜCKEL-IV 3.0. THE META CONNECTED BENZENE MOLECULE HAS NEARLY TWO ORDERS OF MAGNITUDE LOWER TRANSMISSION AND THEREFORE CONDUCTANCE AT LOW BIAS.....	183
FIGURE 6-26. TRANSMISSION PLOTS FOR A SERIES OF 3 MOLECULES INCLUDING A INTERFERENCE SEEN IN A π STACKED MOLECULE.....	184
FIGURE 6-27. CURRENT VOLTAGE CURVES ARE SHOWN FOR THE THREE MOLECULES, USING HÜCKEL IV IN THE FIRST GRAPH AND ATK WITH DISCRETE DATA POINTS IN THE SECOND PLOT.....	186
FIGURE 6-28. COMPARISON OF CURRENT/VOLTAGE RESULTS FROM INTEGRATING 0V TRANSMISSION AND CALCULATIONS AT DISCRETE BIAS VOLTAGES.....	187
FIGURE 6-29. INTERFERENCE IN TRANSMISSION THROUGH π STACKED SIX MEMBERED PHENYL RINGS CALCULATED IN GDFTB.....	189
FIGURE 6-30. THE TRANSMISSION THROUGH ETHENE-1,1-DITHIOL SHOWING A DAMPED INTERFERENCE FEATURE DUE TO THE HYDROGEN-GOLD INTERACTION.	191
FIGURE 6-31. RESONANCE STRUCTURES FOR A CROSS-CONJUGATED MOLECULE	193
FIGURE 6-32. THE BONDING GEOMETRY OF A MOLECULE BRIDGING SOURCE AND DRAIN ELECTRODES CONTROLS	194
FIGURE 6-33. THE TRANSMISSION AND CURRENT THROUGH A CROSS-CONJUGATED MOLECULE (1) COMPARED WITH ITS LINEARLY CONJUGATED COUNTERPARTS (2 AND 3)	195

FIGURE 6-34. A BOND LENGTH ANALYSIS FOR A SERIES OF MOLECULES WITH SECTIONS OF CONJUGATED, NON-CONJUGATED AND CROSS-CONJUGATED CARBON ATOMS	197
FIGURE 6-35. TRANSMISSION AND CURRENT-VOLTAGE CALCULATED IN HÜCKEL-IV 3.0 FOR MOLECULES 4 , 5, 9 AND 14	199
FIGURE 6-36. THESE PLOTS SHOW TRANSMISSION AND I/V CALCULATED FOR THE SAME MOLECULES, 4,5,9 & 14, USING ATK.....	200
FIGURE 6-37. THESE TWO PLOTS SHOW A LINEAR FIT ($I=BV$) TO THE I/V DATA CALCULATED USING HÜCKEL- IV SHOWN ON A LOG/LOG SCALE.....	201
FIGURE 6-38. THE “LONG” AND “SHORT” SYSTEMS ARE DEFINED AS TWO DIFFERENT METHODS OF ATTACHING THE MOLECULE ON THE LEFT TO TWO GOLD ELECTRODES	203
FIGURE 6-39. THE MOLECULAR ORBITAL EIGENENERGIES FOR THE ISOLATED MOLECULES (LEFT) SHOW THE LARGE BAND GAP TYPICAL IN THE SATURATED SYSTEM AND THE MUCH SMALLER GAP IN THE CONJUGATED SYSTEMS	204
FIGURE 6-40. THE TRANSMISSION (LEFT) AND CURRENT (RIGHT) THROUGH THE LONG SYSTEM (GREEN), SHORT SYSTEM (RED) AND DTP (BLACK)	206
FIGURE 6-41. THE ZERO BIAS TRANSMISSION AS A FUNCTION OF ENERGY AND THE CURRENT AS A FUNCTION OF VOLTAGE FOR A GROUP OF COMPARABLE MOLECULES ILLUSTRATING THE UNUSUAL TRANSPORT CHARACTERISTICS OF A CROSS-CONJUGATED SYSTEM	209
FIGURE 6-42. THE ZERO BIAS TRANSMISSION AS A FUNCTION OF ENERGY AND THE CURRENT AS A FUNCTION OF.....	210
FIGURE 6-43. THE TRANSMISSION THROUGH 4 SHOWING INTERFERENCE FEATURES IN THE π SYSTEM TRANSMISSION. THE BLACK TRACES INDICATES TOTAL TRANSMISSION, THE RED TRACES INDICATE TRANSMISSION THROUGH THE Σ SYSTEM IN THE TOP PLOT AND TRANSMISSION THROUGH THE π SYSTEM IN THE BOTTOM PLOT.....	211

FIGURE 6-44. THE TRANSMISSION THROUGH 6 SHOWING NO INTERFERENCE FEATURES IN THE π SYSTEM TRANSMISSION. THE BLACK TRACES INDICATES TOTAL TRANSMISSION, THE RED TRACES INDICATE TRANSMISSION THROUGH THE Σ SYSTEM IN THE TOP PLOT AND TRANSMISSION THROUGH THE π SYSTEM IN THE BOTTOM PLOT.....	212
FIGURE 6-45. ELECTRONIC DEPHASING EFFECTS CALCULATED FOR META & PARA BENZENE COMPARED WITH LINEAR AND CROSS-CONJUGATED SITE REPRESENTATIONS. THE DECAY TIME IS DEFINED AS THE TIME NECESSARY FOR THE TOTAL POPULATION TO DECREASE 95%.....	214
FIGURE 6-46. MOLECULAR DYNAMICS RESULTS FOR MOLECULES 5,9,14	217
FIGURE 6-47. THE TRANSMISSION THROUGH 4 FOR 50 DIFFERENT GEOMETRIES OBTAINED FROM MOLECULAR DYNAMICS CALCULATIONS. IMPORTANTLY, THE ANTIRESONANCE IS PRESENT IN ALL CASES.....	218
FIGURE 6-48. TUNING THE DEPTH AND WIDTH OF A MOLECULAR INTERFERENCE FEATURE.....	220
FIGURE 6-49. ALL CALCULATIONS IN THIS PLOT WERE DONE USING GDFTB TO DIFFERENTIATE BETWEEN THE Σ AND π TRANSPORT	222
FIGURE 6-50. THIS PLOT GIVES A COMPARISON OF THE TRANSMISSION RESULTS FOR THE 4 MOLECULES SHOWN ABOVE CALCULATED IN GDFTB AND HÜCKEL-IV	223
FIGURE 6-51. ELECTRON DONATING AND WITHDRAWING GROUPS ATTACHED TO THE CROSS-CONJUGATED UNIT. THE INTERFERENCE FEATURE IS SHOWN TO BE TUNED $\pm 1.5\text{eV}$ FROM THE FERMI LEVEL BY CHANGING THE ELECTRON DENSITY ON THE CROSS-CONJUGATED BOND. THE QUALITATIVELY SIMILAR RESULTS CALCULATED USING ATK ARE GIVEN IN THE SUPPORTING INFORMATION.	226
FIGURE 6-52. THE SHIFTING OF THE INTERFERENCE LOCATION BY CHANGING THE SUBSTITUENTS.....	228
FIGURE 6-53. THE UPPER HALF OF THIS PLOT IS A REPRODUCTION OF FIGURE 6 IN THE MAIN TEXT. CALCULATIONS MADE USING HÜCKEL-IV ARE SHOWN IN (A) AND (B) WHILE CALCULATIONS MADE USING ATK ARE SHOWN IN (C) AND (D).....	229

FIGURE 6-54. A SYMBOL FOR THE PROPOSED “CROSS-CONJUGATED MOLECULAR TRANSISTOR”	230
FIGURE 6-55. CALCULATIONS OF CONDUCTANCE CHANGE WITH APPLIED GATE VOLTAGE IN THREE TEST MOLECULES	233
FIGURE 6-56. IN MOLECULES WITH MULTIPLE CROSS-CONJUGATED UNITS, AN APPLIED BIAS VOLTAGE WILL SPLIT THE INTERFERENCE FEATURES.	236
FIGURE 6-57. TRANSMISSION SPECTRUM CALCULATED USING GDFTB, ATK AND HÜCKEL-IV	238
FIGURE 6-58. RECTIFIER BEHAVIOR MAXIMIZED IN THE HÜCKEL IV TRANSPORT CODE	240
FIGURE 6-59. THE VOLTAGE DEPENDENT TRANSMISSION FOR THE PROPOSED MOLECULAR RECTIFIER.	242
FIGURE 6-60. TRANSMISSION PLOTS FOR THE MOLECULE SHOWN IN FIGURE 6-58 CALCULATED USING GDFTB, HÜCKEL-IV 3.0 AND ATK.	243

List of Tables

TABLE 1-1. SINGLE MOLECULE RESISTANCE FOR 1,8-OCTANEDITHIOL CALCULATED FROM LOW BIAS CONDUCTANCE.	33
TABLE 1-2. SINGLE MOLECULE RESISTANCE FOR BENZENEDITHIOL CALCULATED FROM LOW BIAS CONDUCTANCE.	33
TABLE 1-3. THE TABLE PROVIDES A LOOK AT THE RESEARCH CONDUCTED TO DATE ON TOPICS THAT INCLUDE THE TERM "SINGLE MOLECULE" AS INDICATED BY A LITERATURE SEARCH USING SCIFINDER.	36
TABLE 4-1. TOTAL MULLIKEN CHARGE ON S ATOMS WITHIN THE JUNCTION, CALCULATED AT EQUILIBRIUM USING TRANSIESTA-C.	79
TABLE 4-2. THE MM3 FORCE FIELD PARAMETERS USED WITHIN TINKER	90
TABLE 6-1. A NUMERICAL COMPARISON OF CURRENT/VOLTAGE RESULTS FROM INTEGRATING 0V TRANSMISSION ($V_{OV,TE}$) AND CALCULATIONS AT DISCRETE BIAS VOLTAGES (V_{SCF})	188

Chapter 1. Addressing Individual Molecules

Chemistry “is the science that deals with the composition, structure, and properties of substances and with the transformations they undergo.”² Over 2500 years ago, Democritus developed a theory of physical processes that included only the void and atoms. The atoms are “invisible; absolutely small, so small that their size cannot be diminished....differences of quality are only apparent, owing to the impressions caused on our senses by different configurations and combinations of atoms.”³ For over 2500 years, the study of chemistry has focused on the ensemble averaged behavior of molecules made up of different combinations of these atoms. Chemical understanding of what happens to the ensemble averaged molecules, which allows visualization and testing of the properties of new substances, has brought the field of chemistry to the forefront of the physical sciences.

In the past few decades, a new era of chemical control has opened up that deals with the ability to manipulate and image single molecules. It is at the level of a single molecule that we can fully discern the intrinsic properties of a molecule and how it interacts with its surroundings, including other molecules, solvents, or surfaces. Without ensemble averaging, we will be able to discern if the characteristics of a bulk sample are dominated by the behavior of a small number of molecules within that sample. Direct understanding of the behavior of a single molecule will afford much greater control in many aspects of chemistry, from drug design to electronics.

In the time I have spent in graduate school, there has been a large amount of hyperbole in the media and popular culture about the great potential for nanotechnology. While nanotechnology research represents progress as usual in the scientific fields, it also represents

the convergence of the scientific disciplines, creating great scientific potential in the exchange of ideas between what are traditional separate research fields. The research here focuses on the limit of a single molecule junction, from the perspective of a chemist, in a research area rich with physicists, electrical engineers, and materials scientists.

This work starts with a review what has been accomplished and understood at the single molecule level. With a thorough understanding of work to date on molecular junctions and single molecule behavior, I will provide motivation for my research.

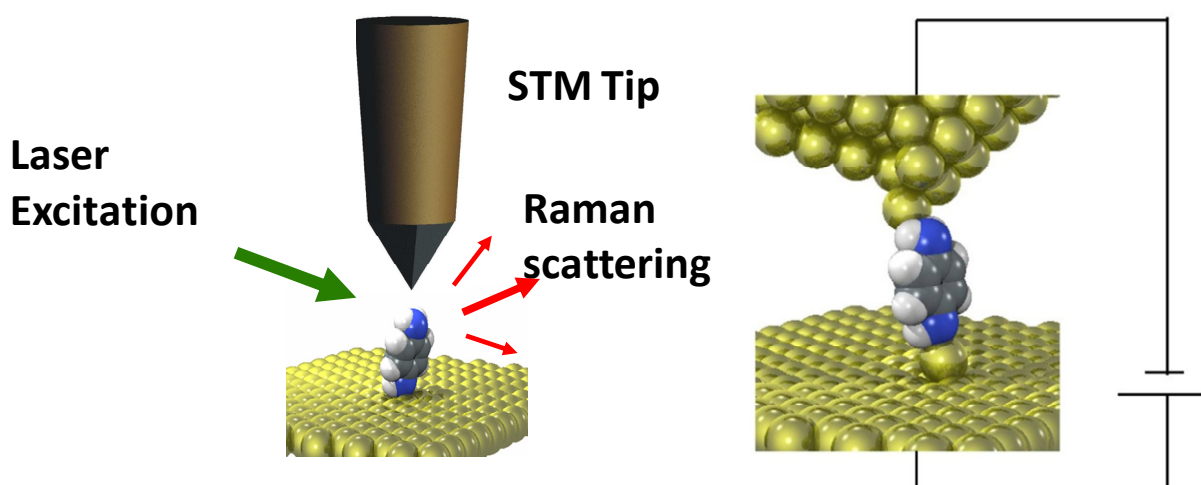


Figure 1-1. Two single molecule junctions shown from a Raman spectroscopy perspective and a molecular electronics perspective.

1.1 Electrical measurements

Charge transport has traditionally been an area of study for electrical engineers and those in related fields. With the miniaturization of electronic elements, the traditional methods of understanding charge transport break down, as quantum mechanical effects come to

dominate the transport behavior. One example of this interesting behavior is the increase in resistance with decreasing size of a metallic wire. Two corrections to Ohm's law are necessary as we approach a single atom wire; there is an interface resistance independent of length, and the resistance changes in quantized values.⁴ At the limit of a single transport channel, or a single Au atom, the resistance of the wire is $12,910\Omega$. It is in this regime, where the charge transport is defined and limited by the molecular or atomic energy levels, that we focus our attention.

The potential for single molecules to be used as discrete electronic elements was raised in the mid-1970s.⁵ Since this time, there has been a large amount of research on understanding charge transport through two-probe systems and the possibility of using molecules as circuit elements. Experimental measurements on single molecules require the ability to manipulate, control, and observe on the angstrom length scale. This level of control has only become possible with recent technological advances. At this level of control, the experiments remain complicated and time consuming.

A more detailed understanding of molecules under a bias voltage, the location of the binding site, the interaction with electrodes, the role of vibrations and thermal motion, and the interactions with the surroundings are a few of the important elements of molecular junctions that are not fully understood. It is our desire to get as much information as possible about molecular junctions and charge transport by the integration of single molecule charge transport measurements with single molecule spectroscopic measurements.

1.2 Spectroscopic measurements

The quest to understand single molecule behavior is not limited to electronics, but there is a convergence of interest within all of chemistry. The motivation to understand single molecule behavior is driven by the ability to control and visualize behavior on the atomic scale. Today, chemical spectroscopic techniques with single molecule resolution are nearly commonplace.

1.2.1 Surface enhanced Raman spectroscopy

The inelastic light scattering off molecules was first noted and seen by C.V. Raman and K. S. Krishnan in the late 1920s.⁶ The probability of an inelastically scattered photon is on the order of one per million scattered photons. This extreme insensitivity limited the usefulness of Raman spectroscopy as a chemical technique. Experimental results in the mid-1970s of pyridine Raman spectra on electrochemically-roughened silver produced inexplicably large spectral peak intensities.⁷ A few years later, this experimental result was repeated and shown not to be a purely surface area effect.⁸ The five to six orders of magnitude enhancement over normal Raman scattering was proposed to occur on any active molecule adsorbed to a roughened noble metal surface, becoming known as surface-enhanced Raman scattering (SERS).⁹ Through improvements in collection efficiency, along with an increase in the engineering of high electromagnetic field enhancing substrates, the inherently weak Raman scattering has now been collected from single molecules.

1.2.2 Single molecule surface enhanced Raman spectroscopy

Single molecule Surface Enhanced Raman Spectroscopy (SMSERS) was first reported at the end of the 1990s by two independent research groups.^{10,11} The work by Nie et al.,

measured the spectrum of rhodamine 6G absorbed on $\approx 35\text{nm}$ Ag nano-particles and their aggregates.¹⁰ It was estimated that the measurements of SERS occurred only in situations where a high signal enhancement factor of 10^{14} occurred. Evidence for single molecule behavior was given by the use of low analyte concentration, polarization dependence of the signal, and spectral changes with respect to time. It was estimated that only 1 in 100-1000 particles and only 1 in 10,000 sites per nano-particle had the necessary conditions for single molecule behavior to be observed.¹⁰ Using atomic force microscopy to image "hot spots," both single particles and aggregates of particles were seen. The Kneipp group measured spectra from 100-150nm Ag clusters dosed with crystal violet molecules at an estimated concentration of 0.6 molecules per nanocluster.¹¹ Both of these single molecule measurements required specific molecules that provided resonant enhancement of the Raman signal.

The proof of single molecule SERS behavior is non-trivial and still remains a relevant issue in current research ten years after the first experiments. In the work by Kneipp et al.,¹¹ a histogram was created of the signal intensity of a specific Raman band for 100 measurements. A Poisson fit with $n=0.5$ shows peaks attributed to having a quantized number of molecules. This analysis has been strongly questioned in the literature, mostly with regard to the assumption, that the signal intensity occurs in quantized multiples, needed for a Poisson fit.^{12,13} The use of a Poisson distribution requires the assumption that intensity fluctuations from localized hotspots on the surface are negligible, in disagreement with the established precedent. Verification of single molecule behavior using more than one technique should provide added confirmation and information on junctions.

Recent work from our group has eloquently proven single molecule behavior by measuring the Raman spectrum from two isotopologues of rhodamine 6G.¹⁴ Even utilizing tunneling electron microscopy (TEM) to investigate single molecule “hot spots,” there is a large amount of speculation as to the exact structures that provide large enough enhancement factors to enable single molecule SERS. An example of one of the many different Ag nano-particle aggregates that can lead to single molecule SERS is shown in Figure 1-2.¹⁴ The smallest structure correlated with a “hot spot” that has been measured to date in our lab is a two particle T shaped structure.¹⁵

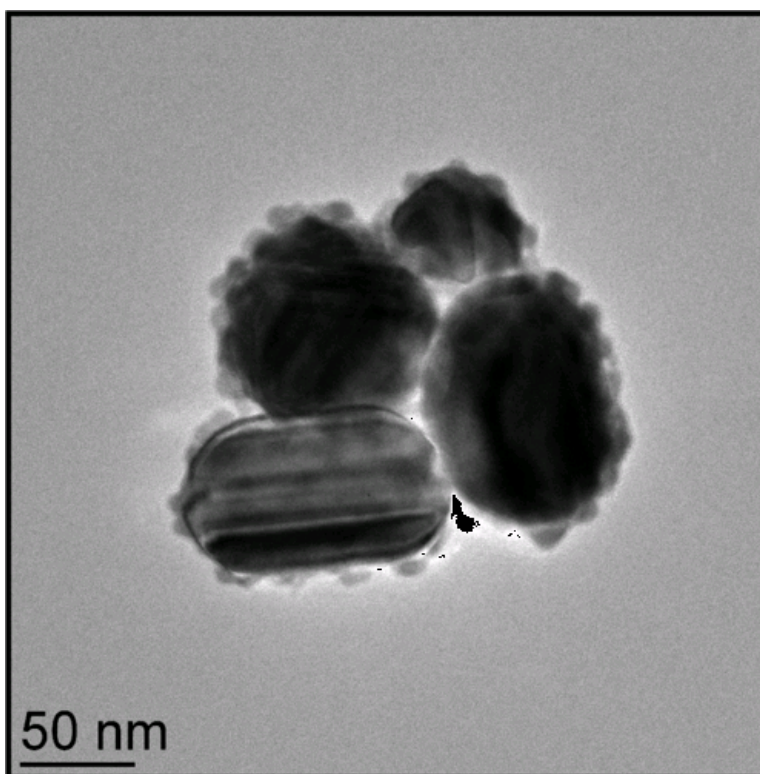


Figure 1-2. An example of a nano-particle aggregate that produced single molecule SERS.¹⁴

While single molecule SERS behavior has been tested using biologically significant compounds,^{16,17} greater control and understanding of the structures that enable single molecule sensitivity will surely increase its application base. In attempting to understand fully large SERS enhancements, detailed images of the SERS active surfaces would greatly aid and develop our understanding. The TEM method provides information on the large scale features of the surface, but we would like a more detailed imaging of the surface provided by scanning probe techniques.

1.2.3 Tip enhanced Raman spectroscopy

In tip enhanced Raman spectroscopy (TERS) a sharp metal tip is used as the enhancing substrate necessary to create surface enhanced Raman spectroscopy.¹⁸⁻²⁰ This direct connection to scanning probe technology provides much of the motivation for this research project, specifically the recent extension of the sensitivity to the single molecule level.²¹⁻²³ The experiments to date, reporting single molecule sensitivity, do so on resonantly enhanced molecules indicating that extension of the technique to a wider range of molecules will require technical advances or better designed experimental situations. The design of our optical nanoprobe instrument starts from the foundation of a high performance STM²⁴ and adds optical access to the tip sample junction.

1.2.4 Fluorescence

Fluorescence spectroscopy has also developed into a useful technique for single molecule studies. Single molecule fluorescence studies currently enjoy greater popularity than single molecule Raman spectroscopy but do not provide detailed vibrational information. The single

molecule studies developed from the measurements of low concentrations of pentacene in p-terphenyl crystals.^{25,26} The advance to making measurements in near field then far field microscopies has rapidly increased the popularity of single molecule fluorescence, with wide use in biological applications²⁷⁻²⁹

1.3 Calculating single molecule behavior

Understanding of charge transport through molecules has developed in large part due to the study of donor-bridge acceptor systems.³⁰⁻³³ The Landauer formalism, which forms the basis for many transport calculations, treats the coherent transport as the product of the quantum of conductance (G_0) and the probability of electron scattering.³⁴⁻³⁶

1.3.1 Computational methods

Calculations on transport properties in the coherent low bias regime have focused on the Landauer method of scattering probability using non-equilibrium Green's functions (NEGF).³⁴ Solving the Green's function is an iterative process where the potential field and the number of electrons are dependent variables.^{4,34,37,38} These methods have been implemented in many codes, including three used here: Hückel IV³⁹ through Purdue University, which utilizes an extended Hückel Hamiltonian matrix, gDFTB⁴⁰⁻⁴⁴, and ATK (formerly Transiesta),⁴⁵⁻⁴⁸ where both of these calculate the matrix elements using density functional theory(DFT).

1.4 Single molecule junctions

In the past twenty years, methods utilized to make and measure atomic wires with quantized conduction channels have included conductive atomic force microscopy (AFM);⁴⁹ mechanically controlled break junctions,⁵⁰⁻⁵² including solid state relays;⁵³ and scanning

tunneling microscopy (STM),⁵⁴⁻⁵⁹ including measurements made in ambient conditions.^{56,57}

Gold wires have been imaged at the single atom limit using electron microscopy⁶⁰, with surprising stability attributed to the limited number of vibrational modes.⁶⁰⁻⁶³

Initial single molecule measurements were made using many of the above techniques, including conductive AFM on isolated dithiol molecules attached to nanoparticles in a monothiol monolayer.⁶⁴⁻⁶⁶ STM has been used to create a large number of break junctions in the presence of molecules with peaks in the histograms of the current versus distance traces attributed to quantized molecular conductance.^{67,68}

1.5 Scanning probe break junctions

Using scanning probe techniques to address single molecules has become a standard in the field. This method has the benefit of being able to quickly create a large number of molecular junctions. The results from scanning probe techniques leave something to be desired in the ease of experimental reproducibility.⁶⁹

1.5.1 Measured conductance

An overview of the measured and calculated results for two common test molecules, 1,8-octanedithiol and para-benzenedithiol, are given in Table 1-1 and Table 1-2 respectively. The purpose of these tables is not to be a fully exhaustive list of the experimental results but to highlight the large 2 order of magnitude discrepancies within experimental measurements and in comparison to theoretical work.

Another important way to make a comparison between experimental and theoretical results is the comparison of trends for a group of related molecules. Doing this provides a much better agreement between theory and experiment. The tables indicate that it is difficult to make single molecule measurements, and a method to verify independently the structure of the molecular junction, the binding site, and the number of molecules in the junction would all greatly aid in the analysis of experimental data.

Table 1-1. Single molecule resistance for 1,8-octanedithiol calculated from low bias conductance.

1,8-octanedithiol	Method	Year	Resistance
Experimental			
	Coulomb blockage, nanocluster ⁷⁰	1995	~9 M Ω
	AFM tip/ Au clusters ⁶⁵	2001	900(+ - 50) M Ω
	AFM tip ⁶⁷	2003	~ 51 M Ω
	STM tip, current vs. distance I (s) ⁶⁷	2003	51(+ - 5) M Ω
	STM tip, current vs. time I(t) ⁷¹	2004	1010(+ - 69) M Ω
	UHV STM I(s) ⁷²	2006	993 M Ω
	AFM tip/ Au clusters ⁷³	2007	62 M Ω , 18 M Ω
Theory			
	B3LYP/CEP-31G ⁷⁴	2004	22 M Ω
	B3YLP/LANL2DZ		15 M Ω

Table 1-2. Single molecule resistance for benzenedithiol calculated from low bias conductance.

BDT	Method	Year	Resistance
Experimental			
	Mechanically controlled break junction ⁷⁵	1997	~22 M Ω
	STM I(s) ⁷⁶	2003	1.174 M Ω
	STM I(s) ⁶⁹ (very broad distribution)	2006	0.30 M Ω

Calculations			
	Extended Hückel, 3 fold contact ⁷⁷	1996	4 M Ω (low bias)
	First Principle Au-PDT-Au ⁷⁸	2000	at 10mv 96 M Ω
	Al-PDT-Al, has P orbital coupling ⁷⁸	2000	at 10mv 2.9M Ω
	UBPW91/6-31G*/SCF Green's Function, 3 fold contact to electrode ⁷⁹⁻⁸¹	2004	~5 M Ω (linear -1(V)to +1(V), calculated from IV graph)
	DFT, siesta ⁸²		20 K Ω – 1.2 M Ω
	Planar arrangement ⁷⁴ B3LYP/CEP-31G B3YLP/LANL2DZ	2004	0.85 M Ω 0.29 M Ω
	Molecular dynamics and Hückel-IV ⁸³	2008	1.78 M Ω \pm 0.8 M Ω

The large discrepancy in experimentally measured conductance is due to the difficulty of making and controlling single molecule wires, compounded with the inability to verify directly that a single molecule is bridging the electrodes. Calculations of molecular conduction still do not effectively address the complexity of molecular motion and contact rearrangement under bias. Small changes in the orientation of the molecule and the arrangement of the contact atoms can lead to conductance variation of a few orders of magnitude.^{80,82,84} Complexity increases with junctions composed of multiple molecules in close proximity,⁸⁵ as well as with environmental effects such as solvation and gate modulation.

1.5.2 Single molecule inelastic electron tunneling spectroscopy

In inelastic tunneling spectroscopy (IETS), the second derivative of the current-voltage behavior of a molecule is analyzed. Peaks or dips in the second derivative occur when the energy of the incident electron interacts with a molecular vibration. Typically, when an incident electron interacts with a molecular vibration, it opens up a new transport pathway resulting in an increase in the current. Single molecule IETS has been measured using two different

experimental techniques. In IETS experiments using a scanning tunneling microscope the molecule of interest is held directly under an atomically sharp probe and the current voltage measurement is taken. Using mechanically controlled break junctions⁸⁶ or electromigration junctions has allowed these measurements in junctions with strong coupling to both electrodes.^{87,88}

With increasing temperature, the vibrational resonances broaden in energy and, correspondingly, the features in the second derivative broaden, making measurements at temperatures above 77K generally impractical. Even at liquid helium temperatures, this is a high noise measurement requiring the use of a lock-in amplifier and large numbers of sequential data points to create a meaningful spectrum. IETS has an absence of vibrational selection rules as found in IR, Raman, and HREELS, yet all vibrations are not observed.^{89,90} The use of Raman spectroscopy on molecules under voltage bias in a junction should provide additional vibration information.

1.5.3 Force spectroscopy and other single molecule techniques

Single molecule force spectroscopy has developed from the use of atomic force microscopy (AFM) with atomic resolution⁹¹⁻⁹³ and, importantly, the ability to break and measure the strength of single covalent bonds⁹⁴. It is now possible to use mechanical control with AFM to directly measure forces greater than 3 pN, including the entropic change in polymers⁹⁵⁻⁹⁷, supramolecular reorganization, bond angle deformation, and the rupture of covalent bonds^{97,98}.

There are a number of different methods to study single molecule behavior. It is helpful to get an idea of which methods of research are current being pursued within the field. To gauge

the current research we analyze the results for a specific search term. Searching for the phrase “single molecule” using SciFinder scholar to search the literature, we find 9245 results. In Table 1-3, the results are shown with the addition of an additional search term. The term fluorescence is present in over 37% of the “single molecule” results. Force spectroscopy and electronics are also present in a large number of results. In the following sections, we focus on single molecule electronics and conductance while striving towards integration with single molecule tip enhanced Raman.

Table 1-3. The table provides a look at the research conducted to date on topics that include the term “single molecule” as indicated by a literature search using SciFinder.

SciFinder search for “single molecule” with an additional word added			
9245 total results			
results	added term	results	added term
3421	fluorescence	319	junction
1566	force	296	Raman
1307	electronics	266	trap
1295	optical	191	STM
737	calculation	188	SERS
601	device	126	inelastic
499	AFM	104	scanning probe
495	conductance	28	IETS
413	FRET	10	tip enhanced Raman

1.6 Motivation

The motivation for this work is to understand and control molecular junctions and interfaces. Nanometer scale features contacted to single molecules in materials that support plasmon resonances led to measurable Raman scattering. Scanning tunneling microscopy allows imaging of the electronic density of states at sub Angstrom resolution. Both techniques

independently allow measurement of the behavior of single molecules in well controlled experimental situations. Integration of these two techniques will enable cross conformation as well as a more detailed look at single molecule junctions. Specifically, the two main goals are to understand charge transport through molecular junctions in the design of potential molecular electronics devices, and to determine the optimal structures for maximum Raman enhancement.

1.7 Note on published work

Parts of this dissertation are taken directly from published or soon to be published work, specifically sections of chapters 4 and 6.

Chapter 2. STM imaging

With the invention of the scanning tunneling microscope⁹⁹ in the early 1980s, the ability to address single atoms became possible. The first atomic scale images were taken of the surface of Au(110) and CaIrSn₄ (110).⁹⁹ This technique has developed into a whole field of research exploiting the ability to image surfaces with resolution ranging from the nanometer to sub-angstrom length scale.

The experimental results presented in this section were collected using a commercially available scanning probe microscope from Agilent technologies (formally Molecular Imaging). The PicoPlus scanning probe microscope is an integrated STM/AFM system. The scanner is oriented on a vertical axis with the tip facing down to an upward facing sample. The upward facing sample allows the use of imaging in liquid solutions with electrochemical control. The tip is held in place by friction to a cylindrical tube soldered directly into a current to voltage preamplifier board. Our lab has three preamplifiers for this instrument which allow imaging at 0.1pA/V, 1nA/V and 1000nA/V. There is also a 10x gain switch built into the top of the scanner implemented after the current to voltage converter stage.

2.1 Highly ordered pyrolytic graphite

Initial work focused on preparing high quality samples suitable for addressing atomic scale features using STM. As an initial test system, highly ordered pyrolytic graphite (HOPG) was imaged repeatedly at atomic scale resolution in an isolation chamber at ambient conditions.

To prepare atomically flat surfaces of HOPG all that is needed is a piece of scotch tape. The tape is applied to the surface of an HOPG sample pressed in place and then lifted off exposing a clean flat surface. Tips were prepared by mechanically cutting a Pt-Ir 80/20 wire with a slight

pulling motion. Tip replacement is straightforward in ambient conditions if good imaging was not achieved within a reasonable timeframe.

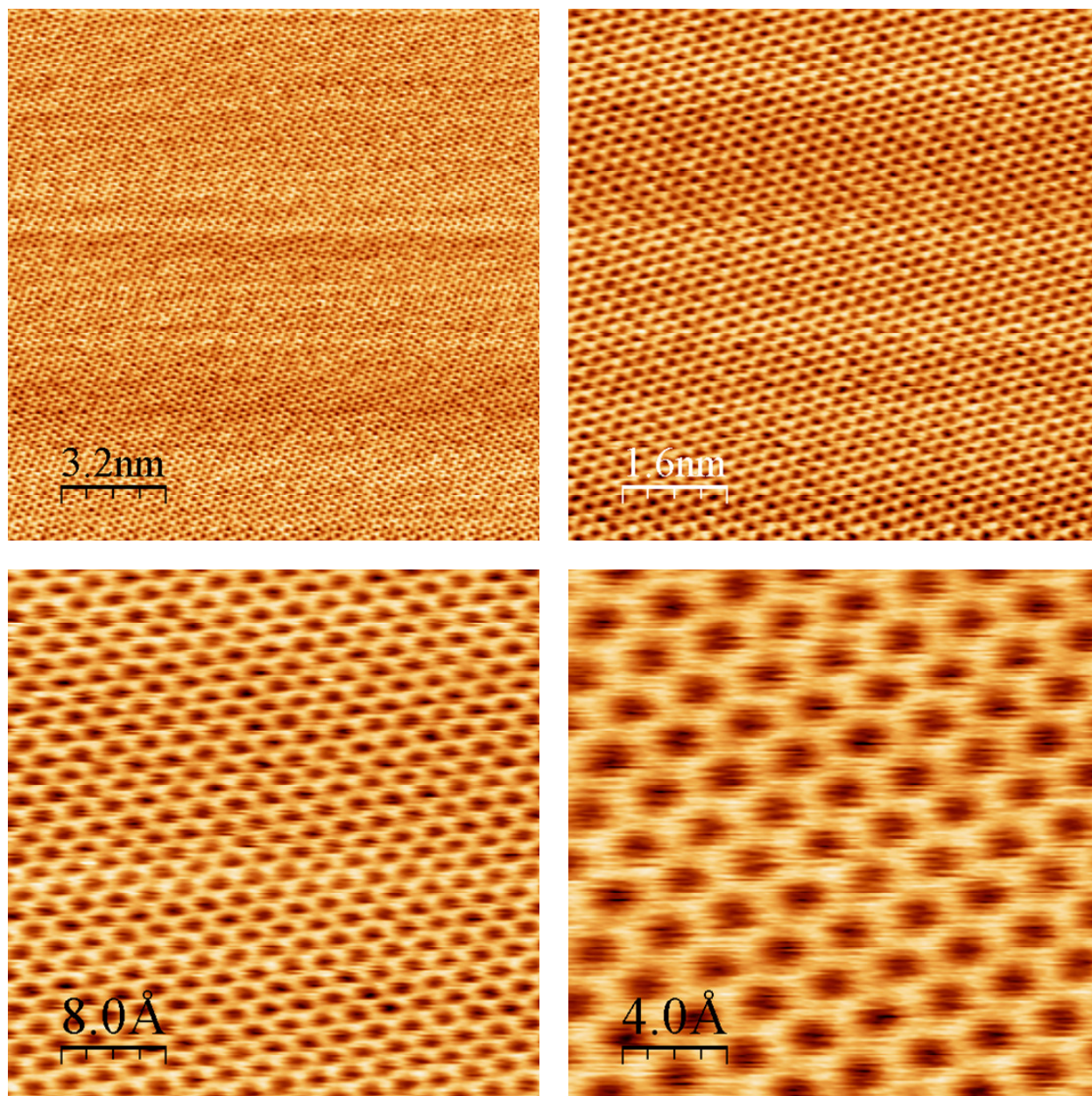


Figure 2-1. STM images of HOPG. The honeycomb pattern is clearly visible with every other atom in the ring showing higher electron density due to overlap with the underlying graphene sheet. Imaging conditions were constant current with a set point of 8.0nA and bias voltage on

the sample of -5mV with a scan rate 81.6 nm/s. The images are flattened and contrast adjusted.

2.1.1 HOPG on the microscope

Atomic resolution was also achieved when imaging the HOPG test system with the STM mounted on an inverted optical microscope atop a floating optical table as shown on the right in Figure 2-2. The noise performance during the testing on the microscope was not as good as in the isolation chamber, as evident from the images. The biggest issue on the microscope was the instability of the tip to ambient noises. To increase stability of the tip-sample junction of the STM while on the microscope, a light locking and acoustic isolation chamber was designed and built to enclose the microscope/STM system.

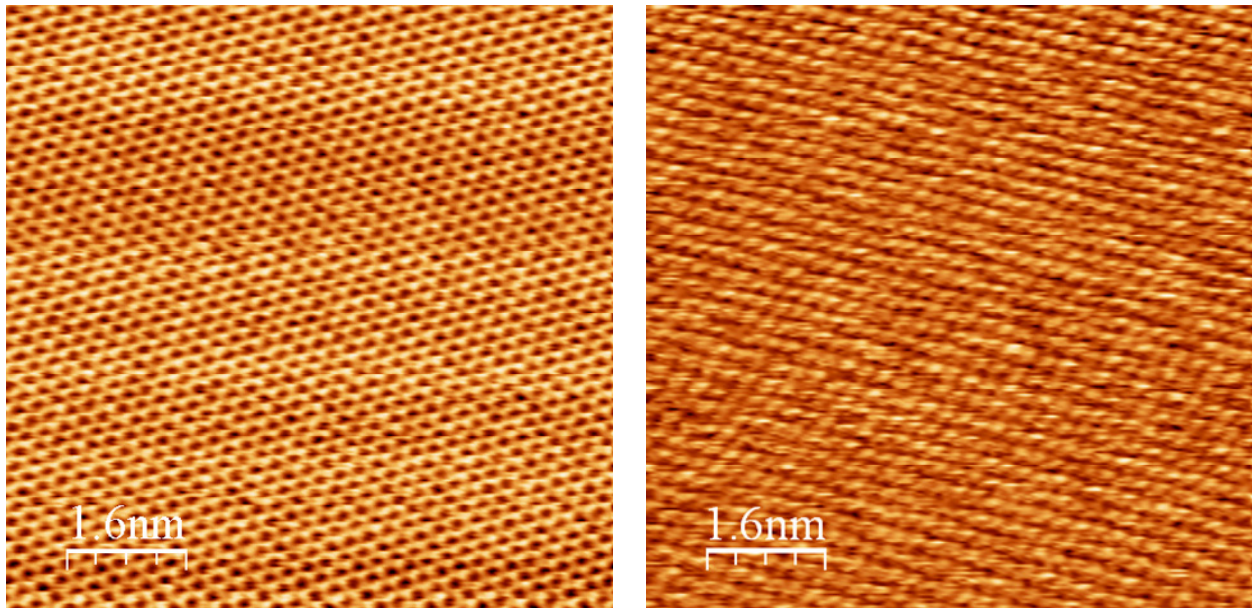


Figure 2-2. Images of HOPG in an isolation chamber and in open air on a microscope. In the left image the scanner and sample are mounted on a bungee cord vibration dampening system

within an acoustic isolation box. In the image on the right the scanner is mounted on top of a Nikon optical microscope in open lab air. Imaging conditions were constant current with a set point of 8.0nA (5.0nA image on right) and bias voltage on the sample -5mV with a scan rate between 80-88 nm/s.

2.1.2 Adsorbed molecules

An image of steric acid molecules on HOPG is shown in Figure 2-3. The sample was prepared by preparing a saturated solution of steric acid in phenyloctane with heating to ≈ 100 °C.^{100,101} A drop of the saturated solution was placed on a recently cleaved graphite substrate and allowed to cool into a gel. The STM tip approached through the gel matrix until tunneling current was achieved. The scan settings were 0.1nA setpoint current and a 10 x 10nm scan range. The imaging of steric acid molecules compares favorably with published results of long alkane chain molecules absorbed on HOPG, shown in Figure 2-4.^{100 101}

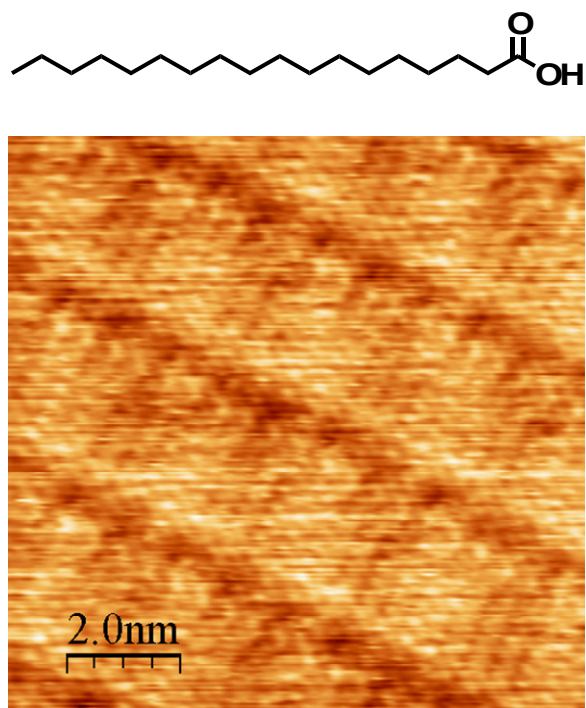


Figure 2-3. Steric acid adsorbed on HOPG. The steric acid molecule has a chain length of ≈ 2.5 nm.

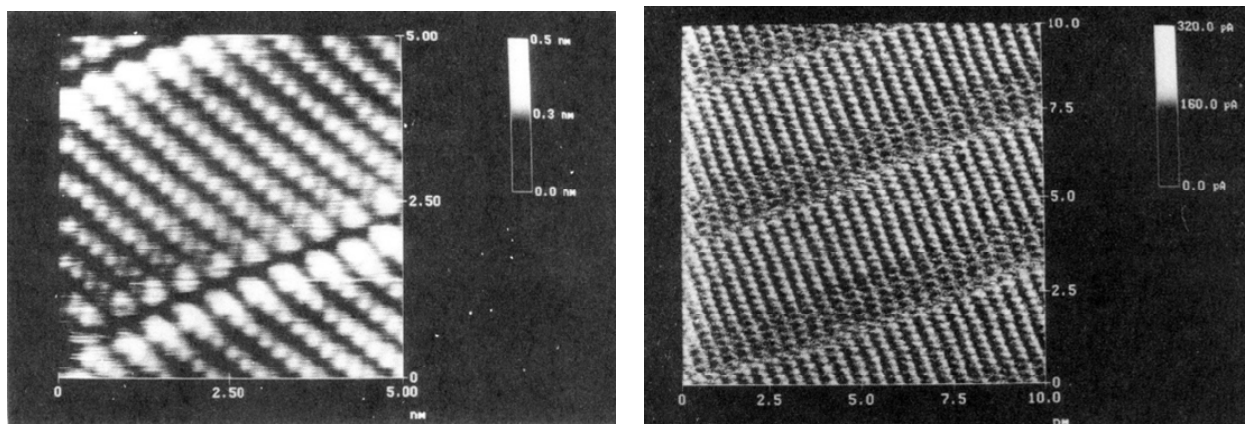


Figure 2-4. Comparison STM images of triacontanol in phenyloctane on graphite.¹⁰¹

2.1.3 Au <111> surface

Epitaxial growth of Au films was achieved on freshly cleaved mica at elevated temperatures to create reproducible surfaces shown to be Au(111) terminated.¹⁰² Freshly cleaving mica is prepared in the same way as HOPG, by exposing a new layer using scotch tape to remove the topmost substrate layers. After mounting into the vacuum deposition chamber the surface was preheated to 300°C at less than 1e-7 torr in a Kurt J. Lesker high vacuum chamber followed by electron beam deposition at 1 Å/sec to a thickness of 100 nm. These samples were allowed to cool in high vacuum to 50°C. Upon removal from the chamber they were flame-annealed with a butane torch until a faint glow was seen in a darkened room. Butane flame-annealed samples prepared in this manner have been shown to increase the terrace size by a factor of 25 as well as remove contamination¹⁰². My testing does not indicate that using a hydrogen torch provides any benefit over a butane torch with respect to hydrogen contamination of the surface. A method that would get around this concern is to heat a Au sample that is placed inside a test-tube under nitrogen flow.¹⁰³ The Au(111) surfaces prepared as described have been characterized by STM both bare and with monolayer coverage. Figure 2-5 includes images of Au(111) samples showing the characteristic herringbone reconstruction pattern arising from the 4% uniaxial compression along the 110 direction.¹⁰⁴

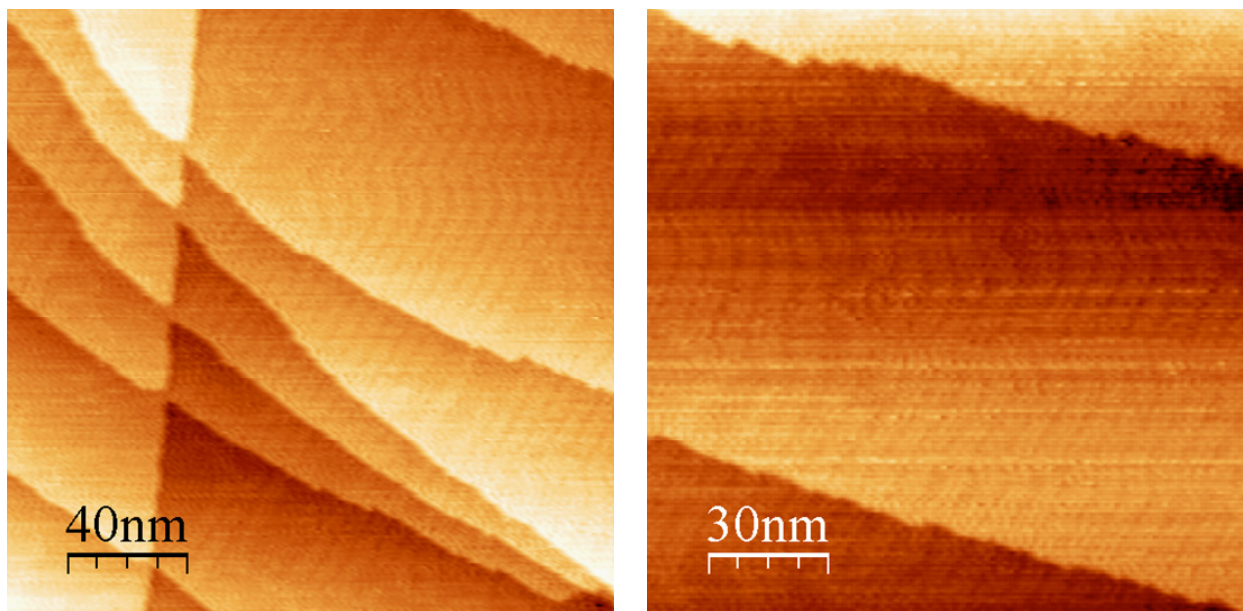


Figure 2-5. Au(111) on mica substrates. The reconstruction and uniaxial compression of the surface can be seen.

There is a rich STM history utilizing the Au(111) surface providing an important benchmark for performance. In Figure 2-6, Figure 2-7, and Figure 2-8, images of the Au surface are presented for comparison and reference. Figure 2-6 shows the Au(111) surface imaged under electrochemical control by the research group of Dieter Kolb.¹⁰⁵ Figure 2-7 shows high resolution UHV STM images. The images on the left have lost much detail due to poor printing in publication. The image on the right is a more recent image taken at 5K, and a color rendered version is utilized in current advertisement for the Omicron UHV-STM. Figure 2-8 shows the herringbone reconstruction imaged in UHV at 4K in the research group of Paul Weiss.¹⁰⁶

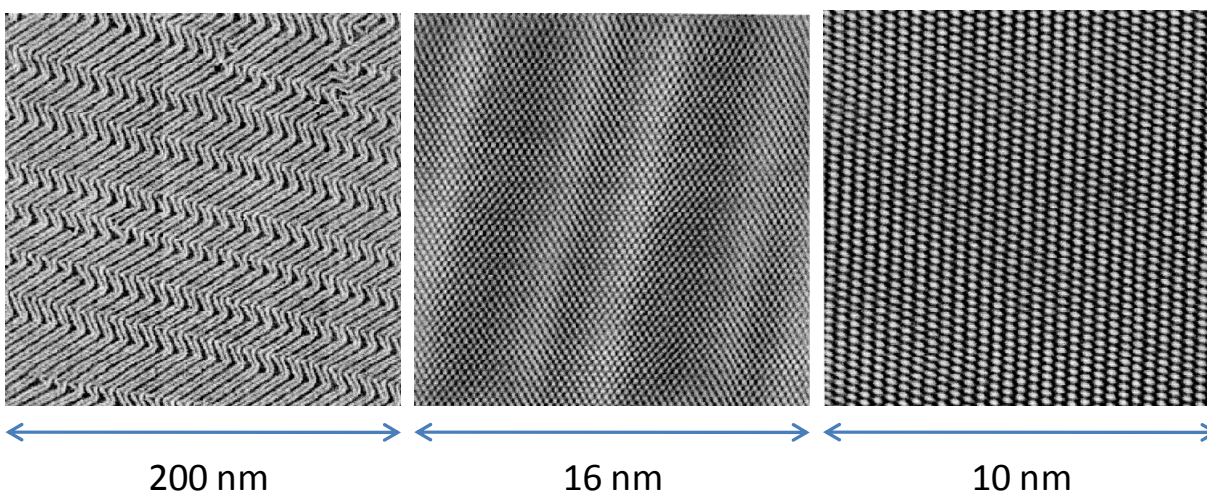


Figure 2-6. High resolution imaging of the Au(111) surface in 0.1 M H₂SO₄. In the left two images, the reconstructed surface shows the herringbone structure, and the image on the far right shows an unreconstructed surface.¹⁰⁵

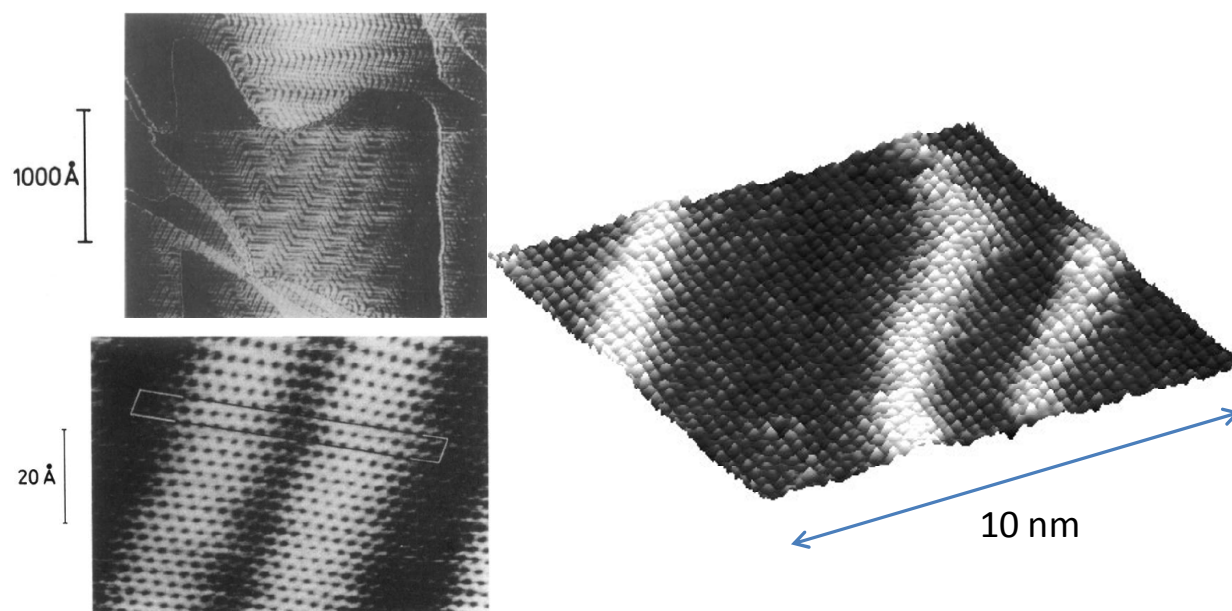


Figure 2-7. The first collection of high resolution UHV-STM images detailing the structure of the Au(111) surface were provided by Barth et al. in 1990.¹⁰⁷ The two images on the left show the

reconstructed surface. The image on the right provides a representative 3D image of a Au(111) surface imaged in UHV conditions at 5K using an Omicron microscope.¹⁰⁸

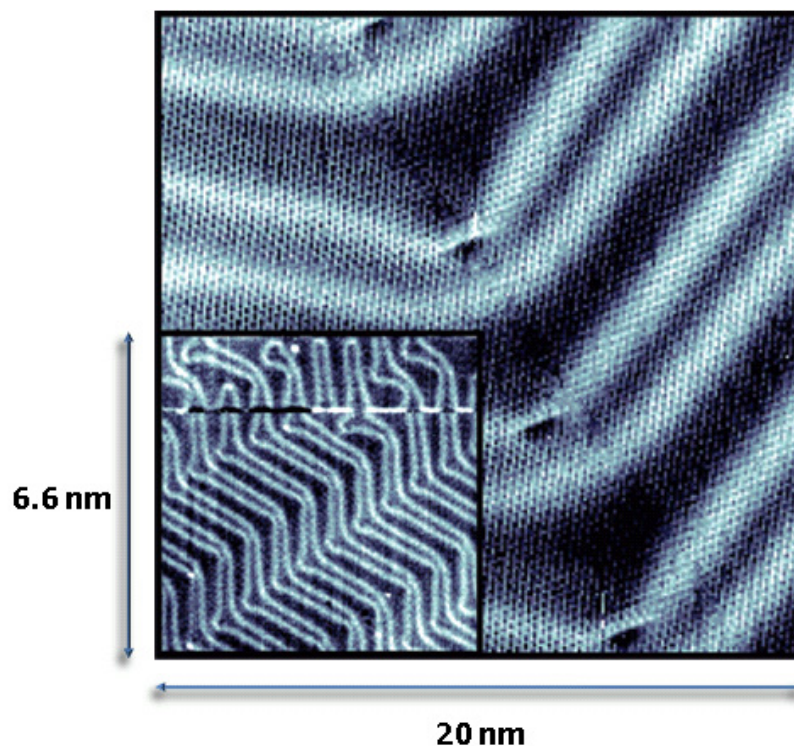


Figure 2-8. Au(111) herringbone reconstruction images recorded in UHV at 4k.¹⁰⁶

2.1.4 Monolayers on Au

Figure 2-9 and Figure 2-10 show monolayers of thiolated molecules on Au surfaces. In Figure 2-9, a Au<111> surface has been incubated for 4 days in a 1mM solution of octanethiol. The Au surface shows the sixty degree step edges indicative of a clean reconstructed surface. The image on the right shows that the mesa tops are $\approx 250\text{nm}$ across and the flat area between then is $\approx 1000\text{nm}$ wide. The dark spots in the image on the right show the characteristic pitting of the Au surface caused by the thiol groups.¹⁰⁹

The monolayer of decanethiol on a Au<111> substrate in Figure 2-10 shows the characteristic $\sqrt{3}\cdot\sqrt{3}$ adsorption pattern as well as pitting of the gold surface. The bright spots in the image on the right are indicative of location of the terminal alkyl group. The spacing matches published results for $\sqrt{3}\cdot\sqrt{3}$ adsorption on a Au<111> surface.¹⁰⁹

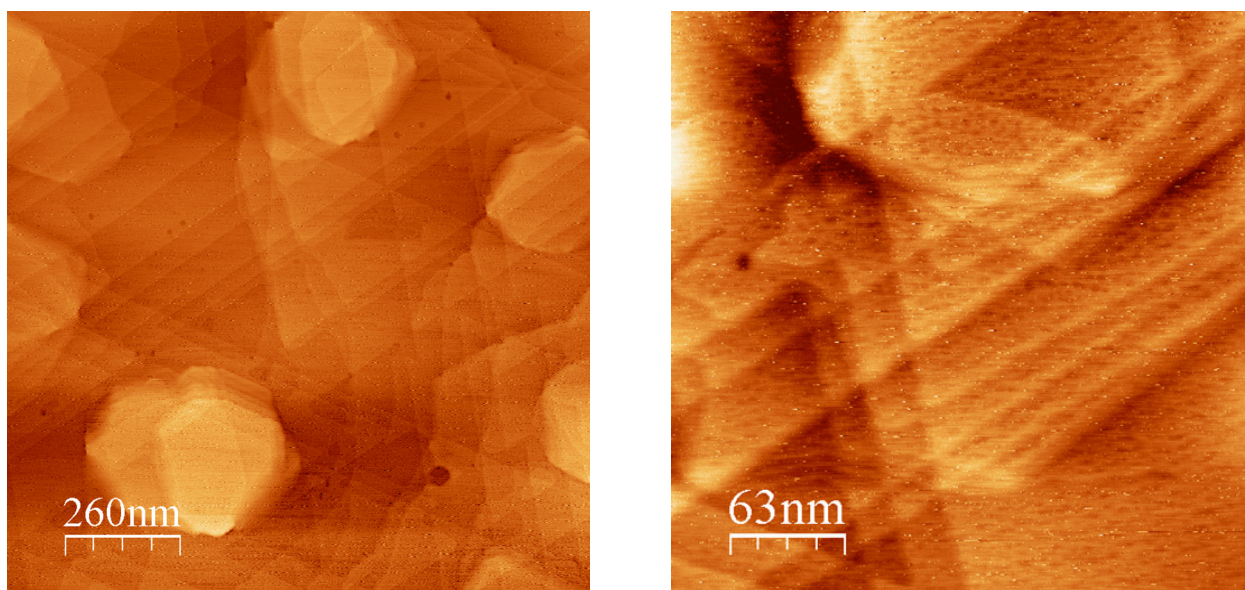


Figure 2-9. Octanethiol monolayer on Au(111) on mica substrate.

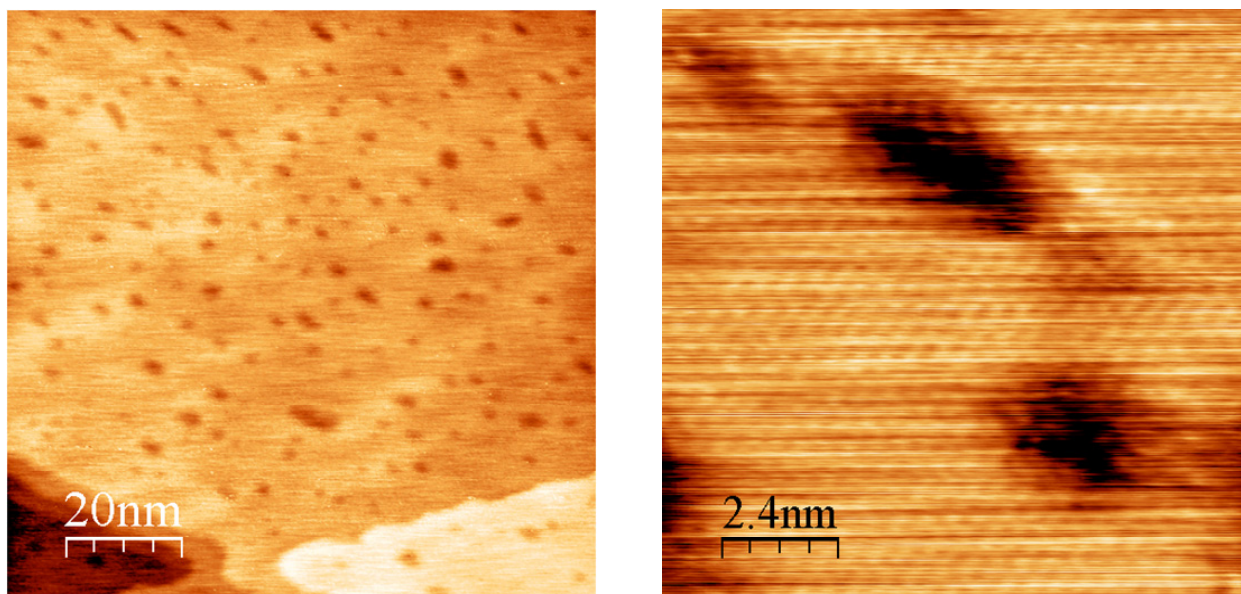


Figure 2-10. Decanthiol monolayer on Au(111) on mica substrate. The pitting of the surface is clearly visible in both images. In the image on the right, the methyl terminal groups are the bright spots visible in rows parallel to a line running from the bottom left to top right corner.

For comparison, two sets of thiol-organic molecules on Au are shown. In Figure 2-11, the image on the left showing the pitting of the Au surface is comparable to my experimental results presented on the left of Figure 2-10. Likewise, the images on the right of Figure 2-10 and Figure 2-11 are comparable, except the right-hand image of Figure 2-11 shows a mixed monolayer. Figure 2-12 shows two images from 2006 with very high resolution of a undecanethiol monolayer on Au(111). These images were taken at room temperature in a RHK UHV-STM after thermal annealing the at 345°C for 4 hours.¹¹⁰

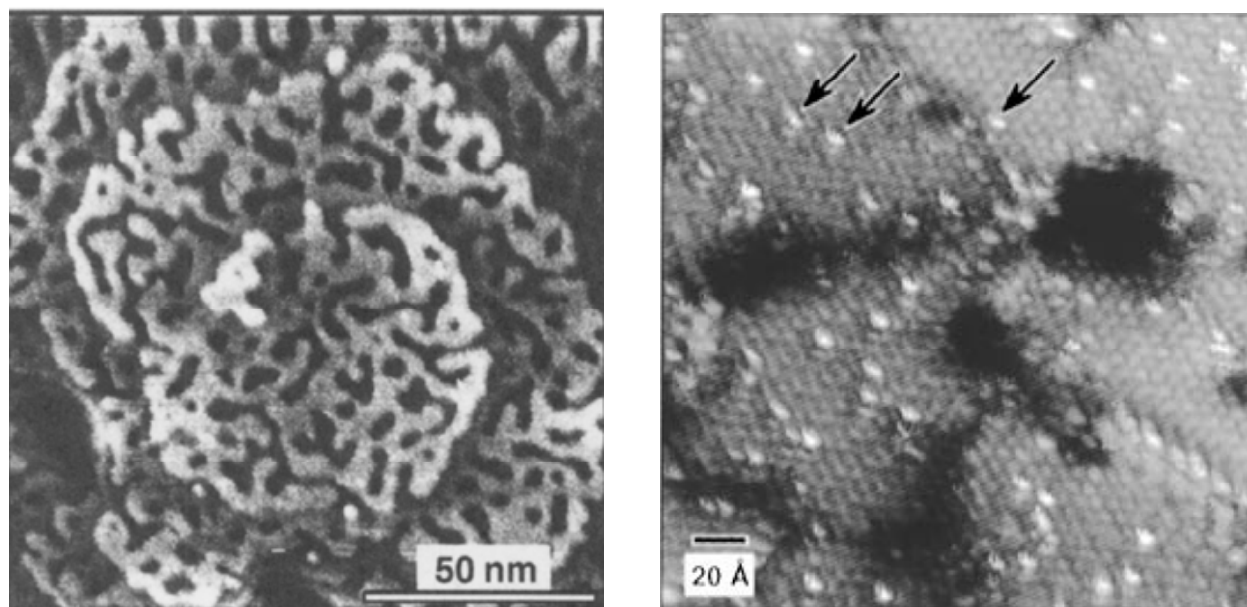


Figure 2-11. Two STM images of organosulfur monolayers on Au. The lefthand images shows a dodecanethiol monolayer.¹⁰⁹ The righthand image shows a mixed monolayer of 5% dodecanethiol and 96% decanethiol.¹¹¹

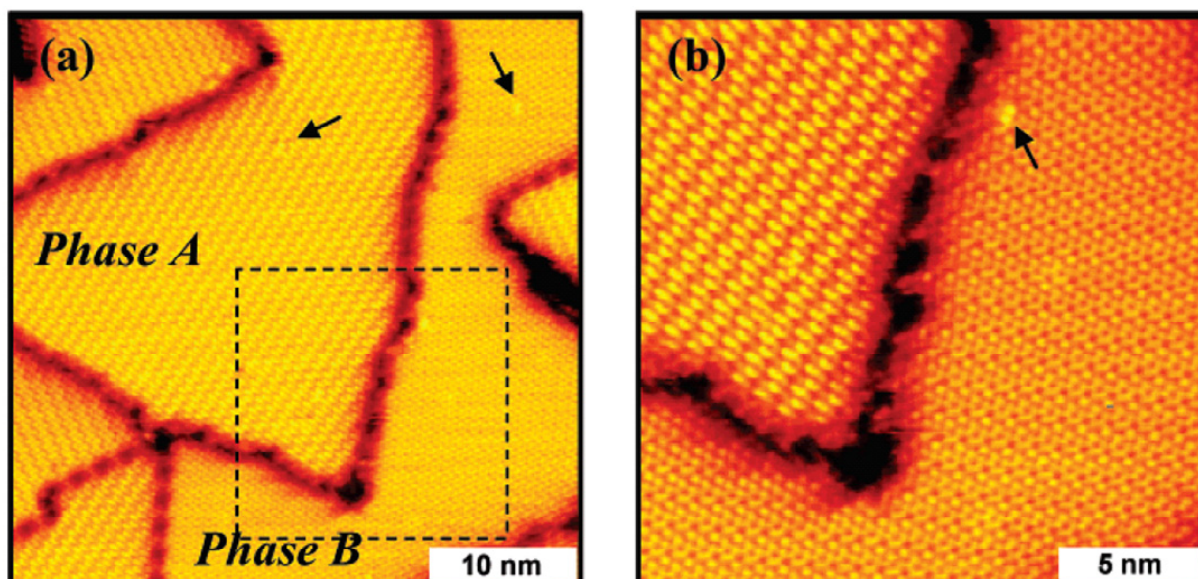


Figure 2-12. Two UHV-STM images of undecanethiol on Au(111).¹¹⁰ The STM imaging was done using an RHK instrument at room temperature with a base pressure of $<5 \times 10^{-10}$.

2.2 Ag nanowells

The nanowells image presented in Figure 2-13 represents an unconventional approach to characterizing large scale features. STM is generally sub-optimal for our nanoparticle characterizations due to the requirement of a conductive substrate along with the greater experimental ease in collecting data using an Atomic force microscope. This image was taken out of a curiosity to test the STM's capability of imaging surface with large scale features. The image of Ag coated nanowells in Figure 2-13 is currently my only published scanning probe result.

The nanowell surface was created by drop coating polystyrene spheres on a glass surface. Using a reactive ion etcher the exposed surface was etched for 10-25 minutes with CF_4 gas. The spheres were then removed and then the glass slide with etched holes was coated in Ag using an electron beam deposition system.¹¹² The sample characterized in Figure 2-13 was made using 510nm polystyrene spheres, an etch time of 10 minutes and a Ag layer of 50nm.

STM images of the film over nanowell surface were collected with a Molecular Imaging PicoPlus SPM in constant-current mode. The rendered image represents the smoothed topographic data. Pt/Ir 80/20 mechanically cut tips were scanned at 1050 nm/s and a set point of 10 pA. The average well is depth $\approx 28\text{nm}$ in agreement with the AFM images having an average well depth of $30.3 \pm 2.8\text{nm}$.¹¹² The image rendering software used was a freeware scanning probe program, WSxM, written and distributed by Nanotec electronica, available at www.nanotec.es.¹¹³

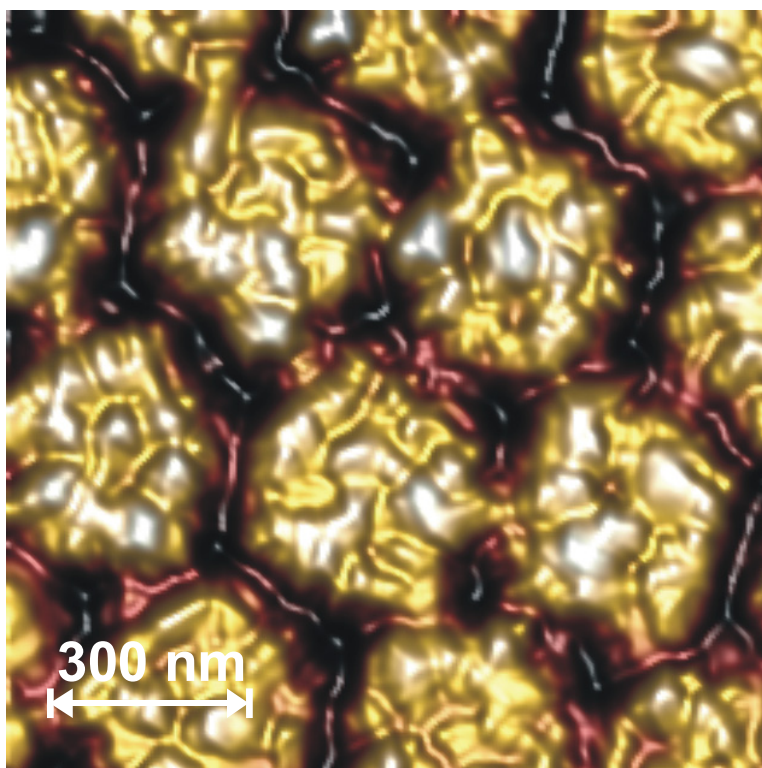


Figure 2-13. An STM image of nanowell surface coated in silver.

STM imaging of large scale features is rarely done because of the large radius of curvature of the tip. In my experience using very low tunneling current which would move the tip as far away from the surface as possible was ideal for imaging these nanowell surfaces. An STM relies on having an exponential tunneling current – tip distance, which indicates that utilizing a pA preamp may only gain an Å in tip surface separation. More testing would need to be completed to verify the reproducibility of imaging large scale conductive surfaces with STM. A large scale image with this resolution, coupled with tip enhanced Raman spectroscopy, could provide a detailed mapping of the enhancement factor on nanoparticles.

Chapter 3. STM Break Junctions

3.1 Experimental setup

The experimental results presented in this section were collected using a commercially available scanning probe microscope from Agilent technologies (formally Molecular Imaging). The tip is held in place by friction to a cylindrical tube soldered directly into a current to voltage preamplifier board. Most of the results in this section are presented using a quasilogarithmic preamplifier to give increased dynamic range. The Au surface was prepared as detailed above in section 2.1.3. Au tips were prepared by mechanically trimming a 0.010" wire ordered from Alfa Aesar. Au is quite malleable and for this experiment a sharper tip may not make a large difference to the repetitive contact of the tip to the surface.

3.2 Derivation of quantized conductance

In contrast to a macroscopic conductor, an atomic scale conductor has a discrete conductance dictated by the finite number of energy levels in the conductor. This discrete conductance is related to the number of transport channels. One of the first tests that should be conducted in break junction experiments is the measurement of the quantum of conductance. The following paragraph details the reason for observing the quantum of conductance. Most of this explanation as well as additional details can be found in the books by Professor Datta^{4,114} and on web resource www.nanohub.org.

We start with the definition of current in terms of electron flow,

$$I = -eN(\#ofelectrons)*Velocity \quad (3.1)$$

The change in current can be through of as the change in the number of electrons,

$$dI = -e \cdot dN \cdot V(\varepsilon) \quad (3.2)$$

The change in electrons is related to the density of states and the change in energy between the two leads,

$$dN = DOS(1D) \cdot dE \quad (3.3)$$

For a free electron gas in 1D this becomes particle in a box physics with the energy of the n^{th} electron given as,

$$E_n = \frac{\hbar^2}{2m} \left(\frac{n\pi}{2L} \right)^2 \quad (3.4)$$

Rearranging the variables we get,

$$n = \frac{2L}{\pi\hbar} (2m \cdot E_n)^{1/2} \quad (3.5)$$

Rearranging equation 3.3 and using equation 3.5

$$DOS(1D) = \frac{dN}{dE} \quad (3.6)$$

$$DOS(1D) = \frac{dN}{dE} = \frac{L(2m)^{1/2}}{\pi\hbar(E_n)^{1/2}} \quad (3.7)$$

Substituting equation (3.4) into equation 3.7 we get

$$V(\varepsilon) = \frac{\hbar \cdot n \cdot \pi}{2 \cdot L \cdot m} \quad (3.8)$$

Substitute eq(3.4) into eq 3.7 and using the definition in equation 3.8

$$DOS(1D) = \frac{1}{\pi\hbar \cdot V(\varepsilon)} \quad (3.9)$$

Then adding dE to both side,

$$dN = DOS(1D) \cdot dE = \frac{dE}{\pi\hbar \cdot V(\varepsilon)} \quad (3.10)$$

Then next

$$dI = \frac{-e \cdot dE}{\pi\hbar} \quad (3.11)$$

The current is the integration of electrons over the relevant energies,

$$I = \frac{-e}{\pi\hbar} \cdot \int_{U_1}^{U_2} dE \quad (3.12)$$

Replacing the integration over the chemical potentials with the bias voltage V ,

$$I = \frac{e^2}{\pi\hbar} \cdot V_{bias} \quad (3.13)$$

Then the current in terms of the chemical potentials U_1 and U_2 ,

$$I = \frac{-e}{\pi\hbar} \cdot (U_2 - U_1) \quad (3.14)$$

At this point all we need are the standard relationships between voltage, current and resistance,

$$V = I \cdot R, R = 1/G_0 \quad (3.15)$$

$$I = G_0 \cdot V_{bias} \quad (3.16)$$

From equation 3.14 this simplifies to the quantum of conductance.

$$G_0 = \frac{e^2}{\pi\hbar} = \frac{2e^2}{h} \quad (3.17)$$

This is the quantum of conductance which is given as $7.748\,091\,733 \times 10^{-5}$ S or $12,906.405 \, \Omega$.

3.3 Experimental quantized conductance

Quantized conductance has been measured using a mechanically cut Au STM tip that contacts a Au<111> substrate on mica. In a histogram of current versus distance, peaks correspond to increased probability of being measured and possibly increased stability. The distribution of peaks shown in Figure 3-1 displays quantized conductance indicative of the formation of atomic Au wires. In this plot higher order multiples of G_0 are seen up to $G_0=3$, indicating three conductance channels. After the last Au-Au contact is broken at $1 G_0$ there are no peaks, indicating a clean sample. The locations of the peaks with respect to G_0 are unchanged with voltage bias and the peak shapes are consistent with published results.^{53,59,67,115} The results are also independent of tip retraction speed. The results are best when the maximum current is limited to $4 G_0$ insuring that the tip does not become completely blunt from pushing it into the surface.

Au-Au scanning probe break junctions 100mV bias

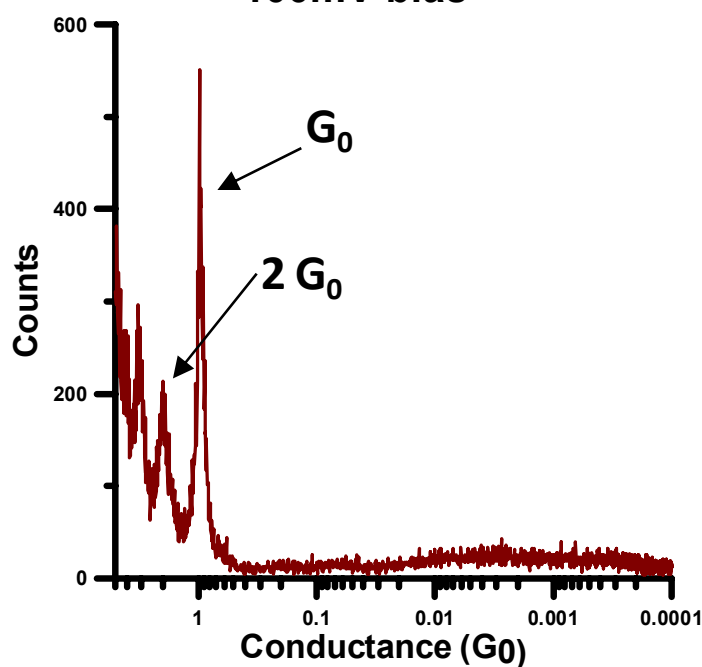


Figure 3-1. Measuring Au quantized conductance using an STM.

3.4 Initial tests on single molecule junctions

Many attempts have been made at repeating the STM break junction conductance traces seen by Tao et al. using alkane-dithiol molecules.⁶⁷ The conductance values recorded following the breaking of a single Au wire show characteristics of the electronic density of states between the bulk contacts. All of this work was completed with a linear current-voltage amplifier before the logarithmic system was available. While the current traces display stable states indicated by the horizontal sections of the traces, the histograms collected from 500-1000 such traces fail to show the quantized peaks that have been reported.^{67,68,76,116} The lack of quantized peaks below G_0 can be attributed to the inability to measure a statistically significant metal molecule metal junction. The reason for this may be an insignificant sample size and/or such a large

variability in the contact-molecule coupling and molecular orientations, creating a broad averaging of values.¹¹⁷ The conductance data should be rich in information due to the changing geometry and binding location providing a dynamic picture of single molecule behavior similar to single molecule spectroscopy techniques.¹¹⁸

Analyzing these results is difficult without characterization of the surface. Initial measurements showed a well-ordered monolayer with the benzene ring 30 degrees off perpendicular.¹¹⁹ A number of measurements have also found disordered surfaces not enabling clear imaging or surfaces with defined domains of molecules.^{120,121} Benzenedithiol molecules on Pt have also shown to have a pendant sulfur atom which should facilitate break junction measurements.¹²² On copper substrates at cryogenic temperatures the thiol-metal linkage shows significant mobility and fluctuation in binding location.¹²³ STM on alkanethiol on Au surfaces even shows phase evolution on the time scale of 6 months.^{124,125}

3.5 Calibration of a log amplifier

To measure the current flow over many orders of magnitude it becomes beneficial to have a logarithmic or quasilogarithmic preamplifier. Molecule imaging, now Agilent technologies, sells such a device for our scanning tunneling microscope. Figure 3-3 shows the basic design of a linear current-voltage converter and a quasilogarithmic current-voltage converter¹²⁶ In (a) the $10 \times 10^9 \Omega$ feedback resistor serves to swing the output voltage 1V per 1nA of current on the input. A standard resistor has a linear resistance function and thus the output is linear with respect to input current. In (b) the quasilogarithmic preamplifier design utilizes a pair or multiple pairs of antiparallel diodes to get nonlinear resistance. The diodes must have

ultra low saturation current and minimal capacitance. The parasitic capacitance does limit the bandwidth of the system but with additional circuitry can be kept in the kHz and higher range.

126

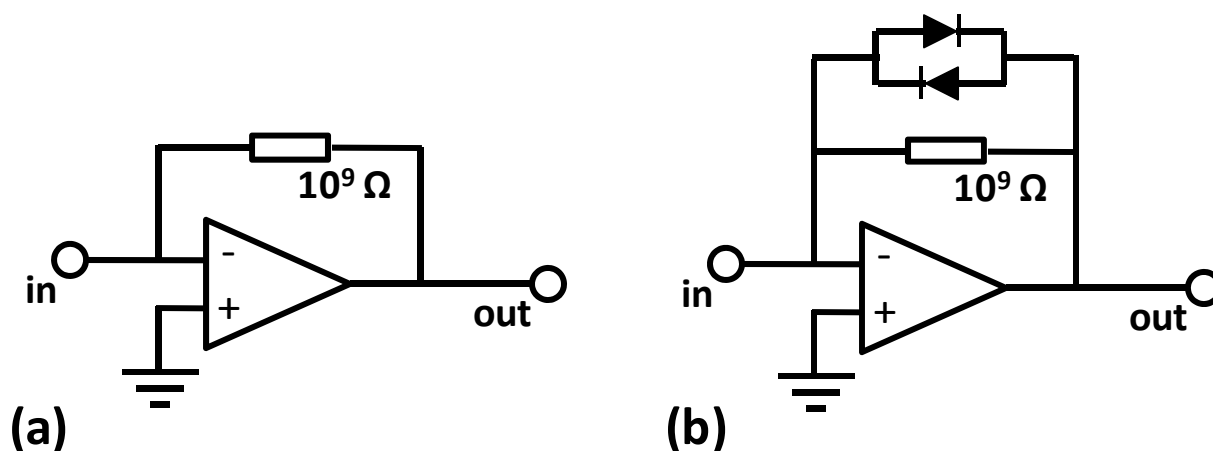


Figure 3-2. Schematic circuit diagram of the current-voltage converters used. (a) shows a linear preamplifier and (b) shows the quasilogarithmic preamplifier.¹²⁶

The scanning probe software provided by Molecular Imaging has no specific control for a quasilogarithmic preamplifier. The control electronic and software functionality work by converting an output voltage of $\pm 10\text{V}$ to a tunneling current. The sensitivity is dictated by the STM scanner installed and the conversion to current is done within the software. Setting the software to control to $1\text{nA} = 1\text{V}$ allows a direct measure of the output voltage (with the result relabeled as nA). The maximum output voltage is then measured as 3.4 Volts.

A full calibration of the amplifier is necessary to be able to convert the output voltage to a tunneling current. For this calibration, I utilized a large number of resistors, measured the resistance, and then adjusted the bias voltage and measured the output voltage, for a range of

tunneling currents. With a range of preamplifier output voltages and the known tunneling currents it is possible to calibrate the preamplifier. I wrote matlab code to iterate a 4 variable equation to get the best fit. The code with an example input and output are given in Appendix A. Shown in Figure 3-3 is the fit to the measured calibration data set with an R-squared value of 0.9996. At current >0.0001 amps the fitting quality decreases, but this is not in a region of interest.

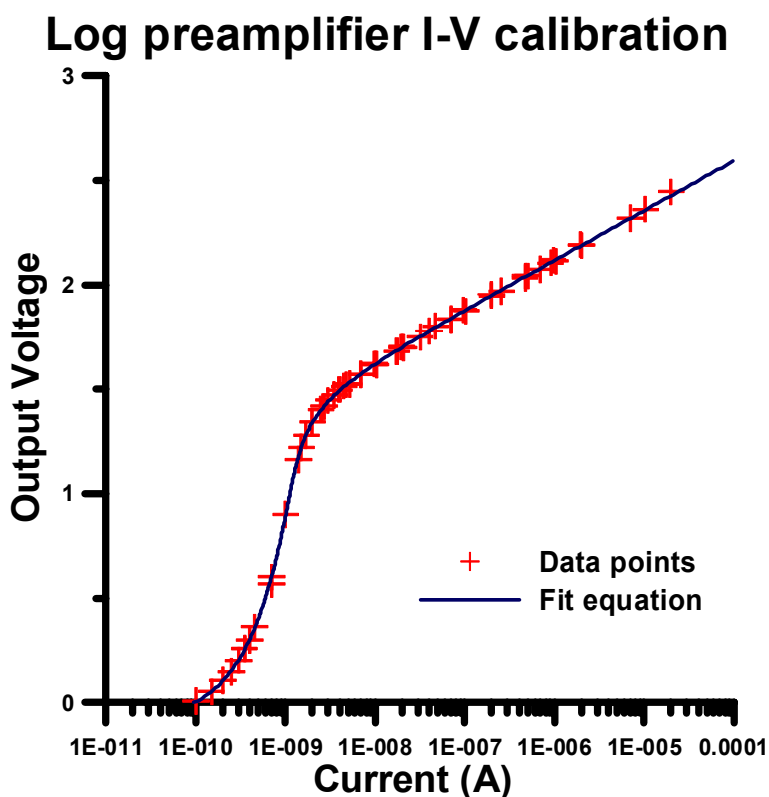


Figure 3-3. Calibration of the logarithmic preamplifier.

3.6 Tests on benzenediamine

A number of research groups have had difficulty reproducing the published results using a dithiol linker molecule but using the same methodology reported promising results using

diamine terminated molecules.^{69,117,127-129} In Figure 3-4 six consecutive current-distance traces are shown. In all six traces characteristics of a 1 or 2 channel Au wire are shown as labeled. Most of the traces also show peaks at near $0.2 G_0$ and at $0.01 G_0$. It should be pointed out that the distance is calculated from the Z-piezo voltage and is thus sensitive to the Z calibration.

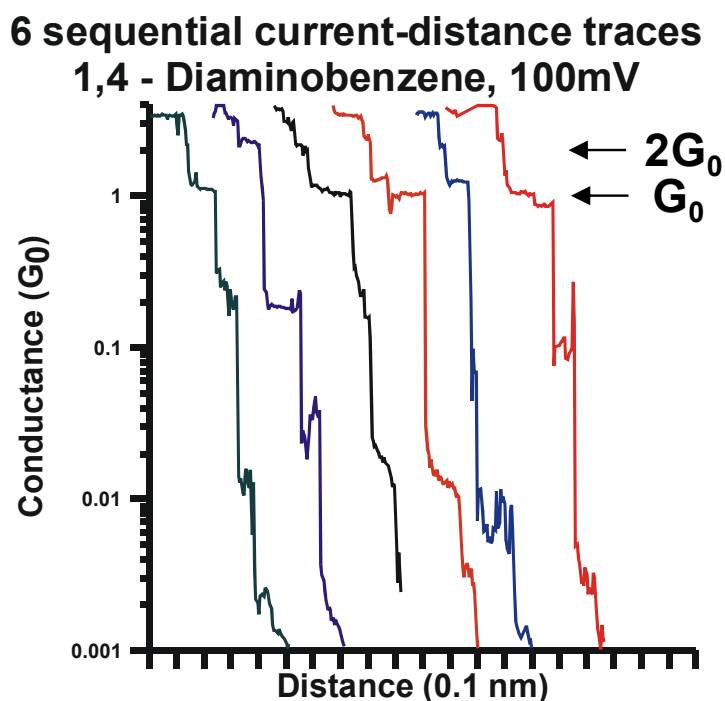


Figure 3-4. Six example traces of the conductance as a function of distance for separating a Au tip from a Au substrate in the presence of 1,4-diaminobenzene.

A histogram showing 3000 such traces is presented in Figure 3-5. The peaks at 1, 2, and 3 G_0 are clearly evident. After the final Au-Au contact is broken, we see peaks over 3 orders of magnitude estimated to be at $0.2 G_0$, $0.01 G_0$, and $0.0008 G_0$. These peaks are clearly seen in Figure 3-6 where the current below 1 G_0 is plotted. The apparent noise in the data is a consequence of the histogram bin size in relation to the number of the data points. This

relationship is illustrated in Figure 3-6, shown in black where the histogram bin width is increased by 5 (and subsequently, the number of counts is divided by 5 for comparison). The published experimental result for conductance through this molecule is $0.0064 \pm 0.0004 G_0$.⁶⁹ A Gaussian fit to the center peak led to a maximum at $0.0082 G_0$, $\approx 28\%$ higher than the published value. The features seen at $0.2 G_0$ and $0.0008 G_0$, have not been commented on in the literature. It is possible that these variations over 3 orders of magnitude represent different diamine-Au surface interactions including laying on the surface, the benzene ring on edge on the surface, or standing perpendicular to the surface. With such a large amount of experimental uncertainty, it would be imprudent to postulate further on the origin of this observation.

1,4 - Diaminobenzene break junctions 100mV Bias

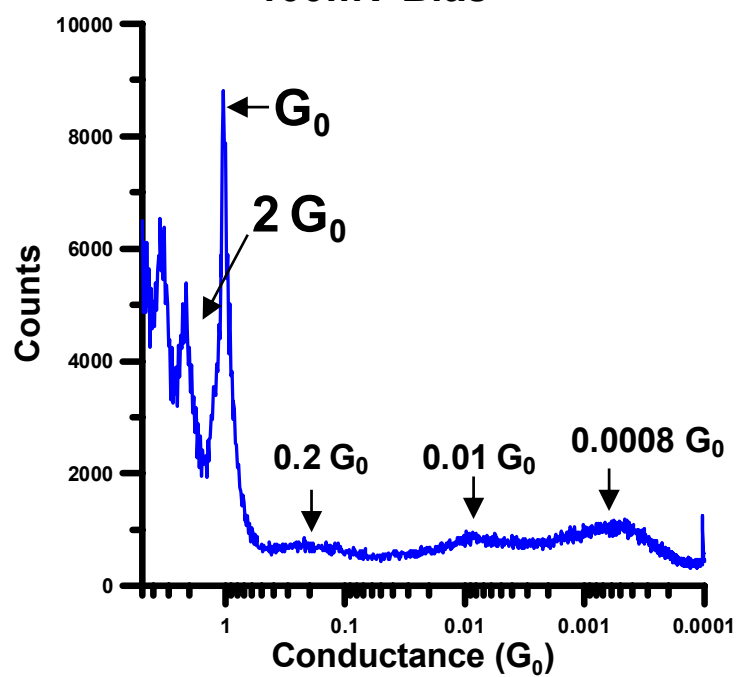


Figure 3-5. A histogram of 3000 conductance-distance traces of 1,4-Diaminobenzene on a Au(111) on a mica surface in 1,2,4- trichlorobenzene.

1,4 - Diaminobenzene break junctions 100mV

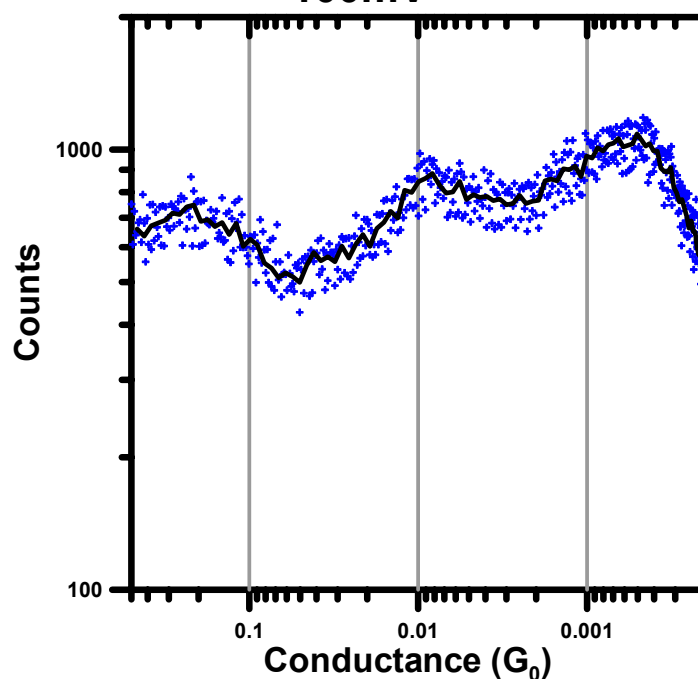


Figure 3-6. A zoomed in image of Figure 3-5 showing the histogram values below $1G_0$. The blue data points correspond to the data points from Figure 3-5, while the black line represents the histogram with the bin width increased 5X (the number of counts is normalized by dividing by 5X to allow direct comparison).

3.7 Conclusions on break junctions

This method of repeatable smashing together a Au surface and a Au tip has provided an interesting new method to study single molecule behavior. It provides a relatively straight forward method for taking a large number of measurements, possibly on single molecules, in a reasonable amount of time, at room temperature, in ambient conditions.

There remains a large uncertainty in the makeup of the molecular junction including the orientation of the molecule, the number of molecules in the junction, the electrode orientation, the role of the solvent molecules, and the time evolution of the system. In the following sections I detail my computational efforts to understand what changes in conductance can be expected from perturbing the idealized structure that is used in many charge transport calculations. This lack of understanding the details of a molecular junction and the large variation in current attributed to a single molecule motivate our development of new instrumentation to characterize the junctions.

Chapter 4. Two probe calculations

4.1 Introduction

Calculations of molecular conduction must address the complexity of molecular motion and contact rearrangement under bias. A recent paper illustrates how different molecular orientations can change the calculated conductance up to 10^3 .¹³⁰ Small changes made in the orientation or arrangement of the contact atoms can also lead to conductance variation between a few percent and an order of magnitude.^{80,82,84,130} Complexity is further increased due to multiple molecules in close proximity⁸⁵ and environmental effects such as solvation and gate modulation.¹³¹ In this chapter we first study the change in current with a varying contact coupling before moving on an integration of molecular dynamics and transport calculations.

4.2 Contact coupling

The molecule *p*-benzenedithiolate (BDT) is studied here to simplify comparison with previous experimental and theoretical results. BDT has been extensively used to test quantum transport because the conjugated π ring should offer delocalized electronic states beneficial to transport, the sulfur atoms form strong coordination bonds to the gold electrodes, and both experimental and theoretical data are available for comparison.⁶⁸ Modeling of the BDT junction has suggested a range of behaviors including both highest occupied molecular orbital (HOMO)⁸⁰ and lowest occupied molecular orbital (LUMO)¹³² mediated conduction, as well as large effects of geometry and contact orientation on the calculated current-voltage (I-V) characteristics.^{79,80,82,84,132-138}

In this section, we focus on clarifying the role of the contact coupling in relation to the molecular conduction at low bias voltages. To obtain a qualitative understanding of the

junction properties, we compare results from the state-of-the-art NEGF-DFT TranSIESTA-C program, to results obtained with the simplified Hückel NEGF method.³⁹ Two groups of researchers have noted an increase in conductance with increasing gold sulfur distance over a small voltage range.⁸⁰⁻⁸² Here, we repeat this calculation in both computational codes and assign this effect to a shifting of the HOMO molecular orbital towards the Fermi level, as well as to charging of the terminal sulfur atom. An additional Au atom on the Au(111) electrode introduces molecular states near the Fermi level, possibly leading to large changes in transmission function near the Fermi Energy. These results are pertinent to single molecule conductance measurements in which the geometry of the metal-molecule-metal junction is both uncontrollable and unknown at the single atom level.

4.3 Computational methods

Our calculations have been based on DFT codes utilizing the NEGF approach. For comparison we utilized the Hückel-IV code, freely available online at Nanohub.org.³⁹ This code uses extended Hückel theory orbitals to calculate the energies of the isolated system with a 3 atom Au pad. The energy level shift is then included through charging in a self-consistent field approach.^{4,114,139,140} We used an optimized molecular geometry that was first relaxed in a planar orientation using B3LYP with an effective core potential using the GAMESS package¹⁴¹. Hückel-IV aims to calculate the qualitative transport behavior of molecular junctions, but is limited in its quantitative capabilities due to the simplicity of the molecular orbital treatment. Two adjustable variables are utilized as fitting parameters: the Fermi level and U , the electron charging energy. The alignment of the electrode Fermi energy level to the BDT molecular levels

is very sensitive to fractional charge transfer; in our system (in accordance with previously published results⁸⁰ and our own TranSIESTA-C calculations) we have located the Fermi level within the HOMO-LUMO gap closer to the HOMO orbital. The Fermi level is held fixed throughout the Hückel calculations.

The electron charging energy describes the net energy change due to the addition or subtraction of an electron from the molecule in the gap. This charging generates a potential field that can shift and broaden the Hückel molecular orbital conductance peaks. This Coulomb charging energy can be estimated as one half the electron affinity (EA) minus the ionization potential (IP) minus the measured vertical optical transition energy (E_g).^{139,142}

$$U = \frac{EA - IP}{2} - \frac{E_g}{2} \quad (3.18)$$

The charging energy of a similar conjugated molecule has been estimated by calculating the energy level change using a Pariser-Parr-Pople Hamiltonian and assuming even electron distribution across the molecule.¹⁴³ The charging energy is included as a constant electrostatic potential across the molecule that rigidly shifts all the energy levels³⁹

$$E_N = E_N^0 + Udn \quad (3.19)$$

U is the charging energy and dn is the change in the number of electrons from the charge neutral level¹⁴⁴ with E_N^0 and E_N representing the molecular orbital energy levels before and after charge transfer. When the charging energy splitting is greater than the electrode induced broadening, the molecule is in the Coulomb blockade regime.³⁹ In this regime transport is

dominated by single electron charging effects. The molecule BDT studied here has been estimated to have a charging energy on the order of 1-2eV.³⁹

The TranSIESTA-C code calculates the electronic density matrix using DFT.^{45,47} We utilized the LDA-PZ exchange correlation functional with a SZP basis (5d,6s,6p) for the gold atoms and a DZ basis set on the molecules. The mesh cutoff was set at 150Ry. The electrodes were the standard default gold FCC electrodes with 36 gold atoms on one electrode and 45 on the other. Within this methodology only the structure of the molecule and the electrodes needs to be set for the transmission and current to be calculated.

In all of our calculations the dithiol is used without a bound hydrogen, becoming a diradical in the singlet state as described in detail elsewhere.⁷⁹ In neither of the studied codes was the molecular geometry allowed to relax upon bonding to the electrodes or under field. All bond lengthening was done perpendicular to the electrodes in a symmetrical manner unless noted.

4.4 Au wire conductance

As a first order comparison the conductance of a Au wire was computed using the Hückel and TranSIESTA-C codes. In the Hückel code a five atom Au wire was placed between the three Au atom pads in the threefold symmetric site. In the TranSIESTA-C 1.3 package the five atom Au wire was placed between two Au electrodes of 36 and 45 atoms, respectively. The expected conductance through an Au wire would be G_0 ($2e^2/h$) corresponding to ballistic conductance through a single quantized channel. In TranSIESTA-C the location of the wire was varied among the 4 binding sites: FCC, HCP, ATOP and the bridge site as shown in Figure 4-1 a. The conductance values calculated for these 4 coordination sites and the three fold Hückel

calculation are compared with varying Au-Au spacing in Figure 4-1 b. The Au-Au atom spacing was varied between 2.35Å and 2.88Å (shown in Figure 4-1 b) in the 5 atom wire and also between the wire and the contact atoms, with the electrodes held fixed. All calculations gave a conductance between 0.5 and 1 G_0 at 1 volt. Within TransSIESTA-C the ATOP site consistently showed the highest conductance values with the FCC site ~0-5% lower, the bridge site ~8% lower and the HCP site 15% lower. The images taken of a single atom Au wire under bias illustrate these fluctuations.⁶⁰ Histograms of current vs. time for breaking Au contacts at room temperature show peaks at specific current values, attributed to quantized conductance. In a statistical ensemble of measurements the current value attributed to a single Au atom wire shows variations with a full width half max in the range of 10%-27%^{53,59}.

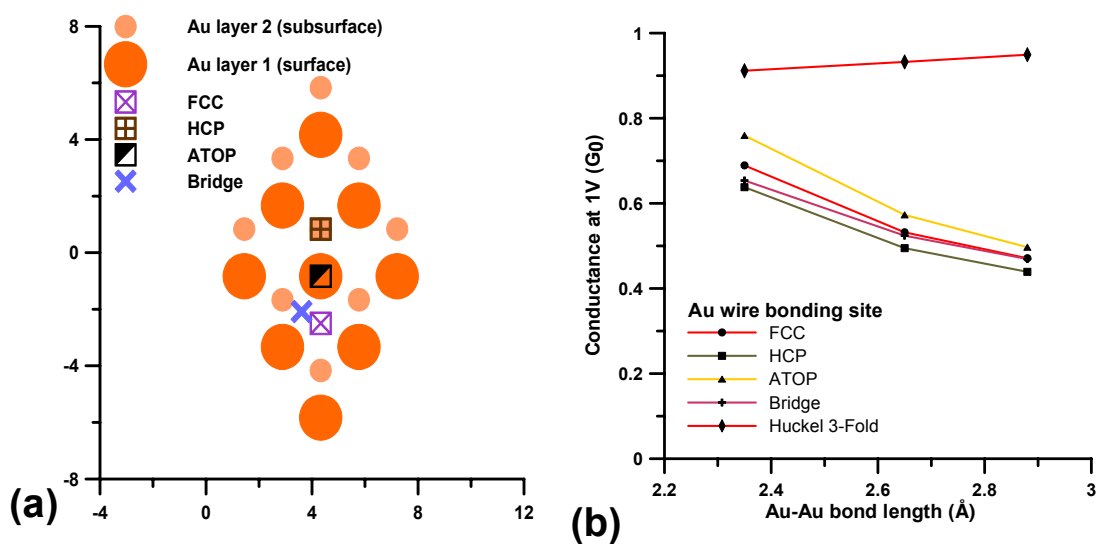


Figure 4-1. Au wire conductance a) The typically utilized surface Au bonding sites FCC, HCP (both 3 fold Au sites), ATOP and twofold bridge site. (b) The conductance at 1 volt through a 5 atom Au wire symmetrically bonded to 36 and 45 atom Au electrodes in TransSIESTA-C and twice to 3 Au atoms in Hückel. The bond length corresponds both to distance between the 5

neighbor atoms in the wire and between the end atoms and the contact. Calculations made by moving a bound BDT molecule between the FCP, HCP and ATOP sites showed a conductance change of 1.5.¹³⁰ In Au-thiol systems these subtle variations in contact geometry¹²⁴ could lead to a large distribution of conductance values even if the molecular geometry were held completely rigid, if differing symmetry situations are encountered.¹³⁰

4.5 Hückel-IV

The uncertainty in orientation of molecules in a self-assembled monolayers,¹²⁴ compounded with the uncertainty in the geometry of single molecule junctions and the distributions of conductance values measured between different sites⁶⁵ and measured at the same location with respect to time,⁷¹ make understanding the effects of contact coupling critical to understanding the transport mechanism. Using the Hückel-IV model we systematically lengthened the Au-S bond while keeping the molecular geometry and the electrode geometry fixed. The sulfur atom is coupled to the electrode in the threefold hollow FCC site. This simplified Hückel model uses a 3 atom Au electrode to represent the S-Au bonding. At low negative bias voltage the Hückel model shows an increase in low bias conductance with increasing Au-S bond length. Figure 4-2 a shows the I/V results with increasing Au-S distance. This behavior of increasing low bias conductance arises from the shift of the HOMO molecular orbital towards resonance with the Fermi level. This behavior is seen in both the case of lengthening one contact and with lengthening both contacts. In the asymmetric case, positive bias shifts the HOMO level away from the Fermi level effectively postponing current onset.³⁹ Figure 4-2 b provides an example of current versus distance for pulling apart this system at a

fixed bias of -0.2 V in Hückel-IV and TranSIESTA-C, showing similar results. From the initial bond length of 2.33 Å the conductance rises to a peak between 3-3.75 Å distance and does not fall below the equilibrium conductance until a bond length of over 4 Å. A similar result was found with an Au electrode that included a single Au atom sitting on the surface bound to the BDT terminal sulfur.

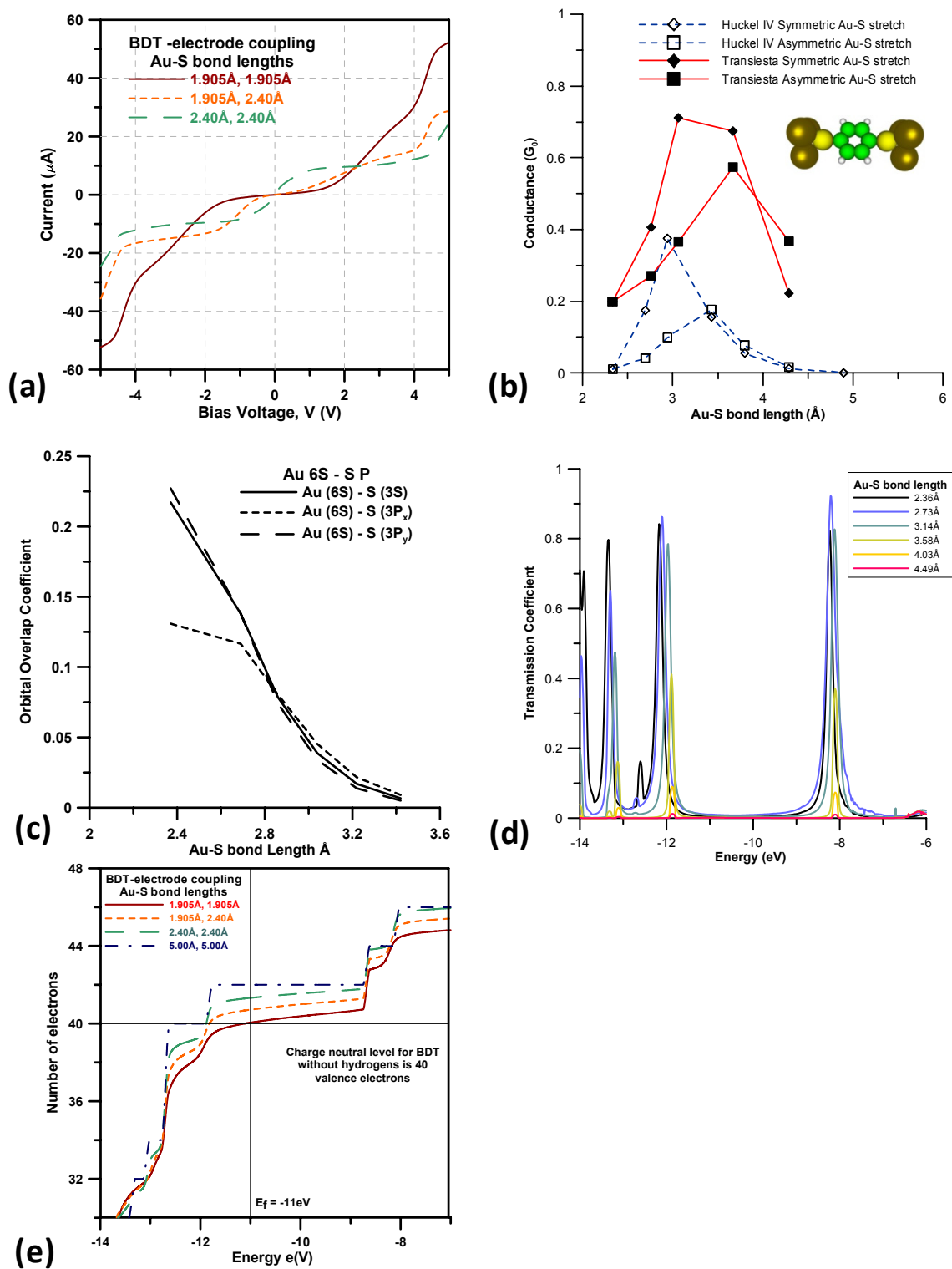


Figure 4-2. The current with increasing Au-S bond length as calculated in Hückel IV(a). At a set voltage of -0.2V symmetric lengthening of both Au-S bonds and asymmetric bond lengthening

of only one Au-S bond are shown to increase the current in both Hückel IV and Transiesta-C (b). Valence orbital overlap between the terminal S atom and the Au electrode (c). The Hückel transmission spectrum (d) shows a slight shift of the HOMO orbital to higher energies with increasing Au-S length as well as a slight shift towards the Fermi Energy level set at -11eV. A calculation of the number of electrons with changing energy indicates a charge transfer to the molecule with increasing bond length, going to the limit of forming the negatively charged benzene-disulfide at large distance (e).

For more detailed information on the NEGF method we refer the reader to references ^{4,38,114} Maximizing the Green's function matrix elements maximizes the conductance. In the simplest picture, the Green's function represents the orbital overlap across the molecule divided by the energy distance of the Fermi level from a molecular resonance.¹⁴⁵ In the following equation our simplified representation assumes that the central molecule and the contacts share the commutative property, $[\Sigma, H_{\text{molecule}}]=0$.

$$G_{\phi_L, \phi_R}(E) = \sum_{\mu} \frac{\langle \phi_L | \mu \rangle \langle \mu | \phi_R \rangle}{(E - E_{\mu} - \Sigma_{\mu})} \quad (3.20)$$

In this case the conductance $G(E)$ is equal to the overlap of the molecular orbitals μ and the terminal atomic orbitals on the left and right electrodes (ϕ_L and ϕ_R) divided by the energy difference between E and a molecular resonance E_{μ} and the self energy Σ_{μ} .

The conductance maximum with increasing distance is not due to overlap. To verify that the molecular orbital overlap drops (as expected) with increasing Au-S bond length, the matrix

elements of the sulfur $3p_x$, $3p_y$ and $3s$ orbital overlap with the electrode $6s$ orbitals were analyzed in the Hückel description. These results show an exponential decay in overlap with increasing Au-S distances, Figure 4-2 c. With the Fermi level set between the HOMO and LUMO orbitals, the increasing bond distance has the effect of decreasing the distance of the Fermi level from the HOMO molecular resonance. Neither the molecular orbital overlap change nor the slight changes seen in the transmission graphs explain the calculated rise in conductance. This non-intuitive result can be explained by plotting the number of electrons on the molecule while changing the energy (Figure 4-2 e). As shown in the plot, the number of electrons on the molecule increases as the bond lengths are stretched. At the decoupled limit, with the sulfur electrode distance at 5.0\AA , there are 42 valence electrons in the now -2 benzenedisulfide ion. In this limit, the conductance is dominated by single electron charging effects as described in the Coulomb blockade model. In the Coulomb blockade regime, the delocalized Au wavefunctions cannot fractionally change the charge on the center molecule. In the Hückel calculation used here the increase in population on the BDT molecule is used with the electron charging energy parameter to shift the potential across the molecule.

Within Hückel IV, this charging parameter is responsible for how much the molecule is allowed to follow the chemical potential. When the applied voltage shifts one of the electrode levels into resonance with a molecular energy level the charging parameter, U , shifts the molecular level corresponding to the change in electron population. For symmetric Au-S bonds the net effect of the charging parameter is a shift towards resonance and a symmetric broadening of the spectral density (effectively an orbital lifetime broadening). In the

asymmetric bond lengthening case the broadening is increased with positive applied bias (Figure 4-2 a). This asymmetric broadening occurs when the strongly coupled substrate potential shifts below the HOMO level. This decreases the HOMO population faster than the positive electrode can increase it, which further shifts the molecular resonance to lower energy.¹⁴⁶

4.6 ATK

The DFT-based NEGF program TranSIESTA-C was also used to calculate the conductance dependence on the Au-S bond length. The TranSIESTA-C calculations show strikingly similar behavior to the Hückel-IV model, with a rise in conductance of 3-5 fold upon initial increase of the gold-sulfur bond distance, similar to what has been reported elsewhere.⁸⁰⁻⁸² A strong dependence in the I/V characteristics has been attributed to charge transfer to the molecule upon binding to the electrodes.^{39,140} The conductance is very sensitive to small fractional charge transfer because the molecular orbitals energies within the junction shift with respect to the electrode Fermi level.³⁹ Table 4-1 includes the valence Mulliken populations found on the end sulfur group as this Au-S bond is manipulated. In the situation with both thiol bonds symmetrically stretched to 2.76 Å, the S population changes from 5.927 to 6.037 for both atoms.

Table 4-1. Total Mulliken charge on S atoms within the junction, calculated at equilibrium using TranSIESTA-C.

Au-S bond length (Å)	2.33	2.76	3.06	3.67	4.29
S Mulliken charge	5.927	6.03	6.064	6.088	6.079
S Mulliken charge (bond length = 2.33 Å)	5.927	5.921	5.916	5.908	5.904

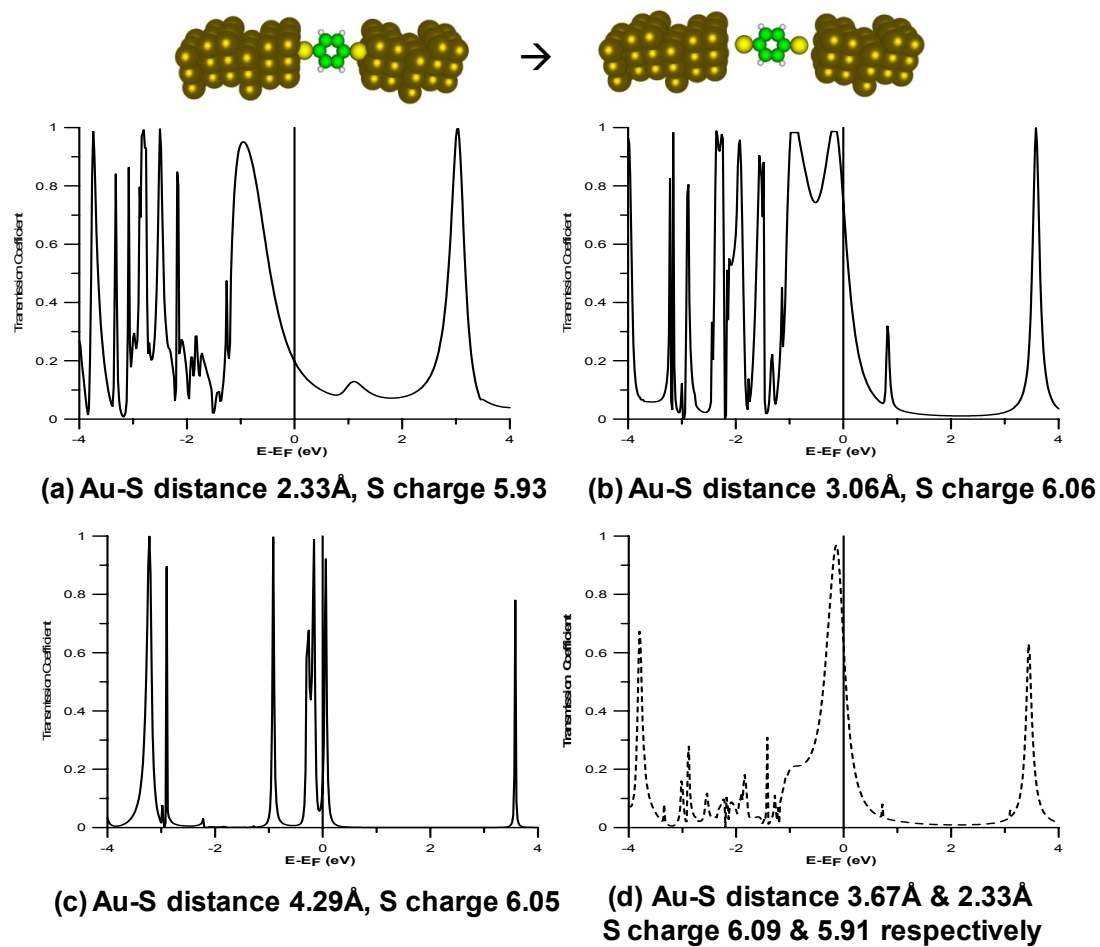


Figure 4-3 Transmission coefficients calculated using NEGF-DFT for BDT in the three fold FCC site with increasing Au-S bond distance, (a,b,c) both Au-S bond lengths are increased, (d) only one Au-S bond length is increased while the other Au-S bond length is kept at 2.33 Å.

Comparing Figure 4-3 a to the symmetric case 3b and the asymmetric case 3d we can see a shift in the peak of the HOMO orbital towards the Fermi energy level. To verify that the HOMO orbital is shifting into resonance, Figure 4-4 shows the molecular projected selfconsistent Hamiltonian (MPSH)⁴⁷ orbitals of the center atoms. Figures 4a and 4c show that the HOMO molecular orbital, which dominates low bias transmission, is unchanged in general electron density upon bond lengthening. The energy level, with respect to the Fermi level shifts from -1.42eV to 0.05eV concurrently with an associated 0.15 electron transfer to the terminal sulfur atom.

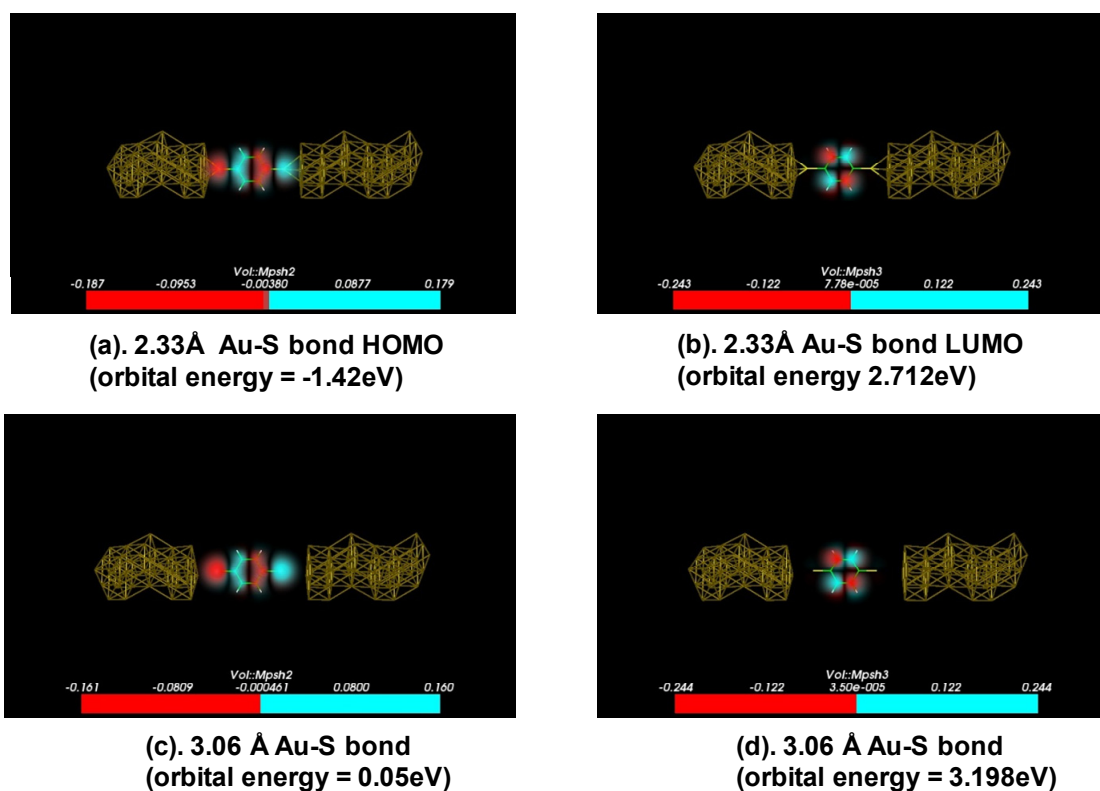


Figure 4-4. (a) and (b) illustrate the HOMO and the LUMO levels for the BDT molecule symmetrically situated on the FCC site between two Au electrodes. The molecule is also calculated with larger Au-S bond lengths, (c,d). The orbital energies are given with respect to the calculated Fermi level.

The situation with the sulfur bound atomically to a single Au atom protruding from the surface has been postulated⁶⁸ as the most likely geometry of the transport junctions experimentally prepared. Past calculations have reported both an increase and decrease in conductance with an additional Au atom on the surface.^{80,82} The increase in conductance has been attributed to being analogous to the lengthening the Au-S bond and a shifting of the HOMO level into resonance.^{80,82,84} Our results differ from those published in that the surface

Au atom adds additional molecular orbitals near the Fermi level. We notice little change in the value of low bias conductance measured as $\sim 0.2G_0$ but this is very sensitive to the alignment of the Fermi level and a small change in the electron density on the molecule could have a large effect here. This can be deduced by comparing the transmission functions in Figure 4-3 a and Figure 4-5 a, and noting the Au induced gap states. All of the MPSH orbitals near the Fermi level are plotted in Figure 4-6. In comparison to the situation with a sulfur atom in the threefold FCC site, the HOMO and LUMO levels are still seen at similar energy values. With the additional Au atom, 4 orbitals are seen within 1eV of the Fermi level within the HOMO-LUMO gap. These Au-induced molecular orbitals make this calculation particularly sensitive to charging and the Fermi energy location, and may help explain the distribution of reported behaviors.^{80,82} Similar to the FCC bonded sulfur atom situation, the conductance increases with increasing Au-S bond distance along with a charging of the terminal S atom, and in this case, a slight decrease in the charge on the single Au atom. As the Au-S distance increases the energy levels of three of the Au induced molecular orbitals shown in Figure 4-6 (b,c,e) are shifted towards the Fermi level, increasing conductance.

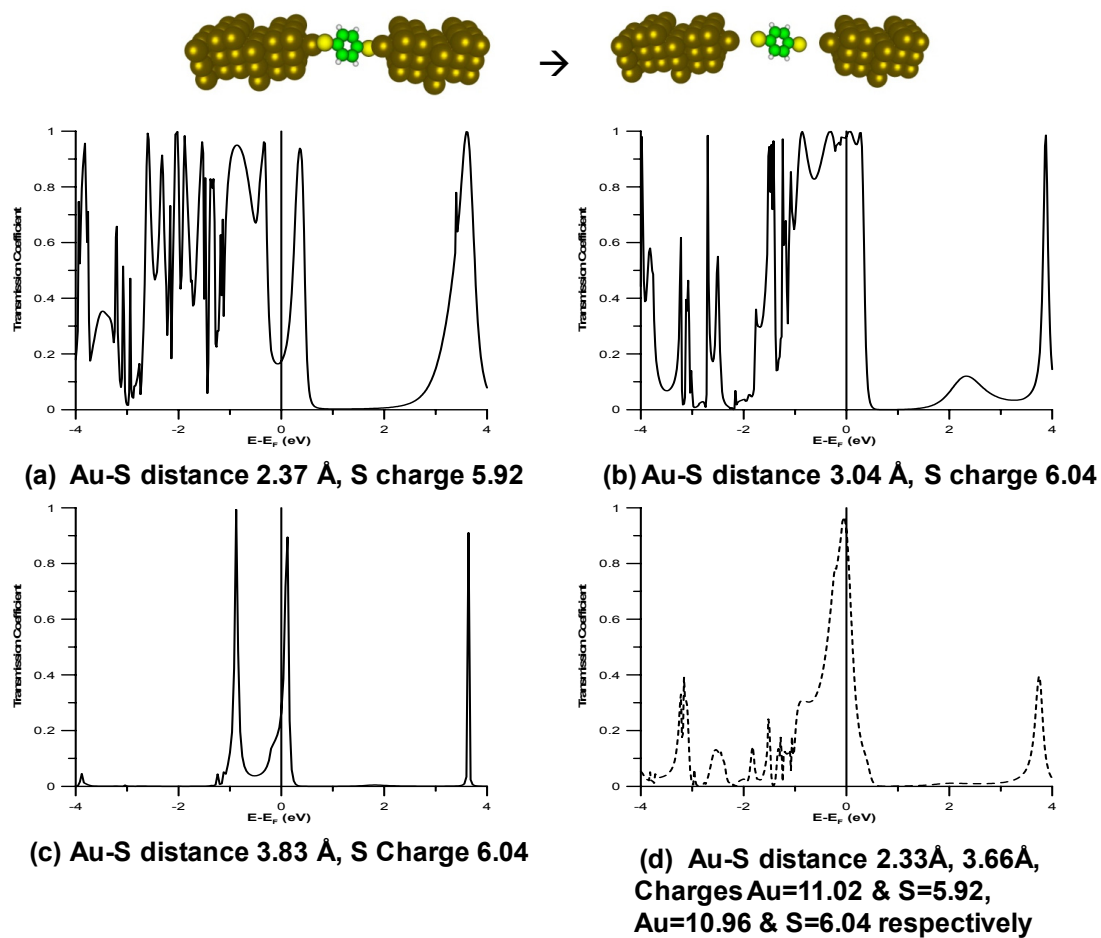


Figure 4-5. Transmission coefficients from NEGF-DFT upon symmetric breaking of the Au-S bond for the model system with a surface Au atom at each electrode. Au-S bond lengths are (a) 2.37Å (b) 3.04Å (c) 3.83Å and an asymmetric stretch of one Au-S bond to (d) 3.66Å. Mulliken populations are given for the S and nearest Au atom.

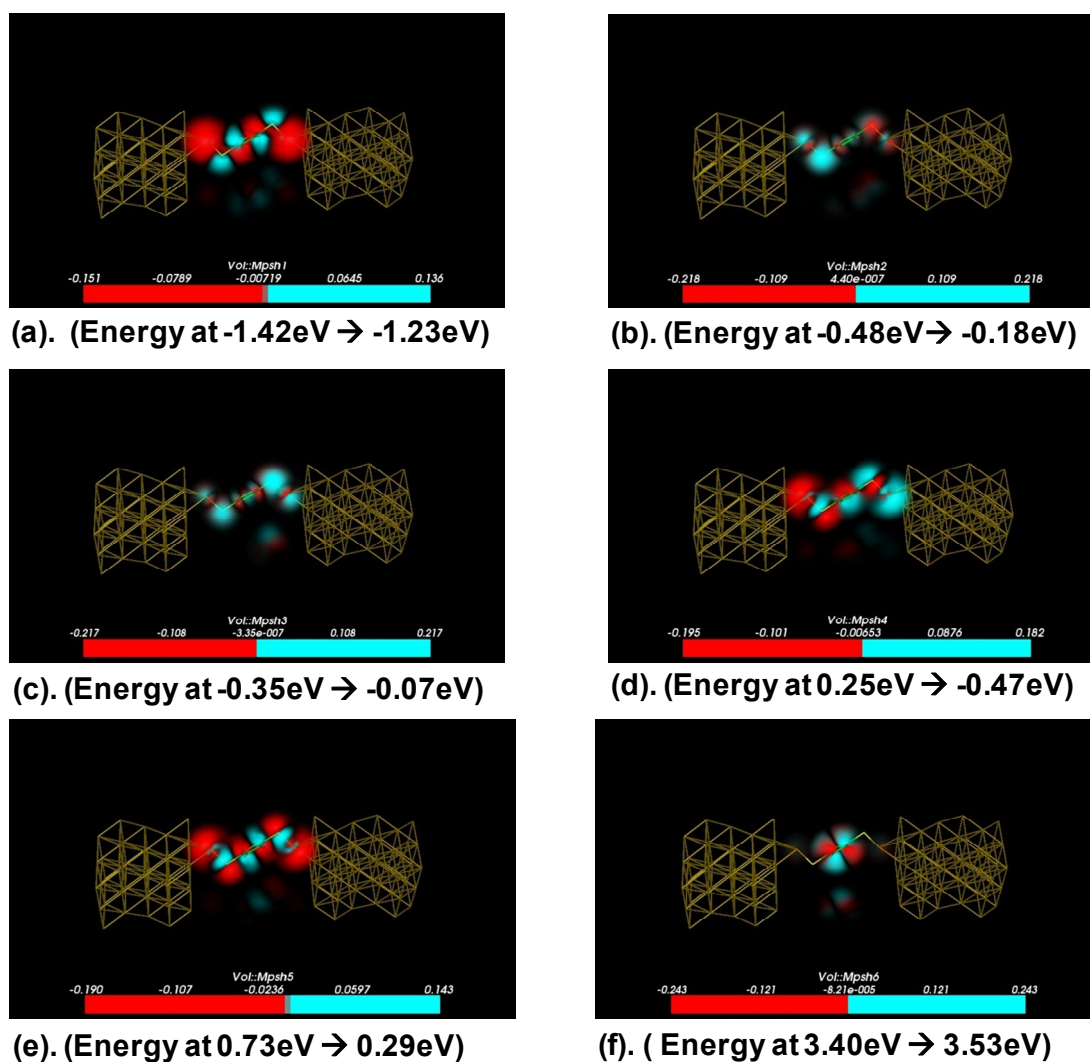


Figure 4-6. Molecular states around the Fermi energy obtained using TranSIESTA-C. The two given energy values correspond to two different Au-S bond lengths of $2.36 \text{ \AA} - 3.14 \text{ \AA}$ respectively. Images a and f are nearly identical to the HOMO and LUMO levels seen in figure 4 for the BDT molecule between two electrodes. The additional Au atom introduces 4 states that contribute to the conductance (b,c,d,e).

4.7 Discussion of contact structure

Most electrochemical molecular transport junctions show large conductance variations between samples and over time.^{65,67,68,147} The uncertainty in molecular structure, contact atom arrangement, and thiol coordination in experimental junctions can lead to “stochastic switching,” and can make modeling molecular transport difficult.¹⁴⁸ It is shown that charge transfer to the terminal S atom shifts the HOMO orbital nearer to the Fermi energy. The molecular orbitals close to the Fermi level are examined to visualize the changes seen on bond stretching. Our calculations with an additional Au atom show the introduction of molecular states within the HOMO-LUMO gap. The sensitivity of the conductance with respect to the location of these introduced states helps explain the large variations seen in previous work. In our case, the conductance near zero voltage bias for the added atom structure was nearly identical to the structure with the sulfur atom in the threefold FCC site.

The counterintuitive rise in conductance with increasing Au-S bond length has been reported previously.^{80,821} The Hückel calculations are helpful in pointing out the extreme sensitivity of the conduction to the electron charging energy. In effect, the molecular states within the junction need to be able to shift with respect to the applied bias. This will be

¹ A reviewer for this paper has commented on our neglecting to mention that the voltage dependence of the vacuum barrier could lead to increased conductance through Fowler-Nordheim tunneling. This is an important issue to address when dealing with extended molecular structures where one might expect fluctuations in the energy levels. In the system studied here consisting of a geometrically fixed benzene ring these contributions are assumed to be negligible.

handled using DFT methods so long as the molecule can be accurately represented in the SCF regime. The Coulomb blockade regime and the strong electrode/ molecule coupling regime are well defined; in the intermediate range, new methods may be required to calculate transport accurately.¹⁴⁹

4.8 Molecular dynamics

Integrating molecular dynamics and charge transport should give a dynamic picture of the charge transport through molecular junctions. The experimental variation in conductance that can be expected through dynamically evolving Au-molecule-Au junctions is approximated using molecular dynamics to model thermal fluctuations and a non-equilibrium Green's function code (Hückel I-V 2.0) to calculate the charge transport. This generates a statistical set of conductance data that can be used to compare directly with experimental results.

The ability to make a large number of molecular junctions was first shown using a mixed monolayer containing thiol and dithiol terminated molecules. Au clusters were then deposited on the surface, sticking only to the molecules with thiol termination exposed. An atomic force microscope probe could then image the surface and record conductance values at each location.⁶⁵ A histogram of over 4,000 such traces using octanethiol/octanedithiol molecules showed peaks at integer multiples of $1.43\text{e-}5 G_0$ ($G_0 = (12.9 \text{ k}\Omega)^{-1}$) with a standard deviation of $\pm 7\%$ for the peak attributed to a single molecule.⁶⁵ Later results by the same group using a similar technique on the same molecules showed two peaks associated to a single octanedithiol molecule at $7.23\text{e-}5 G_0$ and $2.08\text{e-}4 G_0$.⁷³ The two values are attributed to possible differences

in the Au-S binding site. Using the published plots with Gaussian fits, it is possible to calculate the standard deviation for these conductance values as $\pm 16.5\%$ and $\pm 16.8\%$ respectively.

A related method was developed in which a Au scanning tunneling microscope tip is repeatedly moved into and out of contact with a Au substrate in solution containing dithiol molecules.⁶⁷ This method allows for a much greater number of measurements to be taken. The results typically show a broad peak attributed to a single molecule and higher order conductance peaks.^{67,68,76,82,84,150}

These results have been extended using diamine terminated molecules in the junction.^{69,117,127,128} Tens of amine terminated molecules have been measured, showing typical conductance variation on the order of $\pm 40\%$ and never showing peaks at higher multiples of conductance, attributed to multiple molecules in the junctions. The question of conductance scaling in molecular junctions is quite interesting and should be addressed in future work.¹⁵¹

Theoretical approaches to charge transport through junctions have focused on the Landauer/Imry limit, of elastic scattering, calculated using a non-equilibrium Green's function (NEGF).³⁴ One of the simplifications nearly always used to date in molecular transport junctions is the assumption of static geometry. Several recent papers have attempted to calculate charge transport for varying molecular geometries,¹⁵² but due to the cost of transport calculations typically only one or a few molecular orientations were used to calculate transport behavior. Past results from our group and other groups have shown that for a chemisorbed *p*-

benzenedithiol molecule between Au electrodes the molecular orientation and binding site can have an effect of up to 3 orders of magnitude on the conductances.^{130,153-155}

In a recent paper, a large force field molecular dynamics calculation was performed on a monolayer of biphenyldithiol.^{156,157} The molecular dynamics method was then used to find three packing structures that were energetically favorable for biphenyldithiol and the transport behaviors of these three structures were calculated and compared.¹⁵⁸ The main results of this paper indicate that there is a relatively flat potential energy surface with respect to the tilt of the molecule above the Au surface. For two different tilt angles of 15 and 30 degrees, the low bias conductance varied up to half an order of magnitude, attributed to changes in the sulfur-Au coupling.¹⁵⁸

With most experimental measurements at room temperature, the phase space sampled by the molecule and the electrode could have a critical effect on the measured conductance. This dynamic variation is typically neglected from transport calculations. We couple molecular dynamics simulation and charge transport calculations, allowing a computational study of the thermal fluctuation and geometric effects on conductance (Figure 4-7)¹⁵⁹.

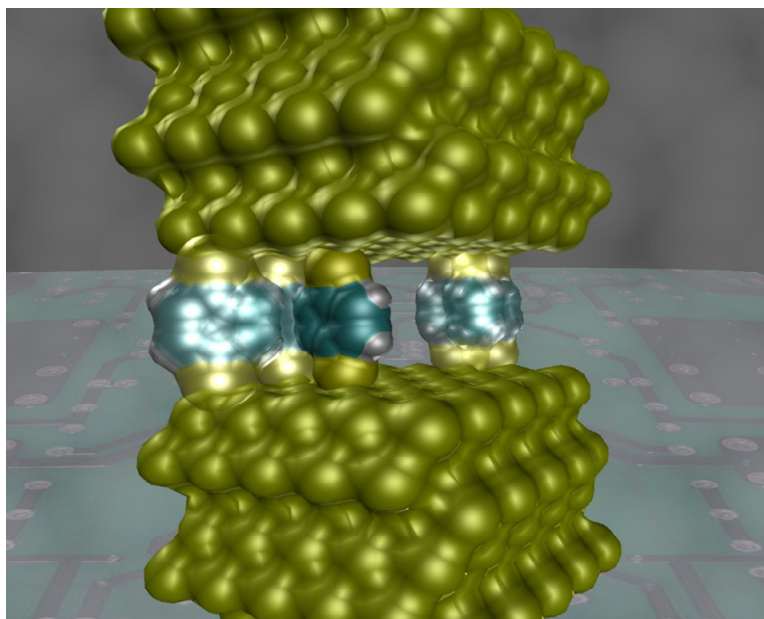


Figure 4-7. The image shows multiple timeshots taken from a 1ns trajectory of a dithiol terminated molecule free to move between two Au electrodes. The slightly opaque molecules represent time steps that have already occurred but are present visually to show the dynamic nature of the Au surface-thiol interaction.

A benefit of doing molecular dynamics simulation is the ability to address the temperature dependence of molecular junction transport. This technique allows a direct calculation of the thermal width of the conductance peaks that would be expected at liquid helium and liquid nitrogen temperatures, which has not been experimentally attempted at this time.

To calculate thermal geometric fluctuations in molecular junctions, we have utilized the Tinker Molecular Dynamics program using the MM3¹⁶⁰⁻¹⁶² force field (<http://dasher.wustl.edu/tinker/>). The MM3 force field was modified by using the parameters calculated by Goddard et al to describe the Au-Au and Au-organic atom interactions.^{156,157} The

Au metal-bond interaction as used is an exponential-6 type function used to reproduce the bulk Au properties. To describe the Au-H₂N interactions, we have used the recent DFT calculations completed by Venkatarman, et al. to describe the strength and distance of the Au-N bond to a single Au adatom.⁶⁹ The force field parameters otherwise used are given within the MM3 force field. Table 4-2 provides the force field parameters used.

Table 4-2. The MM3 force field parameters used within Tinker. If the values were given using a different molecular dynamics program in the associated reference then those parameters were matched using the appropriate equations.

E^{vdW}	$r_{ij}(\text{Å})$	$\epsilon^{\#}(\text{kcal/mole})$		
Au-Au	2.886	2.691		
Au-N ¹⁵⁶	3.082	5.036		
Au-S ¹⁵⁷	2.682	8.008		
Au-H ¹⁵⁷	3.082	0.036		
Au-C ¹⁵⁷	3.561	0.057		
C-C ¹⁶³	3.500	0.057		
H-H ¹⁶³	3.850	0.111		
H-C ¹⁶³	3.13	0.0425		
Angle	$K_{\theta}(\text{md Å}^2/\text{rad}^2)$	θ_1	θ_2	θ_3
C-C-S	0.600	120	0	0
C-C-C	0.760	120	0	0
Au-N-C ⁶⁹	1.2	117.50	0	0
H-N-C ⁶⁹	0.587	109.0	108.5	0
Bond	$l_0(\text{Å})$	$k_s(\text{md}/\text{Å}^2)$		

C-S ¹⁵⁶	3.000	1.70		
N-C ⁶⁹	6.32	1.335		
N-H ⁶⁹	6.42	1.0350		
Au-N	1.25	2.2900		
OPBEND	(md Å /rad ²)			
C-S	0.200			
Torsion	V ₁ (kcal/mole)	V ₂ (kcal/mole)	V ₃ (kcal/mole)	
S-C-C-C	0.000	5.470	0.000	
H-C-C-S	0.000	5.470	0.000	

Mulliken charges were calculated using the ATK transport software.

Benzendithiol

S	0.08
C(S)	-0.14
C	-0.04
H	0.07

Benzenediamine

Au	-0.13
H	0.00
N	0.28
C(N)	0.03
H	-0.05
C	-0.04

One of the critical parameters for simulating the dynamic behavior of benzenedithiol on a Au surface is the Au-S potential. The potential used in this manuscript is an exponential-6 type function.¹⁵⁷ Figure 4-8 shows the Au-S potential scanned over a 5 Angstrom range in both the X and Y directions. At each position the surface-S distance is varied and the minimum energy value is plotted. It is shown to give a visual qualitative feel for the potential energy surface that the sulfur atom sees, with the green spot representing energetically unfavorable sites above a surface Au atom. For comparison a much more thorough DFT calculation of the Au surface sulfur potential has been completed.¹⁶⁴ In this work the authors calculate the energy for a chemisorbed benzenethiol while varying the x,y and z sulfur position above the Au lattice as well as the tilt angle of the benzene ring with respect to the surface. The minimum energy location is calculated to be between the fcc and bridge sites with a tilt angle of $\sim 60^\circ$ to the surface normal.¹⁶⁴

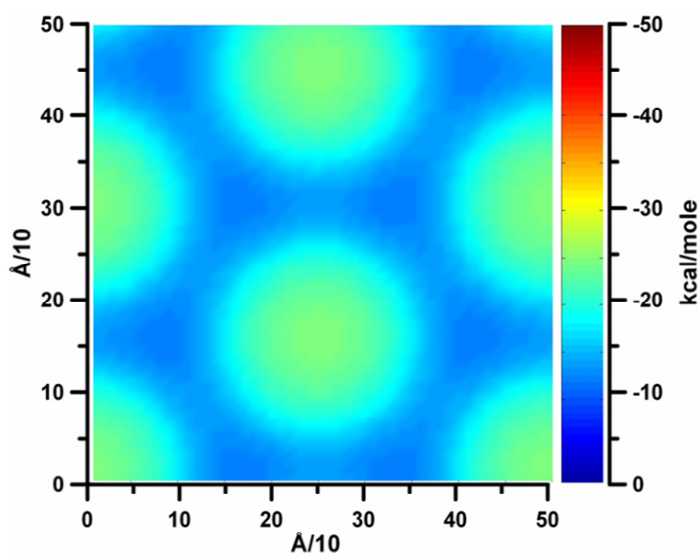


Figure 4-8. The Au-surface potential described by an exponential-6 type function.

The default Au-slab used in the molecular dynamics simulations was a 150 atom Au(111) pad that was 6 layers thick. This Au-slab was coupled with periodic boundary conditions that matched the Au crystal lattice constant in the X-Y plane. In the Z direction, the periodic boundary was set to 100 nm to decouple interactions between the top and bottom electrodes. In all calculations, except those noted otherwise, the Au atoms were constrained to their bulk lattice positions using a $100 \text{ kcal}/(\text{mole}\text{\AA}^2)$ harmonic force constant during the molecular dynamics simulation. The long-range Coulomb interactions were treated using the particle mesh Ewald summation as coded in Tinker.¹⁶⁵ A time step of 1.0fs was used with the Verlet algorithm to integrate the equations of motion for the system. All simulations were carried out as a canonical ensemble (NVT) using the Nose-Hoover thermostat with a relaxation time of 0.1ps to control temperature. The suspending geometry of a molecule between two electrodes is typically a local minimum in the low coverage limit, as the molecule would preferentially lie flat on one surface.

The first step after construction of a molecular junction was minimization within Tinker using the limited-memory quasi-Newton optimization method (L-BFGS). The junction was then heated to 300K over 50ps. The molecular junctions were then allowed to equilibrate at 300K for at least 500ps. Individual junction geometric information was then recorded every picosecond for 500ps.

For charge transport calculations, we utilized the Hückel - IV v2.0/1.0^{39,139} program, a code developed at Purdue University and freely available online at Nanohub.org. The Hückel -IV program has been optimized to run with a three atom Au pad which couples the molecule to

the bulk Au electrode. To use these molecular junctions within the framework of the Hückel -IV program, the 3 Au atoms nearest to the S atom were parsed from the molecular dynamics simulation. In the chemisorbed *p*-benzenediamine system the three nearest Au atoms to the Au adatom were used, giving a total of 4 Au atoms per side. The Au adatom is needed to properly describe the Au-amine interaction.⁶⁹ An image of the *p*-benzenediamine junction is given in Figure 4-9. One assumption made in following this procedure is that there is constant coupling between the three-atom Au pad and the bulk Au electrode. Because of the relative invariance in conductance upon small variations in the Au-Au bond length this assumption should have a minor effect on the calculated behavior.¹⁶⁶

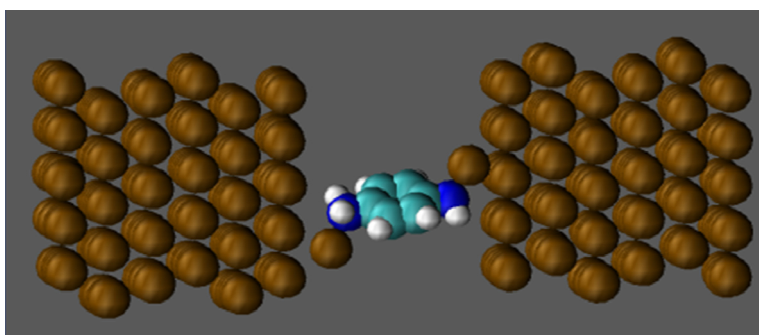


Figure 4-9. The *p*-benzenediamine junction shown with the Au adatoms attached. In the Hückel calculations only the Au adatom and its 3 nearest Au atoms are included in the calculation.

This code uses extended Hückel theory orbitals to calculate the energy of the isolated system with the 3 atom Au pad. There are two parameters, the Fermi level and the charging energy, U . In Hückel -IV v2.0, the energy level shift is then included through charging energy in a self-consistent field approach. In these calculations, the Fermi energy is held constant

throughout the entire distribution of structures. The charging energy U is used to describe how the energy levels shift upon charge transfer to the molecule. In these calculations we have set the charging energy parameter $U=0$. This effectively means that a change in electron transfer to the molecule will not change the energy levels of the molecule. While the charging energy for a molecule like benzenedithiol is expected to be 1-2eV,³⁹ in the low bias regime away from molecular resonance, this should not have a large effect on the conductance.³⁹

First we consider a single chemisorbed *p*-benzenedithiol molecule between two 150 atom Au layers (Figure 4-10 a). In this initial simulation, the 25 atom Au surface layers started at 10.6 Angstroms apart. The periodic boundary was matched to the Au crystal lattice in the X and Y directions. The periodic boundary in the Z direction was set to 50nm, allowing the Au electrodes slabs to vary in distance. The two probe system was free to equilibrate for 500ps at 300K. The data was then collected every picosecond for the next 500ps. The average Au-Au electrode distance was 11.07 Å as shown in the Figure 4-10b. Figure 4-10c and 2d show a histogram of 500 transport calculations completed on this system. The first image is plotted on a linear-linear scale and the second plot is shown on a log-log scale for comparison. Viewing conductance data that spans an order of magnitude or more is easiest on a log scale. To aid readability and maintain consistency between the plots all further conductance plots will be shown on a log-log scale. The average conductance value is $7.26e-3 G_0$ which compares with the published experimental result of $1.1e-2 G_0$.⁶⁸ In Figure 4-10d three molecular orientations are also shown as examples of low, average and high conductance states of the molecule. The image representing low conductance shows the plane of the molecule intersecting one of the

Au fcc triangular faces. The high conductance state shows the plane of the molecule along one of the sides of the Au fcc triangular lattice. The average Au-S distance and the shortest Au-S bond distance showed no direct correlation to the average conductance in these 3 example states. This behavior was consistent through all example orientations checked. This result can be correlated to published results on symmetry breaking and conductance through the chemisorbed *p*-benzenedithiol molecule, showing increased conductance when the molecular π orbitals overlapped favorably with the Au 6S valence orbital.¹³⁰

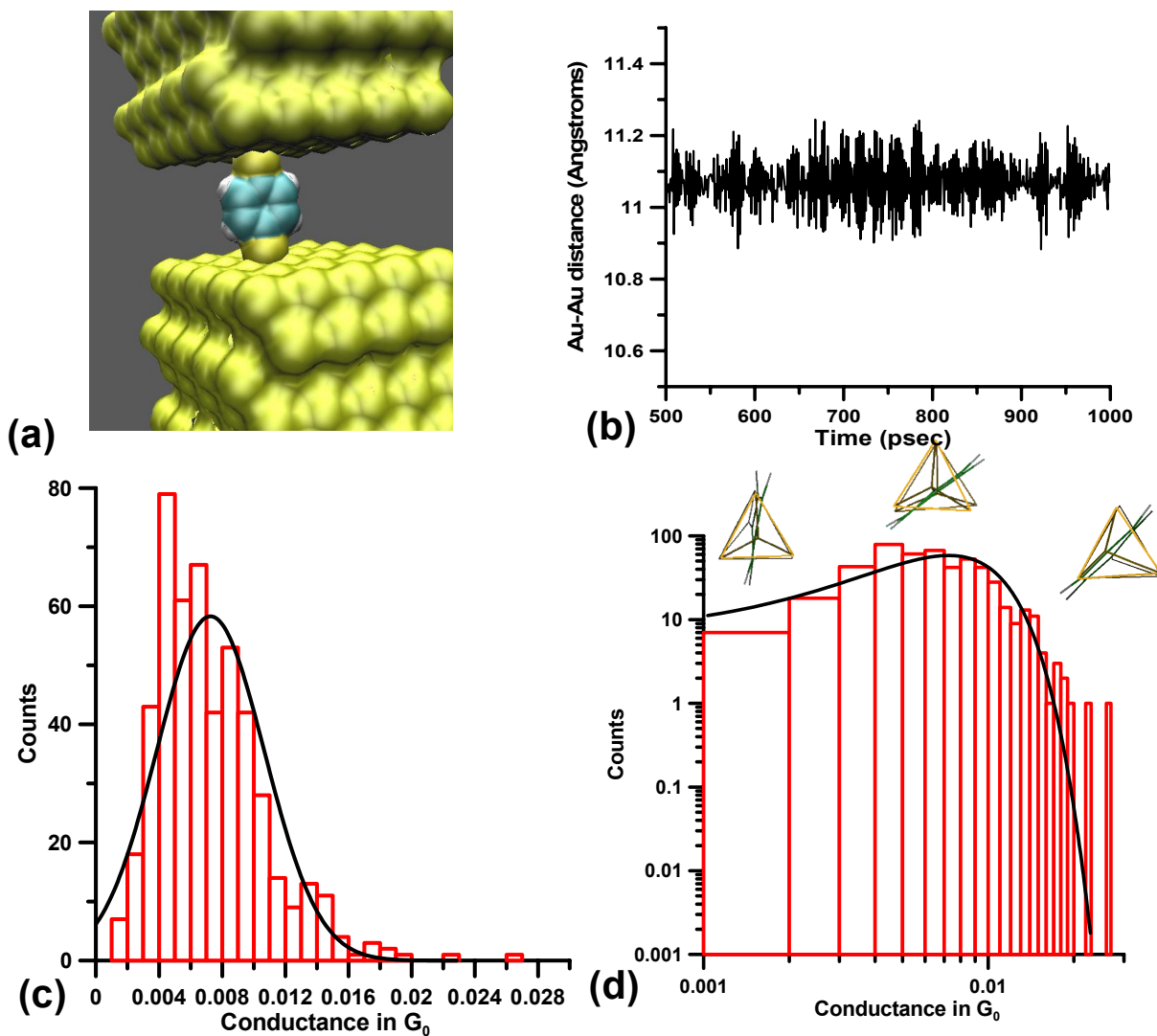


Figure 4-10. (a) The conductance of a chemisorbed *p*-benzenedithiol molecule between Au electrodes. The Au-Au electrode distance is free to vary as shown in b. A histogram was calculated from 500 discrete geometries corresponding to 500ps of molecular dynamics simulations. The bin size of both the histograms is $1e-3 G_0$. Plot (c) is a linear scale and (d) shows the identical data on a log-log scale. Using a Gaussian fit the average conductance is $7.26e-3 G_0$ and the standard deviation is 47%. The most probable conductance value is $5e-3 G_0$. The insets in (d) show a top down view of the molecular junction for three typical structures representing low, medium and high conductance.

In Figure 4-11 we have included a plot showing the transmission variation as a function of energy. This plot shows that the variation in conductance is relatively constant within the HOMO-LUMO gap but would increase if the Fermi energy was in close proximity to a molecular resonance.

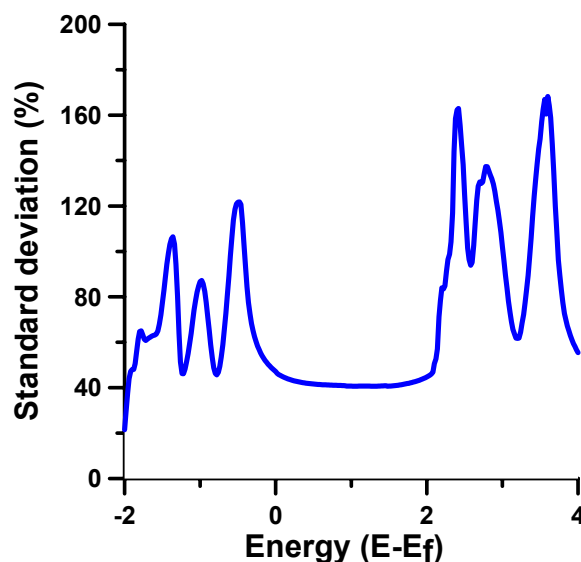


Figure 4-11. The variation in conductance as a function of energy. What we can see from this plot is that within the HOMO-LUMO gap between $\sim -0.25\text{eV}$ and 2eV the variations are a relatively constant percentage of the average current. If the Fermi energy was close in energy to a molecular resonance the current fluctuations would be higher.

We have included a Gaussian and a Lorentz fit to a histogram with a bin width of $0.0001 G_0$, shown in Figure 4-12. The bin width does have an effect on the fits and care must be taken to use an appropriate bin width. The Gaussian fit gave a better overall fit to the calculated conductance frequency than a Lorentz fit over all bin widths tested. The question of how to fit a histogram of conductance data is not completely straightforward. It is easy to conceive of a situation where the potential energy surface for a molecule between two electrodes has a few local minima with distinct conductance characteristics. In this hypothetical situation a multi peaked conductance spectrum could occur; indeed, the data shown here supports just such a junction. Essentially particular geometric configurations provide a much better electrode

coupling than do any of the other others; this is not captured by the simple statistics. Indeed, there is no particular reason why the most conductive geometry should match any particular minimum energy.

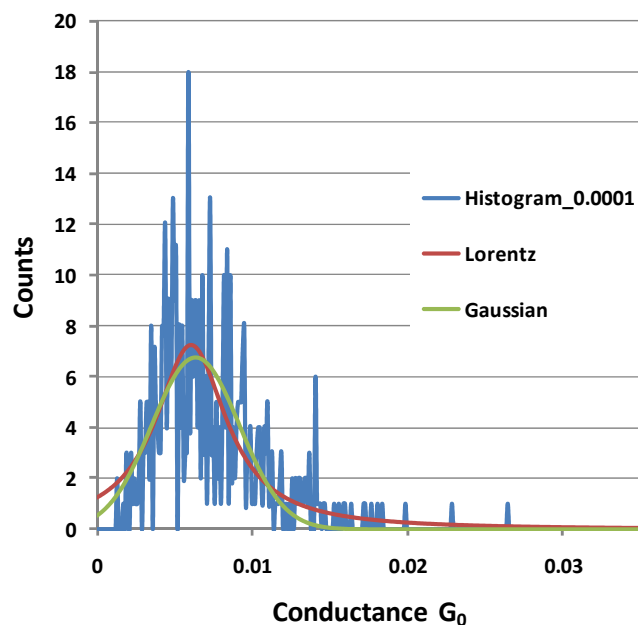


Figure 4-12. Comparison of a Gaussian and Lorentz fit to histogram of conductance data.

The Au-Au electrode distance was then varied between $10. \text{Å}$ and 12.2Å . In these calculations the Au atoms were all confined to their bulk lattice positions through a harmonic force constant of $100 \text{ kcal}/(\text{mole } \text{Å}^2)$. Gaussian fits to each histogram of results using a bin size of $1e-4 G_0$ or $1e-5 G_0$ are shown in Figure 4-13. The height of the peaks is related to the bin size with lower current values giving higher peak heights. Over the 1.5nm that the Au electrodes are separated the average conductance value decreases more than one order of magnitude.

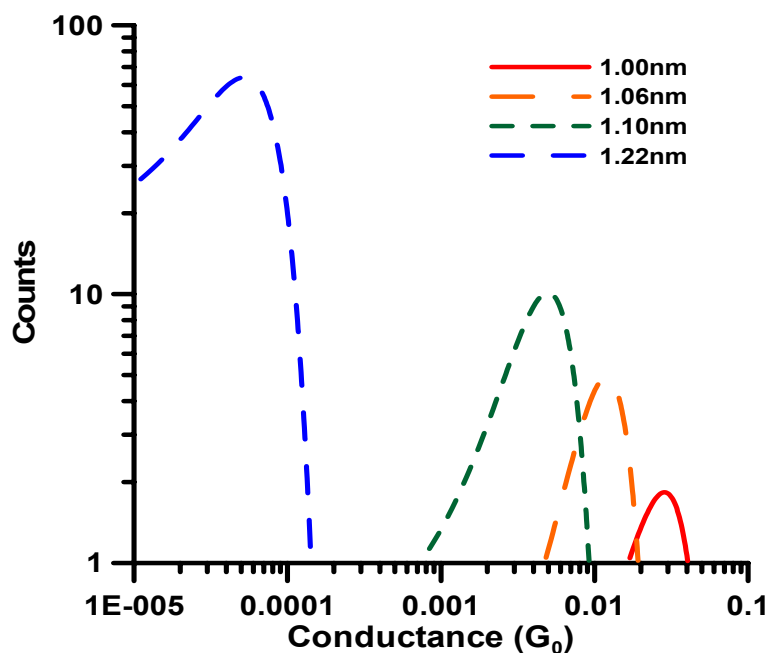


Figure 4-13. Gaussian curves fit to 500 geometries for a chemisorbed *p*-benzendithiol molecule between two Au electrodes. The Au atoms are fixed in each simulation and between simulations the electrode separation is varied from 10 Å to 12.2 Å. The height of the peaks is related to both the standard deviation in conductance and to the histogram bin width, which is $1e-5 G_0$ for 12.2Å and $1e-4 G_0$ for 10 Å, 10.6 Å and 11Å separation.

While most of the current break junction measurements have been completed at room temperature, it is important to examine what variance in conductance could be expected for a molecular junction at lower temperatures. In Figure 4-14 we show the change in conductance for the chemisorbed *p*-benzenedithiol system without harmonically restrained Au atoms. 500 conductance spectra are calculated at liquid helium temperature (4.2K), liquid nitrogen temperature (77K), and at 230K along with the results for 300K previously shown in Figure 4-13. The standard deviation in the conductance decreases from 47% at room temperature to 22.2%

at liquid nitrogen temperature to 6.6% at liquid helium temperature. The mean conductance value also decreases from 0.0112 G_0 at 300K to 0.007 G_0 at 4.2K. This value is very similar to the most probable conductance value of 0.008 G_0 calculated at 300K.

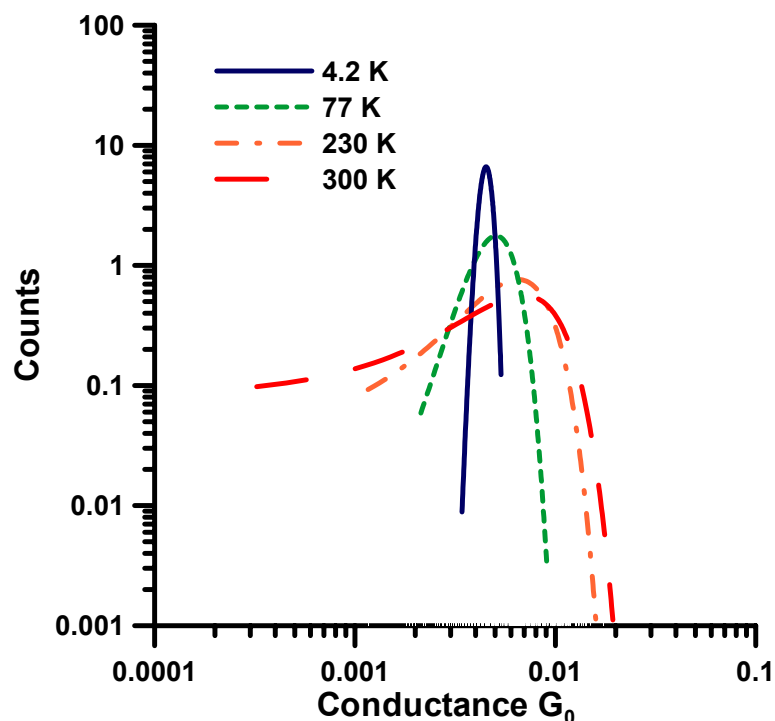


Figure 4-14. Temperature dependence for a Au- chemisorbed *p*-benzendithiol-Au junction. The Au electrodes were free to move in the Z direction but stayed on average 11.05 Angstroms apart. The standard deviation decreases from 47% at 300K to 6.6% at 4.2K.

To compare with other recent experimental results we have also calculated the conductance variation that can be expected for a chemisorbed *p*-benzenediamine molecule between two Au electrodes. The amine Au interaction is weaker than the Au – sulfur interaction, and it is expected that an amine terminated molecule interacts only with a Au adatom on the surface.⁶⁹ In order to model this we have used a Au adatom that is free to move

in our molecular dynamics and transport calculations for the amine terminated molecules. The bulk Au electrode atoms remain harmonically fixed. Figure 4-15 shows the distribution in conductance values for 100 geometries from 100ps of simulation for a fixed Au-Au electrode distance of 11.0 Å. The average conductance value is 0.012 G_0 and the standard deviation is 37%. At an electrode distance of 11.0 Å, this standard deviation is a bit lower than that calculated for the chemisorbed *p*-benzenedithiol system (47%) shown in figure 1. While the average conductance is quite similar to that calculated for the chemisorbed *p*-benzenedithiol molecule, we remind the reader that the Fermi energy is an adjustable parameter in these Hückel IV calculations and a small shift in the Fermi energy toward or away from the highest occupied orbital resonance could have a large effect on the magnitude of the conductance.

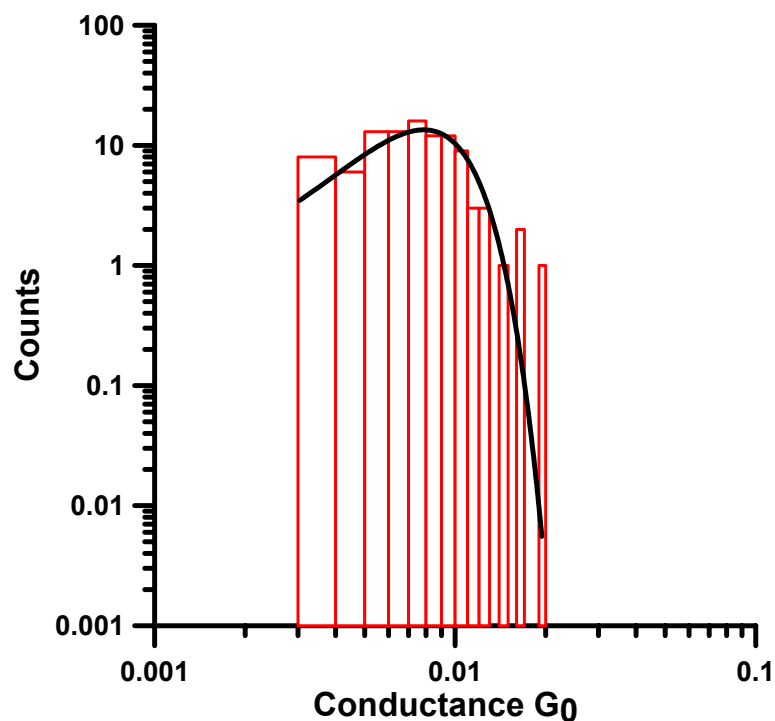


Figure 4-15. A chemisorbed *p*-benzenediamine molecule between Au electrodes at a fixed separation distance of 11 Angstroms. The molecular junction was equilibrated for 900ps and then every picosecond for 100ps a geometry was taken and the transport behavior was calculated. The red bar graph shows a histogram of the conductance with a bin size of 0.01 G₀ while the black line shows a Gaussian fit to the data. The average conductance is $7.8 \times 10^{-3} \text{ G}_0 \pm 37\%$.

To test the change in conductance with the change in electrode distance we varied the electrode distance and calculated the transport values. Figure 4-16 shows the Gaussian fits for 100 geometries at 10, 11, 12 and 13 angstrom electrode separation distance. It should be noted that the peaks in the fit for 10, 11 and 12 angstroms are quite close together. To compare to the chemisorbed *p*-benzenedithiol molecule Figure 4-17a shows a plot of the

average values and the standard deviations upon electrode separation. In the plot it should be noted that the Au-S conductance seems to decrease rapidly upon electrode separation while the Au-amine conductance has a much slower rate of initial change in conductance. For both molecular systems the electrode separation corresponding to the minimum energy also has the smallest deviation in conductance values. The comparison with the published experimental results is shown in Figure 4-17b. Both the peak position and the distribution of calculated values show good agreement.

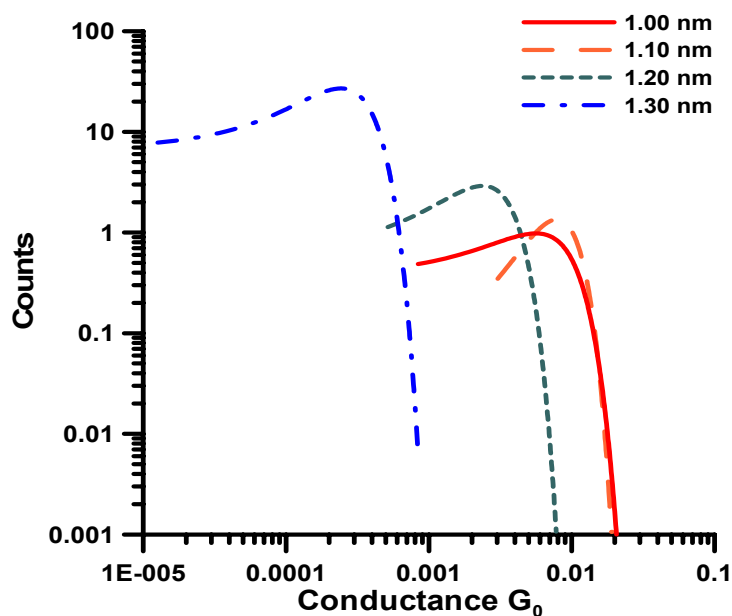


Figure 4-16. A chemisorbed *p*-benzenediamine molecule between Au electrodes at a varied Au electrode distance. A Gaussian fit for 100 geometries from 100ps of simulation are shown. The histogram bin size is held constant at $1e-4 G_0$.

The results presented here mirror single molecule experimental results in showing a wide distribution of current values attributed to a single molecule junction. Our results show similar deviation in conductance values, and assumed a chemisorbed *p*-benzenedithiol molecule on a Au surface and a chemisorbed *p*-benzenediamine molecule bound to a free Au-atom on a Au surface. The chemisorbed *p*-benzenediamine molecule conductance varied little upon stretching the interelectrode distance by 2 \AA . This can be compared to the chemisorbed *p*-benzenedithiol molecule, which showed a rapid decrease in conductance with increasing electrode distance. These results seem to indicate that building single molecule

electronic devices with reproducible conductance at room temperature using Au electrodes with sulfur or amine coupling will be extremely difficult due to the large variances arising from thermal fluctuations.

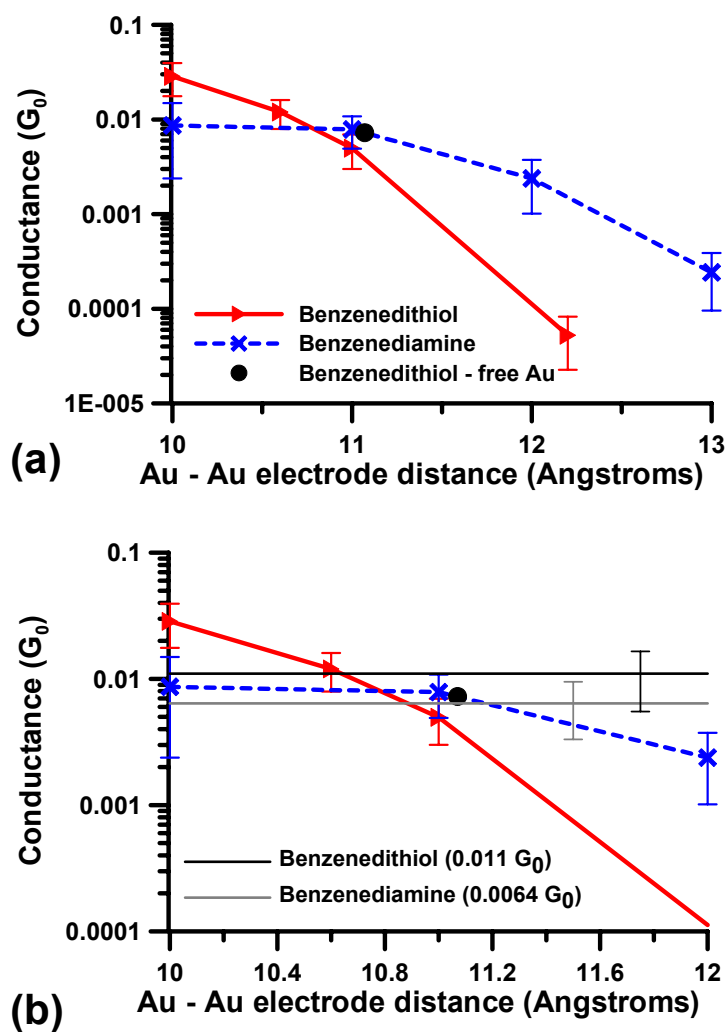


Figure 4-17. (a) Conductance versus electrode-electrode distance for both the chemisorbed p-benzenedithiol and the chemisorbed p-benzenediamine molecules. (b) The calculated results from Figure 7a plotted with published experimental results (black and grey lines) for the conductance through the chemisorbed p-benzenedithiol and the chemisorbed p-

benzenediamine molecules.^{68,69} The error bars on the experimental lines are approximated from the published figures and since the measurements are not associated with an electrode distance only placed on the graph to aid in comparison with our results.

4.9 Conclusions on molecular dynamics

Concerning the accuracy of these calculations there are three main considerations: the description and geometry of a molecular junction, the accuracy of the molecular dynamics force field and the adequacy of the transport code. Our description of the junction geometry is simplified by having two matching FCC terminated Au electrodes with a molecule bridging the gap. In the room temperature scanning probe electrochemical break junction experiments, the repeated motion of bringing a Au tip into contact with a Au surface likely creates disordered electrodes. Upon retracting the Au tip it is also quite likely that a Au neck forms and that this Au neck is more likely to break than the Au-S bond.^{68,167} Attempting to model accurately a Au tip may be important for a comparison with experiment but as a first approximation we have focused on using two defined electrodes.

The Au-Au and the Au-molecule force field potentials have not been extensively tested in the literature. There is a high cost of performing calculations on the large number of Au atoms required to describe the surface and the surface molecule interactions. In the static limit there have been a number of papers describing the location of a sulfur bound molecule above the Au surface (for more detail see ref).¹⁶⁴ While the Au-S interaction is greatly over simplified by using the exp-6 function in the molecular dynamics, we do not believe that this greatly changes our

results on the distribution of geometries and current values that might be measured in a single molecule junction.

In terms of charge transport codes, we have used a robust, well-tested code using extended Hückel molecular orbitals. This code has been shown to have results qualitatively equivalent to computationally more expensive DFT-based codes.^{39,139,166} The importance of the treatment of the electrostatic potential increases with increasing voltage, therefore we have limited our results to the low bias regime, specifically conductance at 20mV. This voltage bias corresponds well with experimental methods^{67,68,127,128}

A recent manuscript computationally addresses the issue of amine and thiol terminal groups in break junction experiments utilizing DFT methods to optimize the structure at various electrode distances.¹⁶⁸ Their results, in contrast to ours, show a quick drop off in the amine terminated conductance, whereas the chemisorbed *p*-benzenedithiol molecules shows a large rise in conductance before decreasing with increasing electrode distance.¹⁶⁸ This is due to a calculated charge transfer to the molecule and the use of self-consistent-field methods and a first-principles Hamiltonian for the molecule.^{80-82,166,169,170} Another recent manuscript, which computes the conductance of 15 distinct Au- *p*-benzenediamine geometries using a DFT code, calculates a distribution of conductance values similar to the experimental results, but an average conductance value seven times higher.¹²⁹ Our method seems to provide a reasonable comparison with experimental results, capturing the dynamics of a charge transport junction and the associated current fluctuations.

Using molecular dynamics and an extended Hückel non-equilibrium Green's function transport code we have modeled transport junctions. We find good agreement with experimental measurements with respect to both the magnitude and width of the measured conductance peaks. This technique of modeling a transport junction as an ensemble of molecular geometries gives insight into how the thermal fluctuations of a junction can provide a large distribution of conductance values. This technique could be valuable in the design and understanding of single molecule junctions with reproducible conductance. As shown in Chapter 6, this method of using molecular dynamics and charge transport calculations proves to be useful in verifying the stability of interference features in the transmission spectrum, calculated for potential molecular device candidates.

Chapter 5. Construction of a UHV-STM

5.1 Motivation

The broad goal is to characterize molecular surfaces and junctions at the single molecule level in more detail than has been previously accomplished. This broad goal can be broken down into four main objectives:

- (1) Utilize tip enhanced Raman spectroscopy to chemically map surfaces and correlate these results with STM imaging,
- (2) Understand what types of junctions lead to single molecule SERS,
- (3) Measure the transport properties of molecules with potential applications in molecular electronics, and specifically study molecules that are strongly coupled to both electrodes,
- (4) Correlate the transport properties with spectroscopic information provided by Raman spectroscopy.

The merging of TERS and STM imaging is a difficult experimental undertaking. To maximize control in the design process, it is necessary to custom fabricate the instrument. The cryogenic UHV-STM presented here is a unique, custom designed and built instrument, a necessary undertaking to ensure extreme stability, cleanliness, and adequate optical access necessary for scanning tunneling microscopy and Raman spectroscopy.

5.2 Design

The underlying design for the cryogenic STM is adapted from an instrument currently in use in the Hersam laboratory.²⁴ The system was primarily designed for single molecule studies

on silicon surfaces as well as metallic surfaces. This instrument allows operation from temperatures of 8.2K to 300K at a base pressure of $< 6 \times 10^{-11}$ torr. The previously built scanner has a drift of 0.008 Å/min at 8.2K. Importantly, the previous generation of this STM instrument operated for more than two years while maintaining UHV conditions.

A number of modifications have been made to the instrument to facilitate our designed operation. The most important change is situating the scanner so that there can be line of sight access to the tip sample junction for both incident and scattered light in a collinear arrangement. The optical setup is illustrated in Figure 5-1 showing the broad incident laser tunability and the liquid nitrogen cooled triple spectrograph CCD detector. The collection optics can be easily adjusted to allow Raman imaging using a liquid crystal tunable filter (LCTF) and an avalanche photodiode (APD). The Cambridge Research & Instrumentation LCTF uses a series of Lyot filter stages to pass a narrow frequency of light. Our two LCTF models produce a narrow transmission bandwidth of 0.25nm from 480-720nm and 0.75nm from 650-1100nm. It is important to note that these filters do not necessarily block all light in the frequencies outside their range, so it is necessary to use a high pass and possibly low pass filter. Use of the LCTF and an APD will allow imaging of specific vibrations. This could be useful in creating Raman images of the surface or in measuring TERS tip-sample distance dependence.

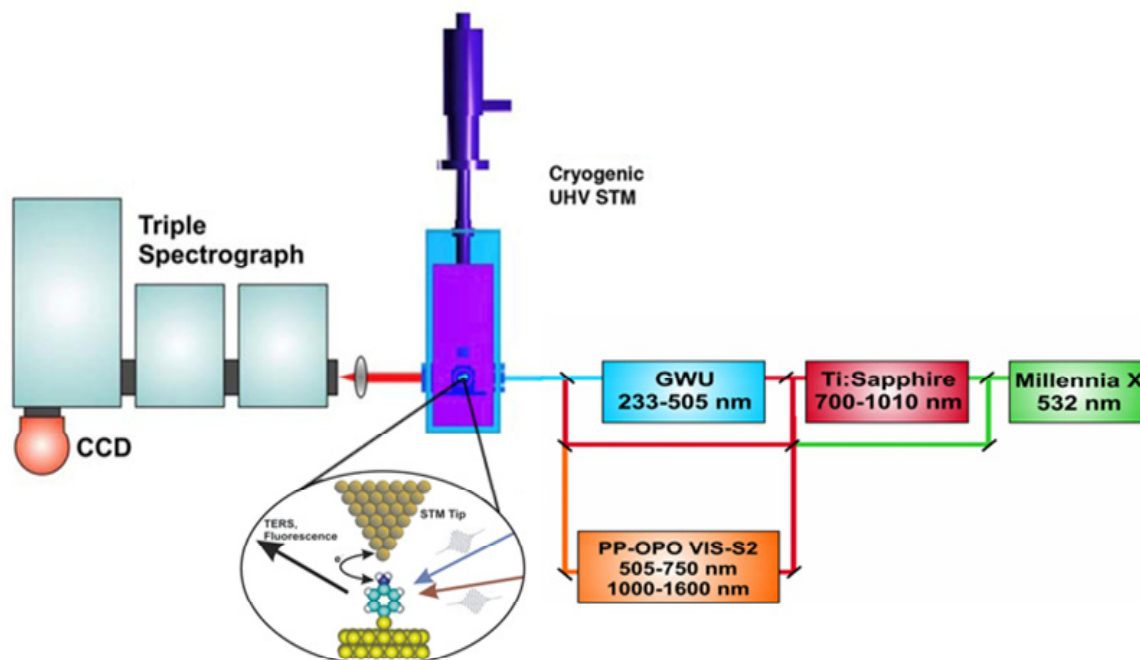


Figure 5-1. A schematic showing the integration of the UHV-STM with broad laser tunability from 233-1600nm.

One big modification from the previous version of the microscope is the inclusion of a preparation chamber as shown on the right of Figure 5-2 and with the internal view in Figure 5-3 (a). This additional chamber is useful for the preparation of both semiconducting and metallic surfaces. The chamber has a conductive heating station that allows for degassing of tips and samples brought into the chamber. The heating also allows for flashing silicon surfaces and for annealing metallic surfaces. A nearby cracking filament is used as a source of atomic hydrogen for preparing hydrogen passivated silicon surfaces. An ion gun and a triple source electron-beam evaporator are mounted on the preparation chamber. Sublimation as well as sample dosing can be done within the preparation chamber. Space in the chamber has been

reserved for possible addition of low energy electron diffraction (LEED) to allow surface characterization.

The entire system is mounted on a 20'x10' t-shaped optical table that can be floated on compressed air to reduce vibrational coupling through the floor of the building to the STM scanner.

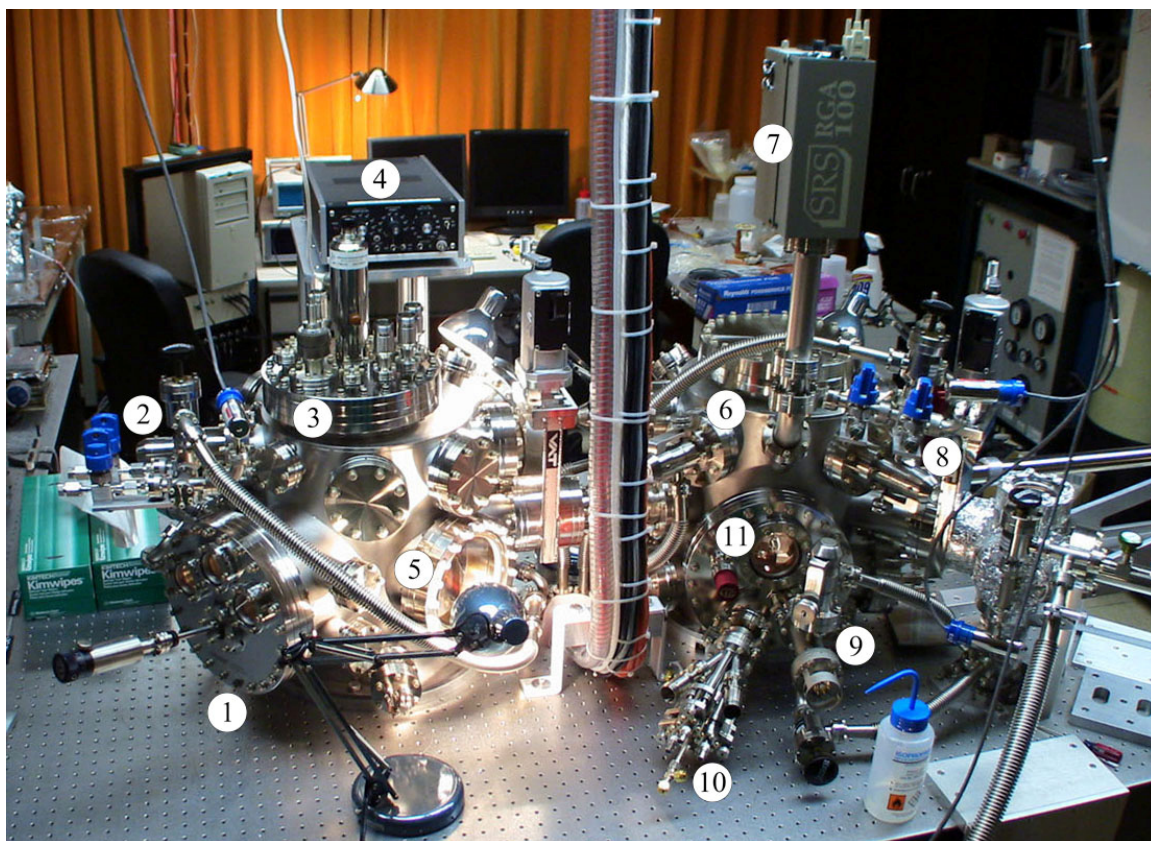


Figure 5-2. Detail of UHV chamber exterior hardware: rear rotary wobblestick (1), dosing mini-manifold (2), STM cryostat flange (3), STM tunneling current preamp (4), and tunable laser excitation viewport (5), and preparation chamber variable leak valve (6), residual gas analyzer

(7), dosing mini-manifold (8), sputter cleaning ion source (9), triple source evaporator (10), and pyrometer viewport (11).¹⁷¹

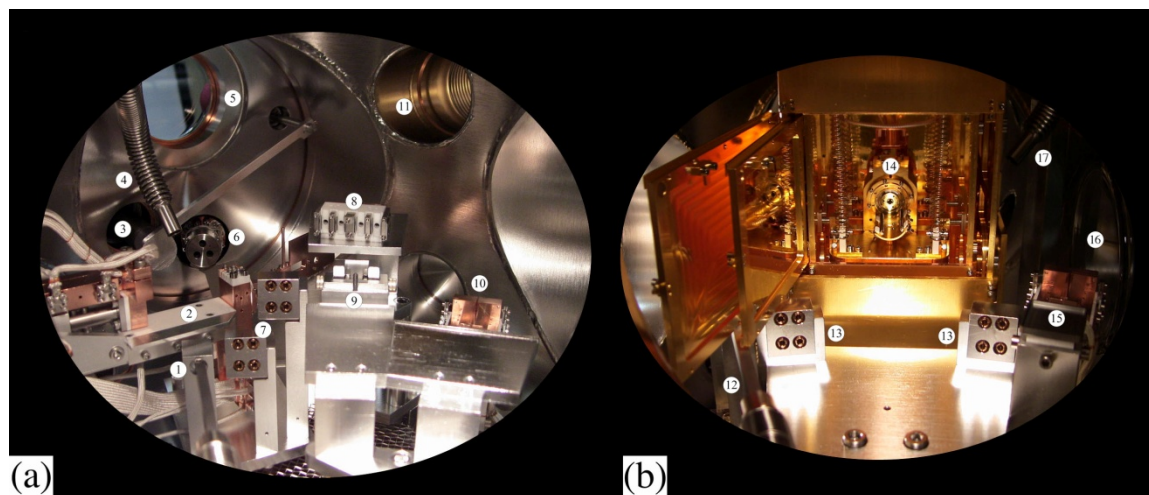


Figure 5-3. Detail of UHV chamber interiors as viewed through the front wobblestick flange viewports showing (a) sample and tip preparation chamber wobblestick garage (1), sample and tip preparation station (2), sputter cleaning ion source with external shutter (3), flex hose leading to variable leak valve (4), pyrometer viewport (5), triple source evaporator (6), tip garages (7), tip heating module (8), tip heating module station for tip loading/unloading (9), sublimation/evaporation module heating station (10), and transfer port to cryogenic UHV STM chamber (11), and (b) cryogenic UHV STM chamber wobblestick garage (12), tip garages (13), STM stage in the raised/locked position for sample and tip exchange (14), sublimation/evaporation module heating station (15), custom viewport for the *ex-situ* light collection optic (16), and flex hose leading to a variable leak valve.¹⁷¹

5.3 Construction details

With most of the design criteria established by Dr. McFarland and Dr. Foley, my primary involvement has been on preparation, construction, and installation of various portions of the instrument.

5.3.1 Polishing the rails

A large number of hours were spent polishing rails for the STM scanner. These rails are a critical piece of the system because the sample is translated along the range of the rails into tunneling range of the tip. The rails are made out of beryllium copper. In my experience, it was necessary to go over the rails initially with 160-200 grit sandpaper to clean up the coarse grooves in the surface from machining. At this point, I sequentially worked through the sandpaper grits of 240, 400, 600, 800, 1200, 2400, and 4000, ensuring that all the marks from the previous grit had been polished away. After the 4000 grit paper, the rails were polished using 1.0 μm , 0.3 μm and 0.05 μm suspensions of alumina particles. A fully polished rail is shown for reference in Figure 5-4. At this point the copper rails were extremely sensitive to the cleanliness of the gloves and solvents that were brought into direct and indirect contact with the surface.



Figure 5-4 . A fully polished beryllium copper rail.

The rails were coated in a layer of titanium nitride or using a composite of titanium nitride and zirconium nitride. These coatings make the surface of the rails much more resilient to scuffing from translation of the sample. In the first 8 sets of polished rails, the coating failed to adhere to the beryllium copper surface, as shown in Figure 5-5, and would flake off with any use. This was solved by using an adhesion layer of nickel electroplated onto the rails before the coating of titanium nitride and zirconium nitride was applied.

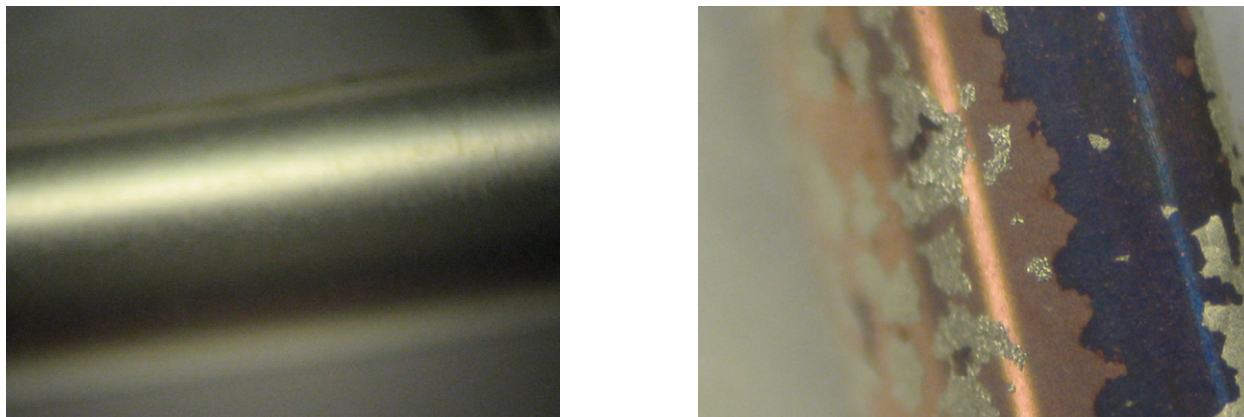


Figure 5-5. Failed coating of the beryllium copper rails with titanium nitride.

5.4 Silicon passivated surface

Initial testing of the STM on a hydrogen passivated silicon surface shows good imaging and noise performance of the instrument. The two images shown in Figure 5-6 show a typical image of a silicon surface. Step edges, indicating a change in height of one atomic layer, are seen clearly in both images by the 90 degree changes in the visible striations on the surface. These strips are indicative of rows of silicon dimers on the surface. The bright colored spots indicate the location of the silicon double bonds and the dark lines are the region between the double bonds. The bright spots on the surface are indicative of contamination on the surface, most likely water caused by outgassing within the chamber. With use, the entire system, including the linear manipulators and gate valves, should outgas less, improving the surface quality. The dark spots, most clearly visible in the right hand image, show silicon vacancies in the surface.

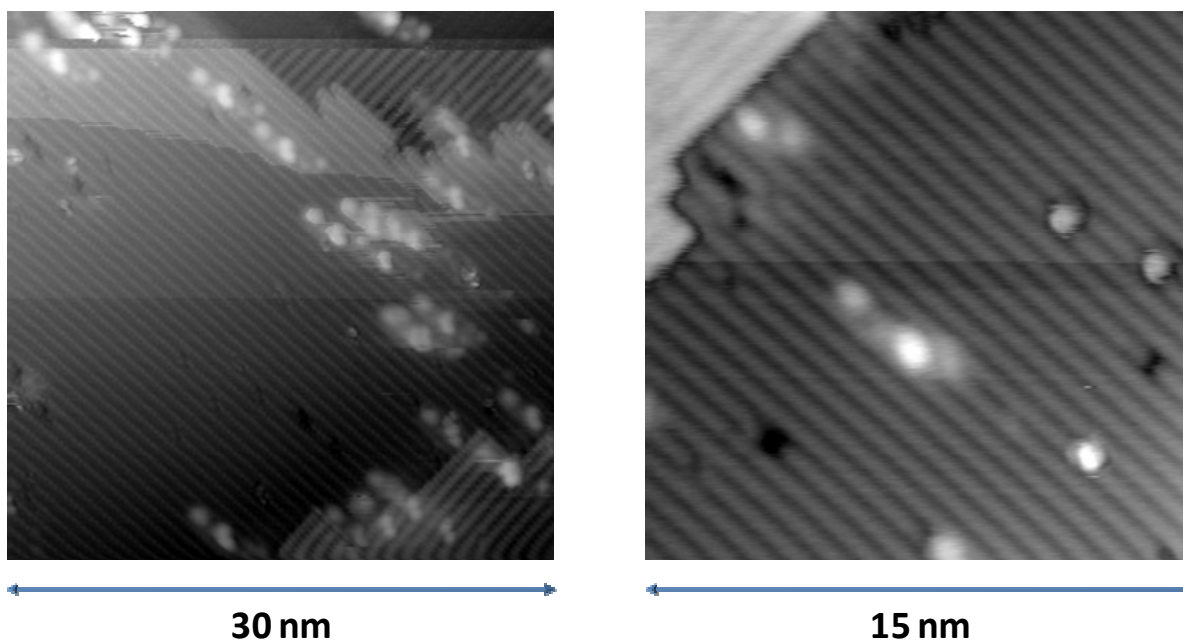


Figure 5-6. Scanning tunneling microscope images of a hydrogen passivated <100> silicon surface.¹⁷¹

For comparison, Figure 5-7 shows two of the highest resolution published STM images of Si(100). The image on the left was taken using the previous version of our current instrument.²⁴ The image on the right was taken using a Unisoku low temperature-STM and RHK SPM1000 control system at low temperature.¹⁷² These two images show clean surface conditions and high resolution in the detail of the silicon dimer rows.

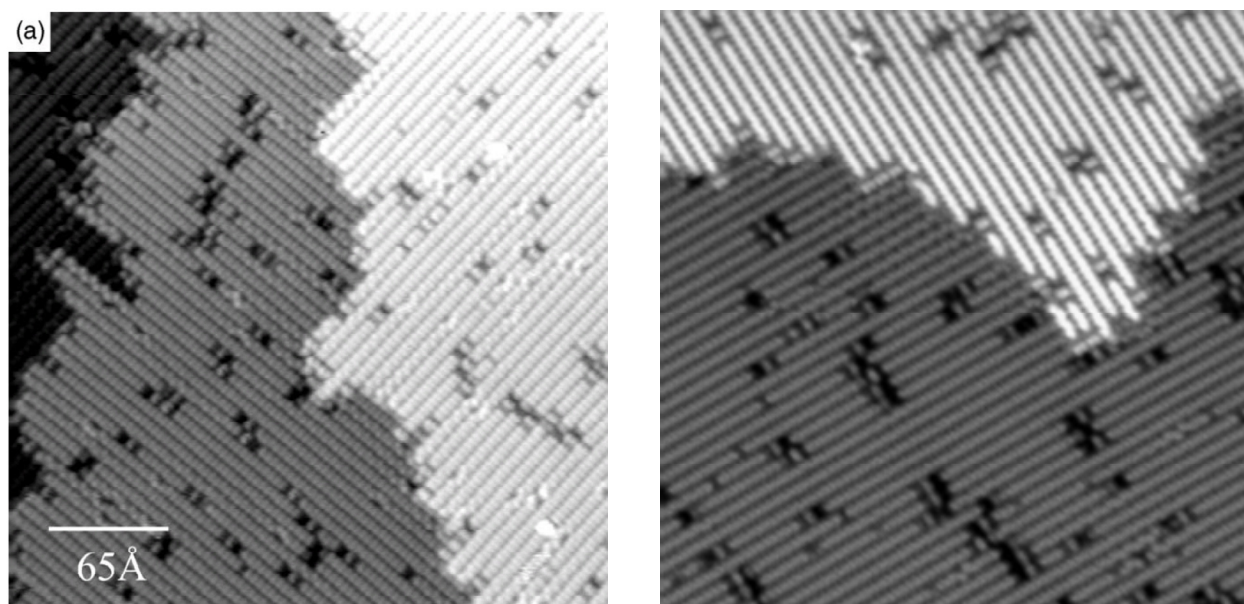


Figure 5-7. Two Si(100) images from published manuscripts. The image on the left was acquired in the group of Prof. Hersam at 300K.²⁴ The image on the right was acquired in the research group of Prof. Hasegawa.¹⁷² The silicon surface was imaged at an unspecified low temperature.

5.5 Competing designs

At this time, our goal of integrating spectroscopy and scanning tunneling microscopy is not unique. It is worth looking at the developments in the field, most of which have occurred in the past five years, and compare them to our design. I will address two families of experimental approaches currently being used to investigate small molecular junctions, tip enhanced Raman microscopes, and break junctions.

The large electromagnetic field created from sharp plasmonic materials, principally Ag and Au, led to the use of scanning probe instruments as the plasmonic material for surface enhanced Raman spectroscopy. In 2000, three different research groups published experimental tip enhanced Raman spectroscopy (TERS) results.¹⁸⁻²⁰ The sensitivity of this

technique, for specifically chosen resonant molecules, has been extended to the single molecule concentration.²¹⁻²³ In a recent development in TERS instrumentation from the Raman field, is work by the Pettinger group on a UHV instrument with a high numerical aperture parabolic mirror for focusing the incident beam and to collect scatter light.¹⁷³ The light is fiber coupled into the system and the only optic that needs adjustment is the parabolic mirror, which can be moved using a piezoelectric actuator.¹⁷³ This instrument is shown to be able to collect Raman scattering but there is no indication that atomic resolution can be achieved. For characterization of silicon surfaces, the base pressure of 10^{-10} torr is insufficient.

In development from within the STM community, the Wilson Ho group, along with Prof. Apkarian at UC Irvine, have constructed a UHV-STM with near two near infrared pulses generated using a pair of nonlinear optics parametric amplifiers. Their instrument design has the STM tip pointed up towards the down-facing sample. The incident laser illumination is brought in from the bottom at ≈ 45 degrees off the tip axis. The scatter light is collected using a piezoelectrically positioned parametric lens that reflects the light out the bottom of the chamber and towards a third meter spectrograph. The collection efficiency is reported to be 35% of the scatter light. Their UHV system is optimized for the preparation and characterization of molecules on single crystal Ag and NiAl surfaces. In terms of incident laser spot size and light collection efficiency, this instrument does seem to offer some advantages over our current design. The ability to have the optics focused on the tip-sample junction is important and it is unclear if their experimental setup hinders the focusing ability. One of the

advantages of working on a silicon support is the ability to use lithography to place a specific number of molecules within the tip region while maintaining a low background.

Mechanically controlled break junctions integrated with Raman spectroscopy have been used to simultaneously measure charge transport through molecular junctions and collect vibration information. In this experimental design, a microscopy objective is used for both incident and collection optics and is brought in close proximity to the sample, a thin Au wire on a silicon support.¹⁷⁴ This experimental apparatus operates in ambient conditions. In initial work, it was shown that the Raman intensity was polarization dependent and also depended on the gap separation.¹⁷⁴ The effect of incident polarization is expected due to the dependence of the electromagnetic enhancement for nano-particles.¹⁷⁵

Using electromigration junctions, simultaneous SERS and conductivity measurements have been made on the single or multiple molecule level.^{176,177} In this experiment, a confocal Raman microscope is used in reflection mode on a silicon sample with Au junctions.¹⁷⁶ Ten to twenty percent of the experimental measurements showed correlation between the SERS and conductance.¹⁷⁷

Both electromigration junctions and break junctions have shown their potential in probing single molecule junctions. The spatial resolution provided by our STM, coupled with the clean operating conditions provided by ultra high vacuum, as well as the temperature control, provide a large advantage over what has been accomplished in the currently published work. The disadvantages arise from the added complexity of the instrument. Operations in UHV

conditions take an order of magnitude longer in preparation time, and there is an inability to quickly make changes to the initial experimental layout. The design of our UHV-STM allows for making novel measurements from an engineering point of view, but it will be the information gleaned from molecular junctions and novel chemical systems that will probe its worth. The following chapter details work on quantum interference in transport systems as potential chemical systems to be studied using our instrumentation.

Chapter 6. Quantum Interference

This chapter on quantum interference is comprised mainly of the material written in five recent manuscripts. Putting this information together gives the opportunity to recompile the story in a more fitting and complete manner than was required for publication. The chapter starts with an overview of what has been accomplished in molecular electronics and what constitutes an ideal switch or molecular device and how it can be designed by analyzing transmission plots. A summary of the calculation methods is detailed in the following section. Our initial attempts at increasing dynamic range and controlling interference features give a perspective on the development of the following work.

We calculate that destructive quantum interference effects can be observed in and can dominate electron transport through cross-conjugated molecules. The interference features in cross-conjugated molecules provide a large dynamic range in electron transmission probability, deviating strongly from the simple barrier tunnelling model for charge transport, and open a new area for addressing electronic functionality in molecules. The interference effects are manifest in the experimentally observable conduction range and, importantly, these results challenge and extend traditional understanding of the trends in molecular electron transfer.

Previous studies of single molecule conduction in the coherent regime have suggested that charge transport in the sub-resonant voltage regime can usually be described using a barrier tunnelling model where the barrier height is controlled by the energy separation between the Fermi energy of the electrode and the closest molecular energy level.¹⁷⁸ So long as this model holds, device performance is limited and it is necessary to utilise other physical processes to induce anything other than simple barrier-tunnelling behaviour.¹⁷⁹ Interference

features show behavior that differs from the barrier tunneling model. This opens up the possibility of achieving very promising conductance characteristics through coherent tunnelling alone, without relying on geometric changes, stochastic motion or vibronic effects. The idea of utilizing antiresonance features in molecular systems has been proposed,¹⁸⁰ yet there has been no success in finding specific molecules.^{181,182}

We find that the directionality of transport through a single carbon-carbon double bond can create interference features in transport. The interference created by a carbon double bond in a cross-conjugated orientation has both high and low conductance states, separated by orders of magnitude, accessible by electronic changes alone. This large dynamic range is accessible through changes in electron density alone, enabling fast and stable switching. Using cross-conjugated molecules, we show how the width, depth, and energetic location of the interference features can be controlled.

These molecules are presented as promising candidates for single-molecule transistors, rectifiers, organic film transistors, memory elements and sensors. In an example of a single molecule transistor, we calculate a change in conductance of 8 orders of magnitude with an applied gate voltage. Using multiple interference features, we propose and calculate the current/voltage behavior of molecular rectifiers with rectification ratios 5 orders of magnitudes higher than previous calculations. Negative differential resistance behavior suggests that the large dynamic range in electron transmission probability caused by quantum interference could be exploited in future electronic devices. In conclusion quantum interference provides a

mechanism by which the requisite dynamic range of conductance for effective electronic devices may be realized with single molecules.

6.1 Motivation and overview of molecular electronics research

Molecular electronics is driven by the goal of producing active electronic elements that rival the performance of their solid-state counterparts, but on a much smaller size scale. Further miniaturization of electronic devices will require fundamental advances in our approach to building and designing electronic components. Electron transfer^{31,183,184} is of fundamental importance in broad areas of research encompassing both natural¹⁸⁵ and artificial systems.¹⁸⁶ Using molecules as discrete electronic elements was initiated by the proposal of a single molecule rectifier.⁵

The potential for molecular electronics is rooted in the unique chemical properties of molecules. The suggestion that single molecules could be used as discrete electronic components was made over thirty years ago.⁵ Since then, experimental studies of charge transport through molecules have largely been completed in an electrochemical or optical donor-bridge-acceptor context. These measurements have been completed on a large range of molecular systems as well as cross conjugated molecules. In electrochemical measurements the energetics of a molecule are studied in the context of single electron redox changes while in optical measurements the transport through the molecules is measured as a charge separation or recombination rate. Single molecule two probe transport measurements have opened up a new area of research; the average transmission through a molecule can be studied without charging the molecule, allowing the ability to tune the incident electron energy. If the charge

transport behavior of a molecule is extremely sensitive to incident electron energy near the Fermi level, this control of voltage bias should yield new information on the transport behavior of molecules.

A number of single molecule electronic devices have been constructed with varied behavior including switching,¹⁸⁷ rectification,¹⁸⁸⁻¹⁹⁰ coulomb blockade,⁸⁸ Kondo resonance,⁸⁸ negative differential resistance (NDR),¹⁹¹ and memory elements.¹⁹² Single molecule transistor behavior has been established in UHV conditions,^{87,193-196} as well in solution using electrochemical gate control.¹⁹⁷⁻²⁰¹ For single molecule switches, there are a number of theoretical studies on how molecular conformational change can lead to large conductance changes,^{202,203} including measurements using photochromic molecules.²⁰⁴ Most methods for creating molecular switches rely on, or result in, conformational change to the molecule of interest.²⁰⁵ For fast and reproducible switching, and integration in useful devices, switching should not result in conformational change. Recent work has highlighted how this can be accomplished with hydrogen transfer in a naphthalocyanine molecule at low temperature, resulting in an on/off ratio of 2.¹⁸⁷

To date, investigations of molecules for electronic applications have predominantly focused on a small subset of conjugated molecules and comparisons with their saturated counterparts. When measurements are made on such systems relatively constant conductance is observed over the accessible range. For electronic functionality such as switching, logic, memory or sensing, however, it is necessary to have both high and low conductance states. To shift conjugated molecules to a low conductance state large perturbations are required, for

example relatively slow conformational change^{206,207}. For many applications, the device performance could be improved if the switching could be induced by electronic changes alone.¹⁸⁷ Understanding biological electron transfer led to the proposal that the vast dimensions of chemical space would yield promising candidates for electronic devices made from single molecules.⁵ There has been extensive experimental and theoretical work to be able to measure the electrical properties of single molecules, with considerable success; however, chemical diversity has, so far, not led to the electrical diversity that was anticipated. The limitation on the performance of molecular electronic devices²⁰⁸ is that, in the coherent tunnelling limit, the conductance characteristics can generally be described by treating the molecule as a simple barrier to electron tunnelling¹⁷⁸.

Measuring transport through single molecules has largely focused on molecular wires. These generally consist of linear molecules (both saturated and unsaturated) or fully conjugated aryl systems. Making these measurements is critical in establishing new experimental techniques and allows comparison among different methods. There has also been strong theoretical development of models to explain the transport behavior in a metal-molecule-metal junction.^{40,45,47,209}

All of the proposed and measured molecular devices hint at the wide variety of electronic functions that can be completed within a single molecule.²¹⁰ Major drawbacks in comparison with solid state devices include the low dynamic range in transport through single molecules and in the vibronic mechanisms²⁰⁵ that result in slow switching speed. This field of research is relatively young and the transport through less common organic structures should

open up new areas of research where the electron transmission probability as a function of energy behaves in unique ways.

6.1.1 The Simmons model

In analyzing the charge transport through molecules in the coherent tunneling limit, the Simmons equation, which treats a molecular junction as a tunneling barrier where the height of the barrier is essentially the distance from the Fermi level to the nearest molecular resonance is often used.^{178,199,211-213} This approximation adopts a common illustration showing the discrete molecular frontier energy states sandwiching the electrode Fermi level. Within this approximation explaining conductance relies on four main factors: the electrode/molecule coupling strength, the associated molecular state broadening, the alignment and distance of the Fermi energy to the frontier molecular orbitals, and the energy level shift of the molecular states upon contact to the electrode.

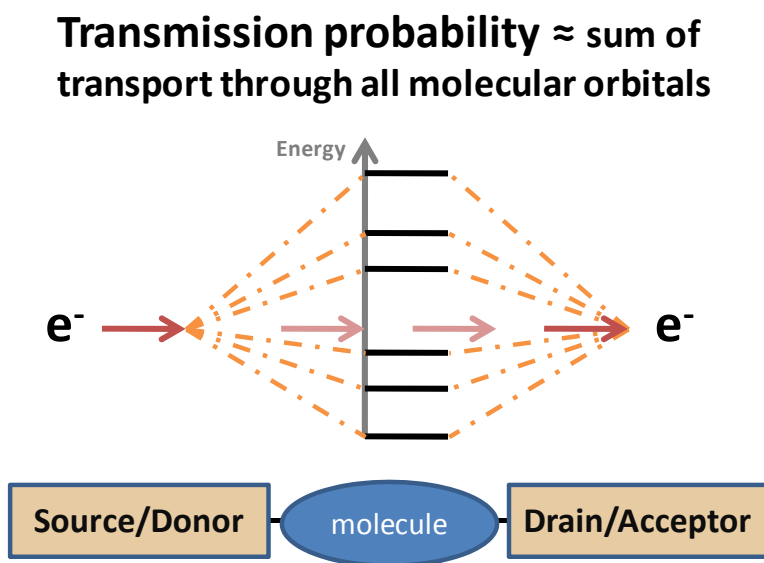


Figure 6-1. The transmission probability is a sum of the orientation-dependent transport channels between source/donor- molecular orbitals – drain/acceptor. The electron “sees” all available molecular orbital pathways in energy space. This can be compared with Young’s double slit experiment; in electron transport destructive interference can occur when summing the coupling terms across the system.²¹⁴

While this picture has proven extremely useful, it is based on an independent electron model that assumes the molecular energy states do not interact in the transport process. We show here that interactions between molecular orbital energy states, sometimes including those far from the Fermi level, can have a very large effect on the transport properties of a molecule in the tunneling regime at low bias voltage. Figure 6-1. shows a diagram illustrating schematically how the transmission probability for an electron to tunnel through a molecule is calculated as the sum of the coupling terms from donor to acceptor.²¹⁴ This figure may seem intuitive and obvious, but the deconvolution of the transport into energetically separated pathways is shown here for the first time in Section 6.4. The coupling terms between donor and acceptor vary with the orientation of the molecule and a single molecule can have drastically different conductance behavior even though the frontier molecular orbitals are similar in both orientations.

The largest deviation from the Simmons model of charge transport occurs when the coupling terms across the molecule destructively interfere in the energy region between the highest occupied molecular orbitals (HOMO) and the lowest unoccupied molecular orbitals (LUMO). In the context of electron transport destructive interference can occur among the

terms that are summed to calculate the transmission probability. At the energy level of a molecular resonance the transmission probability $\rightarrow 1$, conversely when there is quantum interference an antiresonance can occur where the transmission probability $\rightarrow 0$.

6.1.2 Quantum-interference transistors and quantum dots

Interference features have been studied extensively in quantum dots.²¹⁵⁻²¹⁸ Quantum dots provide a discrete energy spectrum similar to molecules and due to the increased size scale, enable greater experimental control. In the quantum dot literature, measurements have been made on the transmission phase in a quantum dot using interferometers.^{215,219} In this work, the transmission phase change going through a resonance was π , but unexpected were the measured abrupt phase changes of π between sequential resonances.²¹⁹ This abrupt phase change was later attributed to a non-spanning node in the specific energy level of the quantum dot.²²⁰ Considering a quantum dot as a rectangular box, a non-spanning node is defined as an in-phase resonance where the change in wave function density leads to a node that touches only one boundary or zero boundaries of a quantum dot.²²⁰ In the limit where a quantum dot can be treated as a large molecule, we show how the phase change in molecular resonances directly correlates to the non-spanning node explanation.

In visual similarity to cross-conjugated molecules, T shaped quantum dots have been proposed as quantum interference devices.^{218,221} Experimentally observing interference effects in nanostructured materials is hindered by the need to maintain electron phase coherence over long distances.^{216,217} Recent progress has been made in measuring the interference in T-shaped conductors but the measured effect is only a 5% change in

conductance that disappears from measurements over 500mK.²²² In a very recently published book the importance of this design is recognized; “the quantum-interference effect provides a new principle of operation for three-terminal devices. These devices are now in an early state of development. However, these approaches portend effective control by small voltage as well as the development of very-high-speed transistors.”²²³ Here we discuss systems that are similar to a T shaped quantum dot system but do not require extremely long electron coherence lengths.

6.1.3 Interference in model systems

The idea of interference in molecular transport is not new. There are a number of cases besides benzene that have been published including interference in transmission through polycyclic hydrocarbons.²²⁴ Outside of benzene-type calculations, most of the work has been done using models to represent molecules. Calculations of interesting transport behavior, including interference, have been completed on many model systems²²⁵ including branched chains²²⁶ and “lollipop resonantors”.²²⁷ While the underlying physics has been established in the model systems, the mapping onto real molecules has remained opaque.

6.1.4 Single molecules

In focusing our research on single molecule effects, it is important to realize that experimental measurements of single molecule junctions are quite involved. Controlling the formation of an Å-nm scale gap, as well as maintaining contact to both electrodes is extremely difficult. Once these measurements are made, care has to be taken in analyzing the data. It has become apparent through many calculations and experimental measurements that

molecules can sample many different geometries and possible mechanistic regimes with respect to time. These fluctuations in current can be of the same order of magnitude as the observable.⁶⁹

Due to the difficulties in controlling small molecular junctions, many early measurements have been reanalyzed.^{65,73,228} For useful device applications, a molecule with novel transport behavior should be stable to geometric fluctuations while still providing interesting transport properties that can be experimentally realized.

To investigate interference features we ask the questions: How can interference occur in model systems? Why is the interference present in cross-conjugated molecules? How stable is this interference feature to electronic dephasing and molecular vibrations? How do the molecular calculations relate and how do they differ from model systems? Can we design potentially useful molecular devices?

6.2 Controlling electron flow

Here, we define the characteristics of an ideal switch, requiring large changes in electronic conductance, and show how its features could appear in a transmission plot. The interference features in cross-conjugated molecules and the breakdown of the barrier tunneling model²²⁹ provide a system that matches our device design criteria. Specifically, by changes in electron density alone, a dynamic range in electron transmission comparable to solid state devices is accessible. We calculate how the interference features can be utilized to create molecular switches and transistors, rectifiers, or negative differential resistors.

6.2.1 Switch design

In designing a single molecule electronic device, it is helpful to ask what transport behavior is necessary for a molecule to function as an ideal transistor (switch), memory element, or a chemical sensor. Figure 1 shows the conductance of a hypothetical single-channel device with a well defined on state and off state. To aid in understanding, we have included a blue line to indicate a perfect insulator. The red line at 1 G0 indicates a perfect conductor representing ballistic single-channel transport, where the probability of an electron back scattering within the molecule is zero. This limit of 1 G0, is a direct result from quantum theory,¹¹⁴ has been measured in chains of Au atoms^{60,230} at high bias of ~2 Volts,^{231,232} and has been verified in calculations^{39,47} With the upper and lower bounds of conductance defined by a perfect conductor and a perfect insulator, it seems trivial that a perfect switch would be a perfect insulator in the off state and a perfect conductor in the on state (Figure 6-2).

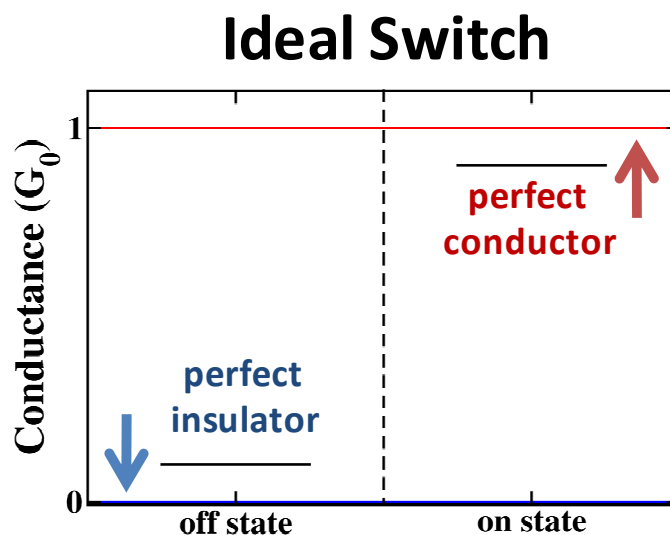


Figure 6-2. In an ideal switch the off state would be a perfect insulator (blue line at 0 G_0) and the on state would be a perfect conductor (red line at 1 G_0). In a single transport channel, ballistic transport through a perfect conductor representing the on state is one G_0 , the quantum of conductance ($\sim 12.91 \text{ k}\Omega$).

All molecules have a non-constant transmission probability as a function of energy and can be considered a switch or transistor (because a change in bias or gate voltage leads to a change in conductance), albeit not necessarily a useful one. We define here the criterion for an ideal switch being: (1) an infinite ratio of the on current/off current ($I_{\text{on}}/I_{\text{off}}$), (2) a subthreshold swing of 0mV/decade indicating a switch that abruptly changes from the off state to the on state at a defined threshold voltage, (3) fast switching times that do not rely on nuclear motion but only changes in the relative electron density, (4) reproducibility and stability²⁰⁵ by minimizing charging and geometric organization, and (5) low bias operation, energetically separated from a molecular resonance. While many other factors including leakage current,

threshold voltage, and cost are extremely important, we focus our discussion on the five criteria listed above, specifically the $I_{\text{on}}/I_{\text{off}}$ ratio and the subthreshold swing.

6.2.2 Voltage switch

In this section we discuss how the conductance through a molecule can switch as a function of voltage. In a two-probe single molecule junction, measurements are limited to the current as a function of voltage, along with the derivative and second derivative of the data. In charge transport calculations, we determine the transmission probability of an incident electron as a function of energy. Integration of the transmission probability over the range of chemical potentials of the left and right leads will give the coherent regime current. The transmission plots provide more detail on the molecular causes of the I/V characteristics; therefore, we focus our discussion on understanding and controlling the electron transmission probability.

In Figure 6-3(a), the transmission through a perfect conductor is shown in red, a perfect insulator in blue, and a candidate for a molecular switch in green. This hypothetical molecule behaves as a voltage switch where it is a perfect insulator near E_f with a transmission probability $\cong 0$ and a perfect conductor at all other energies. Figure 6-3(b) is the same plot with the shaded area representing a discrete bias voltage applied across the molecular switch (assuming the bias shifts the chemical potentials symmetrically about E_f). The current is calculated by integrating the area under the transmission and is shown in Figure 6-3(c). In Figure 6-3(d), the conductance as a function of voltage is shown. In Figure 6-3(d), the

hypothetical molecule is switching from a low conductance state at low bias voltage to a high conductance state at high bias voltage.

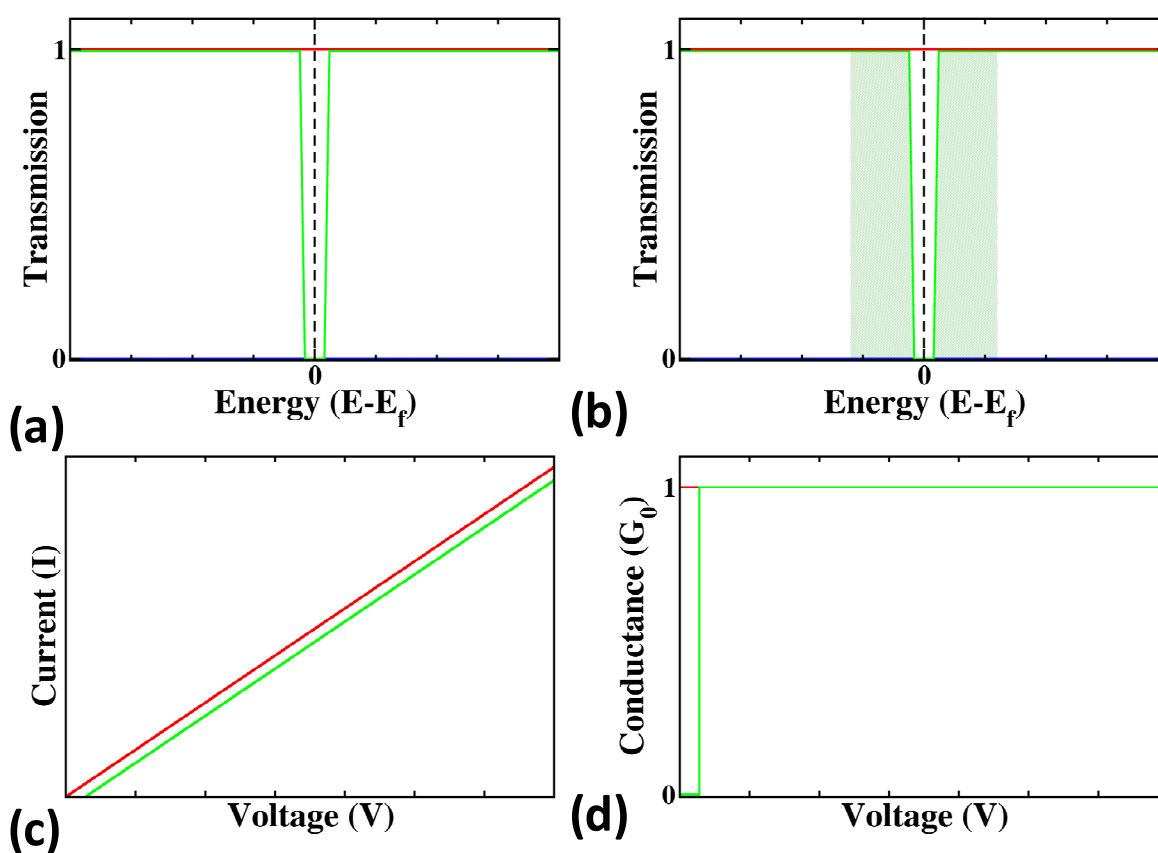


Figure 6-3. The transmission and current/voltage behavior of a perfect voltage switch is shown schematically, where the conductance goes from 0 to $\sim 1G_0$ as a function of voltage. The red line represents a Au wire and the green line represents the molecule of interest. In (a), the transmission plot for a potential device is shown in green having an off state at $E=E_f$ and an on state at all other energies. (b) To calculate the current and conductance of (a), the transmission plot (assuming invariance to applied voltage) is integrated between the chemical potentials of the leads, shown as the shaded region. (c) shows the current/voltage behavior realized by

integrating the transmission plot in (b). The conductance as a function of voltage is shown in (d).

6.2.3 Switching a molecule

Having demonstrated what represents an ideal transmission function for a single molecule with on and off states, we now show a few possible scenarios of how this transmission function can be manipulated to achieve switching behavior. In a three terminal measurement, the maximum $I_{\text{on}}/I_{\text{off}}$ ratio for a specific molecule is defined as the transmission probability at the energetically closest electronics resonances / the transmission probability at the Fermi level.²⁰⁹ When the incident electron energy corresponds to a molecular resonance, the elastic transmission probability is $\cong 1$. To get a large dynamic range, we thus need to create molecular systems where the transmission probability also goes to zero. A molecular insulator has a very low conductance state at the Fermi level and the energetically closest resonance should have a transmission probability of ~ 1 . This would indicate that an imperfect molecular insulator might be a good electronic device, for example, a molecule with saturated alkane groups. We use such a molecule as one of our reference points in the proceeding calculations. The energetic separation of the nearest molecular resonance and the Fermi level define the average subthreshold swing over the maximum dynamic range. To create functional devices, we would like to combine a transmission probability $\cong 0$ at the Fermi level to be energetically near a molecular resonance. In Figure 6-4(b), we show how a gate voltage may shift the transmission zero away from the Fermi energy. For a functional transistor this

behavior would be ideal because at very low source-drain voltage an applied gate could switch the molecule from an on state to an off state.

Figure 6-4(c) and (d) represent two possible scenarios for what can occur in a chemical sensor device. In Figure 6-4(c), a chemical reaction, photoisomerization or possibly a change in the number of electrons on the molecule, causes a very large change in the transmission function. A large change in the molecule of interest would make reproducible switching more difficult to control in a device. While not ideal for fast repetitive switching, this method of charging a device may provide a route to creating a functional memory device with distinct on/off states representing bit storage. Figure 6-4(d) represents a shift of the molecular orbital energies upon chemical or physical binding of a molecular group, switching the molecule from an off conductance state to an on conductance state. It is also conceivable that smaller shifts in the transmission spectrum would allow sequential detection of multiple molecules. Calculations showing both the effects of gating (b) as well as the tuning of a transmission feature (d) will be shown in the following sections.

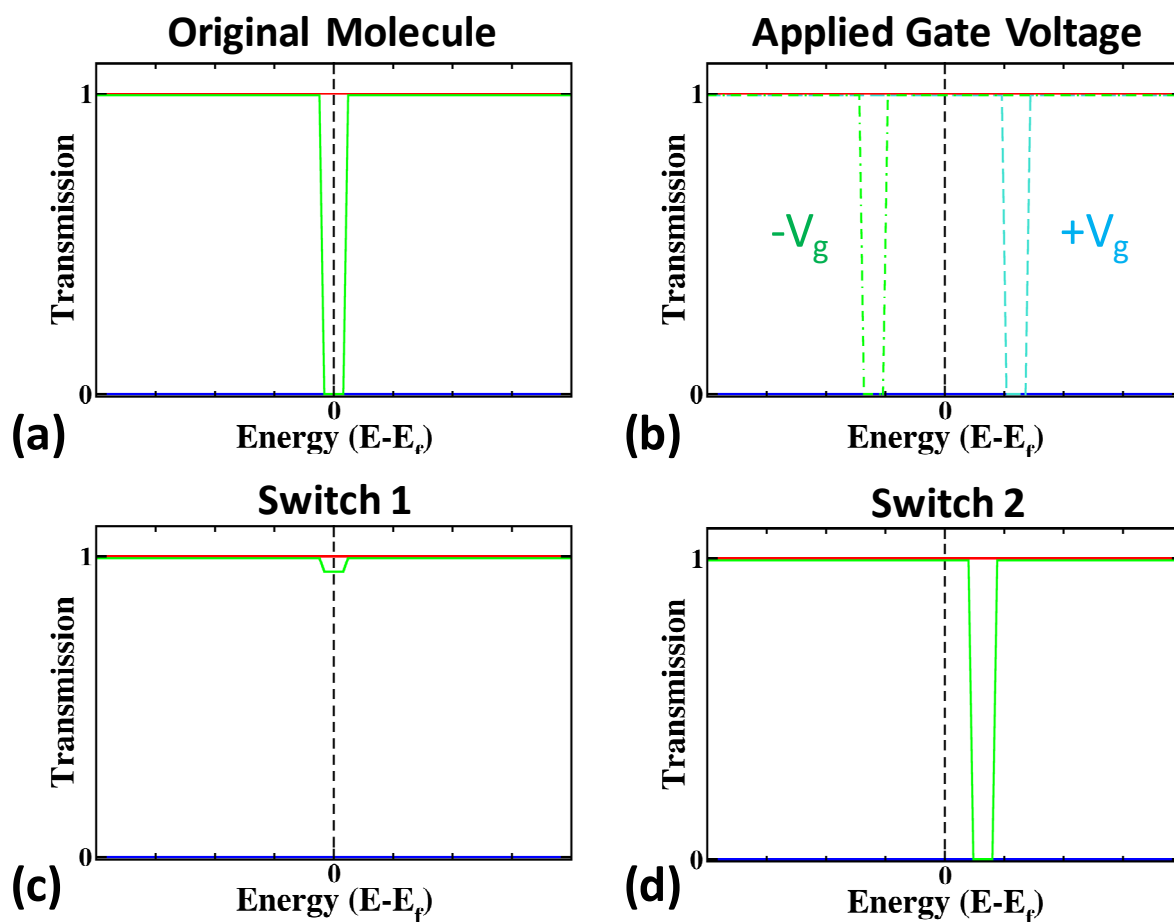


Figure 6-4. Switching shown in transmission plots. The transmission of our hypothetical molecule with distinct on and off states is shown again as the green line in (a). In plots (b), (c), and (d) the molecule has been switched in three different ways from a low conductance state to a high conductance state at low bias voltage. In (b) we show a situation where an applied gate voltage might shift the dip in the transmission spectrum away from the Fermi energy shown as the green and blue dashed lines. In (c) a large change in the molecule occurs causing the transmission to drastically change. (d) A molecular interaction event or change in electron density in the molecule could shift the transmission spectrum.

6.3 Methods

Our work focuses on calculating transport through single molecules in the Landauer-Imry low bias tunneling regime.^{35,233} In the low bias tunneling limit, we assume that the electron does not spend a significant amount of time on the molecule in the junction, leaving the molecule in the neutral state. In the molecules that we analyze here, the interference generally occurs within the HOMO-LUMO gap energetically separated from molecular resonances.

All molecular structures are geometry optimized in the absence of gold electrodes using density functional theory using B3LYP^{234,235} 6-311G** in QCHEM 3.0.²³⁶ The gas phase molecules were chemisorbed (terminal hydrogens removed) to the fcc hollow site of a Au(111) surface with the Au-S bond length taken from the literature.¹⁶⁴ Most transport calculations were initially done using Hückel-IV 3.0^{39,139,209} due to the speed of the calculation.

For calculations using Hückel-IV 3.0 the extended molecule included three gold atoms on each side. A k-point sampling of 17x17 was used and all other settings were at the default values. The results from Hückel-IV 3.0 have been shown to be quite consistent²²⁹ with those done using the more computationally intensive density functional transport codes such as gDFTB⁴⁰⁻⁴⁴ and ATK.⁴⁵⁻⁴⁸

gDFTB transport calculations have also been completed, with the added benefit of the ability to analyze the symmetry components of the transmission. In calculations performed using gDFTB no gold atoms were included in the extended molecule so that the symmetry of the molecule could be used to separate the transmission into σ and π components. The

minimum size of the electrode was a 4x4 atom unit cell with 3 layers in the transport direction. Periodic boundary conditions were used in both gDFTB and ATK. In calculations performed using ATK a 4x4 atom unit cell was also used for the electrodes, however, in this case gold atoms were included in the extended molecule (2 layers on one side, 3 on the other). The k-point sampling used was 6x6x100 for the density matrix and 10x10 for the transmission.

To verify interesting transport behavior the results are compared utilizing all three of these computational codes. In this manuscript, all of our calculations are completed on the geometry optimized structure; however, using molecular dynamics coupled to transport calculations,²³⁷ the interference features have been shown to be stable to geometric fluctuations and the breaking of symmetry.^{214,229} The molecular dynamics calculations were completed using Tinker 4.2 with the mm3 force field.¹⁶⁵ The Au-Au and Au-organic interaction parameters were adapted from literature values.¹⁵⁶ The Au atoms were fixed in a 4x4 atom unit cell with 6 layers in the transport direction. The electrode distance was held fixed at the same value as used in the static geometry calculations.

6.4 Transmission and coupling

The conductance characteristics of a large majority of molecules considered to date can be explained within the conventional coherent tunneling understanding; however, this method breaks down when considering the unusual transmission characteristics of cross-conjugated molecules, the unusual properties of benzene rings connected through the meta position²²⁶ and calculations of interference on branched structures.²¹⁴

There is a direct correlation between the work here on electron transfer through two probe systems and the more developed donor-bridge-acceptor literature. It becomes useful to understand transport through molecular junctions within the notion of coupling.^{35,233} Calculating a coupling term should help elucidate the interference in cross-conjugated molecules if the electronic coupling through the molecule was changing sign, or there was some cancellation of oppositely signed coupling terms.

The coupling and transmission through the molecule can be understood in terms of the contributions from different molecular conductance orbitals by a basis transformation. We can diagonalize G^r and G^a , with the overlap matrix S , and obtain the eigenvectors C_r and C_a (r, a denote retarded and advanced Green's functions).

$$\begin{aligned} G^{r'}(E) &= C_r^{-1} S^{-1} G^r(E) C_r \\ G^{a'}(E) &= C_a^{-1} S^{-1} G^a(E) C_a \\ &= C_r^\dagger G^a(E) S^{-1} C_r^{-1\dagger} \end{aligned} \quad (6.1)$$

Molecular conductance orbitals differ from molecular orbitals in that by diagonalizing $G^r(E)$ instead of the hamiltonian of the isolated molecule they may be complex; however, the molecular orbitals of the isolated molecule constitute their dominant component. In intramolecular electron transfer the nature of the self-energy will be such that the molecular conductance orbitals more closely resemble simple molecular orbitals than they will in the case of a molecule bound to metallic electrodes.

The transmission probability is calculated using the Landauer equation²¹⁴

$$T(E) = \text{Tr}[\Gamma^L(E)G^r(E)\Gamma^R(E)G^a(E)] \quad (6.2)$$

with $\Gamma^{L/R}$ the left and right spectral densities and $G^{r/a}$ the retarded and advanced Green's functions.

Using a transformation to a molecular orbital basis we have shown that the transmission can be calculated as a sum of the squared couplings through each molecular orbital (labeled by i),²³⁸ given by

$$t'_{\alpha\beta}(E) = \sum_i V_{\alpha,i}^{L'\dagger}(E)G_{i,i}^{r'}(E)V_{i,\beta}^{R'}(E). \quad (6.3)$$

Then equation 11 reduces to

$$\begin{aligned} T(E) &= \text{Tr}[\gamma^{L'\dagger}(E)G^{r'}(E)\gamma^{R'}(E)\gamma^{R'\dagger}(E)G^{a'}(E)\gamma^{L'}(E)] \\ &= \text{Tr}[(\gamma^{L'\dagger}(E)G^{r'}(E)\gamma^{R'}(E))(\gamma^{L'\dagger}(E)G^{r'}(E)\gamma^{R'}(E))^\dagger] \\ &= \sum_{\alpha,\beta} \left| \sum_i \gamma_{\alpha,i}^{L'\dagger}(E)G_{i,i}^{r'}(E)\gamma_{i,\beta}^{R'}(E) \right|^2. \end{aligned} \quad (6.4)$$

That is, we define the transition amplitudes, $t'_{\alpha\beta}$, as

$$t'_{\alpha\beta}(E) \equiv \sum_i V_{\alpha,i}^{L'\dagger}(E)G_{i,i}^{r'}(E)V_{i,\beta}^{R'}(E) \quad (6.5)$$

where $V^{L(R)'}$ are transformed by the same transformations as $\gamma^{L(R)'}$. From this expression we can define a useful quantity $t'_{\alpha\beta i} = V_{\alpha,i}^{L'\dagger}(E)G_{i,i}^{r'}(E)V_{i,\beta}^{R'}$ which means the coupling can then be written as a sum of these elements,

$$t'_{\alpha\beta}(E) = \sum_i t'_{\alpha\beta i}. \quad (6.6)$$

Now we have the striking result that the total transmission is given by the sum of contributions through each of the molecular conductance orbitals: each of the $t'_{\alpha\beta}$ is given as a

single index sum of the contributions ($t_{\alpha\beta i}$) from each of the eigenfunctions of G^r . Previous attempts to separate the transmission into contributions of individual molecular conductance orbitals failed to yield such a simple picture as the transmission was dominated by interference between pairs of orbitals.²¹⁴ Similarly, this expression provides a number of advantages for calculating coupling. Generally the donor/acceptor coupling is given by a series expansion; however, by diagonalizing G^r the series reduces to a single index sum. It should be noted that basis rotations that do not preserve the diagonal nature of $G^{r'}$ will result in the recovery of the two index sum; consequently, the interpretation that follows is restricted to the case that $G^{r'}$ is diagonal. Through the use of this permutation of the equations we uncover the simple picture that transmission and coupling through a molecule can be expressed as a sum of the contributions from each of the molecular conductance orbitals.

6.5 Model systems calculations

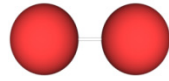
6.5.1 Two site model

To calculate the coupling we represent our system using a Hamiltonian with couplings only between nearest neighbors.

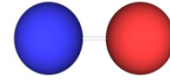
$$H = \sum_i \varepsilon_i a_i^\dagger a_i + \sum_{i,j} \beta_{ij} a_i^\dagger a_j \quad (6.7)$$

We first will start with a calculation for the linear two site model.

linear model 



$$E = \beta$$



$$E = -\beta$$

$$H_{linear} = \begin{pmatrix} \alpha DA & \beta & 0 & 0 \\ \beta & \alpha & \beta & 0 \\ 0 & \beta & \alpha & \beta \\ 0 & 0 & \beta & \alpha DA \end{pmatrix} \quad (6.8)$$

αDA is the donor and acceptor energy, α is the site energies and β is the couplings. For numerical solutions to the coupling equations the site energies α are set = 0 and the coupling strength β is set = -0.5. To get this equation into a form that is comparable to the donor-bridge-acceptor literature and to think about couplings it is necessary to rotate our system into a basis where the sites are orthogonal. The orthonormal matrix for our two site system with coupling β between sites 1 and 2 is given as

$$U = \begin{pmatrix} 1 & 0 & 0 & 0 \\ 0 & \frac{1}{\sqrt{2}} & \frac{1}{\sqrt{2}} & 0 \\ 0 & \frac{1}{\sqrt{2}} & -\frac{1}{\sqrt{2}} & 0 \\ 0 & 0 & 0 & 1 \end{pmatrix} \quad (6.9)$$

To calculate the rotated Hamiltonian for our system we calculate the dot product of the orthogonal matrix U by our linear matrix by the transpose of U

$$H_{linear_tda} = U \cdot H_{linear} \cdot U^\dagger \quad (6.10)$$

This gives us our coupling Hamiltonian in a new basis.

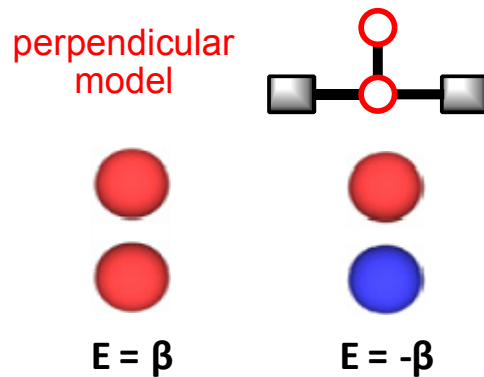
$$H_{linear_tda} = \begin{pmatrix} \alpha DA & -\frac{1}{2\sqrt{2}} & -\frac{1}{2\sqrt{2}} & 0 \\ -\frac{1}{2\sqrt{2}} & -\frac{1}{2} & 0 & -\frac{1}{2\sqrt{2}} \\ -\frac{1}{2\sqrt{2}} & 0 & \frac{1}{2} & \frac{1}{2\sqrt{2}} \\ 0 & -\frac{1}{2\sqrt{2}} & \frac{1}{2\sqrt{2}} & \alpha DA \end{pmatrix} \quad (6.11)$$

Now that our system is in an orthogonal molecular orbital basis the coupling as a function of energy can be calculated as a sum of terms from the coupling to each orthogonal energy state.

$$Tda(\varepsilon) = \frac{H_{linear_tda}[1,2] * H_{linear_tda}[2,4]}{H_{linear_tda}[2,2] + \varepsilon} + \frac{H_{linear_tda}[1,3] * H_{linear_tda}[3,4]}{H_{linear_tda}[3,3] + \varepsilon}$$

$$Tda(\varepsilon) = -\frac{1}{-8(\frac{1}{2} + \varepsilon)} + \frac{1}{8(\frac{1}{2} + \varepsilon)} \quad (6.12)$$

For comparison the coupling through a 2 site perpendicular model is shown.



The Hamiltonian of the system is the similar to equation (6.8), differing only in the connection to the electrodes.

$$H_{cross_conjugated} = \begin{pmatrix} \alpha DA & \beta & 0 & 0 \\ \beta & \alpha & \beta & \beta \\ 0 & \beta & \alpha & 0 \\ 0 & \beta & 0 & \alpha DA \end{pmatrix} \quad (6.13)$$

After rotation into an orthogonal basis.

$$H_{cross_conjugated} = \begin{pmatrix} \alpha DA & -\frac{1}{2\sqrt{2}} & -\frac{1}{2\sqrt{2}} & 0 \\ -\frac{1}{2\sqrt{2}} & -\frac{1}{2} & 0 & -\frac{1}{2\sqrt{2}} \\ -\frac{1}{2\sqrt{2}} & 0 & \frac{1}{2} & -\frac{1}{2\sqrt{2}} \\ 0 & -\frac{1}{2\sqrt{2}} & -\frac{1}{2\sqrt{2}} & \alpha DA \end{pmatrix} \quad (6.14)$$

Calculating the coupling we get,

$$Tda(\varepsilon) = \frac{1}{-8(\frac{1}{2} + \varepsilon)} + \frac{1}{8(\frac{1}{2} + \varepsilon)} \quad (6.15)$$

Comparing the coupling terms for the perpendicular model and the linear model there is only a change in sign of one of the coupling terms. This change in sign of the second term leads to the destructive interference that occurs when the donor and acceptor site energies are degenerate with the bridge site energies as shown in Figure 6-5.

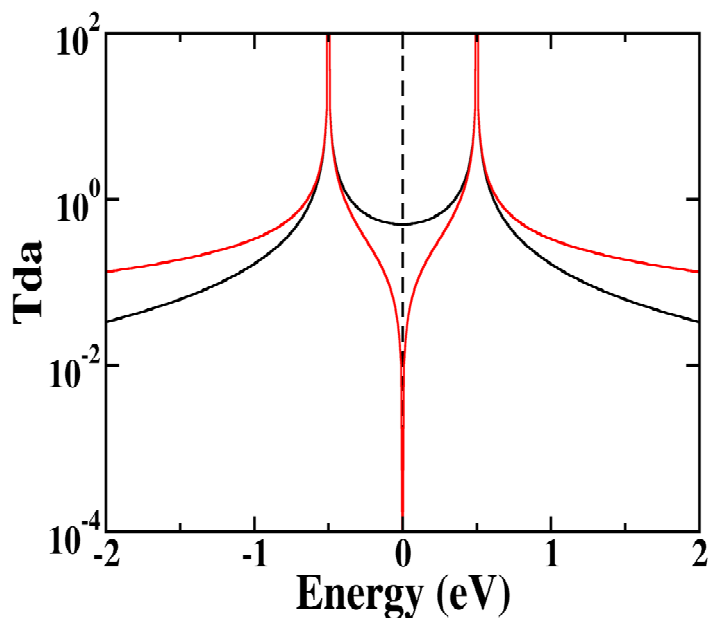


Figure 6-5. The coupling, T_{da} , for the linear (shown in black) and perpendicular (shown in red) two site models.

The transmission can be calculated in the coupling picture by including the self energies of the donor and the acceptor. The inclusion of the self energies broadens the resonances. In Figure 6-6 the transmission is calculated for the two possible orientations for a two site bridge between a donor and an acceptor. In the linear model shown in Figure 6-6 (a) the donor is connected to one site and the acceptor to the other site. In the perpendicular model shown in Figure 6-6 (b) the donor and acceptor are both connected to the same site. Setting the site energy to 0 and the intersite coupling β to -0.5 we calculate the Hückel molecular orbitals, for the isolated two site system as shown.

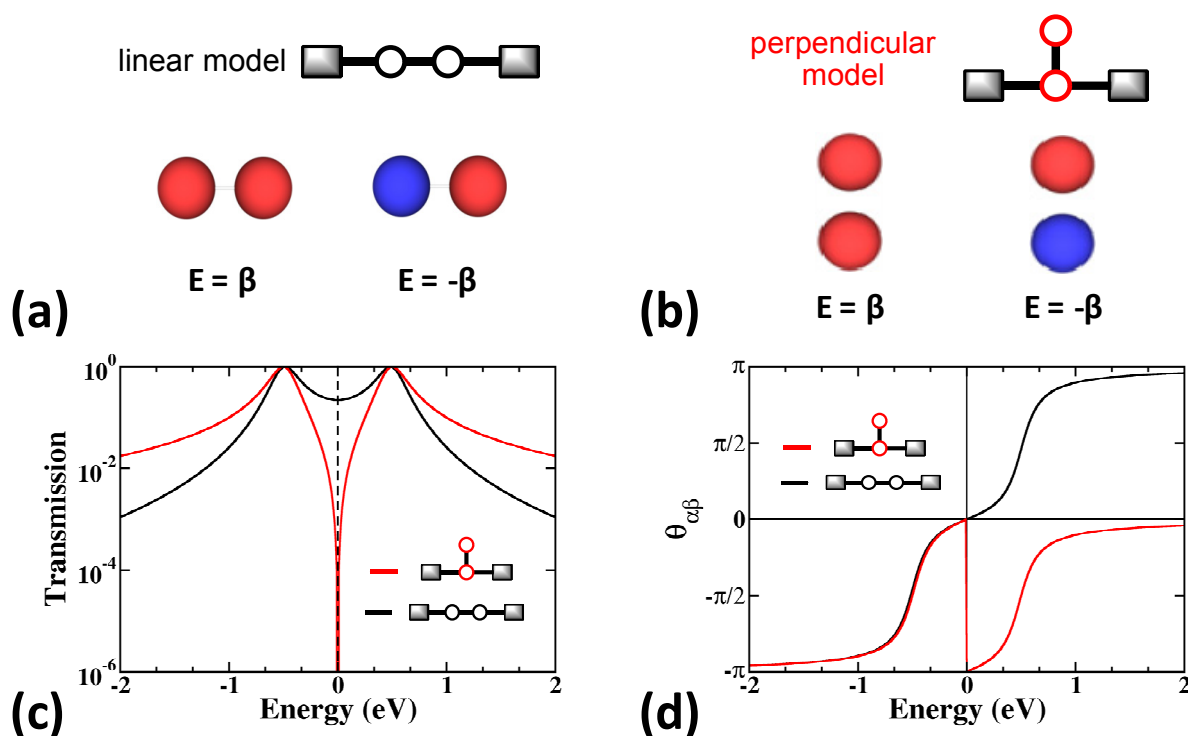


Figure 6-6. Transmission through a two site model. The electrode attachments determine the presence of an antiresonance feature. The plot on the left shows transmission as a function of energy and the plot on the right shows phase as a function of energy. The antiresonance feature in the perpendicular model is seen at $E=0$ as a 0 in transmission and a corresponding phase jump of π .

It is the energy dependent electronic coupling strength between the electrodes that determines the transport properties of a molecular junction. To calculate the coupling between the donor and the acceptor we solve the one-electron Hückel Hamiltonian. This Hückel coupling matrix is then transformed into a molecular orbital basis. This rotation allows for the calculation of each orthogonal molecular orbital and how each orbital couples to the electrodes.²¹⁴

To calculate the coupling as a function of energy we leave the site energies at 0, and sweep the electrode energy. In both the linear model and the perpendicular model, the coupling to the highest occupied molecular orbital (HOMO) level is identical. The coupling to the lowest unoccupied molecular orbital (LUMO) differs only in a sign change. The overall coupling strength can be determined by taking the absolute value of the sum of the individual coupling terms.

At $E=0$ the sum of the coupling terms in the perpendicular two site model is 0. The coupling terms to the HOMO and LUMO molecular orbitals are exactly equal and opposite, leading to destructive interference. This destructive quantum interference gives the perpendicular two site model the sharp antiresonance at $E=0$. To compare directly with two probe measurements we calculate the transmission as a function of energy²¹⁴ as shown in Figure 6-6 (c).

In Figure 6-6 (d) we show the phase of the transmission as a function of energy. The transmission phase is defined as the arctangent of the imaginary/real parts of the transmission coefficient.²²⁰ On sweeping the energy through a molecular resonance the transmission phase always changes by π . In the perpendicular two-site model there is an abrupt phase change of $-\pi$ at $E=0$, the location of the antiresonance. This antiresonance occurs whenever there is a zero in both the real and imaginary plane of the transmission function. A zero in both the imaginary and real components of the transmission need not cause a phase jump of π and for this reason we have included the more complex parametric plots (shown in Figure 6-9). Sweeping the energy from $-\infty$ to $+\infty$ the transmission phase changes by $\pi * n$, n equal to the smallest

number of sites between the donor and acceptor. In the perpendicular two site model there is only one site between donor and acceptor indicating that there will be one abrupt phase change of $-\pi$.

Using a two site model we can see that an antiresonance occurs at $E=0$ for the perpendicular model. This 0 in the transmission is a direct result of the destructive interference caused by the coupling to the HOMO and the LUMO orbitals. In this model the antiresonance is correlated with a non-linear increase in the number of spanning nodes between the donor and the acceptor.

The transmission phase can be determined from the transmission coefficients $t_{\alpha\beta i}$

$$\theta_{\alpha\beta}(E) = \text{ArcTan}[\text{Im}(t_{\alpha\beta}(E))/\text{Re}(t_{\alpha\beta}(E))] \quad (6.16)$$

It is also possible to examine the phase of each of the constituent components of each $t'_{\alpha\beta}$

$$\theta_{\alpha\beta i}(E) = \text{ArcTan}[\text{Im}(t'_{\alpha\beta i}(E))/\text{Re}(t'_{\alpha\beta i}(E))] \quad (6.17)$$

We treat ArcTan as a multivalued function, continuously moving onto the next Riemann sheet each time the branch cut is passed. This then defines the phase of the transmission through each molecular conductance orbital as a function of energy.

We now split the coupling contributions into molecular conductance orbitals. These orbitals differ from molecular orbitals because they can be complex. In the limit where the electrode coupling goes to zero, they are exactly molecular orbitals. The molecular orbitals dominate the contribution and the electrode self-energies can be considered a perturbation. Figure 6-7 and Figure 6-8 show the transmission and phase through each molecular

conductance orbital respectively. The transmission can be calculated from the complex quantities which are summed and squared.

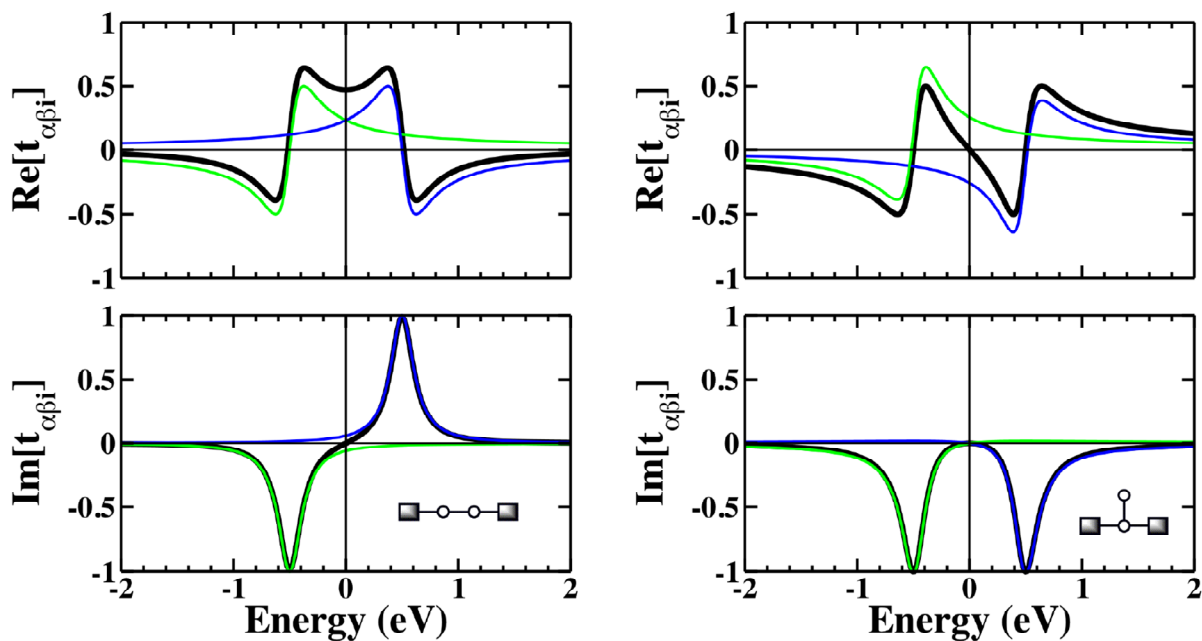


Figure 6-7. The contributions to the coupling from each molecular conductance orbital of the two 2-site systems, linear and perpendicular. The contribution from the bonding orbital is shown in green, the contribution from the anti-bonding orbital in blue and the sum of the two in black. In the case of perpendicular model both the real and imaginary components sum to zero at $E=0$ giving rise to the antiresonance in the transmission.

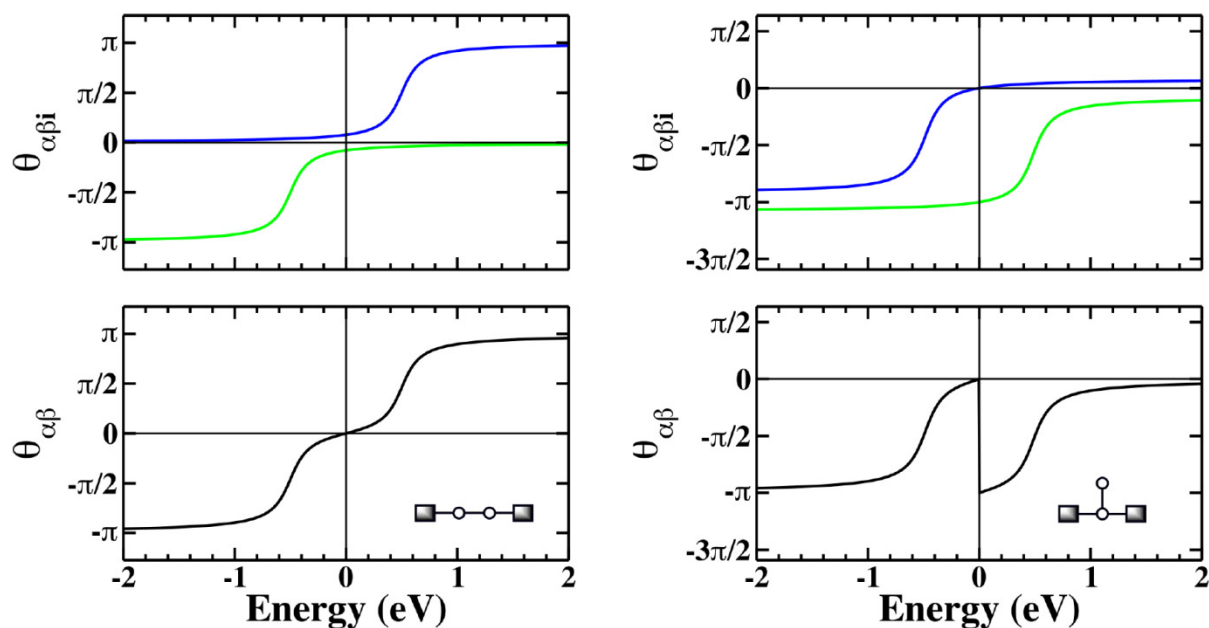
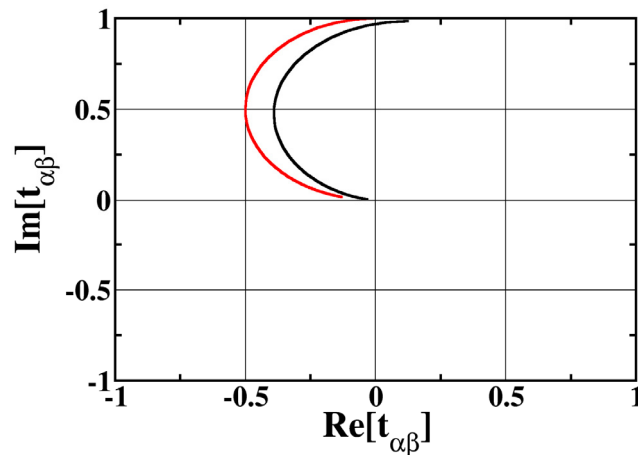
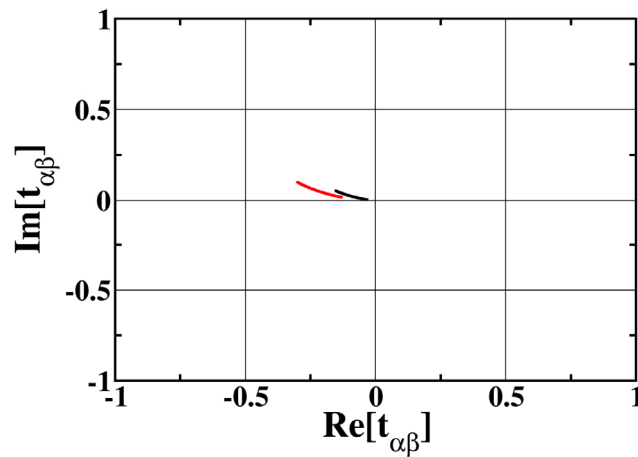


Figure 6-8. The phase of the transmission through each molecular conduction orbital (top) and the total phase of the transmission (bottom) for the two 2-site systems. The contribution from the bonding orbital is shown in green and the contribution from the anti-bonding orbital in blue. At the antiresonance the phases through the molecular conduction orbital are separated by π leading to complete destructive interference.²¹⁴

The molecular conduction orbitals further elucidate how the antiresonance occurs due to equal and opposite coupling. In the transmission for the perpendicular model in Figure 6 9 the direct cancellation is evident in the real portion of the coupling. The phase plots illustrate that as the energy sweeps past each molecular resonance the phase increases by π . In the case of the perpendicular a discontinuous jump of π at $E=0$ occurs at the position of the antiresonance.

For a zero in the transmission function to occur there must be a zero in both the real and imaginary components of the transmission. While the phase jump of π is sufficient to verify an interference feature, it need not always occur. In these cases verification with a parametric plot is necessary. Figure 6 9 shows the plot of the $t_{\alpha\beta}$ in the complex plane. An antiresonance occurs when the trajectory passes through the origin as is the case at $E=0$ for the perpendicular model. The linear model is shown in black and the perpendicular model is shown in red.



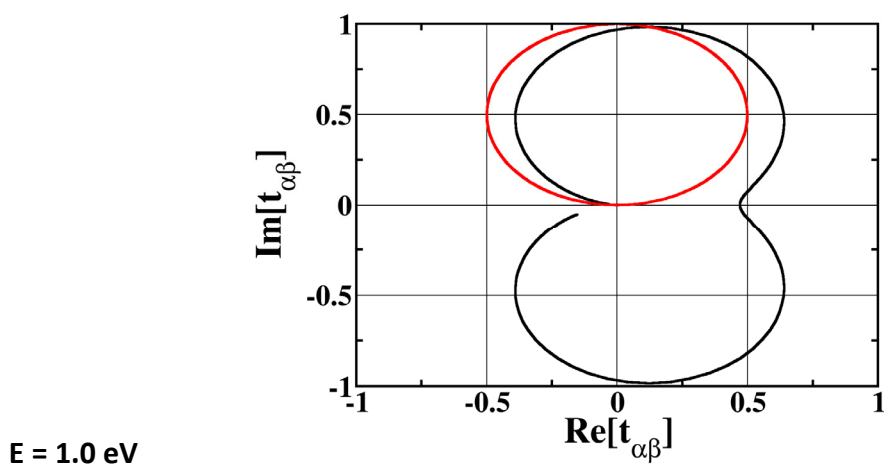
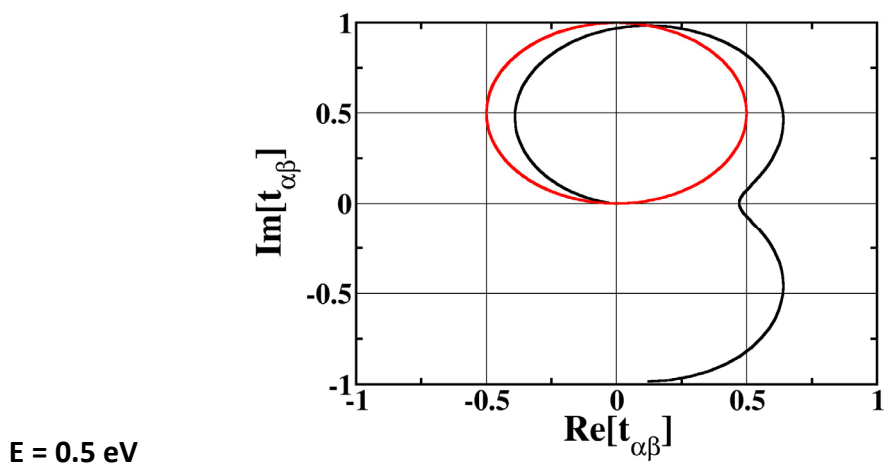
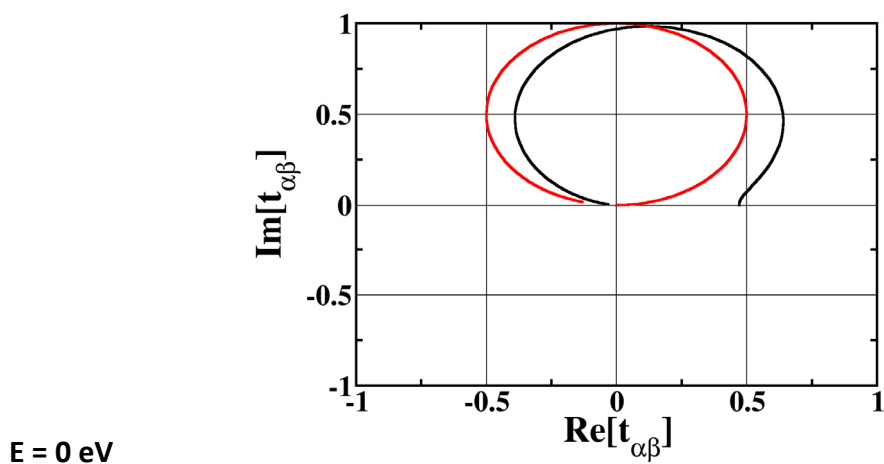


Figure 6-9. Parametric plots for the transmission through both two site systems.

6.5.2 Four site model

It is worth noting how the results obtained above change with increasing system size. It is tempting to assume that interference between two energetically adjacent molecular conductance orbitals will occur at an energy between those orbitals; however, we will show that this is not always the case.

We now look at the coupling through a four-site model shown in Figure 6-10. The Hückel molecular orbitals for the isolated four site system are shown in the upper left. As with the two-site model the isolated molecular orbitals are the same independent of how we connect the donor and acceptor. In the four-site model with degenerate site energies there are 10 different ways to connect the donor and the acceptor. We limit our discussion to the transmission plots for 6 selected systems. A non-spanning node is defined as a node that does not lie in the path between the donor and acceptor ie. a node in a branch off the main chain. Figure 6-10 **(b)** compares the transmission through D1A4 and D1A2. There are two antiresonances, both occurring in the D1A2 model. The antiresonance occurs when there is a molecular energy level that introduces a non-spanning node, a node that is not in the shortest path between the donor and acceptor.

In Figure 6-10 **(c)** D1A3 and D2A3 both have an antiresonance at $E=0$ in the transmission spectrum. In both models a non-spanning node is introduced between the HOMO and LUMO molecular orbitals. In the D2A3 model there are two non-spanning nodes introduced causing the width of the antiresonance to increase.

Figure 6-10 (d) shows two models, D1A1 and D2A2, where the donor and acceptor are both connected to the same site. In this example, each subsequent molecular orbital introduces a non-spanning node in the Hückel orbitals. Correspondently in the transmission plot for both of these four-site models there is antiresonance between each subsequent higher energy molecular orbital. The shift in antiresonance position is due to the energy difference between the site energy and the specific molecular orbitals.

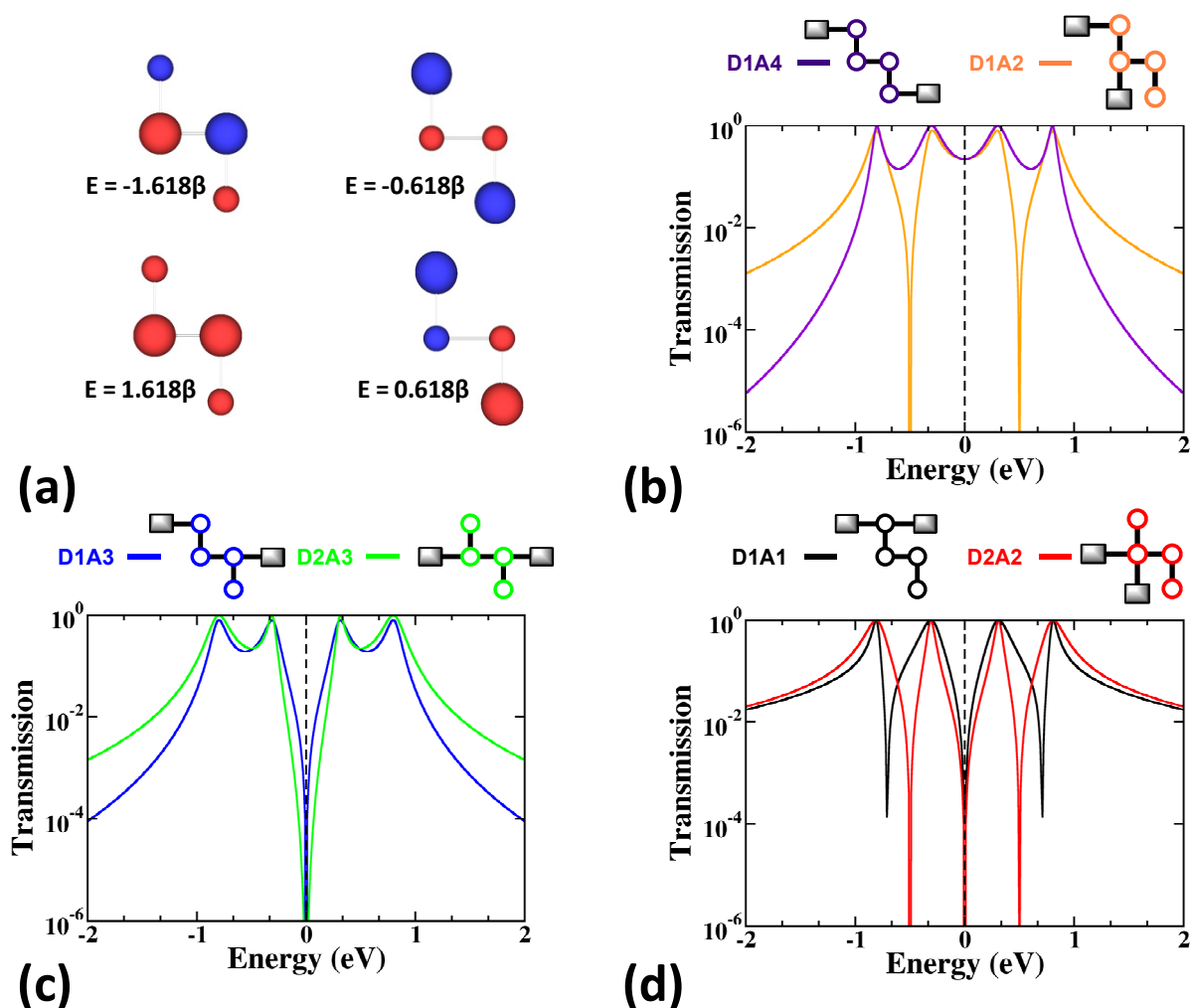


Figure 6-10. 4 site model system with six possible donor-acceptor couplings. In all model systems with a side group there is an antiresonance feature, although not necessary at $E=0$.

The two and four site models show that quantum interference and corresponding antiresonance are quite common in toy systems. Within these controlled systems, an antiresonance occurs whenever there is a zero in both the real and the imaginary components of the transmission coefficient. These transmission zeros appear whenever there are sites that are not in the shortest geometric path between donor and acceptor.

6.5.3 Six site ring

The final example we consider is 6-membered-ring models. The three modes of connection used in the model system mimic the ortho, meta and para connections through a benzene ring. The model is shown schematically in Figure 6-11.

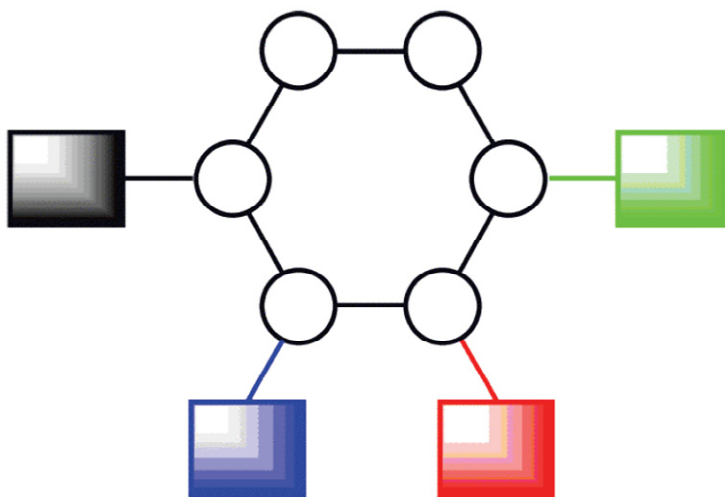


Figure 6-11. The 6-membered ring models. All models include the black electrode, the 6-membered ring and one of the other electrodes, specifically the ortho, meta and para connections use the blue, red and green connections respectively.²¹⁴

Previous work, both experimental¹⁸¹ and theoretical,²²⁰ has noted that the transmission through a benzene ring substituted at the meta position is dramatically lower than that through the ortho or para connections. In Figure 6-12 we illustrate this in the transmission close to the Fermi energy ($E_f=0$) of the electrodes.

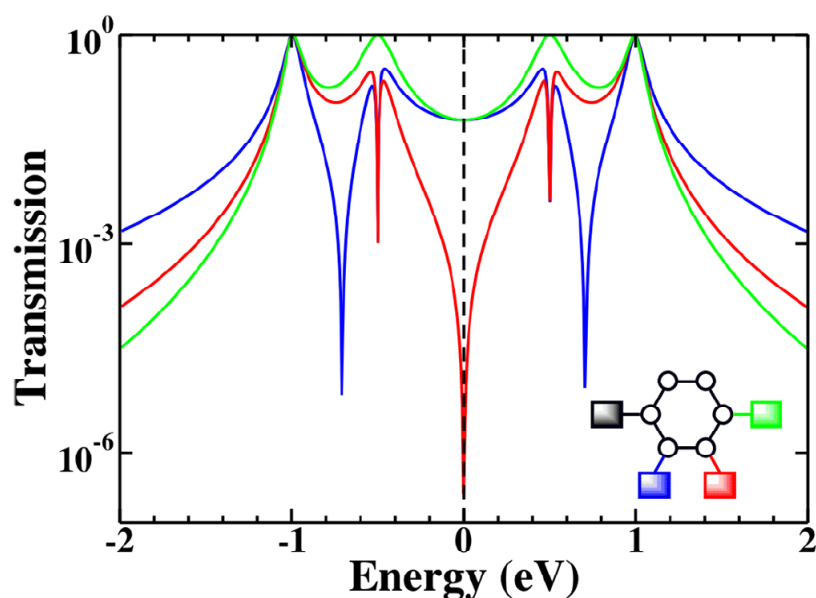


Figure 6-12. The 6-membered ring models. All models include the black electrode, the 6-membered ring and one of the other electrodes, specifically the ortho, meta and para connections use the blue, red and green connections respectively.²¹⁴

Additionally, we show that interference features similar to the one responsible for this difference are evident in the case of the ortho connection; however, in that case they are further from the Fermi energy. Only four resonances are apparent as the 6-membered ring has two pairs of degenerate orbitals which underlie the middle two peaks in the transmission. In the para case one of each of the orbitals in the degenerate pairs does not contribute to the

transmission. The very narrow interference features in both the ortho and meta transmission around $\pm 0.5 eV$ arise from the degeneracy breaking interactions with the electrodes and are not seen if the influence of the electrode (self-energies) are not included in the Green's function. This indicates that every site not in the shortest path between the donor and acceptor leads to an interference feature.

The coupling contributions from the molecular conductance orbitals, in Figure 6-13, show that majority of the antiresonance features in benzene do not arise from simple cancelation between the contributions of pairs of resonances. In fact, the only interference feature that does arise like this is the $0 eV$ feature in the meta case. All other features arise from more complicated combinations of canceling terms. In all cases the cancelation can be predicted from an examination of the coupling and phase transmission through the system. This is a remarkable result because it indicates that resonances far from the Fermi level may play an important role in the low bias conductance.

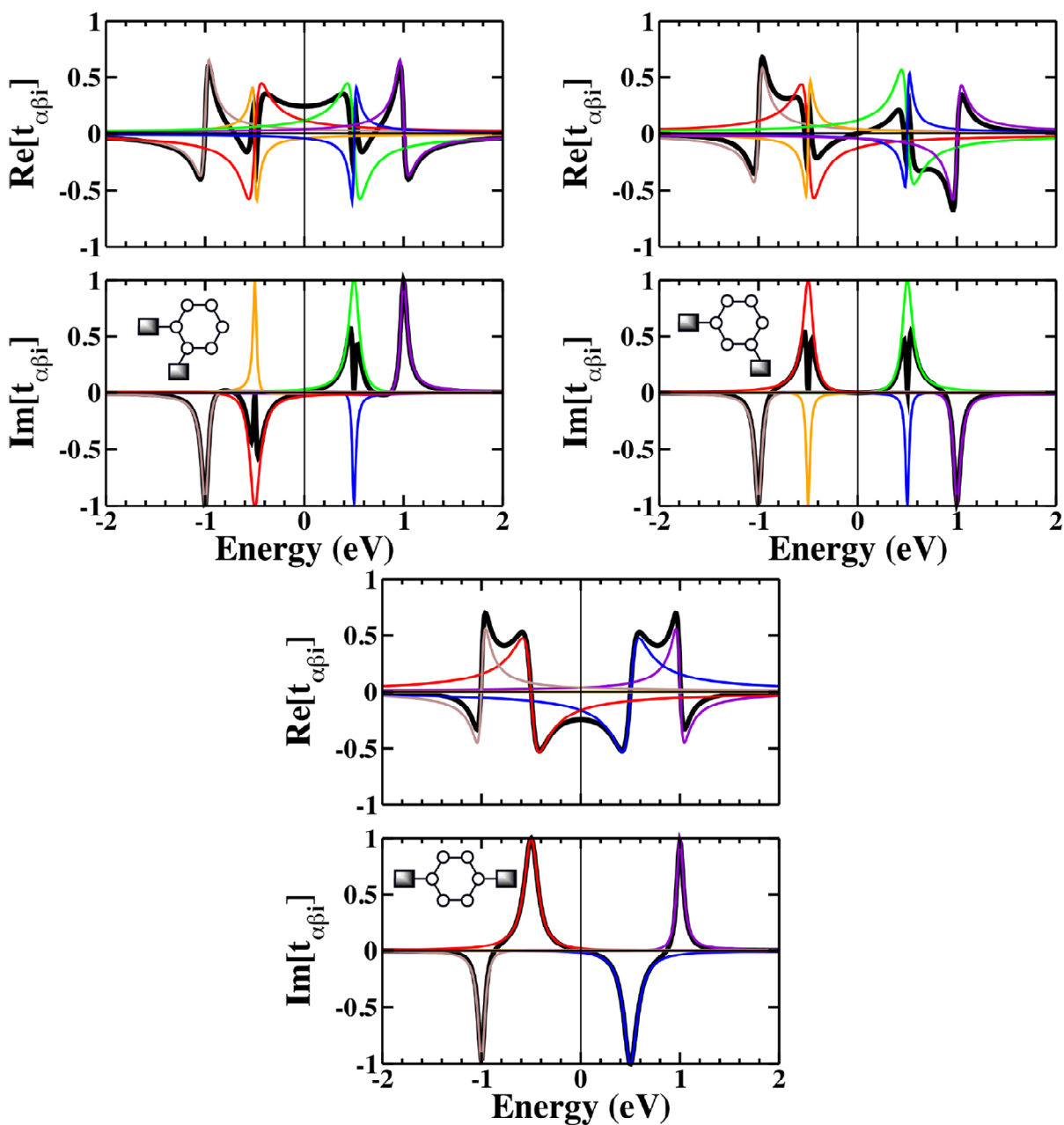


Figure 6-13. The contributions to the coupling for the three 6-membered ring systems with ortho, meta and para connections to the electrodes shown on the left, right and bottom respectively. The brown, red, orange, green, blue and purple curves illustrate the contribution from each of the molecular conductance orbitals and the underlying black line gives the total in each case.²¹⁴

It is interesting to look at the effect of varying one of the site energies and how this changes the interference feature. All site energies are set to 0 except for the site colored in red shown in Figure 6-14. In the six membered ring shown, small perturbations to the site energy cause a large change in the interference at 0eV. At large site energy the interference feature is energetically separated from all the molecular resonances and resembles a Fano lineshape. In the cases of $\alpha > 2$ only five resonances are visible as the sixth lies outside the range of the plot.

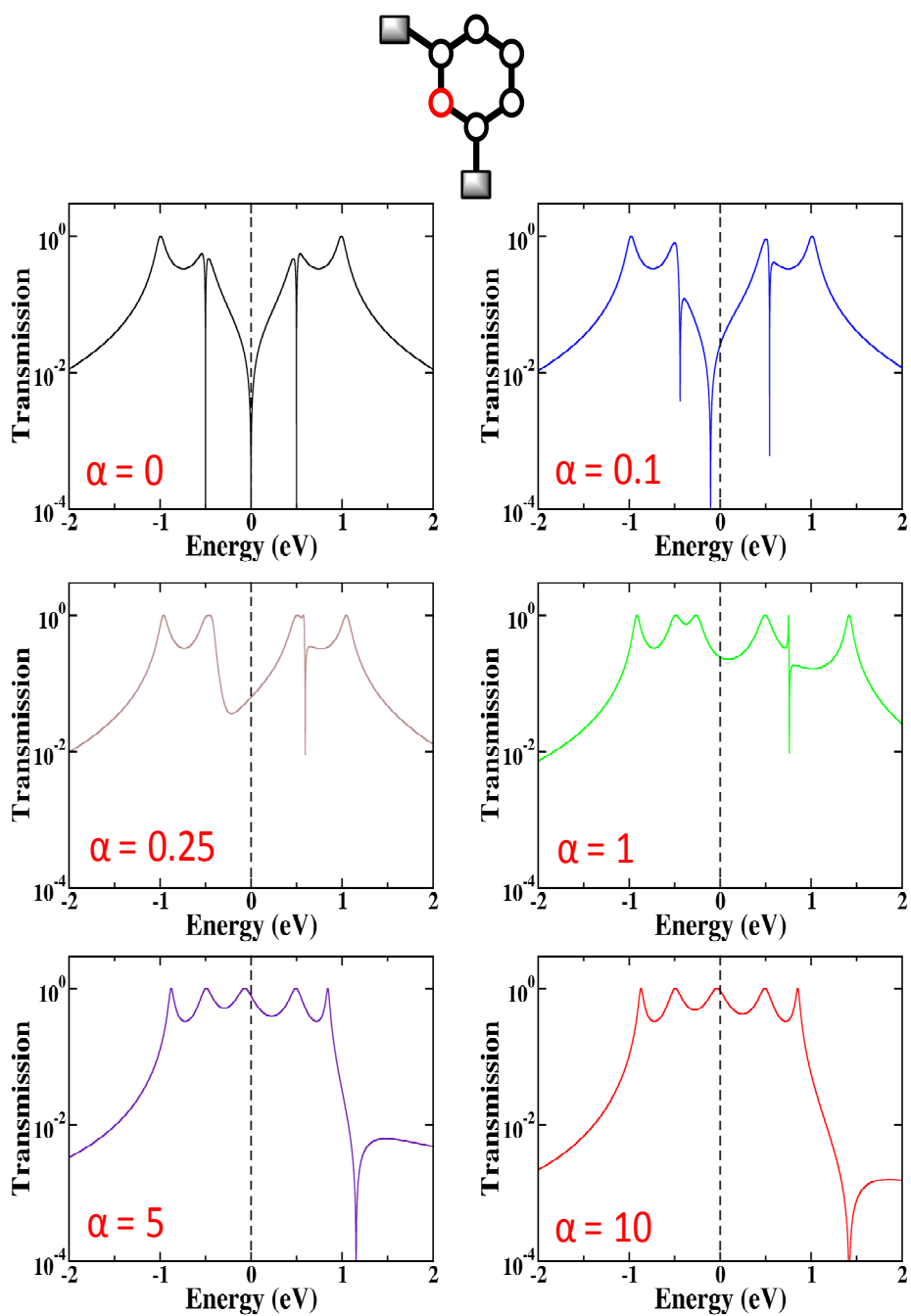


Figure 6-14. Coupling calculations with a single site energy change in a meta-connected six site model. In the cases of $\alpha = 5$ and $\alpha = 10$ only five resonances are visible as the sixth lies outside the range of the plot.

In Figure 6-15 the site energy of the middle site in the longer physical pathway is increased. In this example changing of the site energy has minimal effect on the main interference near the Fermi level. Chemical substitution or energetic fluctuations at this site would likely have little effect on the measured low bias conductance.

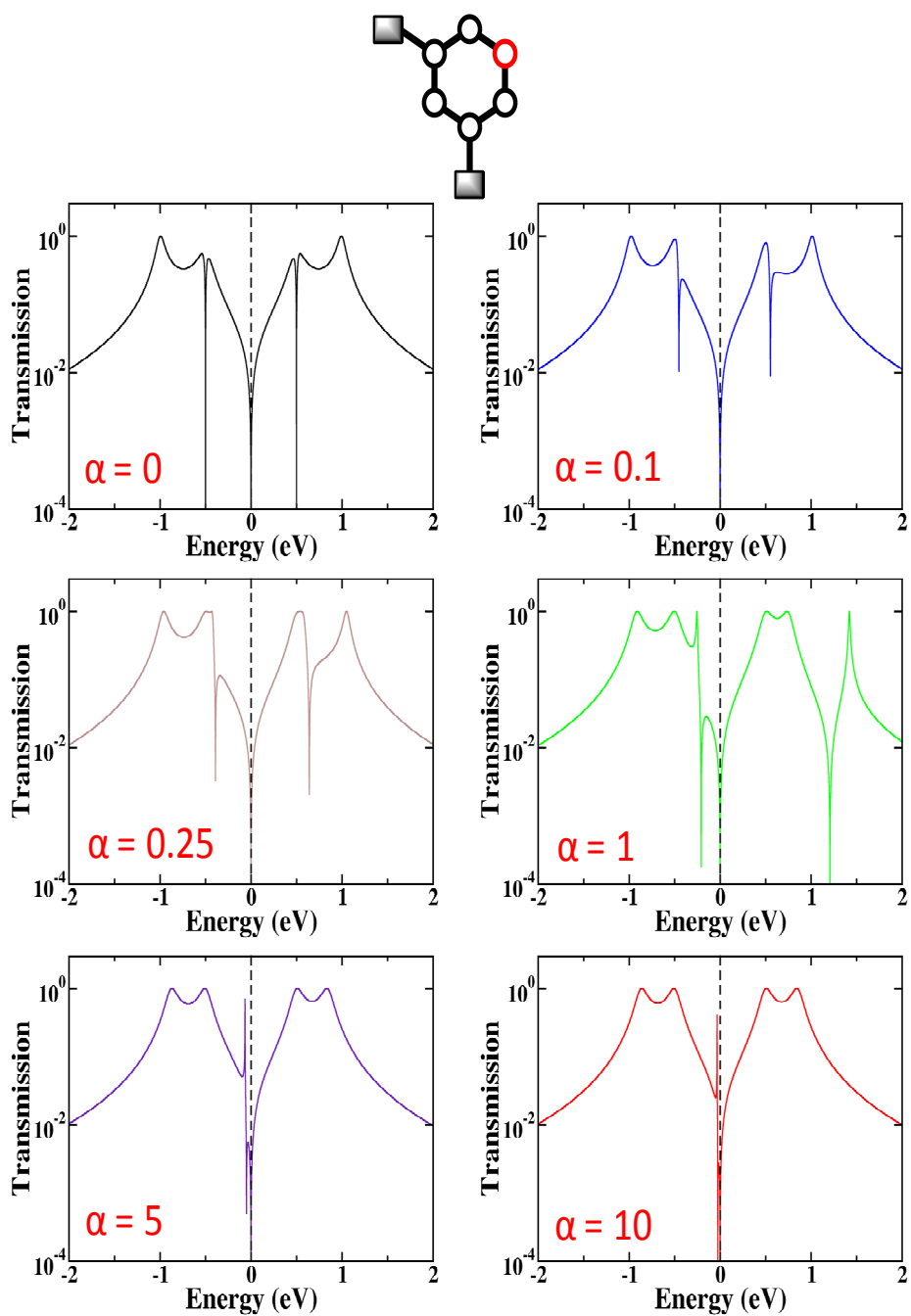


Figure 6-15. Coupling calculations through a meta connected six site model with a changing site energy.

The analysis of coupling and transmission phase through the model systems considered here provides useful information for a path-type picture of quantum interference in molecules. In particular, it can be shown that the interfering components arise from paths which, although orthogonal, are not necessarily spatially separated in terms of the atoms that participate. This presents a challenge for finding a classical analogue for this interference, something reminiscent of a two-slit experiment. In some sense, it is not so surprising that classical analogues fail to describe quantum interference at the single molecule level, but the fact that they do shows us why we need all the intuition we can get for these systems if we want to be able to understand and predict their behavior.

6.6 Comparing model systems with real molecules

One of the big difficulties in finding molecules where quantum interference effects dominate is the non-obvious mapping between site-model systems and the calculations in real molecules. There have been a number of papers looking at interference in branched systems but up until now there has been no connection from those model papers to calculations on the full molecule. Our ability to compute easily the full transmission spectrum as well as calculate the coupling terms in site models should provide an opportunity to understand this mapping.

6.6.1 Meta & para connected benzene

Benzene is a system that has shown interference and where the results correlate with the coupling calculations. In Figure 6-12 the transmission through a six membered ring was calculated in the coupling formalism. In calculations done using gDFTB in Figure 6-16 we see good qualitative agreement with the meta and para six site coupling calculations shown

previously in Figure 6-12. At low bias where the conductance and the transmission are proportional the meta-benzene conducts >1 order of magnitude lower than the para connected benzene. One of the major differences in the comparison is the depth of the interference feature. The lack of a sharp interference feature in the meta connected benzene is due to the short size of the molecule and the strong coupling of the Au atoms. If the meta connected benzene was spaced farther from the electrodes using ethyne spacers the sharpness and depth of the interference would increase and the low bias conductance would be completely dominated by the σ transport.

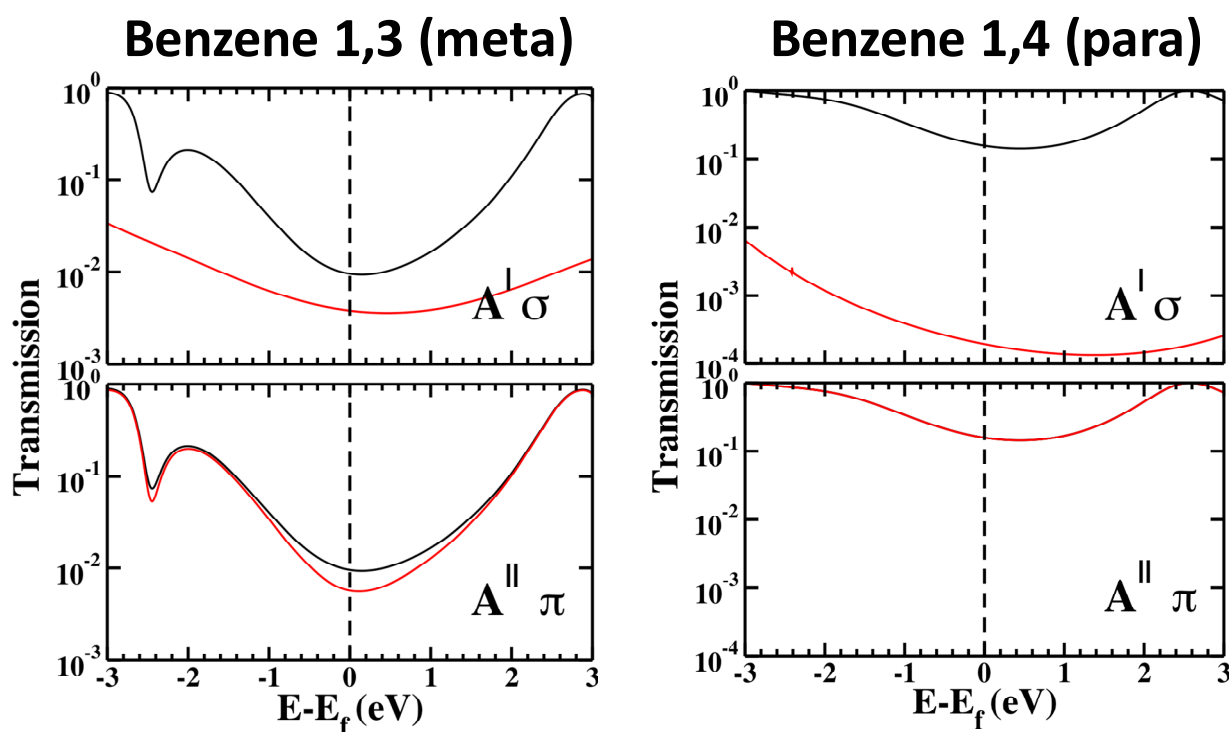


Figure 6-16. The transmission through meta and para benzene. In all of the plots the total transmission is shown in black. In the top plots the red trace shows the σ transport and in the bottom plots the red trace is the π component of the transport.

6.6.2 Interference in fulvene

The fulvene C_6H_6 molecule presents a good opportunity to test our understanding of interference in ring type systems. Figure 6-17 shows a fulvene molecule with the six sites labeled. Using this example of a six site system we will evaluate how well the coupling calculations correlate to the transport through a fulvene molecule. In Figure 6-18, Figure 6-19, and Figure 6-20 the transmission shown for six of the ways of coupling this system to electrodes. For a six site model with no degenerate energy levels we expect six energy states. In all six plots the six energy states are shown using a dotted line. Above the dotted line the calculated Hückel orbitals are shown. One of the first observations is that each molecule does not have a resonance peak at all six energy levels. At an energy level without any electron density on the site connected to the donor or acceptor there is no resonance peak in the transmission. At the same time, the height and width of the transmission peak increase with increasing density on the donor or acceptor connected site.

The transmission shown for molecule D1A3 in Figure 6-18 has only three resonances because the Hückel orbitals for three of the six energy states have no electron density on either one both of sites 1 and 3. In the three energy states without electron density on the donor or acceptor connected site there is an interference feature. This behavior is not consistent through all the molecules as can be seen in the case of D3A6 in Figure 6-20 where there is no interference feature at the energy of the absent resonance.

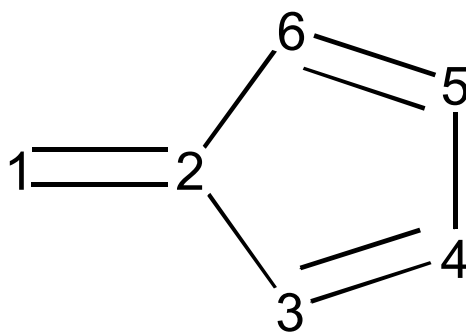


Figure 6-17. A fulvene molecule can be connected to electrodes in 6 different configurations and is used to compare the results using the site model coupling method and transmission calculations done using Hückel-IV.

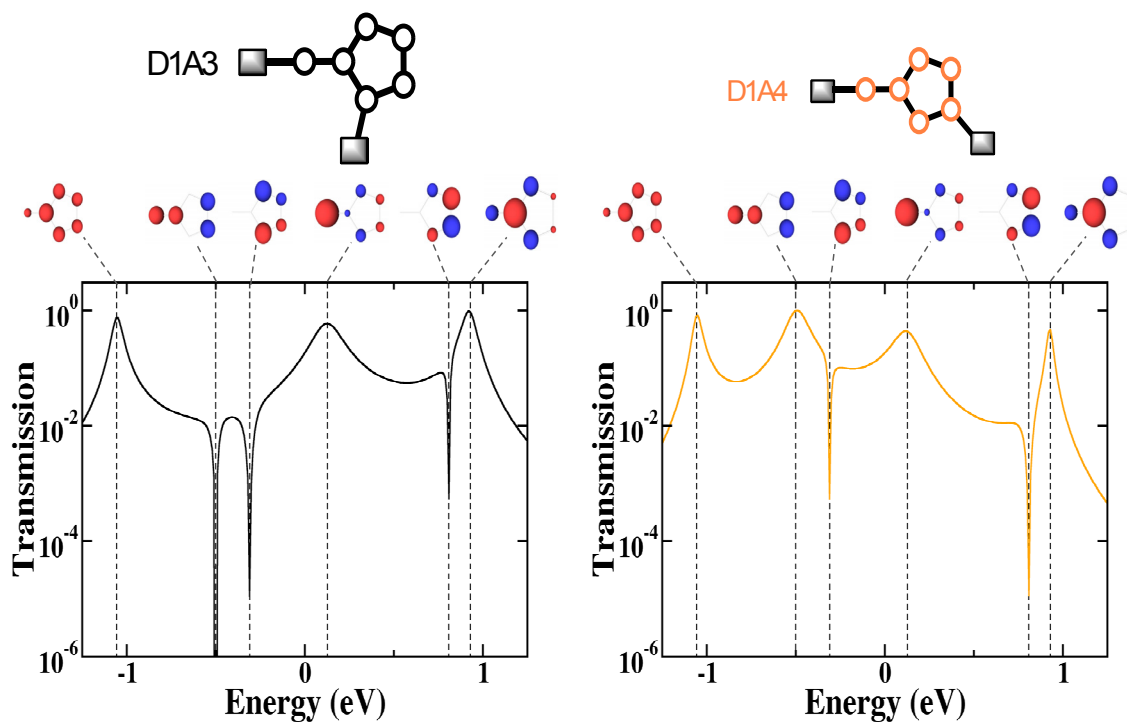


Figure 6-18. Transmission calculated through fulvene model systems D1A3 and D1A4.

With all of these interference features present in the coupling calculation it seems reasonable to make an effort to equate the position of the antiresonances with the form of the

Hückel molecular orbitals. We have tested our ability to predict the number and location of interference features for a large number of molecules showing interference with limited success. It was noted in the transmission phase in quantum dots,^{239,240} as well as in our work here that if there is a zero in the real and imaginary part of the transmission there will be an interference. In many of our test molecules we have found that if the number of orbital nodes between donor and acceptor stays the same or decreases we can expect an interference feature. Based on the strength of the coupling this interference feature need not appear between those two orbitals. This works quite well for cross-conjugated molecules, but ring systems present an interesting challenge because all nodes can be considered spanning nodes between the donor and acceptor. One observation that has held is that the number of interference features calculated is exactly equal to the number of sites not directly between the donor and the acceptor (in a number of cases there are degenerate interference features that can be observed by introducing a small site energy perturbation). We now look at how the site model compares with full transport calculations.

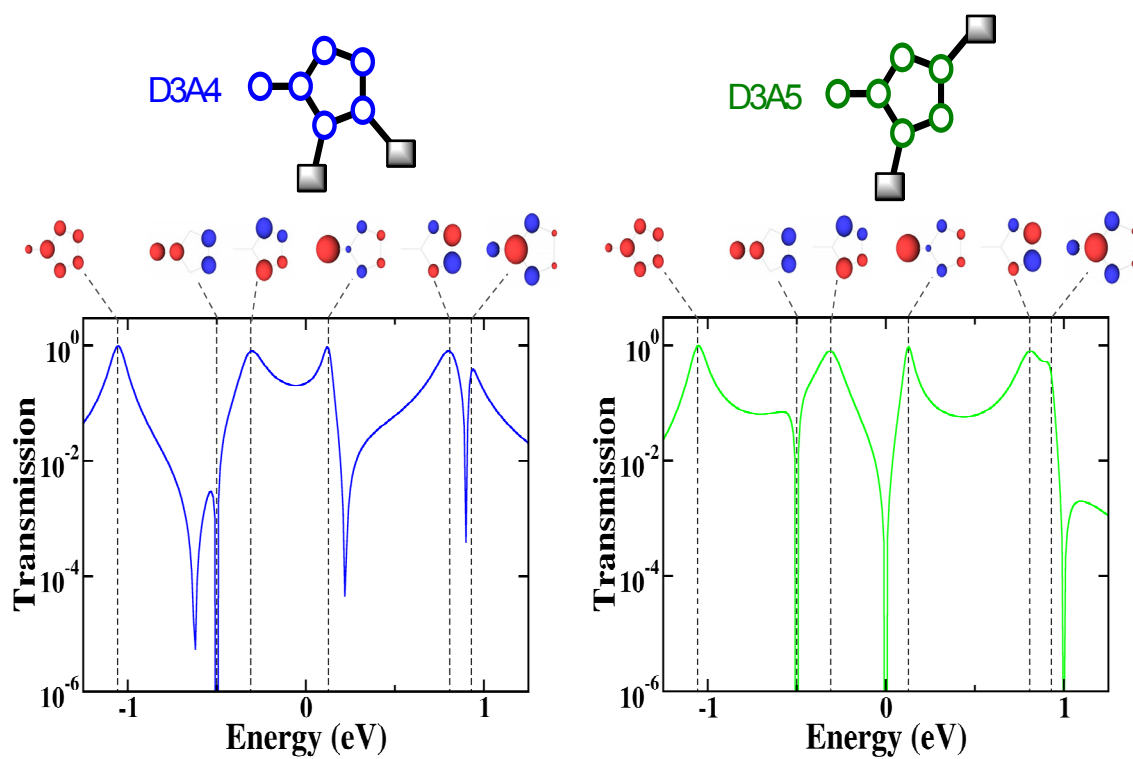


Figure 6-19. Transmission calculated through fulvene model systems D3A4 and D3A5.

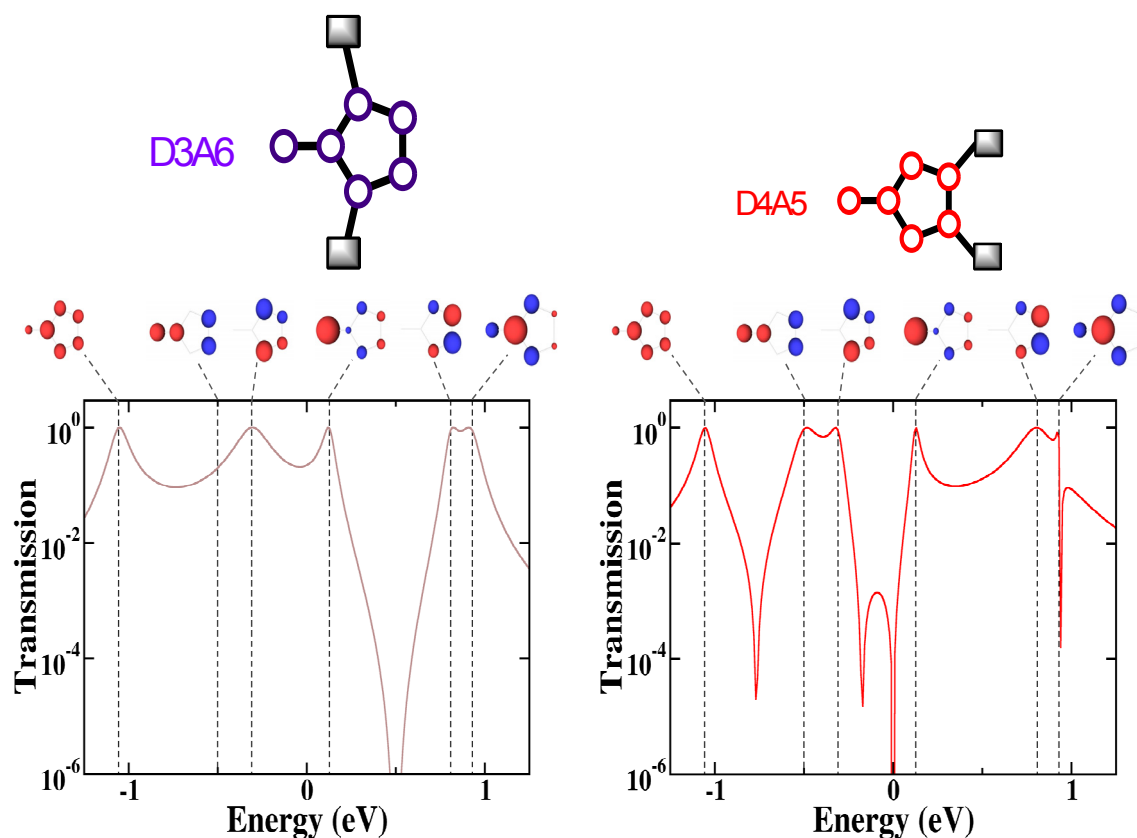


Figure 6-20. Transmission calculated through fulvene model systems D3A6 and D4A5.

To compare the coupling calculations on model systems to transport results on molecular systems we have utilized the Hückel-IV transport code. In all the molecules, a triple bond and thiol linkage were added to the donor and acceptor sites to separate the molecule from the electrodes. In molecules D3A4 and D4A5 a single triple bond was not sufficient so an additional double bond and triple bond was added to each terminal end as shown in Figure 6-21. A few differences between the site model calculations and the full transport calculations are immediately evident. Firstly, in the Hückel-IV results there are almost no sharp interference features seen in the transmission; molecule D3A4 providing the one exception. As we have seen in all other Hückel calculations the σ transport becomes dominant around -1eV making

comparisons in this range difficult. In molecules D3A4 and D4A5 the additional conjugation moves the LUMO resonance to lower energy and adds lower energy, higher order resonances to the picture. We will focus our comparison on the energetic region near the Fermi level.

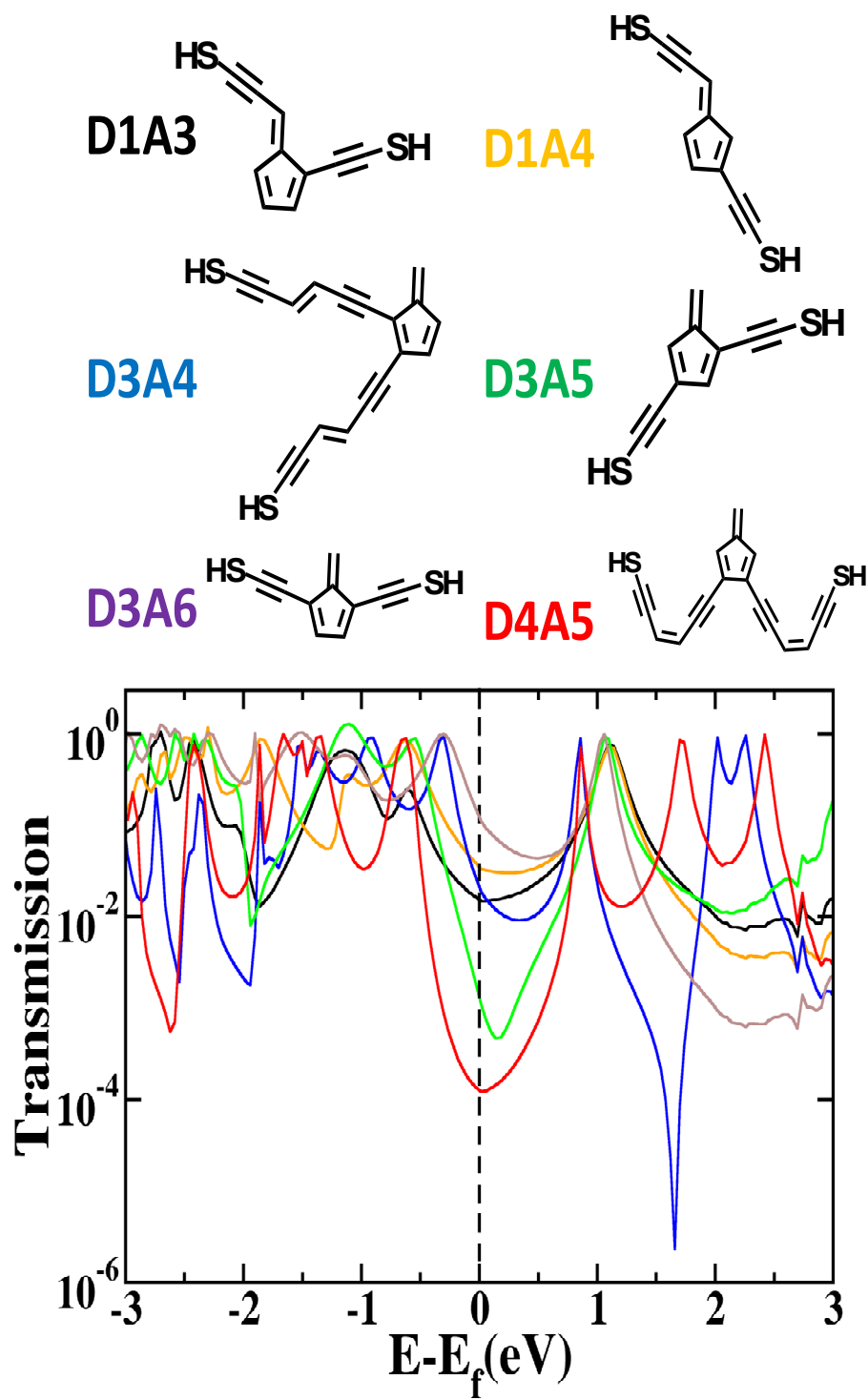


Figure 6-21. Fulvene transport calculations using Hückel-IV.

In the region near the Fermi energy the results from the site model and the full transport calculation in Hückel agree quite well as shown in Figure 6-22. In both calculations the D4A5 molecule shown in red has the lowest transmission at the Fermi energy. The D3A5 molecule subsequently has the next lowest transmission in both calculations. In the region energetically above the LUMO level the Hückel calculations show the sharp interference feature calculated for the D3A4 molecule in blue. The transmission through the brownish purple molecule is also consistent between the methods. The ability to make a more detailed comparison between the subtle details in the results is hindered by the use of different linkage groups used to attach the fulvene to the electrodes. In this example, the site model coupling calculations and the analysis of Hückel orbitals correlates well with the results calculated in Hückel-IV.

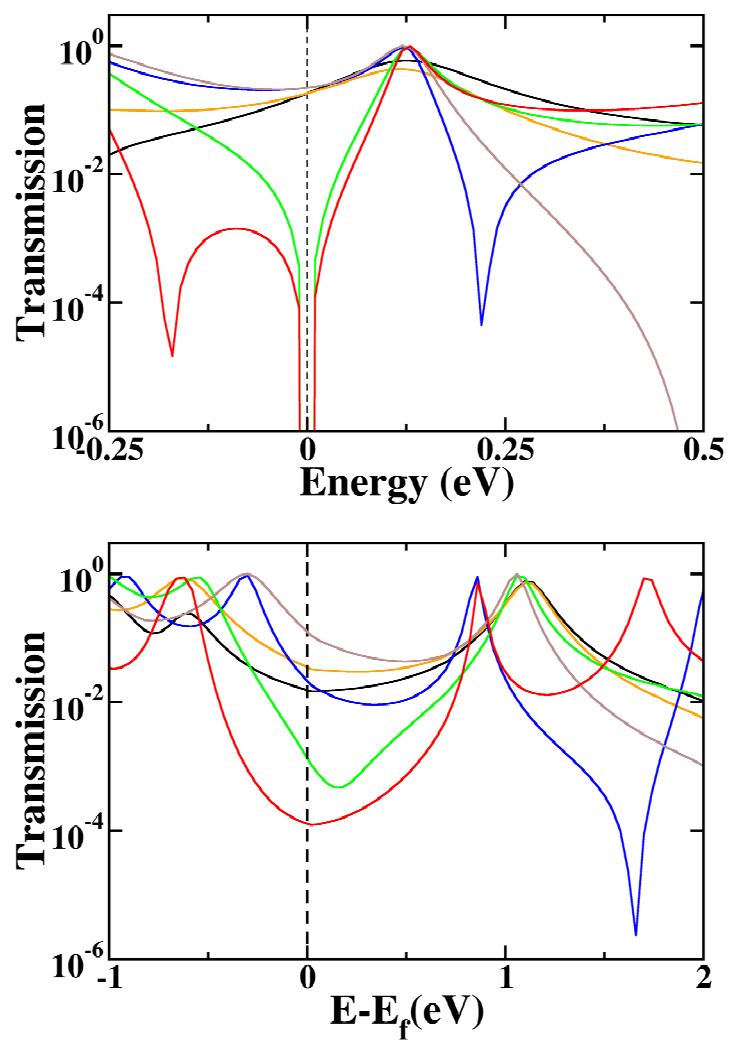


Figure 6-22. Coupling and transmission compared for 6 different possible configurations. The top plot shows the coupling calculation and the bottom plot shows the Hückel-IV calculations. The corresponding plot line colors correspond to equivalent attachment to the fulvene/6 site model (ie. the red line is for D4A5).

6.7 Initial interference work

Most research does not follow a direct linear path towards the results. The work on quantum interference in conductance is no exception to this phenomenon. The introduction given here highlights some of the initial directions and provides a context for the following work. The investigations in this area began when Dr. Solomon brought to my attention a published report showing Fano resonances calculated in the transmission probability for molecules with a fluorenone central unit.²⁴¹ These published results are shown in Figure 6-23 for reference.

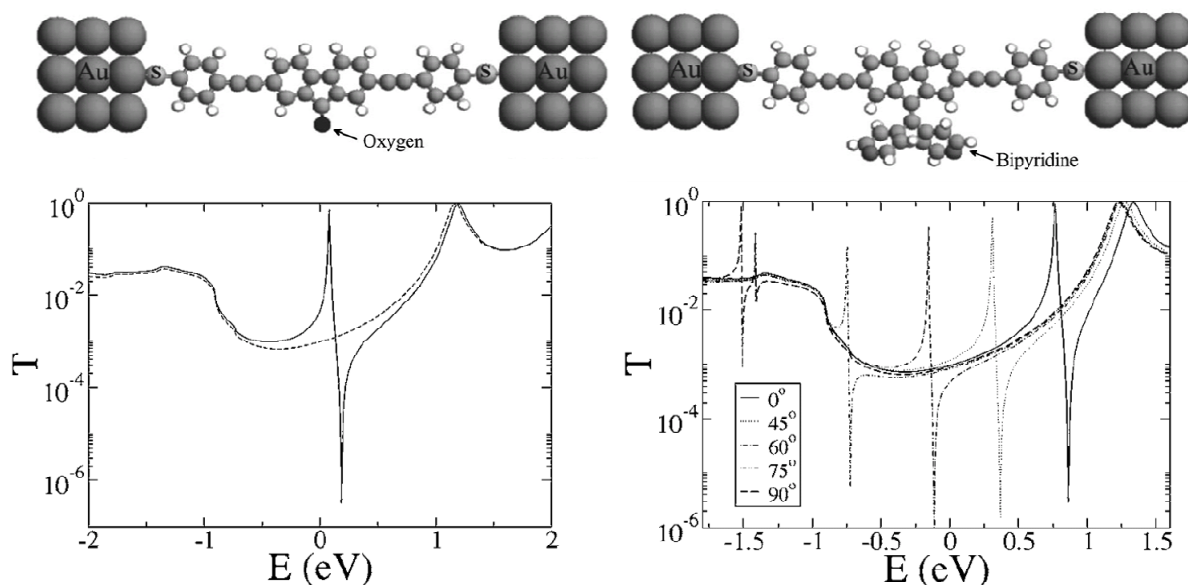


Figure 6-23. Published Fano resonances in transmission plots.²⁴¹ In the plot on the left the oxygen group leads to a Fano resonance near the Fermi energy. In the plot on the right the bipyridine group is unrealistically rotated to show that the Fano resonance can change energetic location.

To verify these published calculations the transport properties of these molecules were calculated using ATK (shown in Figure 6-24). One thing that can be noted is that while we calculate a Fano resonance the energetic location is $\approx 1\text{eV}$ from the Fermi level. This energetic separation indicates that in a current/voltage measurement, on a single molecule, the interesting lineshape will have approximately no effect on the measurement. Calculations were also completed using an applied gate voltage, but due to the narrow line width and energetic separation from the Fermi energy our calculations indicate the Fano resonances in these molecules will have no added potential for molecular devices.

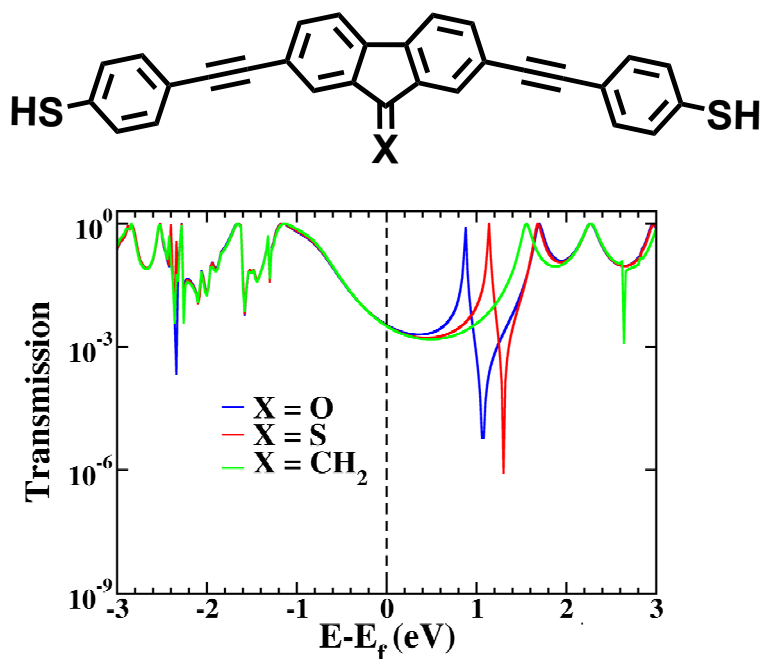


Figure 6-24. Initial calculations on Fano resonance calculated using ATK.

In the following nine months, numerous meetings occurred with Dr. Goldsmith, Dr. Hansen and Dr. Solomon discussing potential molecules and types of molecules that could

move the Fano resonance or interference feature to an experimentally relevant location in close energetic proximity to the Fermi level.

There are a few cases that were found to show quantum interference. Benzene is the best known example of interference with calculations going back twenty years.^{210,242} The interference in benzene correlates well with the ortho-meta-para coupling strength and substitution rates exemplified in organic chemistry classes. In Figure 6-16 we showed the calculated for meta and para benzene done using gDFTB and here we present the qualitatively similar results using Hückel-IV in Figure 6-25. The interference feature is not as sharp as seen in the fluorenone molecules in Figure 6-24. Further on in this chapter we show that this is simply a function of the shorter length and consequently higher σ transport through these systems.

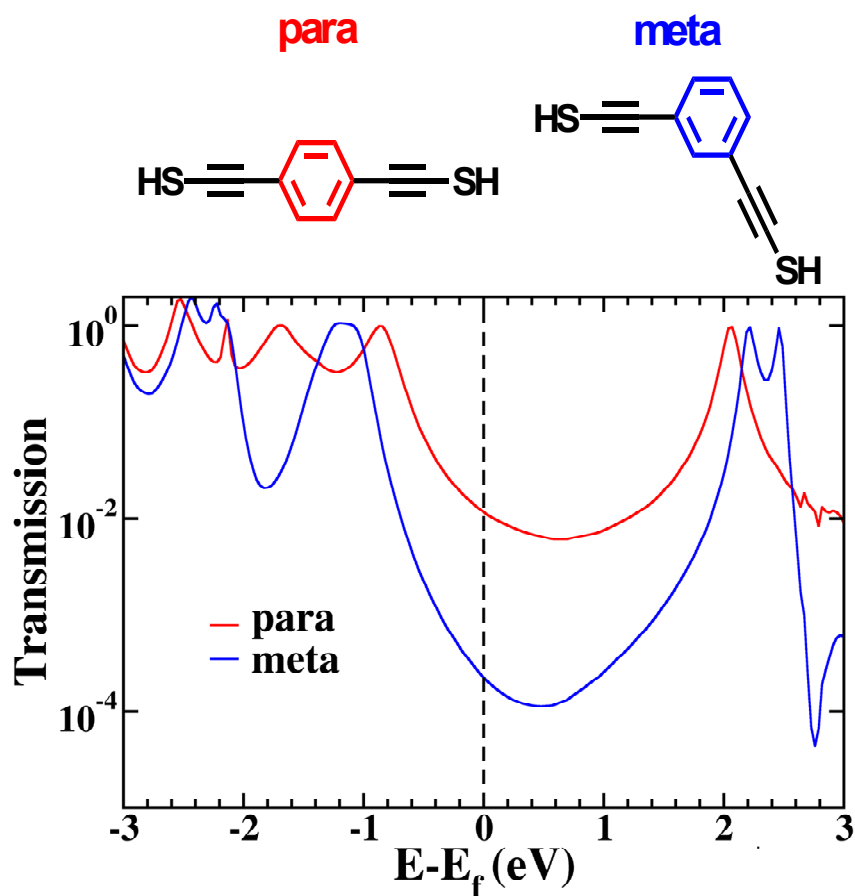


Figure 6-25. The transmission through a meta and a para connected benzene calculated using Hückel-IV 3.0. The meta connected benzene molecule has nearly two orders of magnitude lower transmission and therefore conductance at low bias.

Our investigations have also revealed that interference features can also be observed in “para” type orientation when the simple benzene ring is replaced with a cyclophane, giving a π -stacked path between the electrodes. In Figure 6-26 the molecule in green shows an interference feature at the Fermi level. This interference occurs due to connectivity of the π stacked motif in the center of the molecule rather than the σ connectivity between the rings, as can be seen in the comparison with 3u.

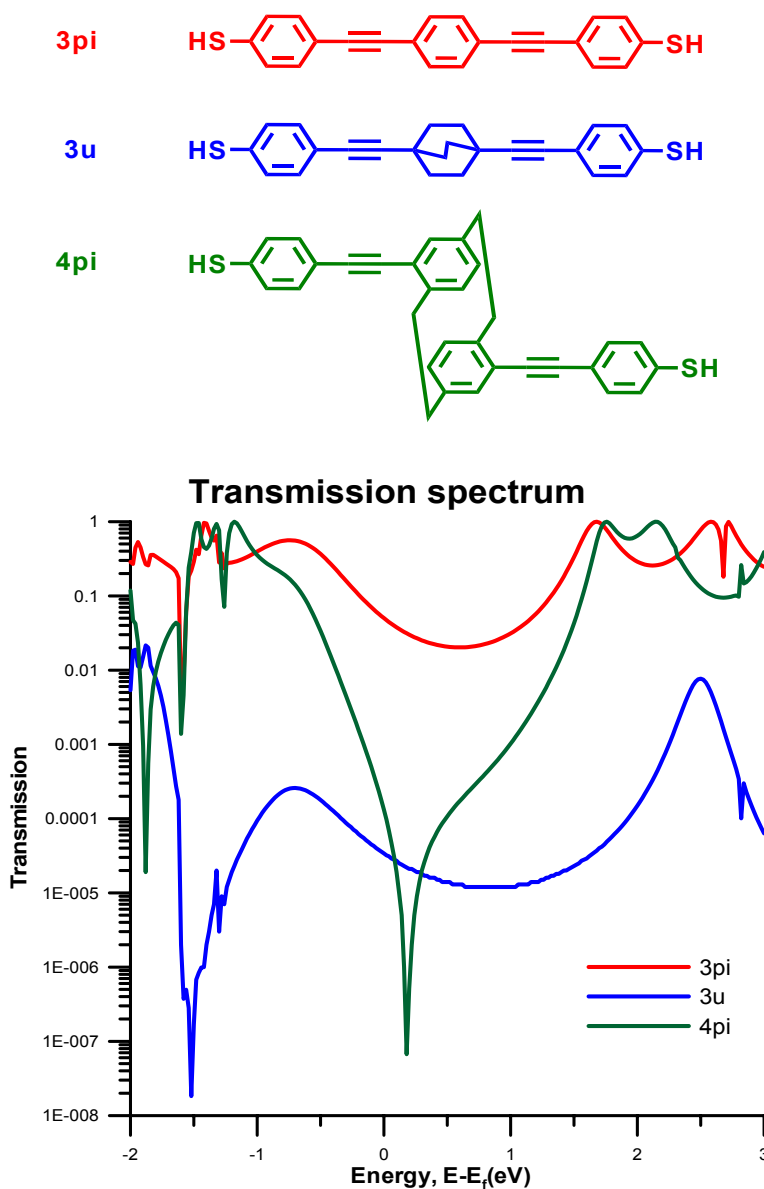


Figure 6-26. Transmission plots for a series of 3 molecules including a interference seen in a π stacked molecule.

The current-voltage calculations shown in Figure 6-27 show this behavior. Looking at the current-voltage characteristics of these molecules we see that the interference feature in the π -stacked system leads to an interesting conductance behavior. The π -stacked molecule has

conductance similar to the molecule with a break in the conjugation at low bias, but as the voltage is increased to 2V current through the π -stacked molecule is closer to the fully conjugated molecule, 3 π , shown in red. In the calculations done using ATK shown on the right we see that over 2 Volts the current through molecules 3 π and 2 u increase ≈ 1.5 orders of magnitude, while the current through the π -stacked molecule increases ≈ 4 orders of magnitude. The results are much more striking in the calculations done using ATK in comparison to Hückel-IV. This variation is due almost entirely to the difference in the calculations of the molecule with a saturated linkage, 3 u . In Hückel-IV the large transmission peak for the HOMO orbital is energetically close to the Fermi level (not shown) resulting in an earlier onset of the current. This result is seen in all the subsequent Hückel-IV calculations presented in this chapter as well as in the transmission plots shown in Appendix B.

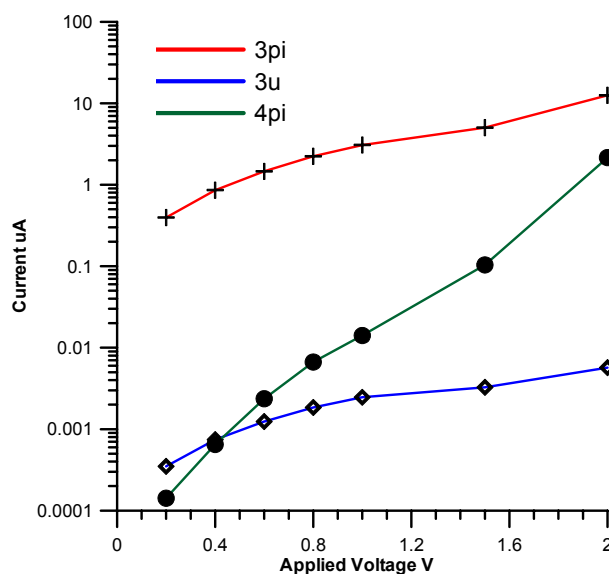
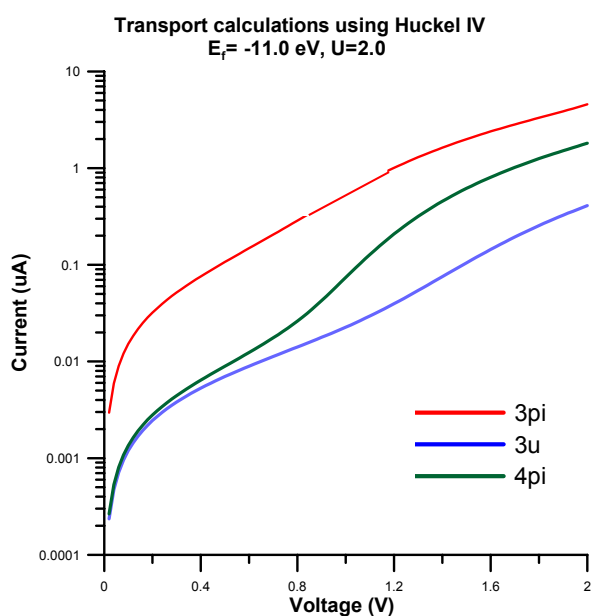


Figure 6-27. Current voltage curves are shown for the three molecules, using Hückel IV in the first graph and ATK with discrete data points in the second plot. The trend is quite similar, but in ATK the low bias voltage current for 3π is much higher and at higher voltage the current values for $3u$ are much lower.

6.7.1 Current from 0V transmission plots

Within the literature, and presented within this work, there are a large number of plots that show only the calculated 0V transmission and proceed to make conclusions about the conductance of the molecule. In the low bias limit, the conductance is proportional to the 0V transmission,^{4,209} but it has been shown that the transmission shifts with an applied potential.³⁸ This will occur for a molecule that has any asymmetry in the molecular geometry with respect to the electrodes or in the coupling strength to the electrodes. In cases with asymmetry, it is critical to look at the transmission shift as a function of voltage, and in the design of a diode, a transmission that shifts with potential is required. In a symmetric molecule that is symmetrically coupled to the electrodes, how close is current-voltage behavior calculated from the 0V potential to the conductance calculated with a bias dependent potential? In Figure 6-28 this comparison is shown for the three molecules calculated above, including the π -stacked molecule with quantum interference. The solid line represents integration of the 0V transmission curve and the marked points represent the discrete voltage calculations.

Current Voltage discrete points and integrated 0V Transmission

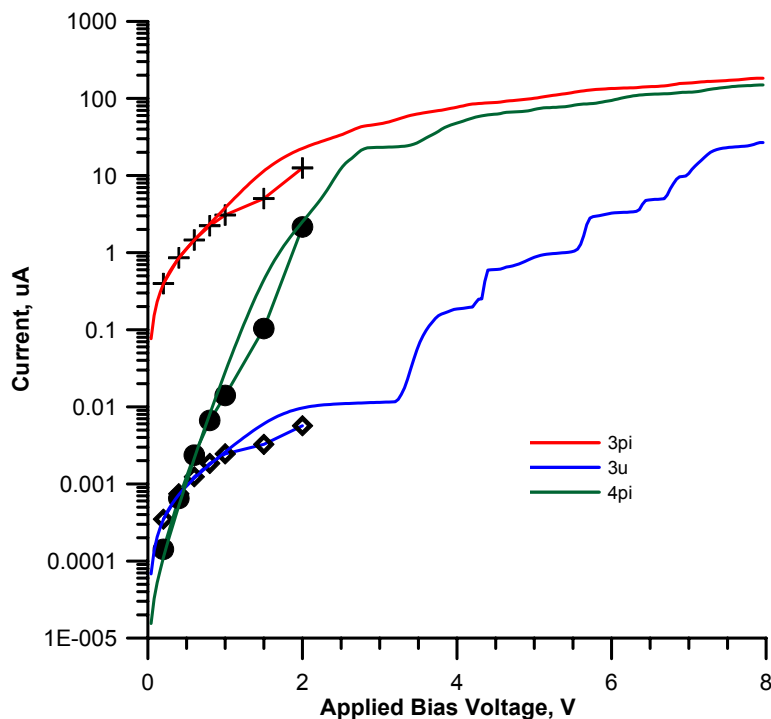


Figure 6-28. Comparison of current/voltage results from integrating 0V transmission and calculations at discrete bias voltages. Comparing with the discrete data point calculations under bias the agreement between the current values in these molecules is quite good up to $\sim 1V$. The trends are very similar for symmetric molecules with symmetric coupling to the electrodes.

In this set of symmetric molecules, there is very good agreement between the current calculated from the 0V transmission and the full voltage calculations. The tabulation of the discrepancy using this approximation in Table 6-1 shows that up to 0.8V the deviation is within

20% in all three molecules. At 2V, the discrepancy at is 80%,70% and 17% and the qualitative trends between the molecules remains consistent.

Table 6-1. A numerical comparison of current/voltage results from integrating OV transmission ($V_{OV,TE}$) and calculations at discrete bias voltages (V_{SCF}). All values are given as a percent difference between the results, calculated as the absolute value of $(V_{SCF} - V_{OV,TE})/V_{SCF}$. Up to 0.8 V bias, the difference between the two methods is less than 25%. This is true for these 3 symmetric molecules with over 5 orders of magnitude difference in conductance values.

voltage	3pi	3u	4pi
0.2	1.184344	0.944537	22.03882
0.4	1.207198	2.715496	19.9628
0.6	0.191992	4.670011	9.255583
0.8	5.81277	3.774612	20.4061
1	24.07944	5.592364	100.2272
1.5			
2	79.48816	70.23471	16.94104

The behavior of an increasingly large π -stacked molecule was investigated using gDFTB (Figure 6-29). The transmission through these molecules decreases with increasing size as generally expected. The molecules with even numbers of phenyl rings in the stacked unit (2 and 4) also exhibit sharp interference features between the HOMO and LUMO evidenced by the sharpness of the dip in the mid gap transmission.

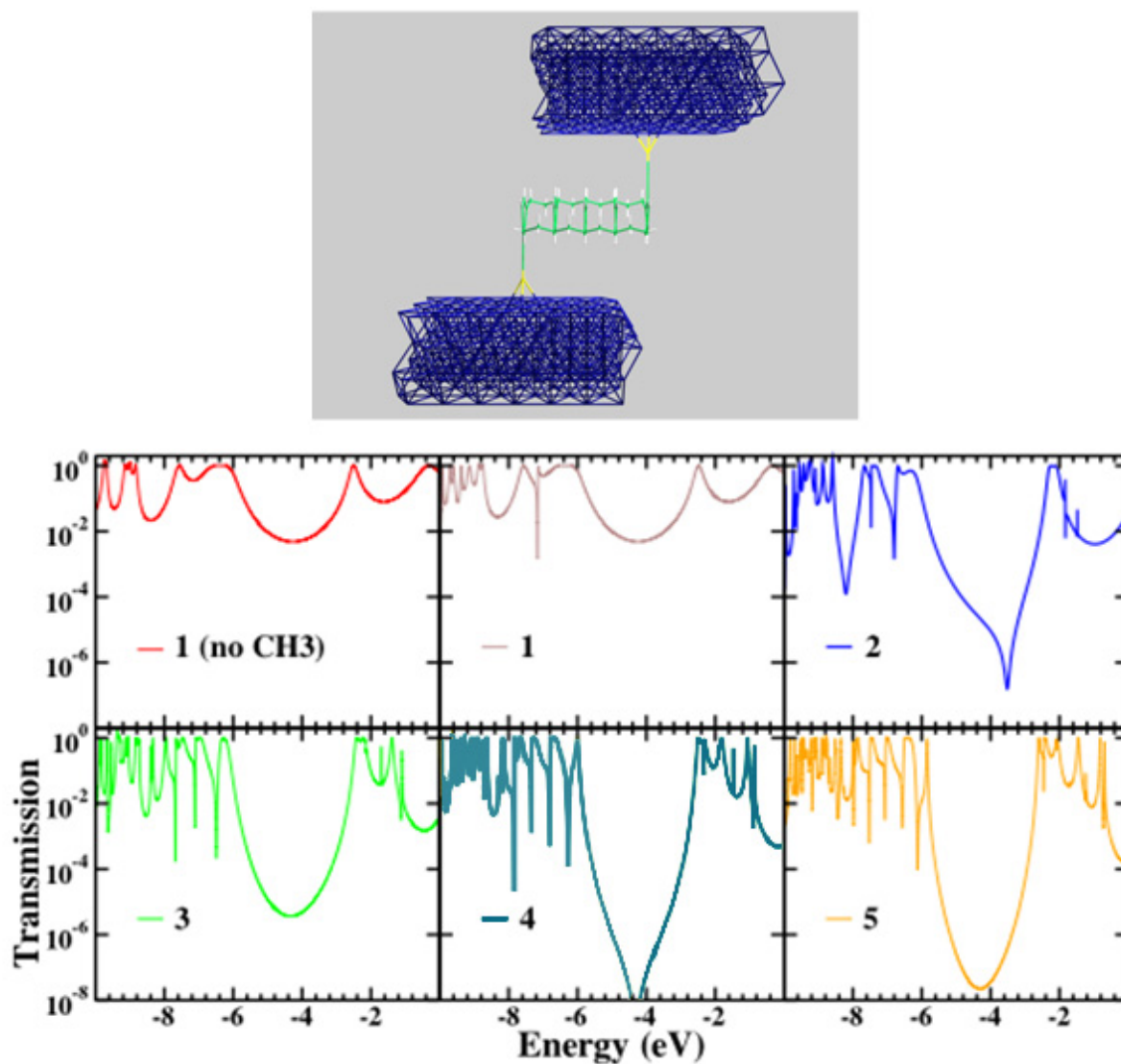


Figure 6-29. Interference in transmission through π stacked six membered phenyl rings calculated in gDFTB. The example structure on top shows 5 phenyl rings connected with two ethane linkages to each of the nearest rings between two Au electrodes. The red curve shows transmission through a para connected benzene, the grey curve includes the two ethane linkages between the phenyl rings. The 4 subsequent transmission plots are done with an increasing number of π -stacked rings.

6.7.2 Directionality of transport: a breakthrough molecule

The π -stacked systems and the benzene ring provided indication that interference could be identified in a number of systems but identification of the simplest unit that creates interference, would help elucidate the causes. Figure 6-30 shows the results obtained using gDFTB for 1,1-ethenedithiol bound to two ad-atoms in a bridge configuration above a flat Au surface. The bridge site ad-atoms minimize the hydrogen-gold interaction and evidence of the interference can be seen in the π component of the transmission. It is this calculation by Dr. Solomon that set the stage for the subsequent work on interference.

The essential element in much of the subsequent work is based on the quantum interference that occurs when the ethylene unit is oriented perpendicular to the transport direction. This unit can exhibit interference features as shown for example in the 1,1-ethenedithiol example, however there are practical problems as the hydrogen atoms in the central CH₂ interact with the electrodes. Looking at Figure 6-30, the transmission probability through the π channel shows a dip near the Fermi energy due to quantum interference. This dip or antiresonance can be viewed as the opposite of a transmission resonance, with the transmission coefficient approaching zero. An antiresonance is defined as a 0 in the transmission probability. Due to the non zero transport through the σ channel we refer to this dip as an interference feature in the transmission. An antiresonance in the transmission would occur if there was interference in all transport channels. It would be ideal to engineer a system with interference in all transport channels because this would create a perfect insulator or a

switch with a perfect off state. While this is not realized in the present work, it is noted and discussed in more detail in the outlook section in chapter 7.

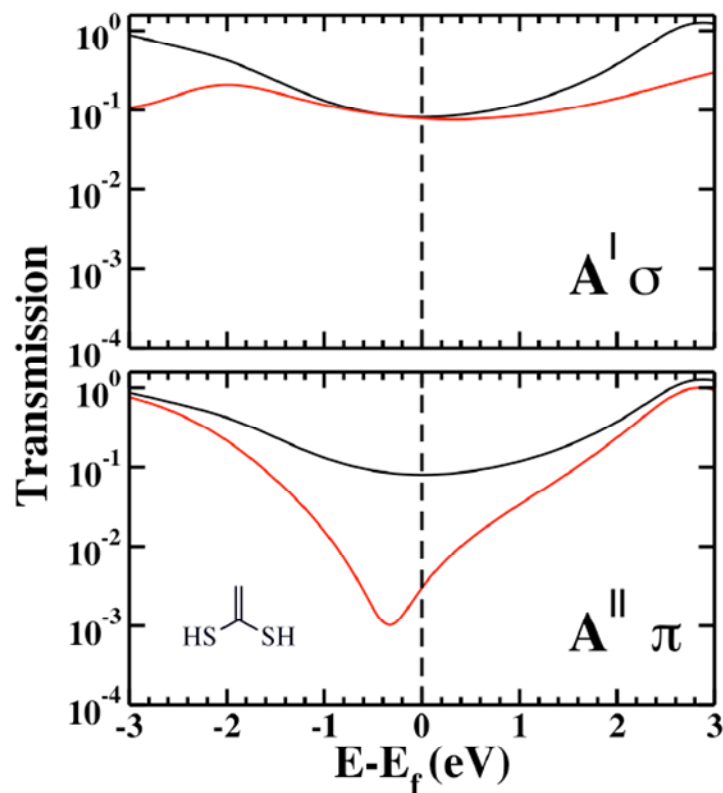


Figure 6-30. The transmission through ethene-1,1-dithiol showing a damped interference feature due to the hydrogen-gold interaction.

The attribution of the unusual conductance characteristics to quantum interference is addressed in more detail in subsequent sections. As later sections show the interference feature in the ethene unit is a local effect and it occurs in the transport calculations through larger molecular systems. Importantly, it is stable to electronic dephasing and molecular dynamics.

6.8 Cross-conjugation

A search on molecules with an ethene unit perpendicular to the main conjugation path led to a description of cross-conjugated molecules.²⁴³ “A cross-conjugated compound may be defined as a compound possessing three unsaturated groups, two which although conjugated to a third unsaturated center are not conjugated to each other. The word ‘conjugated’ is defined here in the classical sense of denoting a system of alternating single and double bonds.”²⁴⁴ By definition, and as illustrated in the resonance picture shown in Figure 6-31, cross-conjugation in transport junctions depends on the position of the electrodes. In a molecule that is fully π -conjugated, this binding dependence will affect the low bias delocalization and whether there can be an odd number of carbon atoms between the donor and acceptor. Electron delocalization and electron transport are correlated^{245,246} and from Figure 6-31 it seems evident that electron transport should behave differently if the electrodes are connected to atoms 1 & 6 versus connection to atoms 1 & 5.

Cross-conjugation is a common motif in organic chemistry, found in a wide range of naturally occurring and synthetic molecules, yet detailed analysis of the electron delocalization and transport properties is sparse. Recent synthetic work has detailed a large number of cross-conjugated molecules.^{239,240} A number of theoretical studies of HOMO's and LUMO's of cross-conjugated molecules have shown that the electron delocalization is split at the cross-conjugated unit.^{245,247} This difference between linear and cross-conjugation has been borne out in absorbance measurements, as the cross-conjugated unit results in a measured blue shift in the absorbance peak.²⁴⁸ In donor-bridge-acceptor systems the cross-conjugated connectivity

leads to measured electron transfer rates lower than those of linearly conjugated systems but generally higher than those of non-conjugated systems.²⁴⁹

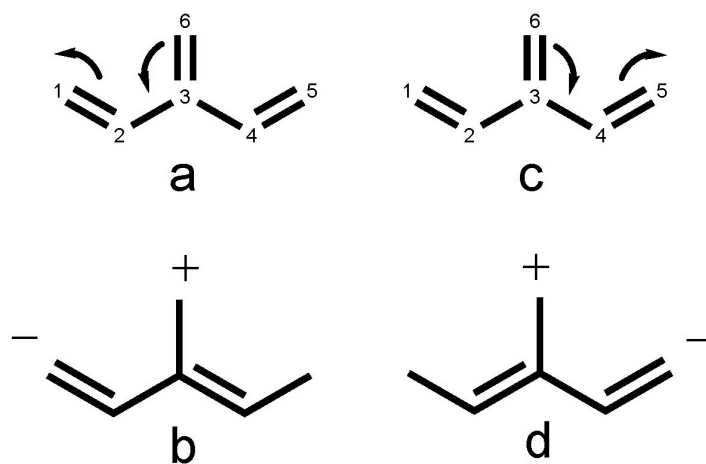
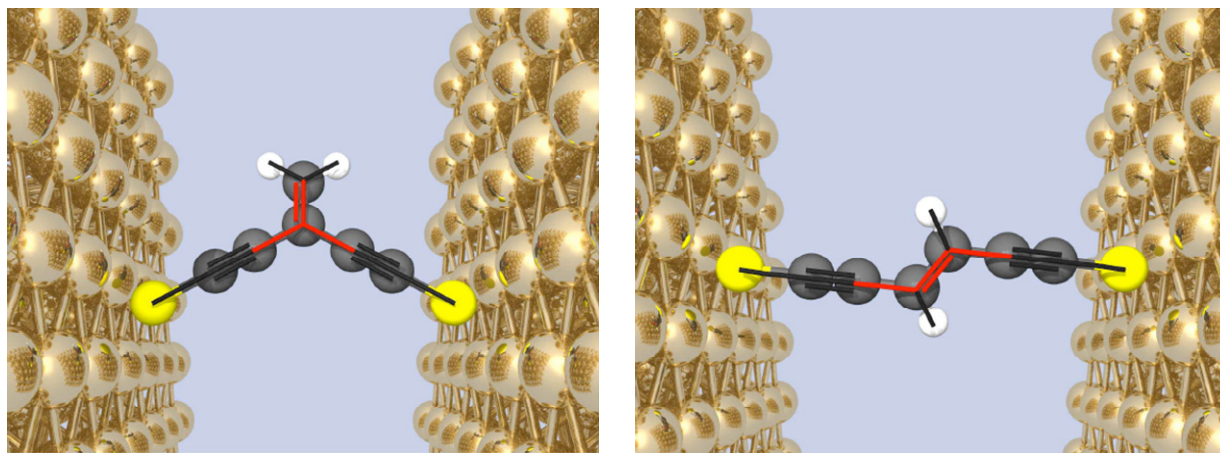


Figure 6-31. Resonance structures for a cross-conjugated molecule. The electron delocalization shown in b and d illustrate how in a three way junction the electron can only delocalize in 2 directions, there is no direct electron delocalization possible between atoms 1 and 5.

As an initial example of the unique behavior of cross-conjugated molecular junctions, we compare the transport behavior of a cross-conjugated molecule and a linearly-conjugated molecule shown in Figure 6-32. The transmission through these three molecules separated by symmetry into the σ and π components²³⁸ is given in Figure 6-33; the red curve gives the σ or π component and the black curve shows the total transmission (the sum of the σ and π transmissions). The cross-conjugated orientation of introduces the distinct antiresonance near the Fermi energy in the π component of the transmission, resulting in a number of unexpected consequences.



(a) A cross-conjugated bridge.

(b) A linearly conjugated bridge.

Figure 6-32. The bonding geometry of a molecule bridging source and drain electrodes controls whether the bridge is cross-conjugated or linearly conjugated.

At the Fermi energy the transmission through a shorter 5-carbon cross-conjugated chain is only a small fraction ($\sim 6\%$) of the transmission through the 6-carbon linearly conjugated chains. All the molecules are fully conjugated indicating that this results is in contrast with the usual trend that transmission decreases with increasing bridge length³³. Second, the transmission resonances occur at approximately the same energy in all three molecules yet there is a substantial difference in the transmission at energies between the resonances, again contrasting with the usual trend that transmission at the Fermi energy can be correlated with the energy gap between molecular orbitals²⁵⁰. Finally, in fully conjugated molecules it is generally the case that the coupling²⁵¹ and therefore low bias conduction are dominated by the π system, however for the cross-conjugated molecules the σ system dominates the transport

behavior near the Fermi energy. These unusual features in the zero-bias transmission while unique in transport calculations remain consistent with the weak coupling reported when cross-conjugated systems are used to bridge between electron donor and acceptor moieties.²⁴⁸

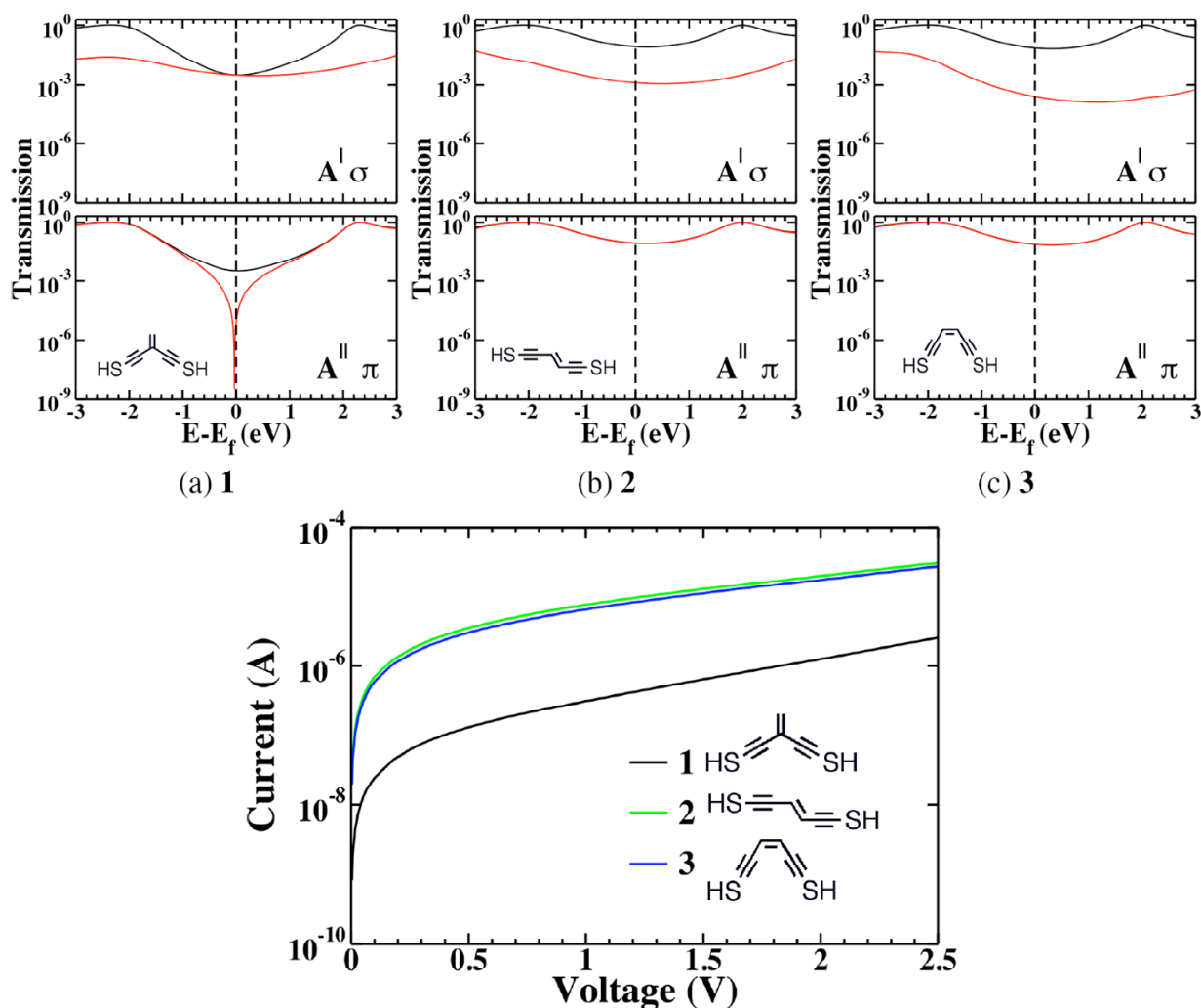


Figure 6-33. The transmission and current through a cross-conjugated molecule (1) compared with its linearly conjugated counterparts (2 and 3). In each case the total transmission is shown in black and the component through either the σ or π system is shown in red. The crossconjugated system has an antiresonance in the π transmission near the Fermi energy,

providing a local minimum in the transmittance, in contrast with the high level of transmission through the linearly conjugated systems.

6.8.1 Bond length analysis

The molecules shown in Figure 6-34 are used to illustrate the fundamental bond length differences between cross-conjugation, linear conjugation and saturated structures. It has been previously established that bond length and bond length alternation are correlated to π electron delocalization in both linear and cross-conjugation molecules.^{245,246,252} In this analysis we compare the bond lengths for 15 molecules with three different central bonding motifs; cross-conjugation, linear conjugation and a saturated carbon atom. Our analysis focuses on the delocalization of the charge between the sulfur atoms because this will be the direction of charge transport in a molecular junction. The cross conjugated molecules labeled 6-10 all have a double bond perpendicular to the direction of charge transport. Within this subset of molecules, 6, 7 & 9 meet the specific definition of cross-conjugation. Molecules 11-15 have a double bond connected in the trans orientation between the thiol terminations. Molecules 11, 12 & 14 are completely linearly conjugated between thiol groups. Molecules 1-5 are the same as molecules 6-10, but with hydrogen atoms replacing the cross conjugated double bond.

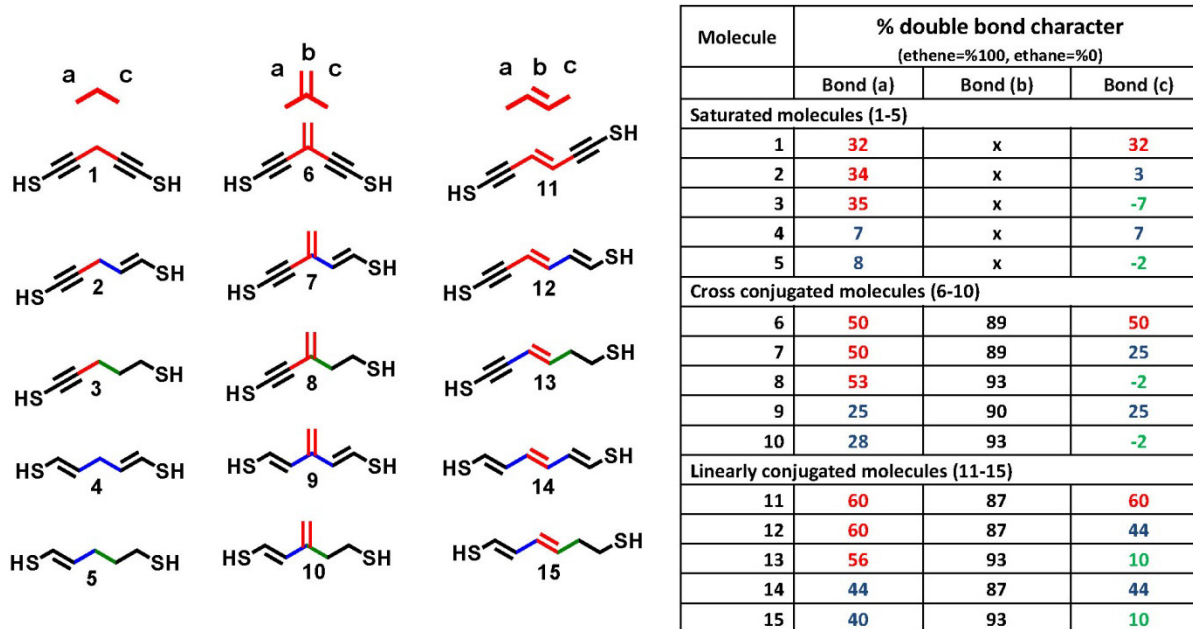


Figure 6-34. A bond length analysis for a series of molecules with sections of conjugated, non-conjugated and cross-conjugated carbon atoms. Red indicates bond a or c is bonded to an alkyne group, blue to an alkene group and green to an alkane group. By definition the ethane bond length has 0% double bond character and the ethene bond length has 100% double bond character. A negative bond length indicates a carbon-carbon bond longer than in ethane.

To simplify the comparison among so many molecules we focus on the bonds labeled **a**, **b**, and **c** in Figure 6-34. Bonds **a** & **c** are both formally single bonds and bond **b** is a double bond. The carbon single bonds are systematically longest in the molecules 1-5 and shortest in the molecules with linear conjugation, 11-15. The corresponding bond lengths in the cross conjugated molecules 6-10 are in-between the length of the saturated and unsaturated linear molecules. The changes in bond lengths agree well with previous studies completed on molecules 1,2,6,7,9.²⁴⁶

To compare the carbon single bond lengths we have calculated the percentage of double bond character. This is done by comparing all the bond lengths with those calculated for ethene and ethane. Ethene by definition has 100% double bond character and ethane has 0% double bond character. This bond length comparison shows that in a cross conjugated molecule the π electron delocalization is less than in a linearly conjugated molecule but greater than in a fully saturated carbon atom.

Using the bond length characterization to analyze this data, we come to three important conclusions. First, a cross conjugated molecule and a linearly conjugated molecule show different behavior with respect to electron delocalization. Second, in cross conjugated molecules the electron delocalization is reduced between the cross conjugated regions of the molecules, as is evident by the increase in both C-C bond lengths. The saturated C-C bond length only changes due to direct coupling to an unsaturated carbon. This effect is local and the bond length changes are largely a nearest neighbor effect. Within the three sets of molecules; 1-5, 6-10, and 11-15 the C-C bond lengths **a** & **c** remain weakly correlated to each other (except when required to match by symmetry in molecules 1,4,6,9,11 & 14), implying that the addition of the cross conjugated bond induces very little electron delocalization across the cross-conjugated carbon atom.

6.8.2 Transport through cross-conjugated molecules

To calculate the transport properties of cross conjugated molecules we look at a representative series of molecules from Figure 6-34, specifically molecules 4,5, 9, & 14. These molecules represent a complete series of double bonded molecules with cross-conjugation,

linear conjugation, and replacing the cross-conjugated unit with a saturated carbon atom or saturation of one double bond. Figure 6-35 shows a series of transmission spectra and I/V plots for this family of molecules. These calculations were completed in Hückel IV 3.0.^{39,209} The qualitatively similar plots calculated using ATK 2.0.4^{45,46,48,253} are shown in Figure 6-36.

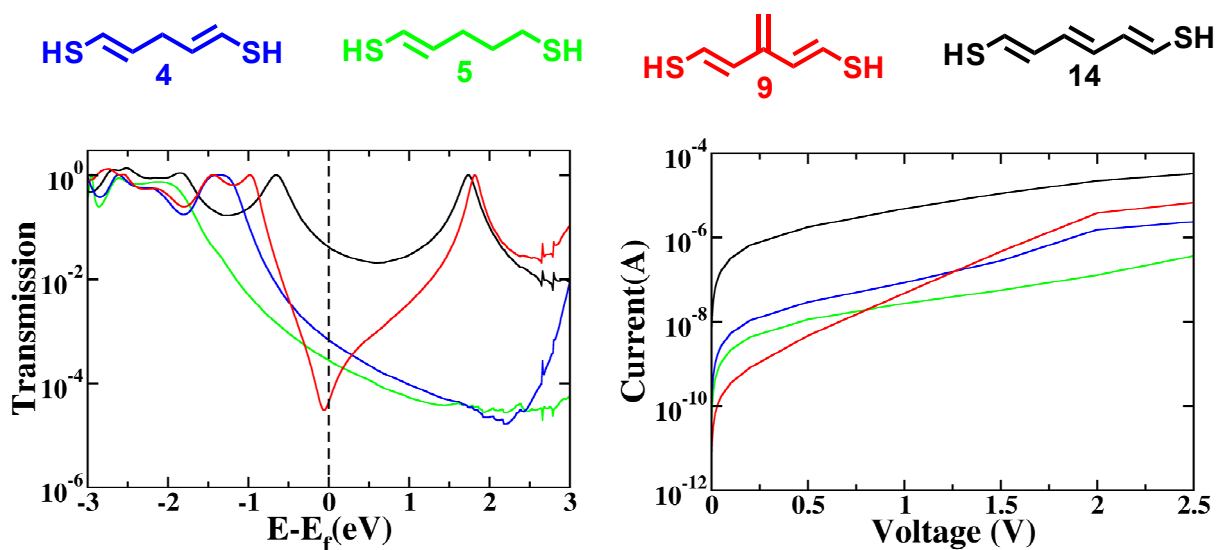


Figure 6-35. Transmission and current-voltage calculated in Hückel-IV 3.0 for molecules **4**, **5**, **9** and **14**. In the transmission plot shown on the left the cross-conjugated molecule **9** shows an interference feature at $E=0$. The corresponding current-voltage plot on the right shows that current through molecule **9** has a greater voltage dependence than molecules **4,5** & **14** (the deviation from linearly in molecule **9** is expounded upon in the supporting information).

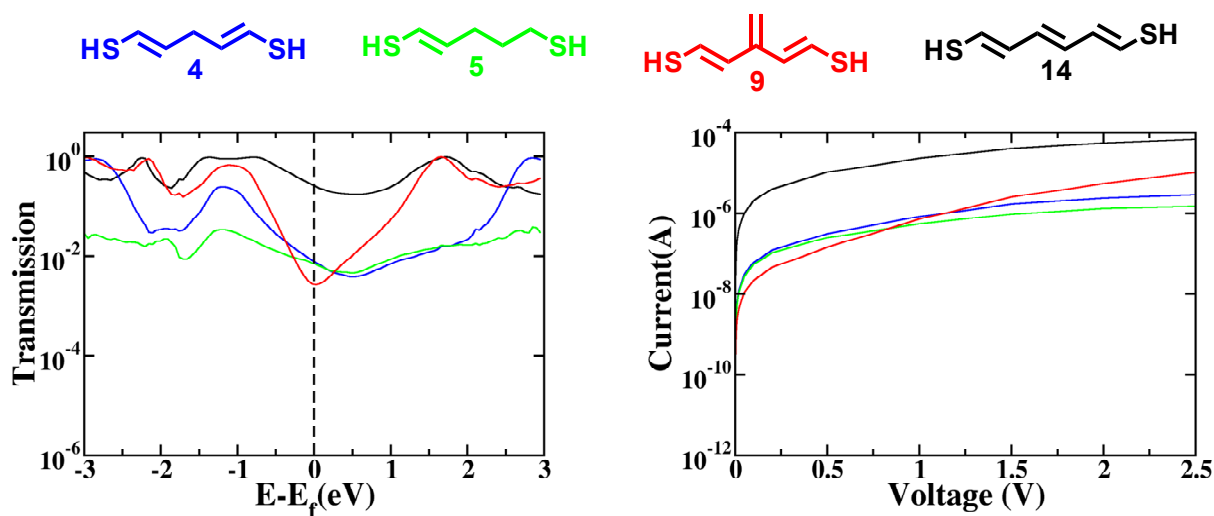


Figure 6-36. These plots show transmission and I/V calculated for the same molecules, 4,5,9 & 14, using ATK. The most striking disagreement between the codes is the depth of the transmission at $E=0$. The transmission and low bias current through all 4 molecules are approximately one order of magnitude higher in ATK vs. Hückel-IV. This order of magnitude difference is also borne out in our previous calculations.²²⁹ Experimental results should help rectify this disagreement.

The transmission plot for the cross conjugated molecule, **9**, has HOMO and LUMO molecular orbitals at similar energy and with similar transmission probability at resonance as the fully linearly conjugated molecular **14**. Yet at $E=0$ the transmission probability through molecule **9** is over three orders of magnitude lower. The transmission probability through the cross conjugated molecule **9** is also lower than through molecules **4** & **5**. This remarkable result occurs because of quantum interference: the coupling terms in the cross-conjugated unit cancel the π contribution to transport near the Fermi energy almost completely. In this examples there is complete destructive interference in the dominate π transport channel but there is still

transport through the σ channel. In the I/V plot shown on the right in Figure 6-35 the current through molecule **9** is the lowest at low voltage but increases at a higher non-linear rate than any of the other molecules. The molecules **4**, **5** & **14** behave more like resistors with approximately linear voltage dependence.

One of the most interesting features of cross-conjugated molecules is the non-linear voltage dependence seen in the I/V calculations (even at very small voltage) due to the interference feature. While most molecules will show non-linear voltage dependence upon approaching a molecular resonance, the behavior seen here is calculated at low bias voltage energetically separated from molecular resonance.

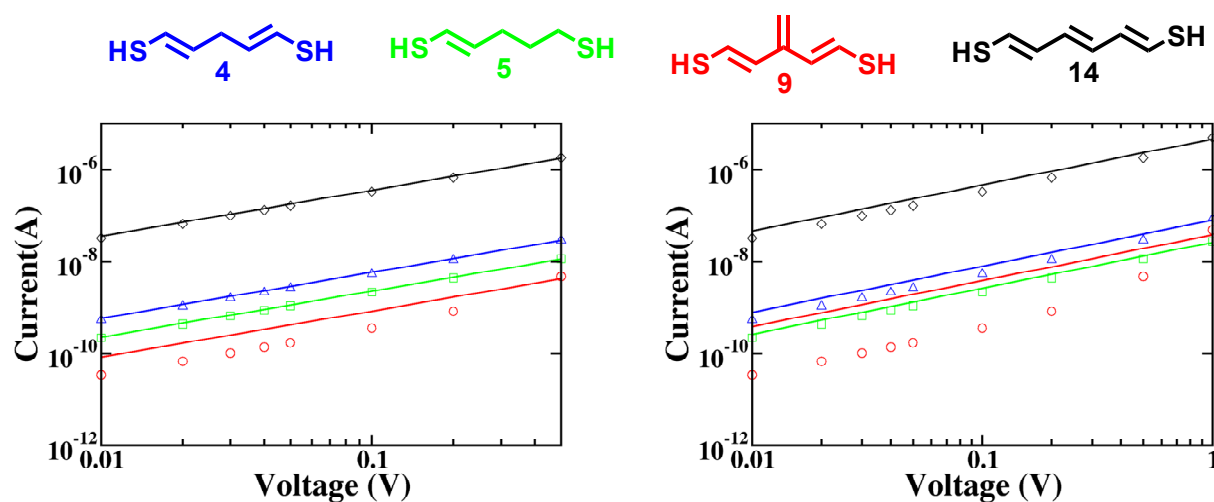


Figure 6-37. These two plots show a linear fit ($I=bV$) to the I/V data calculated using Hückel-IV shown on a log/log scale. In the plot on the left the fit is calculated for all data ≤ 0.5 Volts and in the plot on the right I/V data ≤ 1 Volt is included. In both cases where the data deviates from linearity the fit is controlled by the largest value (here at the highest voltage).

These results calculated are directly comparable to the results calculated using the I/V data from ATK. In ATK large deviation from linearity was seen only in the cross-conjugated molecule 9, for analysis that included data points for a bias from 100mV to 2.5V.

6.8.3 Cross-conjugation: breaking the rules

In the previous section we highlighted the unusual conductance characteristics of cross-conjugated molecules and illustrated that barrier-tunneling models fail to capture their properties. Here we show that interference features result in the breakdown of the conventional understanding of trends in molecular electron transfer.

In the last half century, understanding of molecular electron transfer has advanced significantly, building on the theories of Marcus^{30,183} and Hush^{32,254}. From this body of knowledge three “rules of thumb” for trends in rates of electron transfer can be deduced. **(1)** Increasing molecular length leads to decreasing rate. **(2)** Transport through a fully conjugated bridge is greater than through a saturated bridge. **(3)** A larger energy difference between the donor and acceptor energy levels and the bridge levels leads to decreased electron transfer rates.

This understanding of electron transport is also applied more generally to predict the behavior of molecules bound to electrodes in place of the donor and acceptor. The link between theories that describe these two regimes has been documented.²⁵⁵ Importantly, chemical trends are common amongst these methods. Here we will proceed in the electron transport regime; however, the conclusions that are made apply equally in intramolecular electron transfer.

To illustrate this behavior we calculate the transport through 3 systems shown in Figure 6-38. We consider two different binding orientations giving either a cross-conjugated²⁴⁴ path through the red group (referred to as the “short” system) or the linearly conjugated path through the green group (the “long” system). These systems are compared with 1,5-dithiopentane (“dtp”), a saturated molecule with the same length carbon chain as the short system. Using the “rules of thumb” for electron transport we would expect that conductance would scale as $dtp < long < short$.

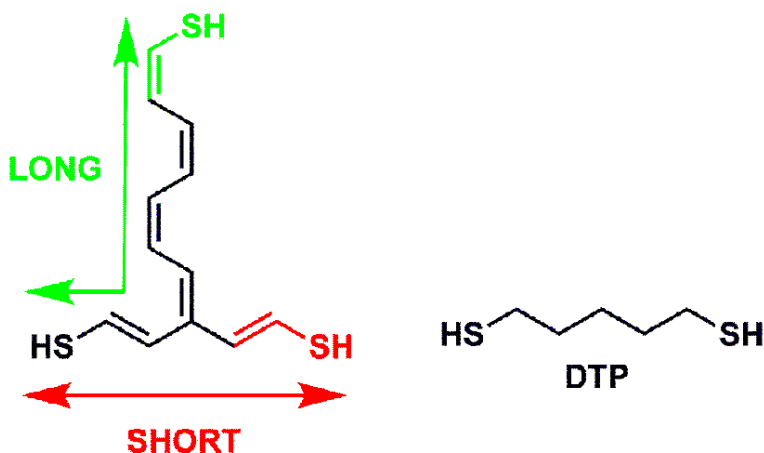


Figure 6-38. The “long” and “short” systems are defined as two different methods of attaching the molecule on the left to two gold electrodes. In both cases one electrode is attached to the thiol group shown in black; the long system utilizes the thiol shown in green and the short system the thiol shown in red. These are compared with dtp (right).

The spectrum of molecular orbital eigenenergies of the isolated molecules was calculated using gDFTB and is shown in Figure 6-39, with the gold Fermi energy set to -5eV. The molecules have C_s symmetry, allowing the molecular orbitals to be separated into A' and A''

symmetry groups, shown in black and red respectively. The A'' orbitals constitute the π -system of the long/short system. The striking disparity between the conjugated and saturated systems is the size of the energy gap between the highest occupied molecular orbital (HOMO) and the lowest unoccupied molecular orbital (LUMO). The fully delocalized HOMO and LUMO of the long/short system are also shown in Figure 6-39 with no indication of a difference in the electronic character of the two paths.

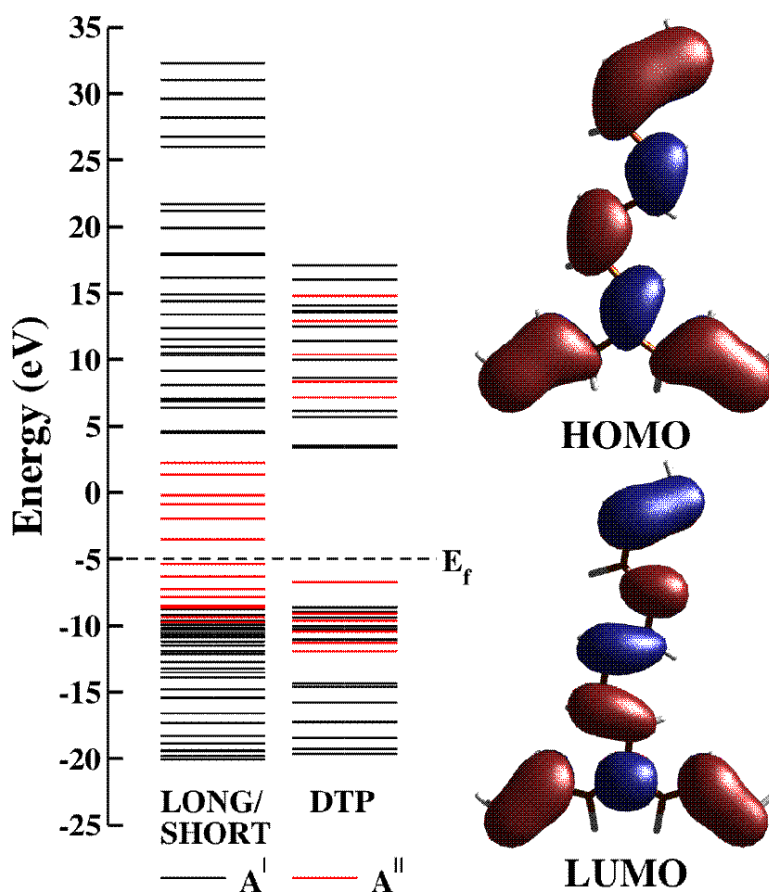


Figure 6-39. The molecular orbital eigenenergies for the isolated molecules (left) show the large band gap typical in the saturated system and the much smaller gap in the conjugated systems. The gold Fermi energy is shown for comparison. The HOMO and LUMO of the long/short

system (right) show delocalization across all three arms, giving no indication that there should be any difference between the different paths beyond their differing length.

Figure 6-40 shows the transmission and current through these three systems. The results show that near the Fermi level the transport scales as $d_{tp} < \text{short} < \text{long}$. The expectation is that transport through a conjugated molecule will be dominated by high levels of transmission through the π -system (A''). This is not the case for the short system, as a consequence of a destructive interference feature near the Fermi energy. As shown in the previous section, the σ -system transport defines the minimum in the interference feature.

Interference features have been documented for other molecules²⁴¹ and there are additional features evident in Figure 3. What is unusual about cross-conjugated paths, typified by the short system, is that there is an interference feature close to the Fermi energy and it is broad and deep.

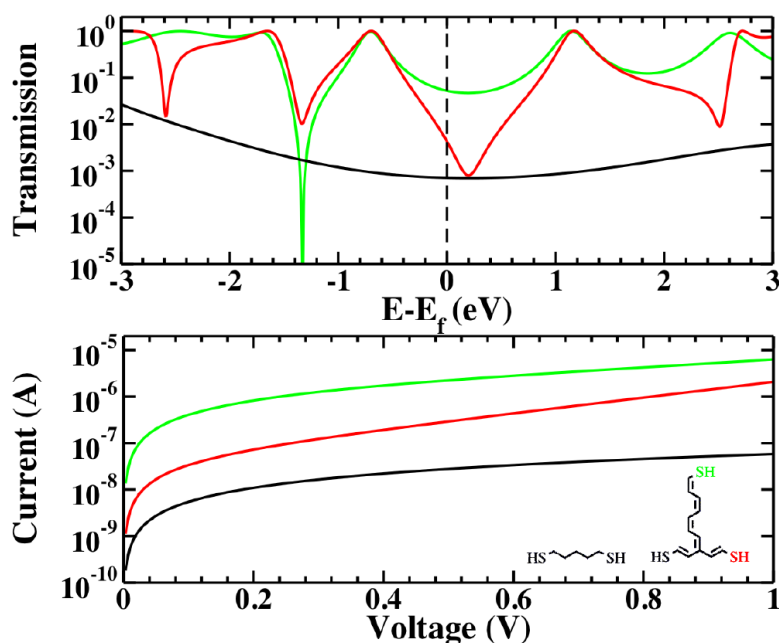


Figure 6-40. The transmission (left) and current (right) through the long system (green), short system (red) and dtp (black). The dramatic differences between the long system and the short system cannot be predicted from conventional understanding of molecular electron transfer.

The implications of these results can be clarified by an examination of each of the three “rules of thumb”. First, there are different path lengths through a similar molecule: the short and long paths through the same conjugated molecule. Conventional understanding would indicate that the transmission through the short system should be much higher (faster rate) than that through the long system; however, the opposite trend is the observed. In this case increasing length leads to an increase in rate.

Second, the differences in transmission through conjugated and saturated bridges can be examined. Unexpectedly, close to the Fermi energy, the transmission through the short system is only slightly greater than the transmission through dtp. Indeed, there are cross-

conjugated molecules that have lower transmission than molecules of the same length with saturated groups in the conduction path as shown in Figure 6-35. While in this case dtp does have lower transmission than the short system, the difference between the two is not nearly so large as would be expected. Further, if the Fermi energy of the electrodes occurred at the base of the trough of the interference feature, as it does in other cross-conjugated systems, these two systems would have very similar conduction characteristics at low voltage.

Finally, there is a comparison of the transmission through two systems with the same energy gap, the long and short systems. By virtue of comprising the same molecule, the molecular resonances for the long and short systems are energetically very close. Dtp on the other hand has a much larger energy gap. Usually, this would indicate that the transmission through the long and short systems was similar and both would be substantially greater than the transmission through dtp. Again, this is not the case. The energy of the frontier molecular orbitals fails to predict the difference in the current and transmission through the short and long systems.

These results clearly show how the established “rules of thumb” for understanding patterns in molecular electron transfer will not always hold. The “rules of thumb” for molecular electron transfer will continue to be of primary importance for understanding the properties of the great majority of systems. It is important to realize, however, how they can fail.

6.8.4 Bigger cross-conjugated molecules

The effect of the antiresonance features shown in the previous examples is mitigated due to the length of the molecules and the magnitude of the σ transport near the Fermi energy,

which defines the “floor” of the dip in the total transmission. The interference effect can be increased simply by lengthening of the molecule, and numerous extended cross-conjugated systems²⁵⁶⁻²⁵⁸ are suitable candidates. For example iso-polytriacylenes are rigid conjugated systems of variable length comprising multiple cross-conjugated units. To illustrate just how unusual the transmission characteristics of cross-conjugated molecules can be, we compare (Figure 6-41) 4 with its linearly conjugated counterpart 5, the partially conjugated 6 and the non-conjugated 7. 4, 6 and 7 all have the same number of carbon atoms in the backbone (20) and 5 is a structural isomer of 4.

Unexpectedly, there is 6 orders of magnitude difference in the transmission at the Fermi energy between 5 and 4, both fully-conjugated molecules. In fact, near the Fermi energy the transmission in 4 resembles 6 where the conjugation is broken with saturated groups throughout 6 the backbone. The comparison with 7 illustrates how the low voltage transmission through 4 is in fact closer to a fully saturated alkane than it is to a linearly conjugated molecule such as 5. The substantially longer length of these molecules compared with those shown earlier results in the σ system transport being orders of magnitude lower at the Fermi energy.

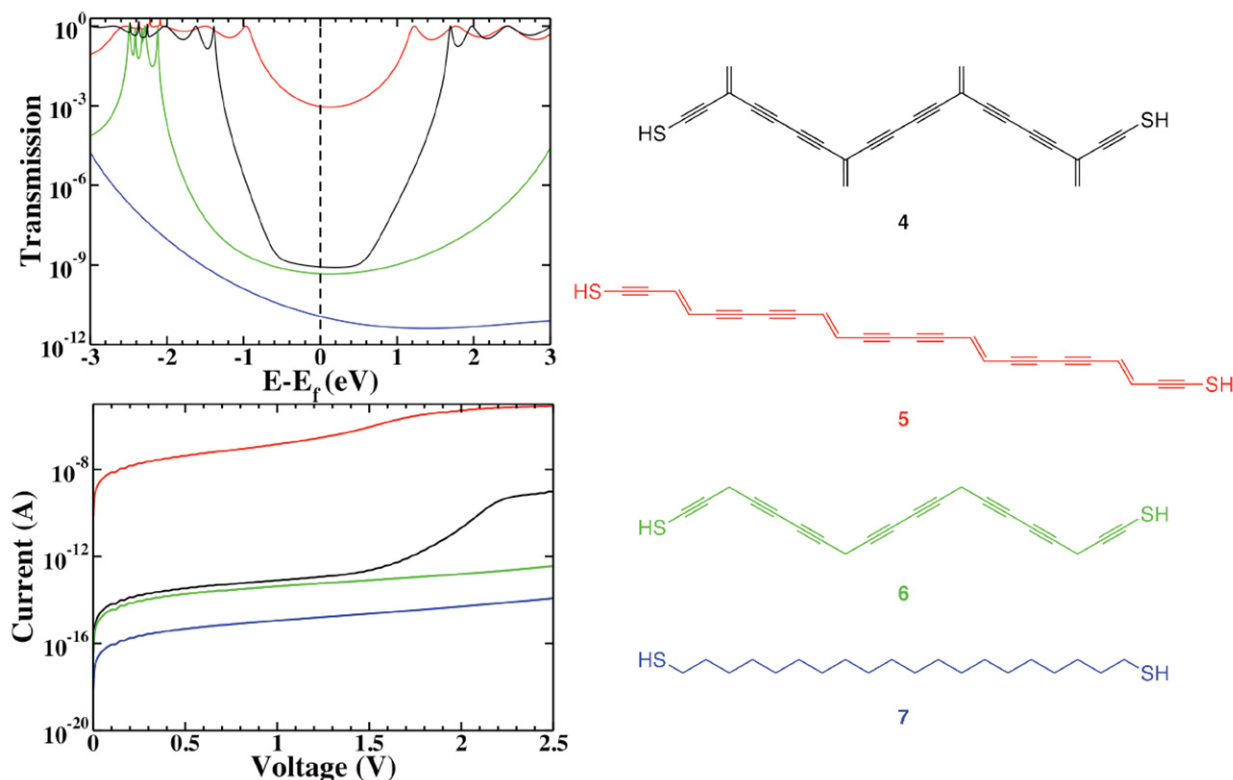


Figure 6-41. The zero bias transmission as a function of energy and the current as a function of voltage for a group of comparable molecules illustrating the unusual transport characteristics of a cross-conjugated system. Specifically, an extended cross-conjugated molecule (4) compared with its linearly conjugated counterpart (5) and with a partially conjugated (6) and a saturated (7) system of the same length.

The results presented using gDFTB are readily comparable to the results obtained using ATK and Hückel-IV. Figure 6-42 shows the transmission obtained from the three methods for the longer series of molecules. The most striking feature of this comparison is that across this diverse series of molecules, the general features of the transmission are common amongst all the crossconjugated molecules discussed here, however, the magnitude of the σ system

transport makes a dramatic difference to what can be seen in the total transmission. It is also important to note that this feature is not present when the conjugation is simply broken as is the case for **6**.

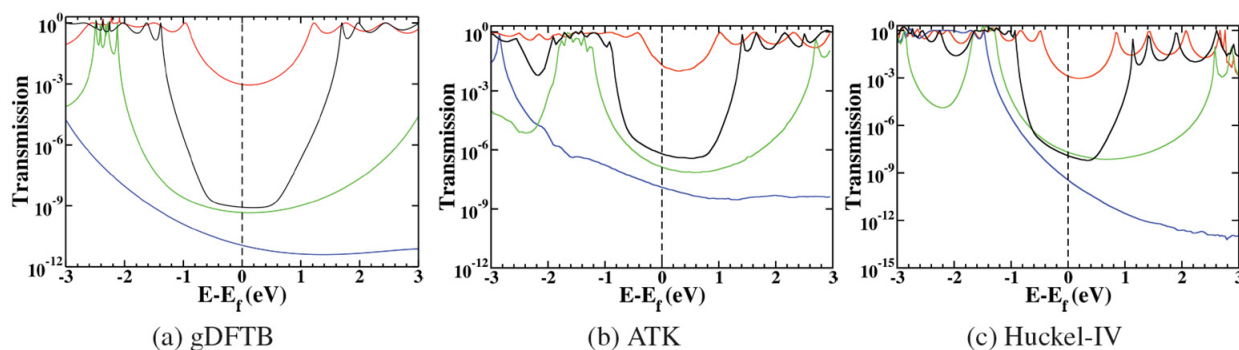


Figure 6-42. The zero bias transmission as a function of energy and the current as a function of voltage for a group of comparable molecules illustrating the similarity in the results obtained by three different theoretical approaches, gDFTB, ATK and Hückel-IV.

Despite the similarity in their representation, the adjacent single bonds in **6** differ from those in **4** as they are not part of a conjugated system. In that case, the π system transmission is low and broad and no interference features are evident, this is shown in the symmetry separated transmission for these molecules shown in Figure 6-44 and Figure 6-43. Simply breaking the conjugation does not provide the dynamic range of the cross-conjugated system because there is no energetically close resonance and the transmission is just low throughout the measurable range.

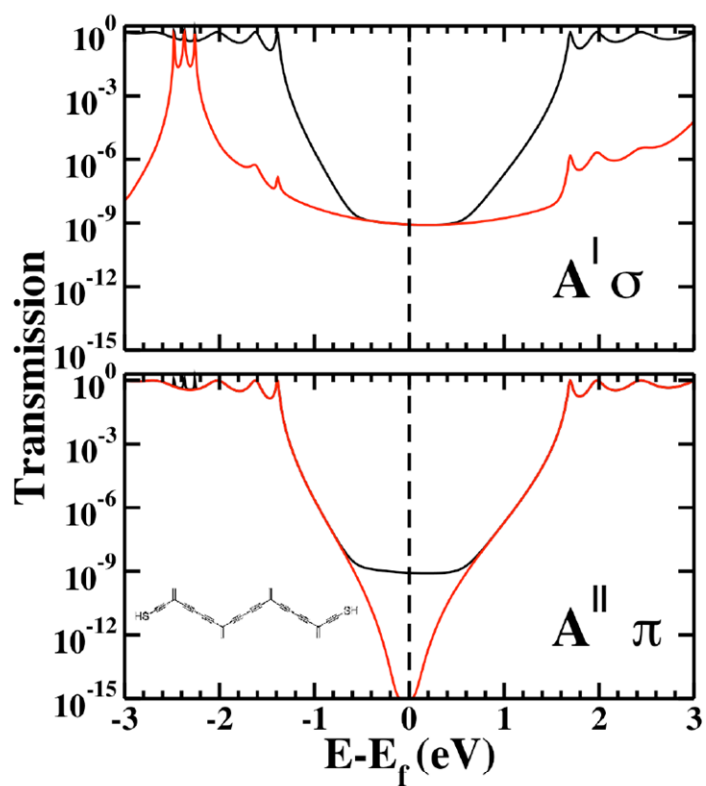


Figure 6-43. The transmission through 4 showing interference features in the π system transmission. The black traces indicates total transmission, the red traces indicate transmission through the σ system in the top plot and transmission through the π system in the bottom plot.

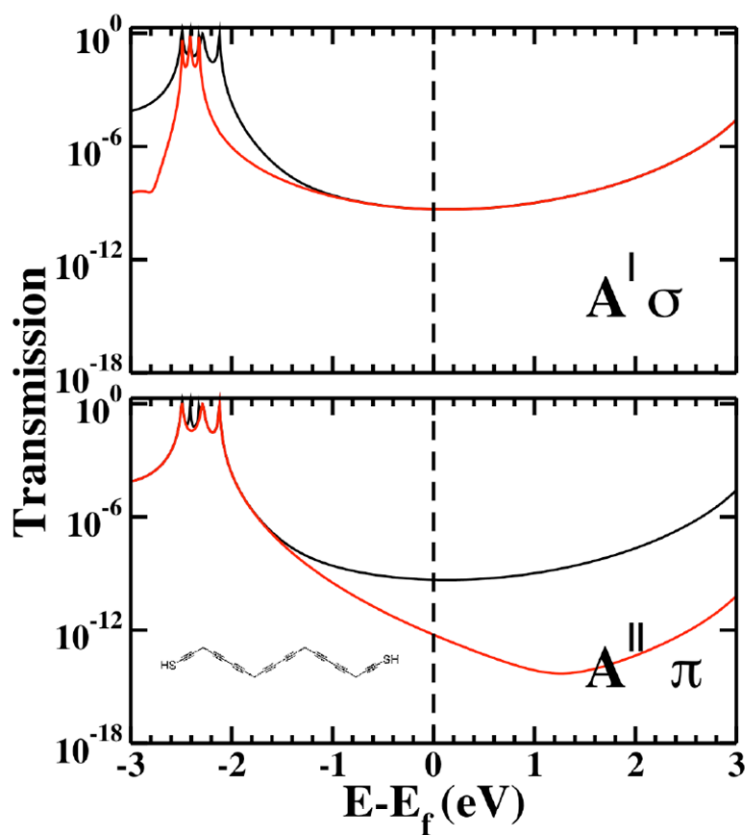


Figure 6-44. The transmission through 6 showing no interference features in the π system transmission. The black traces indicates total transmission, the red traces indicate transmission through the σ system in the top plot and transmission through the π system in the bottom plot.

Potential applications for cross-conjugated molecules can be envisaged from the dramatic current-voltage features in Figure 6-41. Over the 2.5V range considered, the current through 4 increases by ~ 5 orders of magnitude and in particular between 1.5V and 2.0V the current increases by 2 orders of magnitude. Such dramatic changes in the current over such a modest voltage range make this a promising candidate for a molecular switch with a potentially low operating bias and a large on/off ratio.

Cross-conjugated molecules owe their high conductance state to the π system transport, characterized by broad transmission resonances, as this system couples strongly with the electrodes. The low conductance state arises from σ system transport which is characteristically low at the Fermi energy and dominates the transmission spectrum only because quantum interference nearly destroys transmission in the π component. This crossover from low to high conductance as a result of electronic changes alone represents a new transport motif in single molecule electronics. In the low voltage regime, they are neither insulating nor conducting, but are intrinsically both.

6.9 Electronic dephasing

Interference stability is of primary importance for experimental measurement of the unique properties of cross-conjugated molecules. Electronic dephasing,^{259,260} frequently caused by fluctuations in molecular environment or geometry, might lead to decoherence of the transmitted electron and destruction of the interference feature.²⁶⁰ In earlier studies, we looked at how the traditional reactivity series in ortho, meta, and para benzene was examined, showing it to be able to be recast as an interference effect^{259,260} and how this effect could be erased by purely local dephasing.^{257,261} The calculation of transport dynamics is done using the quantum Liouville equation with dephasing included by reducing the magnitude of the off-diagonal elements of the density matrix (coherence).²⁶²⁻²⁶⁶ At $t=0$ all population is placed on the donor/source site while an absorbing boundary condition on the acceptor/drain site is used to simulate irreversible electron transfer. We have calculated the decay time necessary for the total system population to decrease to 5% of the initial value, shown in Figure 6-45. Our results

indicate that a dephasing strength of $\gamma > 100 \text{ cm}^{-1}$ is necessary for coalescence of the transport time through both 2 site models.

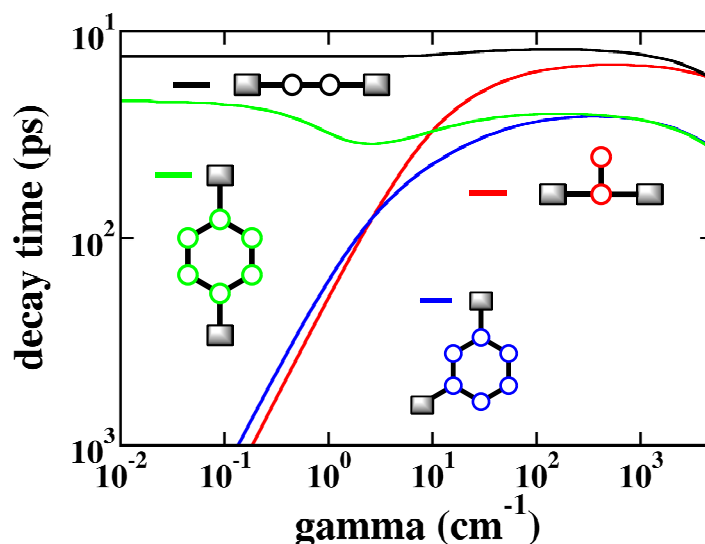


Figure 6-45. Electronic dephasing effects calculated for meta & para benzene compared with linear and cross-conjugated site representations. The decay time is defined as the time necessary for the total population to decrease 95%.

Measuring or estimating an absolute electronic dephasing strength can be difficult with estimates varying from 10's to thousands of cm^{-1} .²⁵⁶ However, the rate of dephasing between two sites will depend on the correlation function between site energies.^{267,268} Indeed, the true dephasing strength for a cross conjugated unit will likely be quite weak, as the stochastic fluctuations in site energy and inter-site communication will likely be strongly correlated within the small cross conjugated unit as the unit is of the same dimension as the individual solvent molecules. The physical processes behind the estimates of dephasing strengths are largely from energy fluctuations from uncorrelated solvent motions between distal molecules in the

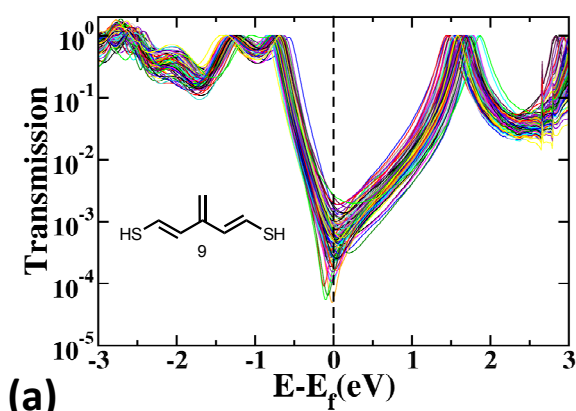
case of photon echo experiments²⁶⁵ or the fluctuating energy gap between ground and excited states in resonance Raman experiments.¹⁸¹ Contrasting these uncorrelated energies with the largely correlated site energies in the small cross-conjugated unit suggests these above estimates should be regarded as an upper limit for dephasing strength.

For comparison, the level of dephasing required for erasing the effect of interference on transport in benzene, a similarly sized molecule to the cross-conjugated unit, is significantly smaller, yet these interference effects persist, have been experimentally measured,^{65,67-69,127,269} and dominate the substitution chemistry of phenyl compounds. Consequently, we believe that the transport interference calculated in cross conjugated molecules will survive electronic dephasing.

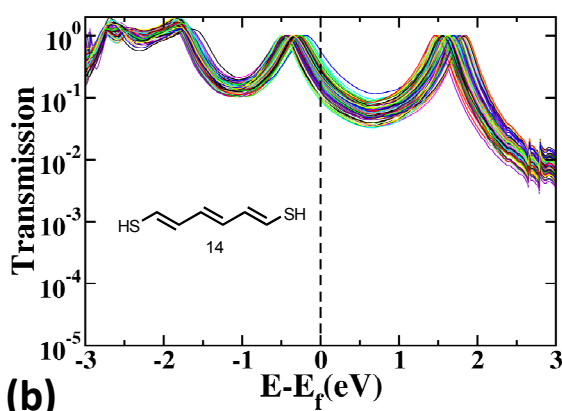
6.10 Molecular dynamics

The transport through a molecule would ideally be constant despite room temperature molecular vibrations and binding site fluctuations. Experimental measurements on single molecule conductance have primarily been made using Au electrodes.^{68,69,128} The Au surface is quite mobile and the distribution of conductance values through a sulfur terminated molecule can be quite large. This variation has been well studied both experimentally and theoretically, with typical distributions of $\pm 60\%$ in conjugated molecules on Au surfaces.²³⁷ The unique conductance characteristics of cross-conjugated molecules are a local effect and should be independent of variations in electrode coupling. To study the interference stability, molecular dynamics simulations have been used to give a thermal geometric distribution.¹⁶⁵ We focus our analysis on the effect of internal fluctuations on the conductance of the molecule. A 1ns

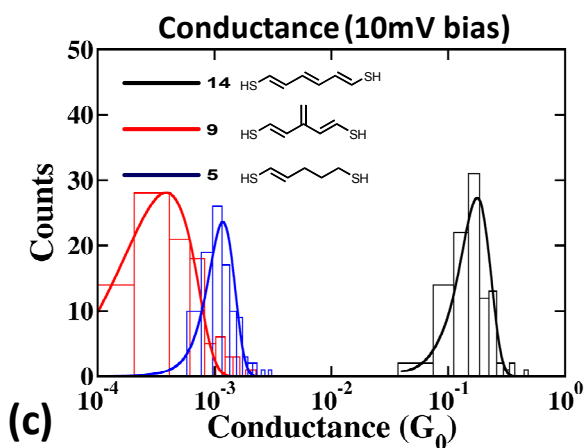
trajectory was run to fully equilibrate the system. For the next 100ps, a snapshot was taken every 1ps and the geometry was parsed. Figure 6-46 (a) and (b) show the transmission plots calculated in Hückel IV 3.0 for 100 geometries for a cross conjugated molecule and a comparable linearly conjugated molecule. The interference calculated in the cross conjugated molecules is stable to geometric fluctuations. The variation in conductance is on the same order of magnitude in all three molecules representing a fully conjugated molecule, a cross-conjugated molecule and a molecule with saturated carbon atoms.



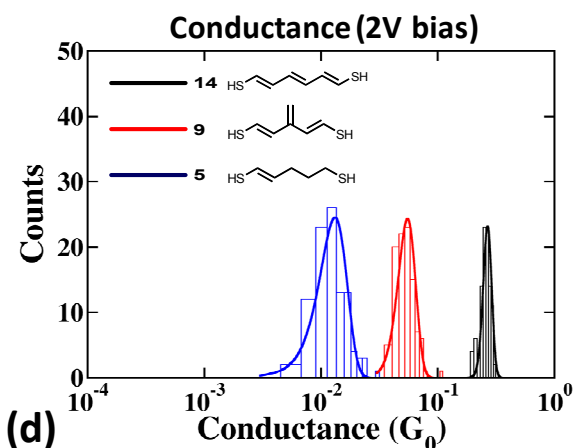
(a)



(b)



(c)



(d)

Figure 6-46. Molecular dynamics results for molecules **5,9,14**. Plot (a) and (b) show 100 transmission traces calculated for molecules **9** and **14**. Plots (c) and (d) show Gaussian fits to the distribution of conductance values calculated at 10mV and 2V.

The statistical conductance distribution is seen in Figure 6-46 (c) and (d) which show a Gaussian fit to a histogram of the transport calculated through 100 molecular geometries. The histogram bin width is set to $2 * \text{interquartile range} * \text{number of data points}^{-(1/3)}$ allowing a direct comparison of the Gaussian fits.^{181,224,242,270,271} The conjugated molecule **14** has a 1.5x increase in conductance when the current is increased from 10mv to 2 volts. The molecule with saturated atoms **5** has a 10x increase in conductance while the cross conjugated molecules **9** shows a > 90x increase in conductance. Together, the dephasing calculations and the molecular dynamics simulations provide strong evidence that actually measuring the transport through cross-conjugated molecules will show the effects of interference features.

Molecular dynamics simulations have also been completed on the extended molecules presented in section 0. The antiresonance in larger molecule, 4, is also present when thermal motion is accounted for by using the geometries obtained from a molecular dynamics simulation completed using Tinker. The last fifty 1-ps snapshots of the 1-ns simulation are used as input files for Hückel IV. Figure 6-47 shows the transmission obtained from the 50 molecular geometries. In the geometric space sampled through molecular dynamics the antiresonance remains.

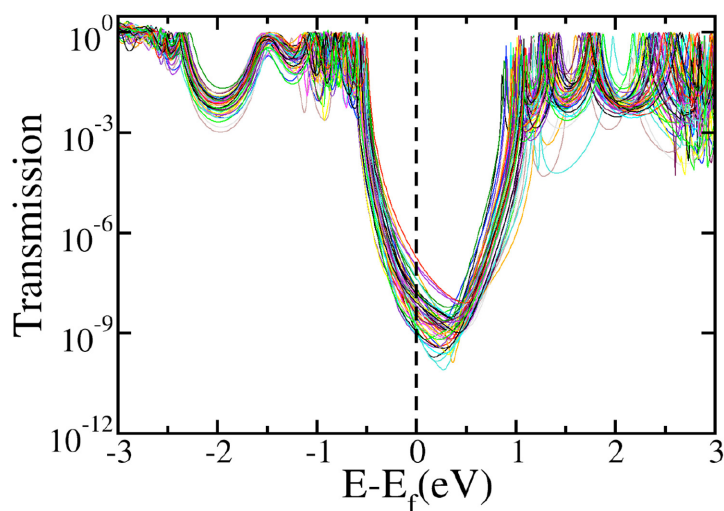


Figure 6-47. The transmission through 4 for 50 different geometries obtained from molecular dynamics calculations. Importantly, the antiresonance is present in all cases.

6.11 Controlling interference features

Having established that cross-conjugation leads to quantum interference that is stable to thermal fluctuations, we look at how the interference feature can be tuned in terms of depth and energetic locations. In Figure 6-48 we show two series of molecules with increasing carbon backbone length. In (a) we add a pair of triple bonds symmetrically to a cross-conjugated molecule. Shown in (b) is a series of molecules where the cross-conjugated backbone has been synthesized,^{245,246,248,252} with an increasing number of cross-conjugated units separated by triple bonds. Comparing the position of the HOMO and LUMO for both sets of molecules, shown in (a) and (b), there is a noticeable difference between the shift in energy of the resonances near -1eV and 1eV. In (a), the addition of two triple bonds to the molecule increases the length of electron delocalization and decreases the HOMO-LUMO gap spacing. In (b), with the addition of a cross-conjugated bond and a triple bond the HOMO level remains unchanged and the

LUMO orbital shifts slightly lowering the energetic gap. This behavior is indicative of the cross-conjugated unit breaking electron delocalization.²³⁸

As the depth of interference features in cross-conjugated molecules is determined by the σ transport, we need only lower the σ coupling across the molecule to lower the interference minimum. In (a), the increased electrode separation caused by the addition triple bonds results in a relatively small reduction in the interference minimum. In (b), the transmission minimum decreases ~ 1.5 orders of magnitude and the interference width increases for each 3 carbon atom repeat unit added. This is a much greater sensitivity to length than in (a) where each pair of triple bonds decreases the transmission ~ 0.3 orders of magnitude for each repeat unit.

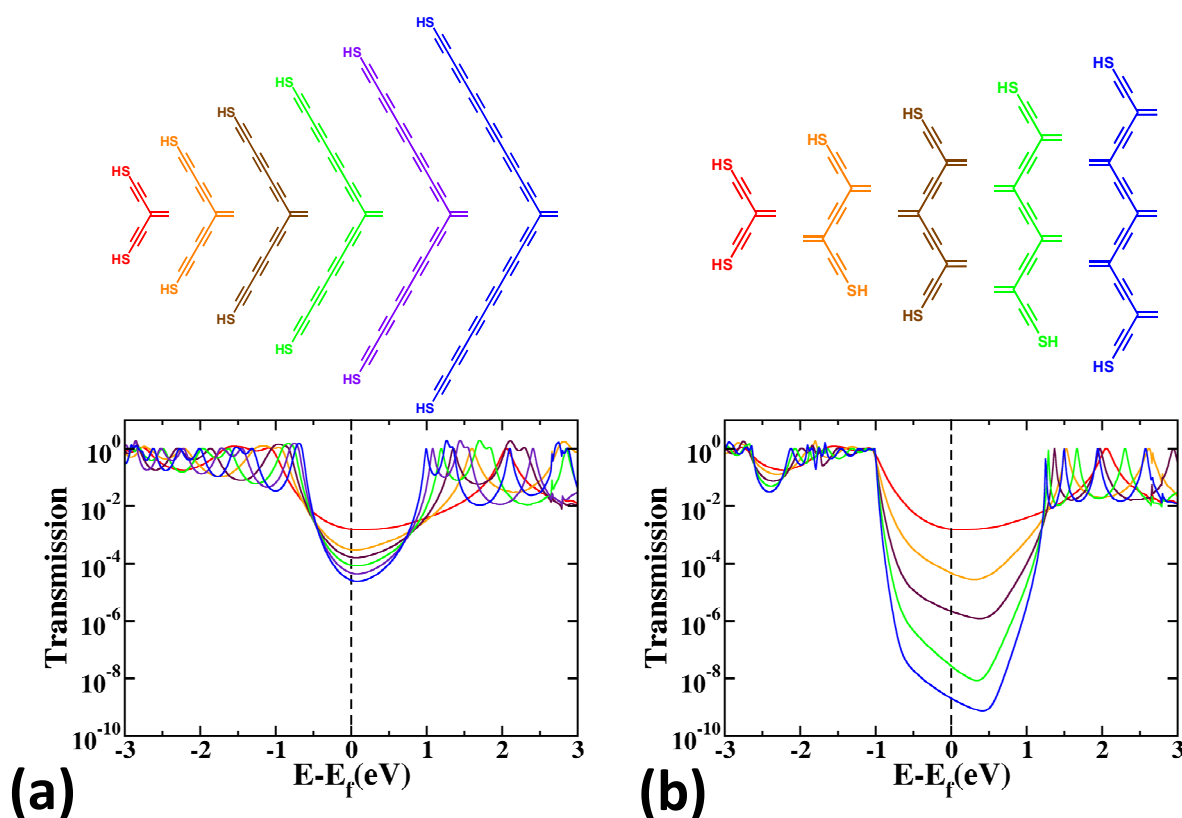


Figure 6-48. Tuning the depth and width of a molecular interference feature. (a) and (b) show the behavior of the HOMO and LUMO energies and the interference minimum with increasing molecular length. In the series of molecules shown in (a), one triple bond and one single bond is added to each end of the molecule. This increased conjugation length leads to a smaller HOMO-LUMO gap and a small decrease in the transmission minimum. In (b), a cross-conjugated unit and a triple bond are added leading to little change in the HOMO-LUMO gap but a large decrease in the transmission minimum.

To address the different behavior of these two classes of molecules, we calculated the transmission for a series of molecules with 17 carbon atoms in the backbone, shown in Figure 6-49(a). All plots in Figure 6-49 are calculated in the gDFTB code so that a symmetry

analysis^{214,229} could be performed. From the plot shown in Figure 6-49 (a), it seems that an increasing number of cross-conjugated units increases both the width and depth of the interference feature. To separate the contributions from decreasing σ coupling across the molecule and the increasing number of cross-conjugated units, we have included a plot of the σ transport through all 4 molecules (c). This plot indicates that it is the σ transport and not the number of cross-conjugated units that defines the transmission minimum. Thus, at low bias it is possible to directly measure the σ transport in conjugated molecules. Cross-conjugated molecules may thus provide a template for studying σ transport through bridged molecules, including alkene, alkyne, and aryl systems.

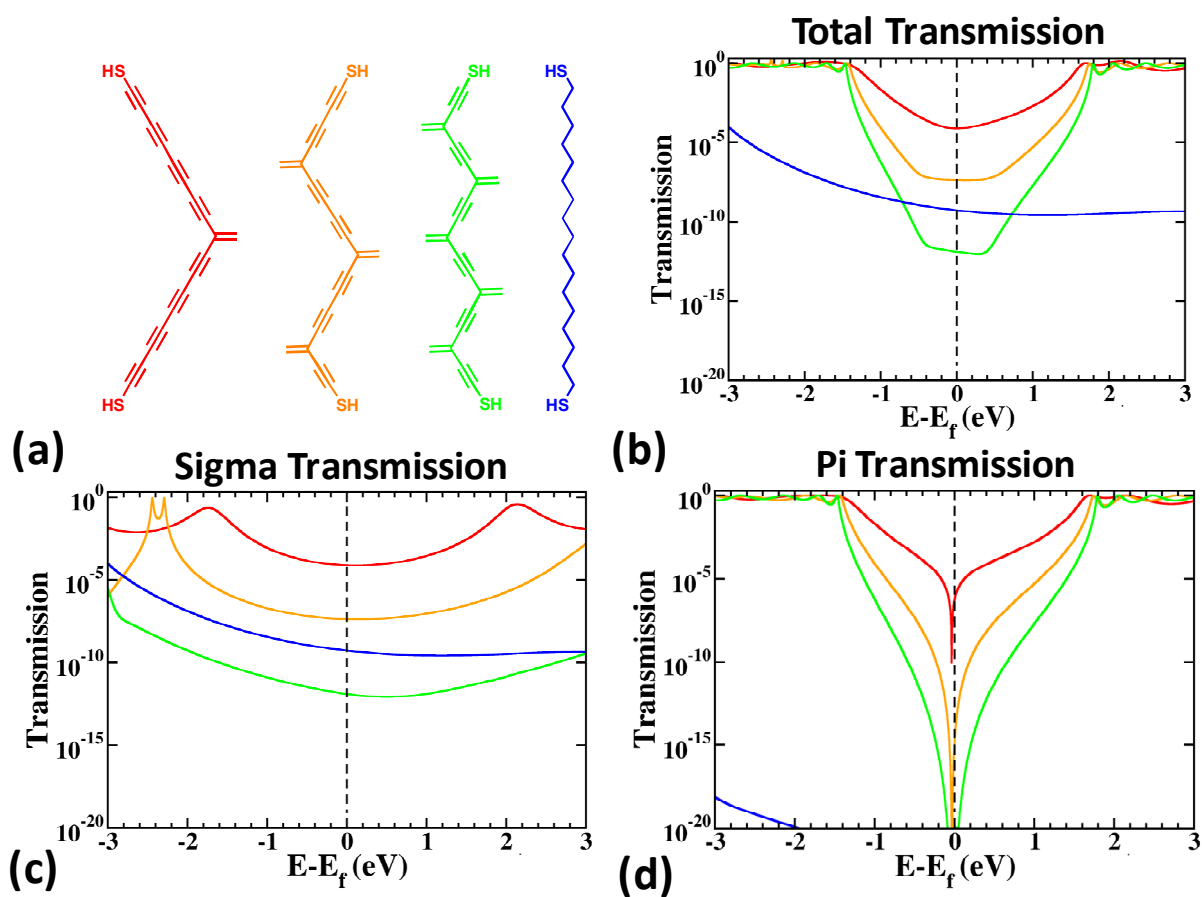


Figure 6-49. All calculations in this plot were done using gDFTB to differentiate between the σ and π transport. In (a), four molecules with a 17 carbon atom backbone are shown: three conjugated molecules with 1, 3, and 5 cross-conjugated units, and one saturated carbon chain. In (b), the total transmission through the 4 molecules is shown with ~ 8 orders of magnitude variation in transmission at E_f . In (c), the σ transmission at E_f decreases ~ 2 orders of magnitude for each added cross-conjugated bond. The kinks in the carbon backbone in the cross-conjugated molecule decrease the σ coupling. The π component of the transmission is shown in (d). What can be seen is that both the depth and width of the interference feature increases with added cross-conjugated units.

To simplify the symmetry analysis in gDFTB in terms of the σ and π contributions the calculations were done with the sulfur atom above the bridge site in the Au electrode surface.

Figure 6-50 shows a comparison of the results calculated using gDFTB and Hückel-IV.

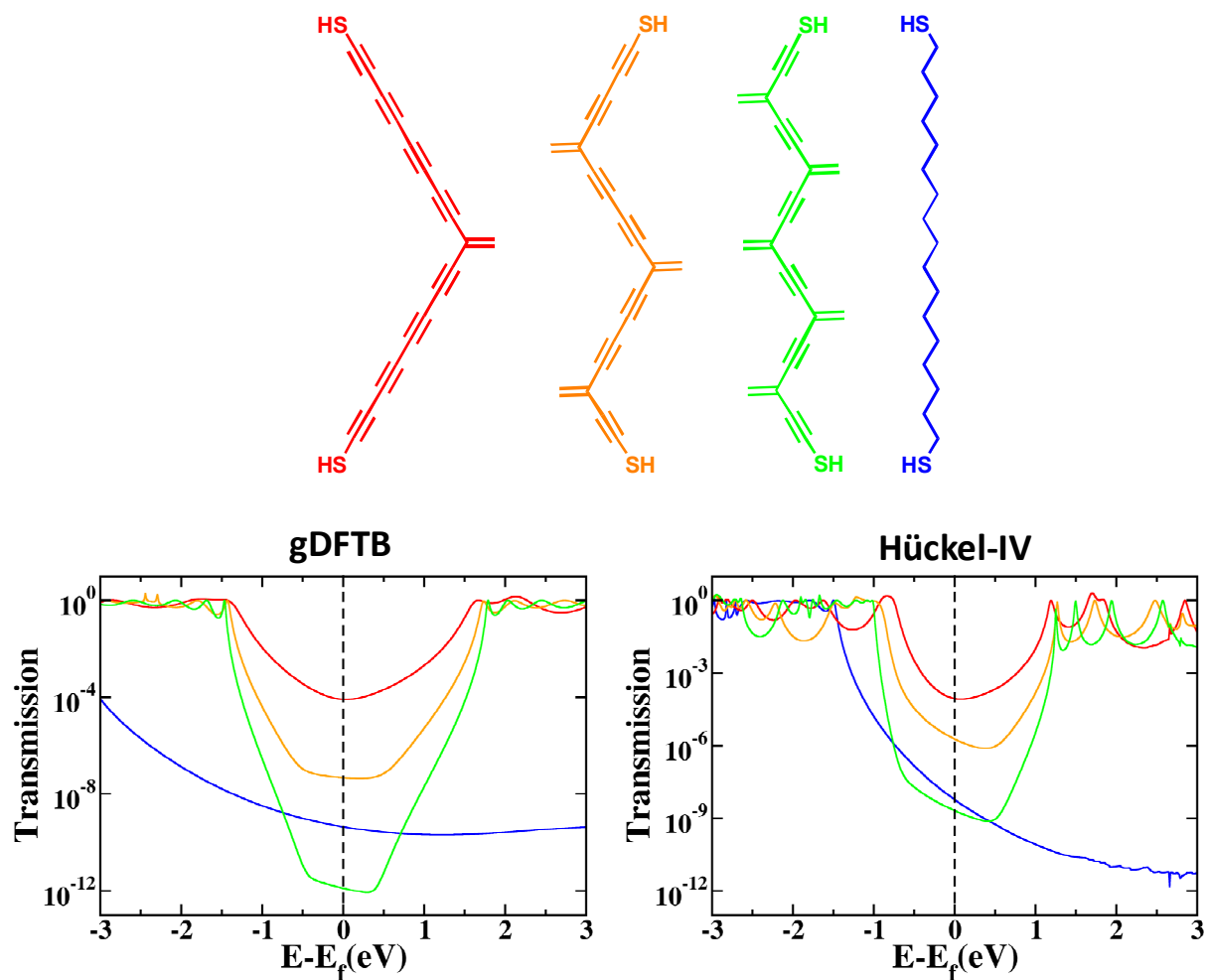


Figure 6-50. This plot gives a comparison of the transmission results for the 4 molecules shown above calculated in gDFTB and Hückel-IV. The line shape of the interference feature and the location of the resonances shifts between the codes but the underlying structure and conclusions made in the text remain constant.

6.12 Transistor Design

We have calculated the dynamic range in transmission probability accessible near the Fermi level to be ~ 9 orders of magnitude.²²⁹ This interference behavior opens the possibility of having a molecule that acts like an insulator (alkane) at low bias and a π conjugated molecule at slightly higher bias. The position of the HOMO and LUMO levels are unchanged with respect to other conjugated molecules, thus it is conceivable to design a molecule with a small HOMO-LUMO gap and extremely low mid-gap conductance due to quantum interference. This behavior matches well with the specifications that we showed earlier in Figure 6-3 and Figure 6-4.

6.12.1 Tuning the interference location: Simulated gate control and switching

To investigate the sensitivity to changes in electron density, we investigate the effects of attaching electron withdrawing and electron donating groups. These calculations are all performed using Hückel-IV. Using a known molecular scaffold²⁴⁰ with a single cross-conjugated unit, we calculated the change in transmission upon binding a series of electron donating and electron withdrawing groups to the cross-conjugated unit.

Figure 6-51(a) shows the effect of increasing electron withdrawing strength groups bonded to the cross-conjugated unit. The electron withdrawing groups have two major effects on the transmission near the Fermi level. The first effect is the movement of the LUMO from $\sim 1.5\text{eV}$ for the hydrogen terminated cross-conjugated molecules to $\sim 0.4\text{eV}$ for the NO_2 substituted molecule. This correlates with a similar shift in the interference feature to lower energy. In the CHO and NO_2 substituted molecules, the interference feature is seen at an

energy below the HOMO molecular level. The low bias conductance for these molecules changes by $\sim 10^3$ with increasing electron withdrawing strength.

In Figure 6-51 (b), the electron donating groups provide similar behavior to the electron withdrawing groups, but in the opposite energy direction. In most cases both the HOMO and LUMO shift to higher energy. The one exception to this is the phenyl substituted group shown in blue, where the increased electron delocalization provided by the aryl ring narrows the HOMO-LUMO gap. In all of the molecules with electron donating substituents, the interference features shift to higher energy and towards the LUMO molecular orbital. These calculations suggest that the interference feature is broadly tunable across the HOMO-LUMO gap region. In designing molecular devices, this broad tunability should allow alignment of the Fermi level with the interference minimum, providing an off state at zero voltage bias. To aid in experimental studies, we have included a section calculating the transmission through cross-conjugated molecules with a variety of capping groups used in the synthetic literature for cross-conjugated compounds as shown in Figure 6-52.³⁹

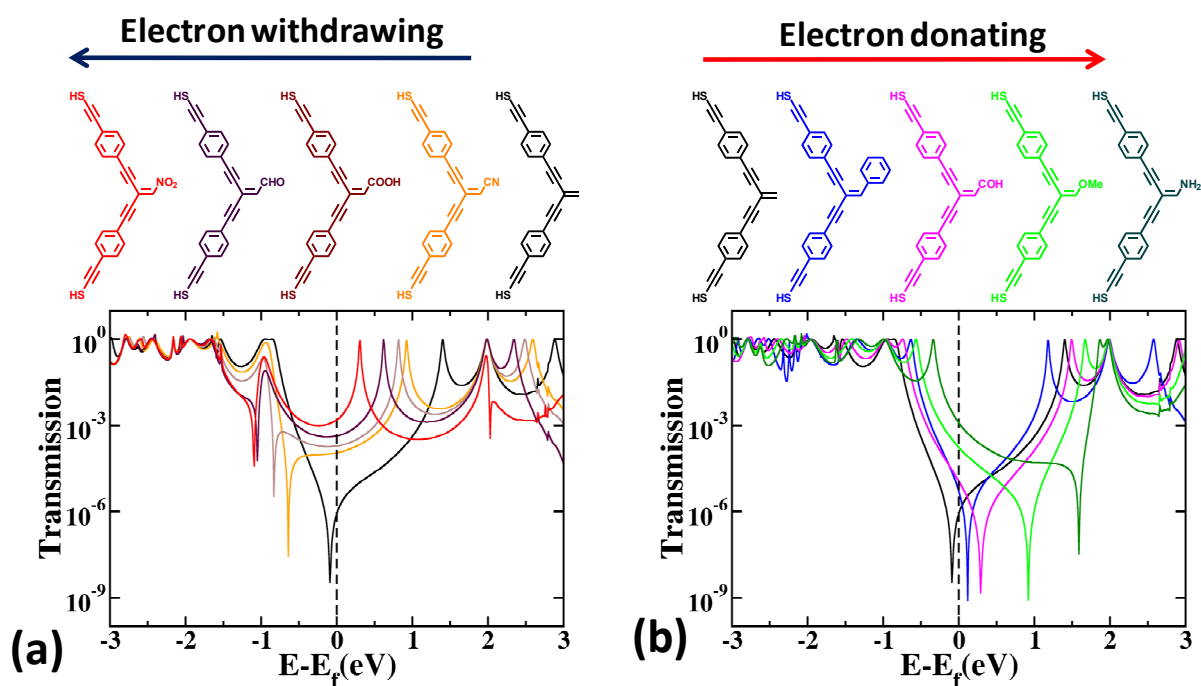


Figure 6-51. Electron donating and withdrawing groups attached to the cross-conjugated unit.

The interference feature is shown to be tuned $\pm 1.5\text{eV}$ from the Fermi level by changing the electron density on the cross-conjugated bond. The qualitatively similar results calculated using ATK are given in the supporting information.

6.12.2 Interference depth and the relative position of the Fermi level

One uncertainty in molecular electronics calculations is the position of the Fermi level with respect to the frontier molecular orbitals. In early versions, the Hückel IV transport code the Fermi level was designed to be a user adjustable parameter.²⁷² A recent measurement of the Seebeck coefficient in a Au-benzenedithiol-Au molecular junction calculated from experimental values the energy gap between the Fermi level and the HOMO the molecular orbital.²⁴⁰ There still remains a reasonable amount of uncertainty in the exact location of the

Fermi level with respect to the frontier orbitals. In experiments using different leads, or even different molecules, the position of the Fermi level in the HOMO-LUMO gap is expected to shift.

A difficulty in calculating the Fermi level with respect to the frontier molecular orbitals is the great sensitivity to small charge transfer from the leads to the molecule. This sensitivity is compounded by the fact that in most cases the low bias conduction is not overly sensitive to the position of the Fermi level. In designing functional molecular devices utilizing the properties of cross conjugated molecules, it will most often be ideal to have the Fermi level line up with the minimum of conductance, or the valley of the interference feature. In the two plots shown in Figure 6-51, electron donating and electron withdrawing groups attached to the cross-conjugated unit shifted the antiresonance $\pm 1.5\text{eV}$ from the Fermi level. With the low bias transmission probabilities sensitive to the position of the Fermi level it seemed pertinent to investigate the effects side groups that have been attached off the cross-conjugated bond.

The transmission properties for a series of molecules with different synthetic functional groups off the cross-conjugated unit are shown in Figure 6-52. All of these functional groups have been synthesized attached to cross-conjugated molecules,²⁴⁰ but not necessarily on this exact molecule. These results should be general for different cross-conjugated molecules. What we can see from looking at Figure 6-52 is that the hydrogen terminated cross-conjugated molecule shown in black in both plots is always at the lowest energy. Substitution off the cross-conjugated unit moves the antiresonance to higher energy. This is true when looking at the position of the antiresonance as a percentage of the distance between the HOMO and LUMO molecular orbitals. The shift in the position of the interference feature is found to be

uncorrelated to the length of the cross-conjugated double bond. In comparison with the results presented in Figure 6-51 the interference shifts to higher energy would indicate that all of these functional groups have a similar effect to the electron donating substituents.

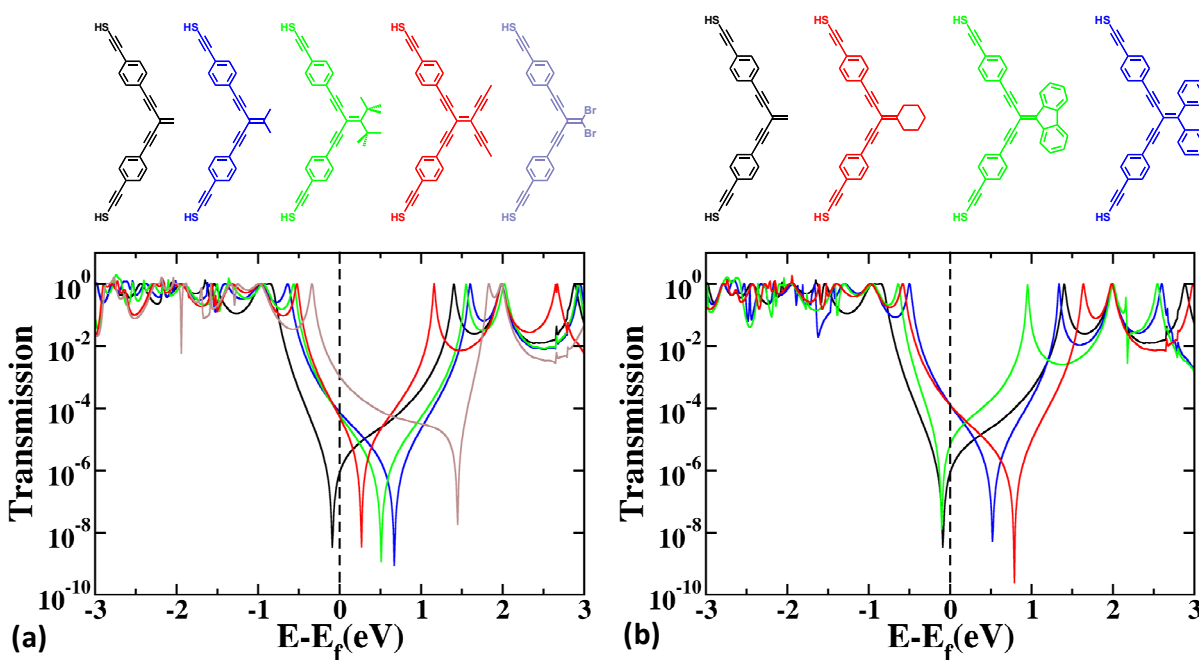


Figure 6-52. The shifting of the interference location by changing the substituents. These chemical groups attached to the cross-conjugated unit have been used in the synthesis of various cross-conjugated molecules.^{87,273,274}

We have plotted the effect of the electron withdrawing and donating groups calculated in both ATK and Hückel-IV. Again we see a good qualitative agreement between the transport codes. The major difference in the results that we calculate between the codes is the magnitude of the interference dip. This magnitude difference is consistent throughout our calculations and is attributed to the increased electron delocalization in density functional theory.

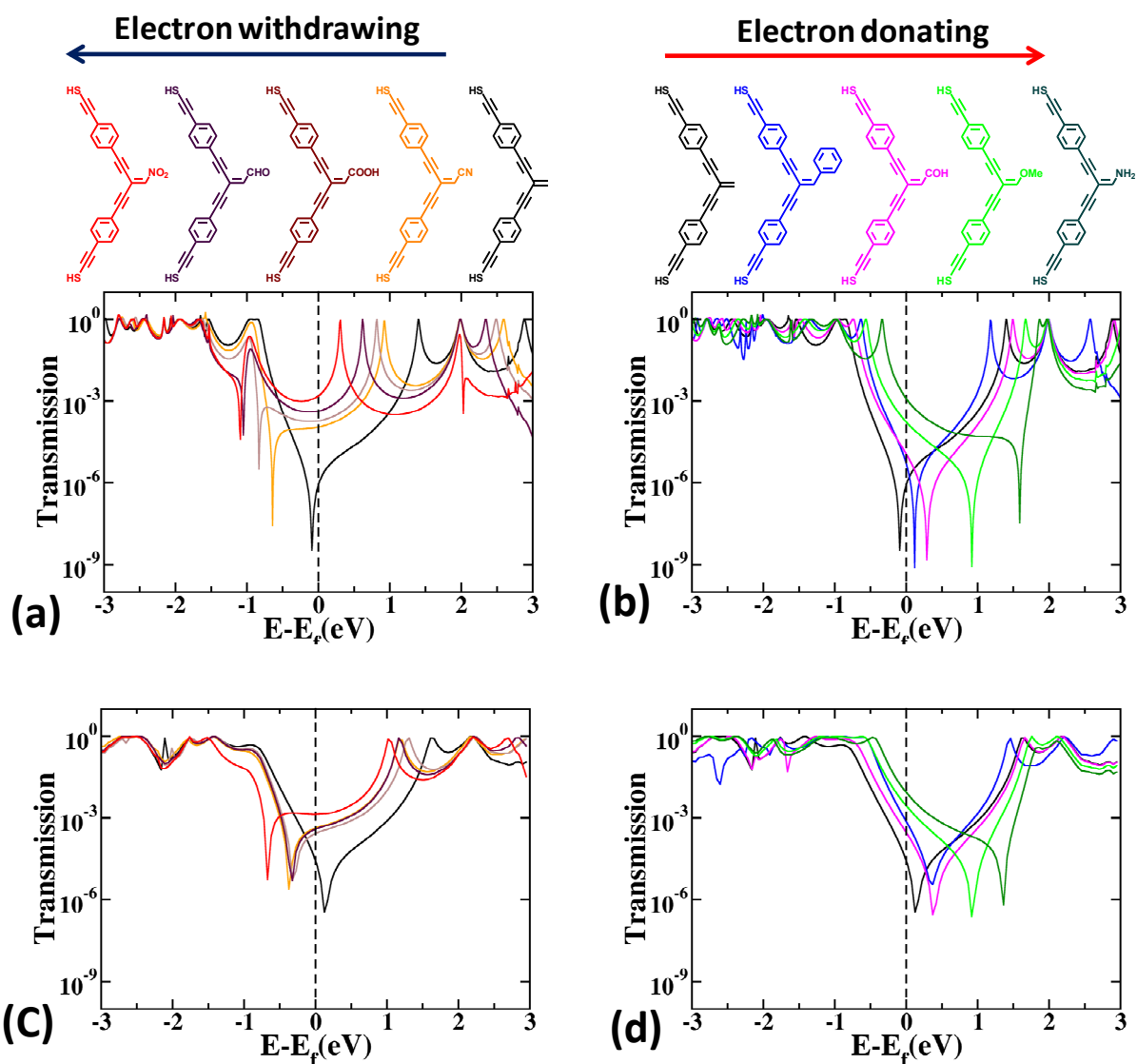


Figure 6-53. The upper half of this plot is a reproduction of Figure 6 in the main text.

Calculations made using Hückel-IV are shown in (a) and (b) while calculations made using ATK are shown in (c) and (d).

6.12.3 A molecular transistor

We described above the ideal transistor as a molecule with a high conductance state provided by a molecular resonance in close proximity to a low conductance state near the

Fermi energy. There have been a number of experimental measurements on single molecule transistors.²⁷⁵ To illustrate a potential molecular transistor, we use a cross-conjugated oligo(phenylene-enynylene) molecule with 3 repeat units.⁴⁸

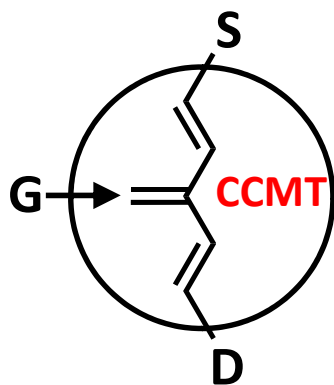


Figure 6-54. A symbol for the proposed “cross-conjugated molecular transistor”. The application of a gate voltage or potential should change the source-drain resistance. More generally the gating of a molecule with interference and not necessarily cross-conjugation will provide the desired dynamic range in the on/off ratio.

In Figure 6-55, we compare the cross-conjugated molecule to a molecule where the conjugation is broken and to the full conjugated oligo (phenylene-enynylene). In part (b), the transmission curves for these three molecules are calculated using two different transport codes: ATK shown with solid lines and Hückel-IV shown as a dotted line. Given that the transmission spans ≈ 16 orders of magnitude, the two transport codes agree very well. The differences between the two codes lie in the exact position of the resonances and the minima between them. Experimental results are required to calibrate the performance of these methods; however, the trends are consistent. We can see from Figure 6-55 (b) that the cross-

conjugated molecule shown in black has a change in transmission probability of ~ 16 orders of magnitude over 0.88eV range in incident electron energy. In comparison, for the molecule shown in green, with CH_2 groups breaking the conjugation, the electron transmission changes ~ 8 orders of magnitude over 1.2eV. In Figure 6-55 (c), the transmission probability is shown with a 5V applied gate voltage calculated in ATK. To compare the gate voltage effect, the low bias conductance is plotted in (d). As the bias voltage goes to zero the conductance is proportional to the transmission at the Fermi level. In (d), we have defined the off state as no perturbation to the system, and the on state as 5V gate voltage. The gate voltage is applied as an external electrostatic potential localized to the molecular region and not a physical electrode.⁵

The conductance through the cross-conjugated molecule changes by 8 orders of magnitude with an applied gate voltage of 5V. Where the cross-conjugated units are replaced by saturated carbons, the conductance changes 3 orders of magnitude, and the fully conjugated molecule, shown in red, changes 1.5 orders of magnitude. All of these molecules have not reached a molecular resonance with a 5V applied gate potential, so the subthreshold swing is just the slope of the conductance change. These results could be even further optimized by engineering the interference minimum to occur directly at the Fermi level. The on state could possibly be increased 5 orders of magnitude in the case of the cross-conjugated molecule by increasing gate voltage shifting the HOMO-orbital closer to the Fermi level; however, approaching resonance increases the probability of electron charging and molecular rearrangement. The cross-conjugated molecule has a subthreshold swing of $\sim 625\text{mV/decade}$,

which is ~ 2.5 and ~ 5.25 times lower than in the conjugated and saturated molecules. It is the comparison between these rates that is most important because the implementation of the gate voltage in the calculations and the gate electrode in the experiment will have a large effect on the measured change. The large dynamic range, sensitivity to incident electron energy, and switching based on changes in electron density make cross-conjugated molecules a promising candidate for molecular transistors.

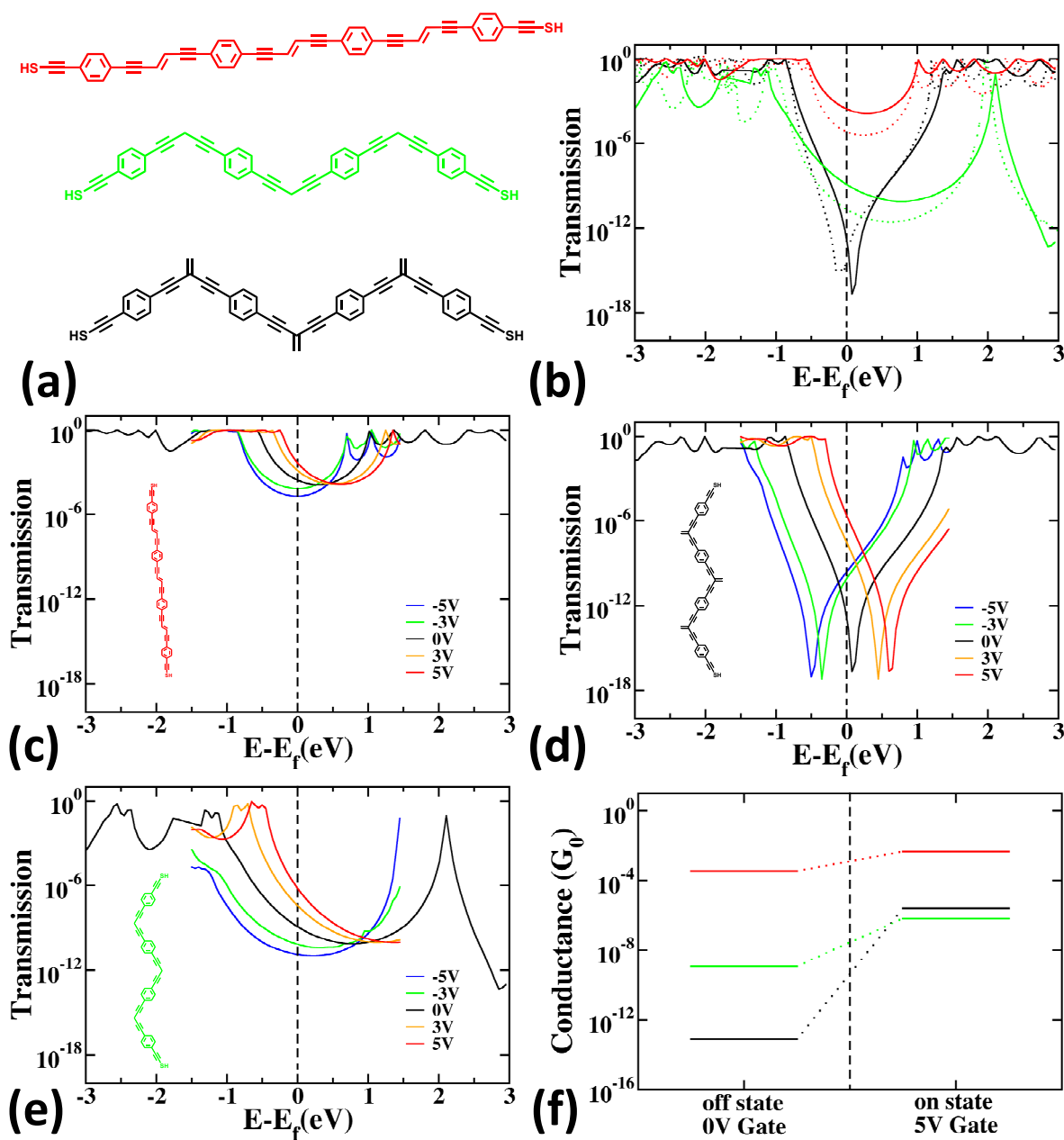


Figure 6-55. Calculations of conductance change with applied gate voltage in three test molecules. In (b), the transmission spectrum calculated for the molecules shown in (a) includes a promising potential molecular transistor, the cross-conjugated molecule in black. The solid lines are calculated using ATK and the dashed lines calculated using Hückel-IV. (c) (d) and (e)

show the effect of gate voltage on the conductance plot. (f) shows the calculated change in conductance between on and off state of ~ 8 orders of magnitude in the cross-conjugated molecule.

6.13 A molecular rectifier

Our analyses of cross-conjugation and interference effects in transmission have dealt with the case of a single (sometimes degenerate) interference peak in symmetric molecules. In asymmetric molecules, we calculate a splitting of the interference peaks and more complex transmission features. By engineering the interference locations and using asymmetric molecules, more complex devices can be designed. The field of single molecule electronics is rooted in the proposal of a single molecule rectifier.⁵ This proposal was based on having a donor and acceptor group in a single molecule with a saturated molecular spacer separating the groups.⁵ The saturated linkage between the functional parts of the molecule reduces communication between these distinctly separate groups.²⁷⁶⁻²⁷⁸ In the intervening years, many experimental attempts have been made to measure a rectification ratio in single molecule transport, with marginal success in comparison with solid state devices.

It has been noted that having asymmetric coupling to the electrode also leads to an increased rectification ratio.^{279,280} The rectification ratio as a function of voltage is defined as the current in one bias direction divided by the current in the other bias direction. Measurements of rectification in thin films have been completed for over 40 years.²⁸¹ Recent experimental measurements on thin films of molecules have measured rectification ratios of up to 3000.²⁸¹ While molecules in a thin film can behave differently than at the single molecule

level, experimental advances have been made towards understanding systems at both limits.^{277,278,282,283}

A number of published experimental and theoretical investigations show molecular rectifiers with rectification ratios typically $\ll 100$.²⁰⁸ Very recent work using the barrier tunneling model for transport suggests that the rectification ratio for single molecules will never be greater than 100.²⁸¹ All of these results are a far cry from typical solid state rectification ratios that can be $>10^5$.

In this section, we focus on the electronic responses that can occur when multiple non-degenerate interference features are found in a single molecule. Essentially, most of the desired electrical elements can be redesigned in molecules with interference features to take advantage of the increased dynamic range. To illustrate these effects, we show model calculations on candidate molecules. It should be cautioned that in molecules that are very sensitive to Fermi level placement (band lineup), the accuracy of the calculation is limited. While the molecules presented here show extremely interesting behavior, small changes in the relative position of the Fermi level and the molecular resonances could have large consequences in the measured response. The extreme sensitivity to these features will surely test the computational codes but will also provide a direct way to improve their accuracy by comparison with future experimental measurements. Much of the uncertainty lies in the location of the Fermi level. It would be ideal if the Fermi level could be varied and tuned to test the behavior of the molecule (perhaps using an alloyed or coated tip).

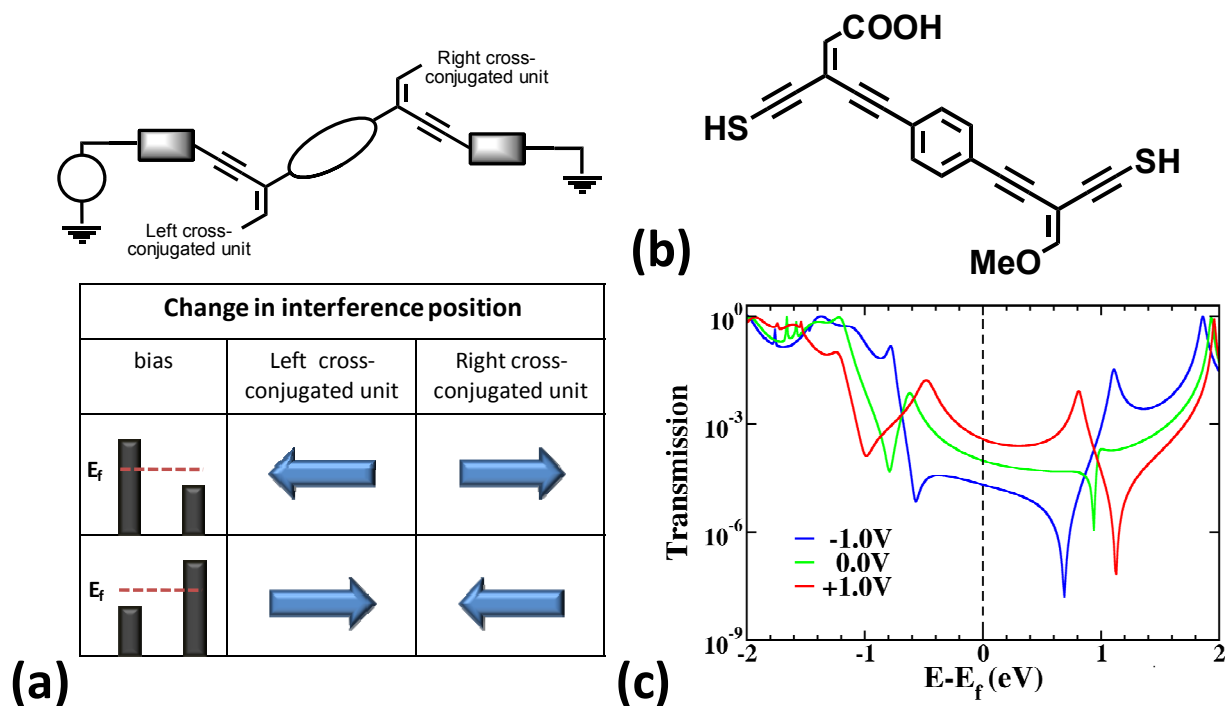


Figure 6-56. In molecules with multiple cross-conjugated units, an applied bias voltage will split the interference features. This splitting occurs because an applied bias has an electron donating or withdrawing effect that moves the interference position as shown in Figure 6-51. Shown in (a), the more positive an electrode is, the more it moves the interference feature of the closest cross-conjugated group to lower energy and conversely the more negative an electrode, the more it moves the interference feature to higher energy. In (b), we show an asymmetric molecule with the corresponding transmission plots shown in (c). The asymmetry causes 2 antiresonance features at different energy. At negative bias these antiresonance feature move together and at positive applied bias they move apart.

In Figure 6-51, electron donating and withdrawing groups were shown to move the interference peak over ± 1.5 eV from the Fermi energy. Using the effects of the electron

donating and withdrawing groups on the position of the molecular resonance, we propose a class of single molecule rectifiers as shown in Figure 6-56. This molecule consists of two cross-conjugated units (or other groups that produce interference features, e.g., meta substituted benzene) with split interference features, separated by a conjugated spacer. With an applied bias across the molecule, the interference positions are expected to move towards each other or away from each other as shown in Figure 6-56 (a). This is a result of the interference response in cross-conjugated molecules to electron donation and withdrawal.

We calculate this response with Hückel-IV as shown in Figure 6-56 (b). This molecule has a cross-conjugated unit with a methyl ether and a cross-conjugated unit carboxyl termination. In this context, the carboxyl terminated cross-conjugated unit is the more “electron withdrawing” group and the ether terminated unit is the more “electron donating” group. In Figure 6-56 (c), the transmission through this molecule is shown at three different voltage points -1, 0, +1. The interference dips come towards each other at negative bias and split farther apart at positive bias. In Hückel-IV we calculate a rectification ratio of 249 at 1.2V as shown in Figure 6-57 (b). Also shown in Figure 6-57 is the variation calculated in the rectification ratio among three transport programs. The maximum rectification ratios are calculated to be 18.6 at 1.0V in gDFTB and 17.6 at 0.6V in ATK. The behavior of the molecules to applied bias is nearly consistent between the codes with the interference features moving $\sim 0.25\text{eV}$ per 1V bias.

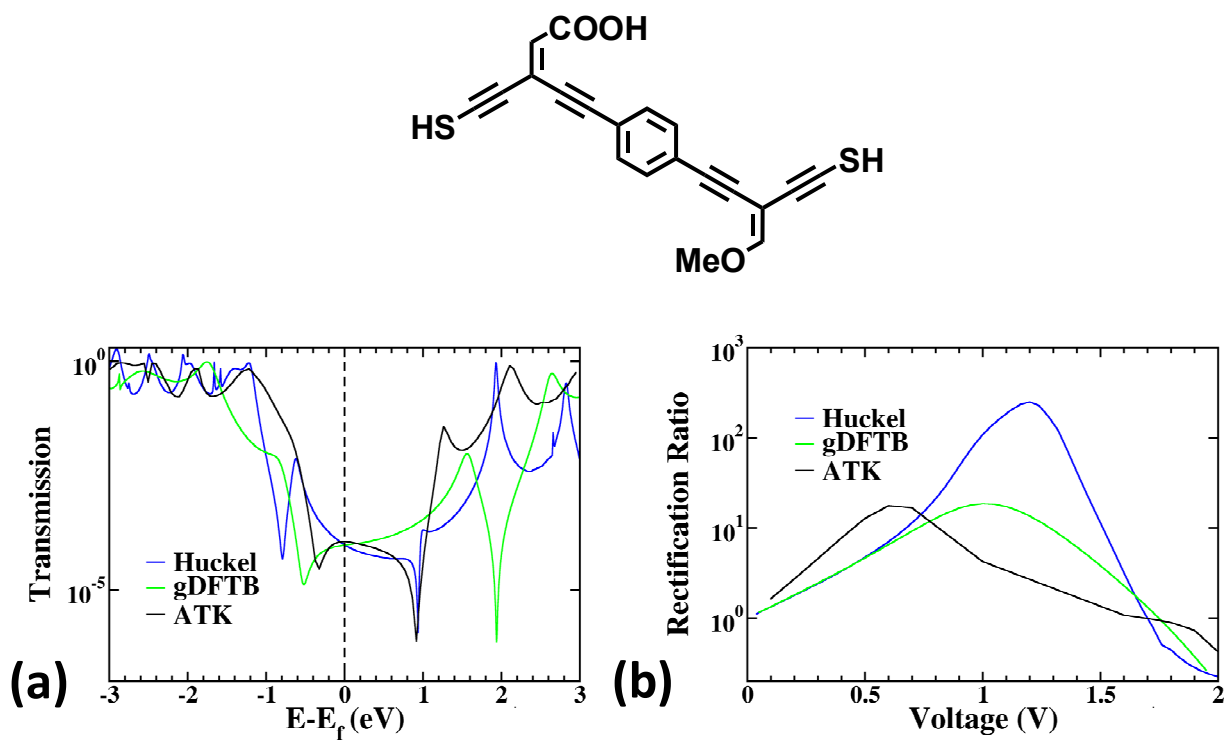


Figure 6-57. Transmission spectrum calculated using gDFTB, ATK and Hückel-IV is shown in (a), and the rectification ratio as a function of voltage calculated using these programs is shown in (b). Differences in the location of the resonance and interference features between the codes leads to a change in the voltage and magnitude of the maximum rectification ratio. More importantly, the behavior of the antiresonances is consistent between codes.

In all of our transport calculations, increasing the conjugated spacer length in the center of the molecule leads to a corresponding increase in the rectification ratio. One other limiting factor is the low change in transmission probability between the dip in the interference features and the highest transmission point between the interference dips. This region between the split interference features has a large effect on the maximum rectification ratio. The magnitude of the transmission between the split interference features can be increased

dramatically by having a molecular resonance near the Fermi level with interference features separated equally energetically above and below this resonance.

Oxygen containing molecules can have molecular resonances near the Fermi level. A molecule that has been experimentally measured and calculated²⁸⁴ contains the anthraquinone functional group, a cyclic cross-conjugated group. This group has the characteristics of interest, an interference feature below the Fermi energy and a localized resonance just above the Fermi energy.^{191,285} To create a molecule with a resonance split by two antiresonance peaks, we have asymmetrically added a cross-conjugated unit. As shown in Figure 6-58, we have taken the anthraquinone functional group, added a large conjugated spacer and two methyl-terminated cross-conjugated groups (the second cross-conjugated unit orients the sulfur termination towards the Au electrodes).

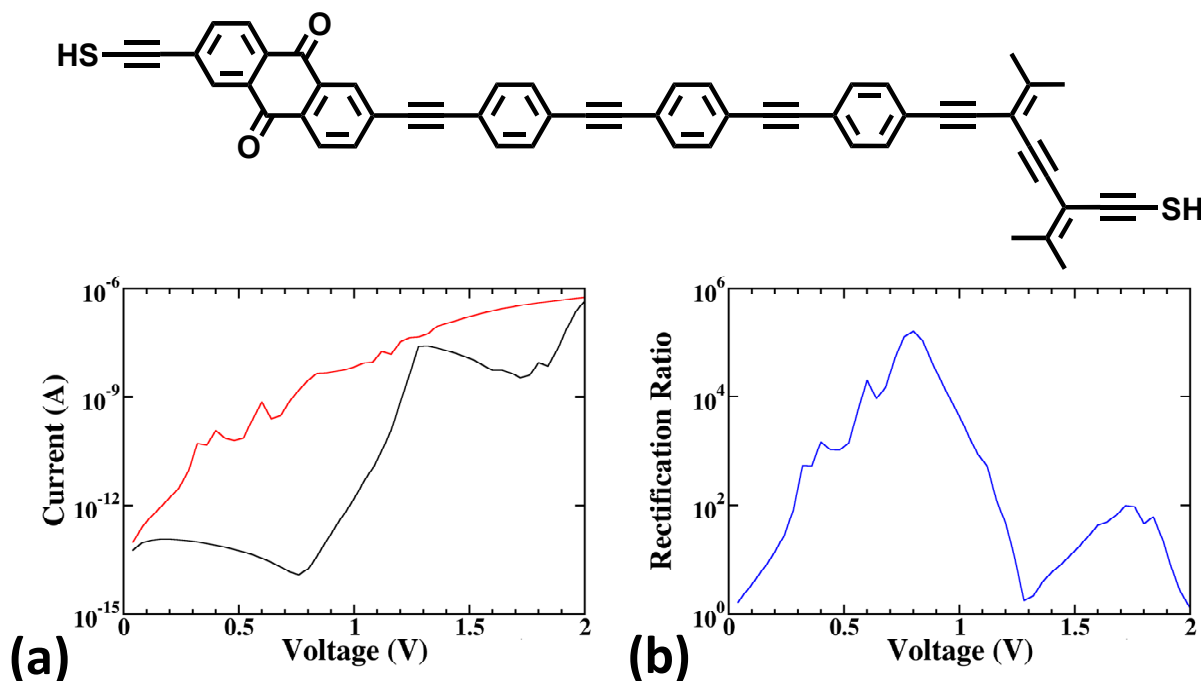


Figure 6-58. Rectifier behavior maximized in the Hückel IV transport code. In (a), the positive bias current/voltage behavior is shown in red and the negative bias current/voltage behavior is shown in black. The rectification ratio is calculated by dividing the positive voltage bias by the negative voltage bias. In (b), the rectification ratio as a function of voltage shows a peak of >150,000 at 0.8V applied voltage.

In Figure 6-58, we show the current voltage behavior and the rectification ratio for our proposed rectifier. As the interference features come together (Figure 6-60) with negative bias, the current decreases from 0.2-0.8 Volts, while in the positive bias, the current increases as the interference dips move apart. The rectification ratio increases steadily from 0-0.8V where it quickly falls off. At 0.8V the rectification ratio of >150,000 is orders of magnitude higher than other published single molecule rectifier calculations or experiments, without relying on asymmetric binding to the electrodes. This result indicates that molecular devices may function as coherent (fast) electronic devices.

The choice of molecule was dictated by the location of the resonances and the interference features within one transport code. Any candidate molecular rectifier would show slightly different behavior using the three transport programs that we have chosen. While we are calculating the rectification behavior maximized for one code we believe that this behavior could be optimized for the other codes and, more importantly, in experimental measurements with different functional groups chosen to control the position of the resonances and interference locations.

The large rectification ratio presented in is caused by the voltage dependence of split interference features in an asymmetric molecule. As shown in Figure 6-57 the interference features will move farther apart in energy or closer together depending on the sign of the applied bias. In Figure 6-59 below, the similar behavior is seen for the proposed rectifier. The interference features at $\pm 0.6\text{eV}$ (the interference at $+0.6\text{eV}$ is split due to the two cross-conjugated units) shift to $\pm 0.15\text{eV}$ at -1.0V applied bias. At $+1.0\text{V}$ bias the interference features have shifted to $\approx \pm 1\text{eV}$. The localized oxygen resonance on the anthraquinone group amplifies the conductance change of the interference splitting effect. Comparison with experimental results should help clarify the location of the interference and resonance energetic locations.

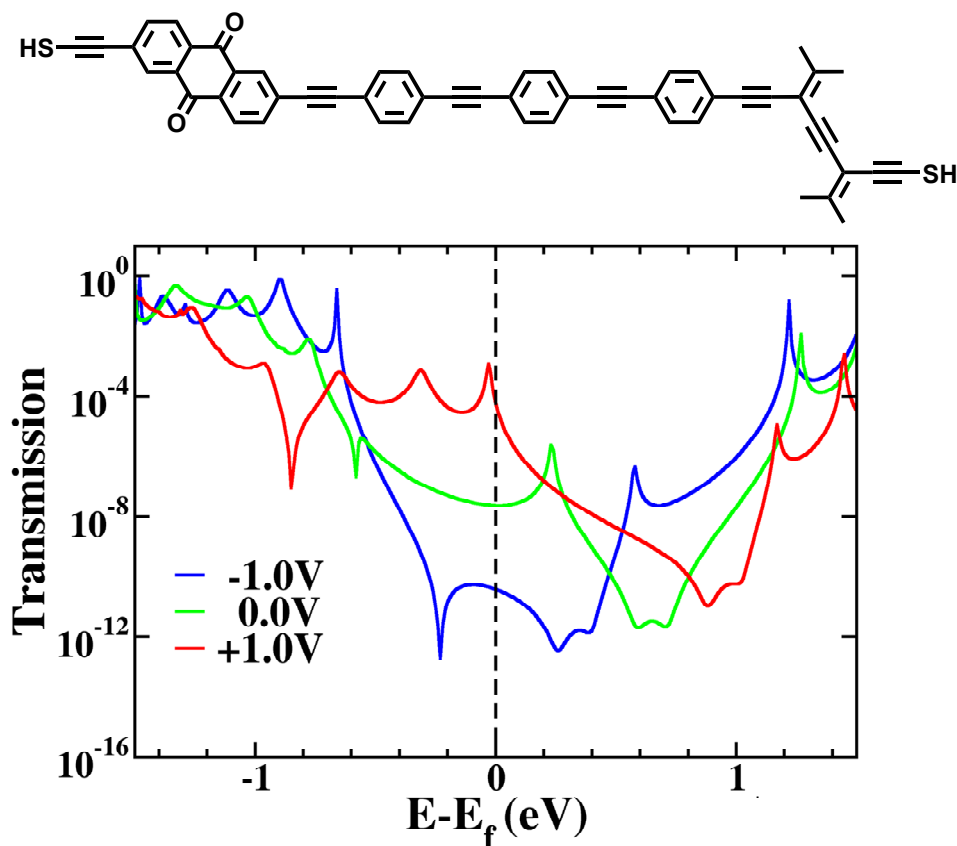


Figure 6-59. The voltage dependent transmission for the proposed molecular rectifier.

In Figure 6-60, the zero voltage transmission is shown using the three different transport codes. These changes in the transmission features, specifically the lack of split antiresonance features in ATK, have a noticeable effect on the calculated maximum rectification ratio. In gDFTB, the maximum rectification ratio is 501 at 0.52V and in ATK the maximum rectification is 83.5 at 1.5V. While these rectification ratios are very high for calculations on single molecule rectifiers, they are much lower than the value calculated in Hückel-IV. This is not surprising and is a direct consequence of the variations between transport codes. All three of these results will likely differ from experimental measurements because of the sensitivity to interference and resonance peaks. This sensitivity is a direct result of having a large dynamic range in transmission probability, where small changes in the energy have large effects on the transport behavior.

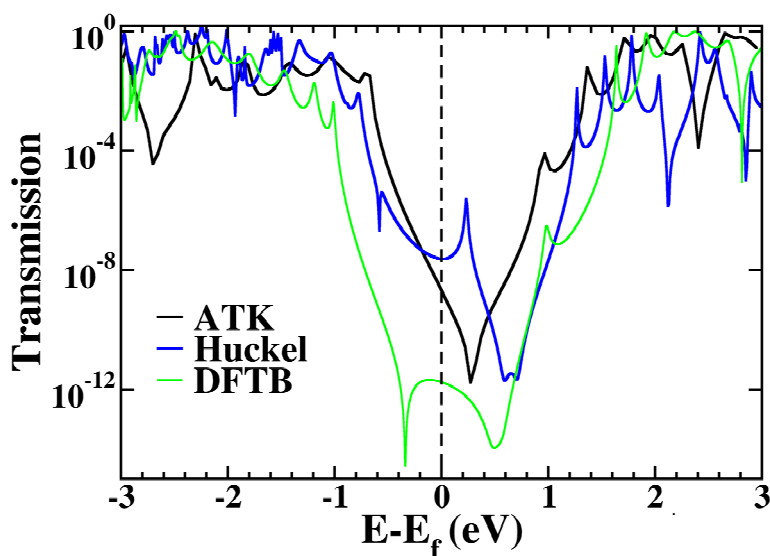


Figure 6-60. Transmission plots for the molecule shown in Figure 6-58 calculated using gDFTB, Hückel-IV 3.0 and ATK. The differences in the transmission spectrum are largely due to the energetic positioning of the antiresonance features and the localized oxygen resonance. The changes in the transmission spectrum lead to large changes in the maximum rectification ratios calculated from >150,000 in Hückel-IV, to 501 in gDFTB, to 83.5 in ATK.

6.14 Negative differential resistance

One other feature observed in the current-voltage behavior of some of these cross-conjugated molecules is a rapid decrease in current with increasing voltage, or negative differential resistance (NDR). An NDR-like behavior is most strikingly seen in the plot shown in Figure 6-58 (a) where the current in the negative voltage direction decreases 1 order of magnitude between 0.2 and 0.7 volts. This is a result of interference features moving together with increasing voltage.

In reported NDR in molecules on silicon surfaces, the conductance dip is attributed to the conduction band edge passing a molecular resonance.^{205,286} Interference features in a transmission spectrum are equivalent to resonant peaks but with an opposite sign in transmission plots. If the transport is dominated by the band edge this indicates that interference dips should provide NDR behavior similar to that reported in the literature for the case of sweeping through molecular resonances. The advantage of observing NDR features caused by interferences (or by resonance without charging) is that these can occur without geometry change in the low bias tunneling regime. This could lead to a much faster response, enhanced stability, and longevity of potential devices.

6.15 Conclusion

We have shown that quantum interference is quite common in model systems. The unique transport behavior calculated in model systems correlates well with the behavior calculated for cross-conjugated molecules. From bond length analysis, we calculate uncorrelated bond lengths and associated electron delocalization across the cross-conjugated bond. This unique feature of cross-conjugated molecules is borne out in the interference position and in the unique transport behavior calculated for these molecules. Geometric molecular distributions and dephasing are shown not to destroy this interference feature, increasing the possibility of experimental realization.

Cross-conjugated molecules and their extreme sensitivity to incident electron energy open up new possibilities in single molecule electronics. Most switching and nonlinear behavior in molecules has relied on tuning the incident electron energy past a molecular resonance or

conformation change. This can lead to charging of the molecule and possible device instability.^{114,209} With cross-conjugated molecules, we calculate a large dynamic range in electron transmission probability to occur in a chemically tunable range between the frontier molecular orbitals. This allows complex electronic behavior such as switching, NDR, and rectification to occur in the low bias electron tunneling regime without charging the molecule.

The depth of the interference feature is tunable by minimizing the σ transport. The location of the interference feature is shown to be tunable across the HOMO-LUMO gap. This tunability should allow for manipulation of the interference feature by chemical means so that it occurs at the Fermi level. To minimize the off-state current, having the interference minimum at the Fermi level is important, and also results in the maximum dynamic range. To study molecules with such sensitivity to the band lineup,²⁸⁷ it would be ideal if the Fermi level could be experimentally tuned, as this might prove easier than chemical modification. These molecules and their sensitivity to the location of the Fermi level should provide a useful means of calibrating experimental results and theoretical methods.

Cross-conjugated molecules could be useful in chemical sensors where an extremely small change in electron density must be measured. We have calculated that changing the electron donating or withdrawing ability of a side group attached to the cross-conjugated unit can produce a 3 order of magnitude change in the conductance. This sensitivity of the cross-conjugated unit to electron density also indicates that attaching a third terminal to the cross-conjugated double bond could be used to gate the molecule. Experimental realization of three terminal devices with single molecules is exceedingly difficult but these cross-conjugated

molecules seem to be promising candidates for initial tests. Using a calculated electrostatic potential to gate cross-conjugated molecules, our calculations suggest that the large dynamic range in electron transmission probability could be used to tune the Fermi level along the 16 orders of magnitude change in electron transmission probability.

If the interference features could be generated in all symmetry components of the transmission, it would be conceivable to have a near-perfect insulator in close proximity to a molecular resonance, increasing the dynamic range of the system. Cross-conjugated molecules serve as an interesting case where quantum interference effects dominate the transmission spectrum near the Fermi level and the correlation of molecular conductance and energetic proximity to a frontier molecular orbital break down. These molecules are an example of the interesting and unexpected behavior that can occur on the size scale of a single molecule.

Chapter 7. Outlook & Perspective

This research project focuses on single molecule junctions, a construct that is at this time difficult to control and characterize. High precision instrumentation with sub Angstrom sensitivity is still not commonplace, which necessitates custom machinery. The experimental difficulties do not hamper the desire and scientific need to understand single molecule behavior. The integration of Raman spectroscopy and charge transport will offer the ability to collect a time trajectory for individual molecules in non-equilibrium conditions.

The work on quantum interference shows interesting potential for the design of future electronic elements. The experimental measurements of devices with predicted quantum interference effects will provide great opportunities to compare results. Molecules with large energetically accessible dynamic range in transmission probability will be sensitive to the location of the Fermi energy and the molecular resonances. This sensitivity could provide a useful way to calibrate calculations with experimental results. Tuning the properties of the molecule to the electrode is a large synthetic task. Tuning the position of the Fermi level by modifying the electrodes through doping could provide a new avenue to study the transport through single molecules without modifying the molecule.

In the limit of a single molecule, the large experimental variations and uncertainty could make measuring quantum interference effects difficult. The great sensitivity to incident electron energy and geometry of charge transport make the systems even more susceptible to measurement conditions. One concern in scaling the effects calculated on single molecules to films of molecules or even to observations on single molecule measurements is a “short circuit” where the electron bypasses the quantum interference unit. The question of what happens to

these molecules in films is quite interesting and will need to be addressed in future studies. In a film it might be necessary to decrease or stop electron transfer between molecules. One way to avoid the shorting effect in the design of electronic elements could be to make the molecule longer or possibly surround the cross-conjugated units in insulating groups.

The research on single molecule behavior is extremely young from a historical perspective. The progress made here is just a small contribution to the understanding within the field. As evidence of the rapid growth, the number of publications addressing *single molecule* has increased an order of magnitude in each of the past two decades, according to a SciFinder search on the topic. It is the technological advances in measurements and observations of single molecules and interfaces that will continue to further our scientific understanding. There remain a large number of unknowns in single molecule behavior. Future studies, both theoretical and experimental, should fill in our gap in understanding.

Cross-conjugated molecules and molecules with quantum interference effects necessitated a re-evaluation of our common understandings in charge transport through small organic molecules. The unsynthesized and unstudied organic molecules, estimated to number in the range of 10^{60} , should provide new and unexpected behavior as well as ample job security for generations of graduate students and researchers.²⁸⁸

References

- (1) Staff. Noted With Pleasure. The New York Times, *November 15, 1987*.
- (2) In *Merriam-Webster Online Dictionary*; <http://www.merriam-webster.com/>; 2007.
- (3) Democritus. Retrieved March 17, 2008, <http://www.britannica.com/eb/article-9029904>.
- (4) Datta, S. *Electronic Transport in Mesoscopic Systems*; Cambridge University Press: Cambridge, UK, 2003.
- (5) Aviram, A.; Ratner, M. A. Molecular rectifiers. *Chem. Phys. Lett.* **1974**, *29*, 277.
- (6) Raman, C. V.; Krishnan, K. S. A new type of secondary radiation. *Nature* **1928**, *121*, 501-2.
- (7) Fleishman, M.; Hendra, P. J.; McQuillan, A. J. Raman Spectra of Pyridine Adsorbed at a Silver Electrode. *Chemical Physics Letters* **1974**, *26*, 163-166.
- (8) Jeanmaire, D. L.; Van Duyne, R. P. Surface Raman Spectroelectrochemistry Part I. Heterocyclic, Aromatic, and Aliphatic Amines Adsorbed on the Anodized Silver Electrode. *Journal of Electroanalytical Chemistry* **1977**, *84*, 1-20.
- (9) Van Duyne, R. P. In *Chemical and Biochemical Applications of Lasers*; Moore, C. B., Ed.; Academic Press: New York, 1979; Vol. 4, p 101-184.
- (10) Nie, S.; Emory, S. R. Probing Single Molecules and Single Nanoparticles by Surface-Enhanced Raman Scattering. *Science* **1997**, *275*, 1102-1106.
- (11) Kneipp, K.; Wang, Y.; Kneipp, H.; Perelman, L. T.; Itzkan, I.; Dasari, R. R.; Feld, M. S. Single Molecule Detection Using Surface-Enhanced Raman Scattering (SERS). *Physical Review Letters* **1997**, *78*, 1667.
- (12) Etchegoin, P. G.; Meyer, M.; Ru, E. C. L. Statistics of single molecule SERS signals: is there a Poisson distribution of intensities? *Physical Chemistry Chemical Physics* **2007**, *9*, 3006-3010.
- (13) Ru, E. C. L.; Etchegoin, P. G.; Meyer, M. Enhancement factor distribution around a single surface-enhanced Raman scattering hot spot and its relation to single molecule detection. *The Journal of Chemical Physics* **2006**, *125*, 204701.
- (14) Dieringer, J. A.; Lettan, R. B.; Scheidt, K. A.; VanDuyne, R. P. A Frequency Domain Existence Proof of Single-Molecule Surface-Enhanced Raman Spectroscopy. *J. Am. Chem. Soc.* **2007**.
- (15) Dieringer, J. A.; Camden, J. P.; Wang, Y.; Marks, L.; VanDuyne, R. P. *In preparation* **2008**.

- (16) Kneipp, K.; Kneipp, H.; Kartha, V. B.; Manoharan, R.; Deinum, G.; Itzkan, I.; Dasari, R. R.; Feld, M. S. Detection and identification of a single DNA base molecule using surface-enhanced Raman scattering (SERS). *Physical Review E* **1998**, *57*, R6281-R6284.
- (17) Xu, H.; Bjerneld, E. J.; Käll, M.; Börjesson, L. Spectroscopy of Single Hemoglobin Molecules by Surface Enhanced Raman Scattering. *Physical Review Letters* **1999**, *83*, 4357-4360.
- (18) Mark, S. A. Locally enhanced Raman spectroscopy with an atomic force microscope. *Applied Physics Letters* **2000**, *76*, 3130-3132.
- (19) Stöckle, R. M.; Suh, Y. D.; Deckert, V.; Zenobi, R. Nanoscale chemical analysis by tip-enhanced Raman spectroscopy. *Chemical Physics Letters* **2000**, *318*, 131-136.
- (20) Hayazawa, N.; Inouye, Y.; Sekkat, Z.; Kawata, S. Metallized tip amplification of near-field Raman scattering. *Optics Communications* **2000**, *183*, 333-336.
- (21) Zhang, W.; Yeo, B. S.; Schmid, T.; Zenobi, R. Single Molecule Tip-Enhanced Raman Spectroscopy with Silver Tips. *J. Phys. Chem. C* **2007**, *111*, 1733-1738.
- (22) Domke, K. F.; Zhang, D.; Pettinger, B. Toward Raman Fingerprints of Single Dye Molecules at Atomically Smooth Au(111). *J. Am. Chem. Soc.* **2006**, *128*, 14721-14727.
- (23) Catalin, C. N.; Jens, D.; Nicolas, B.; Markus, B. R. Scanning-probe Raman spectroscopy with single-molecule sensitivity. *Physical Review B (Condensed Matter and Materials Physics)* **2006**, *73*, 193406.
- (24) Foley, E. T.; Yoder, N. L.; Guisinger, N. P.; Hersam, M. C. Cryogenic variable temperature ultrahigh vacuum scanning tunneling microscope for single molecule studies on silicon surfaces. *Review of Scientific Instruments* **2004**, *75*, 5280-5287.
- (25) Moerner, W. E.; Kador, L. Optical detection and spectroscopy of single molecules in a solid. *Physical Review Letters* **1989**, *62*, 2535.
- (26) Orrit, M.; Bernard, J. Single pentacene molecules detected by fluorescence excitation in a p-terphenyl crystal. *Physical Review Letters* **1990**, *65*, 2716.
- (27) Ha, T.; Ting, A. Y.; Liang, J.; Caldwell, W. B.; Deniz, A. A.; Chemla, D. S.; Schultz, P. G.; Weiss, S. Single-molecule fluorescence spectroscopy of enzyme conformational dynamics and cleavage mechanism. *Proceedings of the National Academy of Sciences* **1999**, *96*, 893-898.
- (28) Weiss, S. Measuring conformational dynamics of biomolecules by single molecule fluorescence spectroscopy. *Nat Struct Mol Biol* **2000**, *7*, 724-729.
- (29) Weiss, S. Fluorescence Spectroscopy of Single Biomolecules. *Science* **1999**, *283*, 1676-1683.

- (30) Marcus, R. A. *Journal of Chemical Physics* **1956**, *24*, 966.
- (31) Marcus, R. A. On the Theory of Oxidation-Reduction Reactions Involving Electron Transfer. I. *The Journal of Chemical Physics* **1956**, *24*, 966-978.
- (32) Hush, N. S. Adiabatic theory of outer-sphere electron-transfer processes in solution. *Trans. Farad. Soc.* **1961**, *57*, 577.
- (33) McConnell, H. M. Intramolecular Charge Transfer in Aromatic Free Radicals. *The Journal of Chemical Physics* **1961**, *35*, 508-515.
- (34) Landauer, R. Conductance determined by transmission: probes and quantized constriction resistance. *Journal of Physics: Condensed Matter* **1989**, *1*, 8099-81100.
- (35) Landauer, R. Spatial Variation of Currents and Fields Due to Localized Scatterers in Metallic Conduction. *IBM Journal of Research Development* **1957**, *1*.
- (36) Buttiker, M.; Imry, Y.; Landauer, R.; Pinhas, S. Generalized many-channel conductance formula with application to small rings. *Physical Review B* **1985**, *31*, 6207-6215.
- (37) Datta, S. In *Electron Devices Meeting* 2002.
- (38) Xue, Y.; Datta, S.; Ratner, M. A. First-principles based matrix Green's function approach to molecular electronic devices: general formalism. *Chemical Physics* **2002**, *281*, 151-170.
- (39) Zahid, F.; Paulsson, M.; Datta, S. In *Advanced Semiconductors and Organic Nano-Techniques Part III: Physics and Technology of Molecular and Biotech Systems*; Morkoc, H., Ed.; Elsevier Academic Press: 2003; Vol. III, p 1-40.
- (40) Pecchia, A.; Carlo, A. D. Atomistic theory of transport in organic and inorganic nanostructures. *Reports on Progress in Physics* **2004**, *67*, 1497-1561.
- (41) Elstner, M.; Porezag, D.; Jugnickel, G.; Elsner, J.; Haugk, M.; Frauenheim, T.; Suhai, S.; Seifert, G. Self-consistent-charge density-functional tight-binding method for simulations of complex materials properties. *Phys. Rev. B* **1998**, *58*, 7260-7268.
- (42) Frauenheim, T.; Seifert, G.; Elstner, M.; Hagnal, Z.; Jungnickel, G.; Porezag, D.; Suhai, S.; Scholz, R. A Self-Consistent Charge Density-Functional Based Tight-Binding Method for Predictive Materials Simulations in Physics, Chemistry and Biology. *Phys. Stat. Sol. (b)* **2000**, *217*, 41-62.
- (43) Frauenheim, T.; Seifert, G., et al. Atomistic simulations of complex materials: ground-state and excited-state properties. *Journal of Physics: Condensed Matter* **2002**, *14*, 3015-3047.

- (44) Porezag, D.; Frauenheim, T.; Kohler, T.; Seifert, G.; Kaschner, R. Construction of tight-binding-like potentials on the basis of density-functional theory: Application to Carbon. *Phys. Rev. B* **1995**, *51*, 12947-12957.
- (45) Brandbyge, M.; Mozos, J.-L.; Ordejón, P.; Taylor, J.; Stokbro, K. Density-functional method for nonequilibrium electron transport. *Physical Review B* **2002**, *65*, 165401.
- (46) Taylor, J.; Guo, H.; Wang, J. Ab initio modeling of quantum transport properties of molecular electronic devices. *Physical Review B* **2001**, *63*, 245407.
- (47) Stokbro, K.; Taylor, J.; Brandbyge, M.; Ordejon, P. TranSIESTA: a spice for molecular electronics. *Annals of the New York Academy of Sciences* **2003**, *1006*, 212-226.
- (48) Atomistix A/S; www.atomistix.com: 2007.
- (49) Erts, D.; Lohmus, A.; Lohmus, R.; Olin, H.; Pokropivny, A. V.; Ryen, L.; Svensson, K. Force interactions and adhesion of gold contacts using a combined atomic force microscope and transmission electron microscope. *Applied Surface Science* **2002**, *188*, 460-466.
- (50) Muller, C. J.; Krans, J. M.; Todorov, T. N.; Reed, M. A. Quantization effects in the conductance of metallic contacts at room temperature. *Physical Review B: Condensed Matter* **1996**, *53*, 1022-5.
- (51) Landman, U.; Luedtke, W. D.; Salisbury, B. E.; Whetten, R. L. Reversible manipulations of room temperature mechanical and quantum transport properties in nanowire junctions. *Physical Review Letters* **1996**, *77*, 1362-1365.
- (52) Smit, R. H. M.; Untiedt, C.; Yanson, A. I.; van Ruitenbeek, J. M. Common Origin for Surface Reconstruction and the Formation of Chains of Metal Atoms. *Physical Review Letters* **2001**, *87*, 266102/1-266102/4.
- (53) Hansen, K.; Laegsgaard, E.; Stensgaard, I.; Besenbacher, F. Quantized conductance in relays. *Physical Review B: Condensed Matter* **1997**, *56*, 2208-2220.
- (54) Olesen, L.; Laegsgaard, E.; Stensgaard, I.; Besenbacher, F.; Schioetz, J.; Stoltze, P.; Jacobsen, K. W.; Noerskov, J. K. Quantized conductance in an atom-sized point contact. *Physical Review Letters* **1994**, *72*, 2251-4.
- (55) Olesen, L.; Laegsgaard, E.; Stensgaard, I.; Besenbacher, F. Quantized conductance in an atom-sized point contact. Reply to comments. *Physical Review Letters* **1995**, *74*, 2147.
- (56) Pascual, J. I.; Mendez, J.; Gomez-Herrero, J.; Baro, A. M.; Garcia, N.; Vu Thien, B. Quantum contact in gold nanostructures by scanning tunneling microscopy. *Physical Review Letters* **1993**, *71*, 1852-5.

- (57) Agrait, N.; Rodrigo, J. G.; Vieira, S. Conductance steps and quantization in atomic-size contacts. *Physical Review B: Condensed Matter and Materials Physics* **1993**, *47*, 12345-8.
- (58) Untiedt, C.; Yanson, A. I.; Grande, R.; Rubio-Bollinger, G.; Agrait, N.; Vieira, S.; van Ruitenbeek, J. M. Calibration of the length of a chain of single gold atoms. *Physical Review B: Condensed Matter and Materials Physics* **2002**, *66*, 085418/1-085418/6.
- (59) Costa-Kramer, J. L.; Garcia, N.; Garcia-Mochales, P.; Serena, P. A.; Marques, M. I.; Correia, A. Conductance quantization in nanowires formed between micro and macroscopic metallic electrodes. *Physical Review B: Condensed Matter* **1997**, *55*, 5416-5424.
- (60) Ohnishi, H.; Takayanagi, K. Quantized conductance through individual rows of suspended gold atoms. *Nature (London)* **1998**, *395*, 780-783.
- (61) Torres, J. A.; Tosatti, E.; Dal Corso, A.; Ercolessi, F.; Kohanoff, J. J.; Di Tolla, F. D.; Soler, J. M. The puzzling stability of monoatomic gold wires. *Surface Science* **1999**, *426*, L441-L446.
- (62) Stepanov, I. A. The puzzling stability of monoatomic gold wires is the result of small fluctuations. *Surface Science* **2000**, *463*, 211-212.
- (63) Torres, J. A.; Tosatti, E.; Dal Corso, A.; Ercolessi, F.; Kohanoff, J. J.; Di Tolla, F. D.; Soler, J. M. Reply to: \"The puzzling stability of monoatomic gold wires is the result of small fluctuations\". *Surface Science* **2000**, *463*, 213.
- (64) Lindsay, S. M. Single Molecule Electronics. *The Electrochemical Society Interface* **2004**, *Spring 2004*, 26-30.
- (65) Cui, X. D.; Primak, A., et al. Reproducible measurement of single-molecule conductivity. *Science* **2001**, *294*, 571-4.
- (66) Tomfohr, J.; Ramachandran, G. K.; Sankley, O. F.; Lindsay, S. M. In *In Introducing Molecular Electronics*; Cuniberti, G., Fagas, G., Richter, K., Eds.; Springer-Verlag: Berlin, 2005.
- (67) Xu, B.; Tao, N. J. Measurement of single-molecule resistance by repeated formation of molecular junctions. *Science* **2003**, *301*, 1221-3.
- (68) Xiao, X.; Xu, B.; Tao, N. J. Measurement of Single Molecule Conductance: Benzenedithiol and Benzenedimethanethiol. *Nano Letters* **2004**, *4*, 267-271.
- (69) Venkataraman, L.; Klare, J. E.; Tam, I. W.; Nuckolls, C.; Hybertsen, M. S.; Steigerwald, M. L. Single-Molecule Circuits with Well-Defined Molecular Conductance. *Nano Lett.* **2006**, *6*, 458-462.

- (70) Dorogi, M.; Gomez, J.; Osifchin, R.; Andres, R. P.; Reifenberger, R. Room-temperature Coulomb blockade from a self-assembled molecular nanostructure. *Physical Review B: Condensed Matter* **1995**, *52*, 9071-7.
- (71) Haiss, W.; Nichols, R. J.; van Zalinge, H.; Higgins, S. J.; Bethell, D.; Schiffrin, D. J. Measurement of single molecule conductivity using the spontaneous formation of molecular wires. *Physical Chemistry Chemical Physics* **2004**, *6*, 4330-4337.
- (72) Suzuki, M.; Fujii, S.; Fujihira, M. Measurements of Currents through Single Molecules of Alkanedithiols by Repeated Formation of Break Junction in Scanning Tunneling Microscopy under Ultrahigh Vacuum. *Japanese Journal of Applied Physics* **2006**, *45*, 2041-2044.
- (73) Morita, T.; Lindsay, S. Determination of Single Molecule Conductances of Alkanedithiols by Conducting-Atomic Force Microscopy with Large Gold Nanoparticles. *J. Am. Chem. Soc.* **2007**.
- (74) Tada, T.; Kondo, M.; Yoshizawa, K. Green's function formalism coupled with Gaussian broadening of discrete states for quantum transport: application to atomic and molecular wires. *Journal of Chemical Physics* **2004**, *121*, 8050-8057.
- (75) Reed, M. A.; Zhou, C.; Muller, C. J.; Burgin, T. P.; Tour, J. M. Conductance of a Molecular Junction. *Science* **1997**, *278*, 252-254.
- (76) Li, X. L.; He, H. X.; Xu, B. Q.; Xiao, X. Y.; Nagahara, L. A.; Amlani, I.; Tsui, R.; Tao, N. J. Measurement of electron transport properties of molecular junctions fabricated by electrochemical and mechanical methods. *Surface Science* **2004**, *573*, 1-10.
- (77) Datta, S.; Tian, W. Application of the Friedel sum rule to symmetric molecular conductors. *Physical Review B: Condensed Matter* **1997**, *55*, R1914-R1917.
- (78) Di Ventra, M.; Pantelides, S. T.; Lang, N. D. First-Principles Calculation of Transport Properties of a Molecular Device. *Physical Review Letters* **2000**, *84*, 979-982.
- (79) Xue, Y.; Ratner, M. A. End group effect on electrical transport through individual molecules: A microscopic study. *Physical Review B: Condensed Matter and Materials Physics* **2004**, *69*, 085403/1-085403/5.
- (80) Xue, Y.; Ratner, M. A. Microscopic study of electrical transport through individual molecules with metallic contacts. II. Effect of the interface structure. *Physical Review B: Condensed Matter and Materials Physics* **2003**, *68*, 115407/1-115407/11.
- (81) Xue, Y.; Ratner, M. A. Microscopic study of electrical transport through individual molecules with metallic contacts. I. Band lineup, voltage drop, and high-field transport. *Physical Review B: Condensed Matter and Materials Physics* **2003**, *68*, 115406/1-115406/18.

- (82) Ke, S.-H.; Baranger Harold, U.; Yang, W. Contact atomic structure and electron transport through molecules. *Journal of Chemical Physics* **2005**, *122*, 074704.
- (83) Andrews, D. Q.; Van Duyne, R. P.; Ratner, M. A. Stochastic Modulation in Molecular Electronic Transport Junctions: Molecular Dynamics Coupled with Charge Transport Calculations. *Nano Lett.* **2008**, *8*, 1120-1126.
- (84) Ke, S.-H.; Baranger, H. U.; Yang, W. Molecular Conductance: Chemical Trends of Anchoring Groups. *Journal of the American Chemical Society* **2004**, *126*, 15897-15904.
- (85) Liu, R.; Ke, S.-H.; Baranger, H. U.; Yang, W. Intermolecular effect in molecular electronics. *Journal of Chemical Physics* **2005**, *122*, 044703/1-044703/4.
- (86) Smit, R. H. M.; Noat, Y.; Untiedt, C.; Lang, N. D.; van Hemert, M. C.; van Ruitenbeek, J. M. Measurement of the conductance of a hydrogen molecule. *Nature* **2002**, *419*, 906-909.
- (87) Liang, W.; Shores, M. P.; Bockrath, M.; Long, J. R.; Park, H. Kondo resonance in a single-molecule transistor. *Nature* **2002**, *417*, 725-729.
- (88) Park, J.; Pasupathy Abhay, N., et al. Coulomb blockade and the Kondo effect in single-atom transistors. *Nature* **2002**, *417*, 722-5.
- (89) Alessandro, T.; Mark, A. R. Modeling the inelastic electron tunneling spectra of molecular wire junctions. *Physical Review B (Condensed Matter and Materials Physics)* **2005**, *72*, 033408.
- (90) Gemma, C. S.; Alessio, G.; Alessandro, P.; Thomas, F.; Aldo Di, C.; Jeffrey, R. R.; Noel, S. H. Understanding the inelastic electron-tunneling spectra of alkanedithiols on gold. *The Journal of Chemical Physics* **2006**, *124*, 094704.
- (91) Ohnesorge, F. M. Towards atomic resolution non-contact dynamic force microscopy in a liquid. *Surface and Interface Analysis* **1999**, *27*, 379-385.
- (92) Takeshi, F.; Jason, I. K.; Suzanne, P. J. Phase modulation atomic force microscope with true atomic resolution. *Review of Scientific Instruments* **2006**, *77*, 123703.
- (93) F.J. Giessibl, H. B. S. H. J. M. Imaging of atomic orbitals with the Atomic Force Microscope - experiments and simulations. *Annalen der Physik* **2001**, *10*, 887-910.
- (94) Grandbois, M.; Beyer, M.; Rief, M.; Clausen-Schaumann, H.; Gaub, H. E. How Strong Is a Covalent Bond? *Science* **1999**, *283*, 1727-1730.
- (95) Sonnenberg, L.; Parvole, J.; Borisov, O.; Billon, L.; Gaub, H. E.; Seitz, M. AFM-Based Single Molecule Force Spectroscopy of End-Grafted Poly(acrylic acid) Monolayers. *Macromolecules* **2006**, *39*, 281-288.

- (96) Schirmeisen, A.; Weiner, D.; Fuchs, H. Measurements of metal-polymer adhesion properties with dynamic force spectroscopy. *Surface Science* **2003**, *545*, 155-162.
- (97) Oesterhelt, F.; Rief, M.; Gaub, H. E. Single molecule force spectroscopy by AFM indicates helical structure of poly(ethylene-glycol) in water. *New Journal of Physics* **1999**, *1*, 6.
- (98) Beyer, M. K.; Clausen-Schaumann, H. Mechanochemistry: The Mechanical Activation of Covalent Bonds. *Chem. Rev.* **2005**, *105*, 2921-2948.
- (99) Binning, G.; Rohrer, H.; Gerber, C.; Weibel, E. Surface Studies by Scanning Tunneling Microscopy. *Physical Review Letters* **1982**, *49*, 57.
- (100) Takajo, D.; Nemoto, T.; Isoda, S. Structures of Adsorbed Initial Layers of Stearic Acid at the Liquid/Solid Interface. *Jpn. J. Appl. Phys.* **2004**, *43*, 4667-4670.
- (101) Venkataraman, B.; Breen, J. J.; Flynn, G. W. Scanning Tunneling Microscopy Studies of Solvent Effects on the Adsorption and Mobility of Triacontane/Triacontanol Molecules Adsorbed on Graphite. *J. Phys. Chem.* **1995**, *99*, 6608-6619.
- (102) Dishner, M. H.; Ivey, M. M.; Gorer, S.; Hemminger, J. C.; Feher, F. J. Preparation of gold thin films by epitaxial growth on mica and the effect of flame annealing. *Journal of Vacuum Science & Technology, A: Vacuum, Surfaces, and Films* **1998**, *16*, 3295-3300.
- (103) Nogues, C.; Wanunu, M. A rapid approach to reproducible, atomically flat gold films on mica. *Surface Science* **2004**, *573*, L383-L389.
- (104) Kolb, D. M. Reconstruction phenomena at metal-electrolyte interfaces. *Progress in Surface Science* **1996**, *51*, 109-73.
- (105) Kibler, L. A., University of Ulm, Preparation and Characterization of Noble Metal Single Crystal Electrode Surfaces 2003.
- (106) Han, P.; Mantooth, B. A.; Sykes, E. C. H.; Donhauser, Z. J.; Weiss, P. S. Benzene on Au{111} at 4 K: Monolayer Growth and Tip-Induced Molecular Cascades. *J. Am. Chem. Soc.* **2004**, *126*, 10787-10793.
- (107) Barth, J. V.; Brune, H.; Ertl, G.; Behm, R. J. Scanning tunneling microscopy observations on the reconstructed Au(111) surface: Atomic structure, long-range superstructure, rotational domains, and surface defects. *Physical Review B* **1990**, *42*, 9307.
- (108) Becker, T.; Hövel, H.; Tschudy, M.; Reihl, B. Applications with a new low-temperature UHV STM at 5 K. *Applied Physics A: Materials Science & Processing* **1998**, *66*, S27-S30.
- (109) Sondag-Huethorst, J. A. M.; Schonenberger, C.; Fokkink, L. G. J. Formation of Holes in Alkanethiol Monolayers on Gold. *J. Phys. Chem.* **1994**, *98*, 6826-6834.

- (110) Riposan, A.; Liu, G. y. Significance of Local Density of States in the Scanning Tunneling Microscopy Imaging of Alkanethiol Self-Assembled Monolayers. *J. Phys. Chem. B* **2006**, *110*, 23926-23937.
- (111) Poirier, G. Characterization of Organosulfur Molecular Monolayers on Au(111) using Scanning Tunneling Microscopy. *Chem. Rev.* **1997**, *97*, 1117-1128.
- (112) Hicks, E. M.; Zhang, X.; Zou, S.; Lyandres, O.; Spears, K. G.; Schatz, G. C.; VanDuyne, R. P. Plasmonic Properties of Film over Nanowell Surfaces Fabricated by Nanosphere Lithography. *J. Phys. Chem. B* **2005**, *109*, 22351-22358.
- (113) Horcas, I.; Fernandez, R.; Gomez-Rodriguez, J. M.; Colchero, J.; Gomez-Herrero, J.; Baro, A. M. WSXM: A software for scanning probe microscopy and a tool for nanotechnology. *Review of Scientific Instruments* **2007**, *78*, 013705.
- (114) Datta, S. *Quantum Transport: Atom to Transistor*; Cambridge University Press, 2005.
- (115) Shu, C.; Li, C. Z.; He, H. X.; Bogozzi, A.; Bunch, J. S.; Tao, N. J. Fractional Conductance Quantization in Metallic Nanoconstrictions under Electrochemical Potential Control. *Physical Review Letters* **2000**, *84*, 5196-5199.
- (116) Xu, B.; Xiao, X.; Yang, X.; Zang, L.; Tao, N. Large gate modulation in the current of a room temperature single molecule transistor. *Journal of the American Chemical Society* **2005**, *127*, 2386-2387.
- (117) Ulrich, J.; Esrail, D.; Pontius, W.; Venkataraman, L.; Millar, D.; Doerrer, L. H. Variability of Conductance in Molecular Junctions. *J. Phys. Chem. B* **2006**, *110*, 2462-2466.
- (118) Nitzan, A.; Ratner Mark, A. Electron transport in molecular wire junctions. *Science* **2003**, *300*, 1384-9.
- (119) Wan, L. J.; Terashima, M.; Noda, H.; Osawa, M. Molecular Orientation and Ordered Structure of Benzenethiol Adsorbed on Gold(111). *J. Phys. Chem. B* **2000**, *104*, 3563-3569.
- (120) Yoshimoto, S. Molecular Assemblies of Functional Molecules on Gold Electrode Surfaces Studied by Electrochemical Scanning Tunneling Microscopy: Relationship between Function and Adlayer Structures. *Bulletin of the Chemical Society of Japan* **2006**, *79*, 1167-1190.
- (121) Seo, K.; Borguet, E. Potential-Induced Structural Change in a Self-Assembled Monolayer of 4-Methylbenzenethiol on Au(111). *J. Phys. Chem. C* **2007**, *111*, 6335-6342.
- (122) Yang, Y. C.; Yau, S. L.; Lee, Y. L. Electrodeposition of Au Monolayer on Pt(111) Mediated by Self-Assembled Monolayers. *J. Am. Chem. Soc.* **2006**, *128*, 3677-3682.

- (123) Kin, L. W.; Ki-Young, K.; Ludwig, B. Surface dynamics of benzenethiol molecules on Cu(111). *Applied Physics Letters* **2006**, *88*, 183106.
- (124) Noh, J.; Hara, M. Final phase of alkanethiol self-assembled monolayers on Au(111). *Langmuir* **2002**, *18*, 1953-1956.
- (125) Noh, J.; Hara, M. Molecular-Scale Desorption Processes and the Alternating Missing-Row Phase of Alkanethiol Self-Assembled Monolayers on Au(111). *Langmuir* **2001**, *17*, 7280-7285.
- (126) Durig, U.; Novotny, L.; Michel, B.; Stalder, A. Logarithmic current-to-voltage converter for local probe microscopy. *Review of Scientific Instruments* **1997**, *68*, 3814-3816.
- (127) Venkataraman, L.; Klare, J. E.; Nuckolls, C.; Hybertsen, M. S.; Steigerwald, M. L. Dependence of single-molecule junction conductance on molecular conformation. *Nature* **2006**, *442*, 904-907.
- (128) Venkataraman, L.; Park, Y. S.; Whalley, A. C.; Nuckolls, C.; Hybertsen, M. S.; Steigerwald, M. L. Electronics and Chemistry: Varying Single-Molecule Junction Conductance Using Chemical Substituents. *Nano Lett.* **2007**, *7*, 502-506.
- (129) Quek, S. Y.; Venkataraman, L.; Choi, H. J.; Louie, S. G.; Hybertsen, M. S.; Neaton, J. B. Amine-Gold Linked Single-Molecule Circuits: Experiment and Theory. *Nano Lett.* **2007**, *7* 3477-3482.
- (130) Basch, H.; Cohen, R.; Ratner, M. A. Interface Geometry and Molecular Junction Conductance: Geometric Fluctuation and Stochastic Switching. *Nano Lett.* **2005**, *5*, 1668-1675.
- (131) Selzer, Y.; Cai, L.; Cabassi, M. A.; Yao, Y.; Tour, J. M.; Mayer, T. S.; Allara, D. L. Effect of Local Environment on Molecular Conduction: Isolated Molecule versus Self-Assembled Monolayer. *Nano Letters* **2005**, *5*, 61-65.
- (132) Ke, S.-H.; Baranger, H. U.; Yang, W. Models of electrodes and contacts in molecular electronics. *Journal of Chemical Physics* **2005**, *123*, 114701-114709.
- (133) Basch, H.; Ratner, M. A. Binding at molecule/gold transport interfaces. I. Geometry and bonding. *Journal of Chemical Physics* **2003**, *119*, 11926-11942.
- (134) Basch, H.; Ratner, M. A. Binding at molecule/gold transport interfaces. II. Orbitals and density of states. *Journal of Chemical Physics* **2003**, *119*, 11943-11950.
- (135) Basch, H.; Ratner, M. A. Molecular binding at gold transport interfaces. III. Field dependence of electronic properties. *Journal of Chemical Physics* **2004**, *120*, 5761-5770.

- (136) Bauschlicher, C. W.; Lawson, J. W.; Ricca, A.; Xue, Y.; Ratner, M. A. Current-voltage curves for molecular junctions: the effect of Cl substituents and basis set composition. *Chemical Physics Letters* **2004**, *388*, 427-429.
- (137) Forzani, E. S.; Zhang, H.; Nagahara, L. A.; Amlani, I.; Tsui, R.; Tao, N. A Conducting Polymer Nanojunction Sensor for Glucose Detection. *Nano Letters* **2004**, *4*, 1785-1788.
- (138) Xue, Y.; Ratner, M. A. Theoretical principles of single-molecule electronics: A chemical and mesoscopic view. *International Journal of Quantum Chemistry* **2005**, *102*, 911-924.
- (139) Tian, W.; Datta, S.; Hong, S.; Reifengerger, R.; Henderson, J. I.; Kubiak, C. P. Conductance spectra of molecular wires. *Journal of Chemical Physics* **1998**, *109*, 2874-2882.
- (140) Xue, Y.; Datta, S.; Ratner, M. A. Charge transfer and "band lineup" in molecular electronic devices: A chemical and numerical interpretation. *Journal of Chemical Physics* **2001**, *115*, 4292-4299.
- (141) Schmidt, M. W.; Baldrige, K. K., et al. General atomic and molecular electronic structure system. *Journal of Computational Chemistry* **1993**, *14*, 1347-63.
- (142) Ohno, T. R.; Chen, Y.; Harvey, S. E.; Kroll, G. H.; Weaver, J. H.; Haufler, R. E.; Smalley, R. E. Fullerene (C60) bonding and energy-level alignment on metal and semiconductor surfaces. *Physical Review B: Condensed Matter and Materials Physics* **1991**, *44*, 13747-55.
- (143) Paulsson, M.; Stafstrom, S. Self-consistent-field study of conduction through conjugated molecules. *Physical Review B: Condensed Matter and Materials Physics* **2001**, *64*, 035416/1-035416/10.
- (144) Tersoff, J. Theory of semiconductor heterojunctions: The role of quantum dipoles. *Physical Review B: Condensed Matter and Materials Physics* **1984**, *30*, 4874-7.
- (145) Jortner, J.; Nitzan, A.; Ratner, M. A. In *In Introducing Molecular Electronics*; Cuniberti, G., Fagas, G., Richter, K., Eds.; Springer-Verlag: Berlin, 2005.
- (146) Zahid, F.; Ghosh, A. W.; Paulsson, M.; Polizzi, E.; Datta, S. Charging-induced asymmetry in molecular conductors. *Physical Review B: Condensed Matter and Materials Physics* **2004**, *70*, 245317/1-245317/5.
- (147) Ochs, R.; Secker, D.; Elbing, M.; Mayor, M.; Weber, H. B. Fast temporal fluctuations in single-molecule junctions. *Faraday Discussions* **2006**, *131*, 281-289.
- (148) Moore, A. M.; Dameron, A. A., et al. Molecular Engineering and Measurements To Test Hypothesized Mechanisms in Single Molecule Conductance Switching. *J. Am. Chem. Soc.* **2006**, *128*, 1959-1967.

- (149) Datta, S. Electrical resistance: an atomistic view. *Nanotechnology* **2004**, *15*, S433–S451.
- (150) Chen, F.; Hihath, J.; Huang, Z.; Li, X.; Tao, N. J. Measurement of Single-Molecule Conductance. *Annual Review of Physical Chemistry* **2007**, *58*, 535-564
- (151) A. Landau; L. Kronik; Nitzan, A. Cooperative effects in molecular conduction. *Condensed Matter* **2007**.
- (152) Hu, Y.; Zhu, Y.; Gao, H.; Guo, H. Conductance of an Ensemble of Molecular Wires: A Statistical Analysis. *Physical Review Letters* **2005**, *95*, 156803-4.
- (153) Geng, W. T.; Jun, N.; Takahisa, O. Impacts of metal electrode and molecule orientation on the conductance of a single molecule. *Applied Physics Letters* **2004**, *85*, 5992-5994.
- (154) Hu, W.; Jiang, J., et al. Electron Transport in Self-Assembled Polymer Molecular Junctions. *Physical Review Letters* **2006**, *96*, 027801-4.
- (155) Solomon, G. C.; Reimers, J. R.; Hush, N. S. Overcoming computational uncertainties to reveal chemical sensitivity in single molecule conduction calculations. *The Journal of Chemical Physics* **2005**, *122*, 224502.
- (156) Jang, S. S.; Jang, Y. H., et al. Structures and Properties of Self-Assembled Monolayers of Bistable [2]Rotaxanes on Au (111) Surfaces from Molecular Dynamics Simulations Validated with Experiment. *J. Am. Chem. Soc.* **2005**, *127*, 1563-1575.
- (157) Jang, Y. H.; Jang, S. S.; Goddard, W. A. Molecular Dynamics Simulation Study on a Monolayer of Half [2]Rotaxane Self-Assembled on Au(111). *J. Am. Chem. Soc.* **2005**, *127*, 4959-4964.
- (158) Kim, Y.-H.; Jang, S. S.; Goddard, W. A. Conformations and charge transport characteristics of biphenyldithiol self-assembled-monolayer molecular electronic devices: A multiscale computational study. *The Journal of Chemical Physics* **2005**, *122*, 244703.
- (159) Humphrey, W.; Dalke, A.; Schulten, K. VMD - Visual Molecular Dynamics. *J. Molec. Graphics* **1996**, *14*, 33-38.
- (160) Allinger, N. L.; Yuh, Y. H.; Lii, J. H. Molecular mechanics. The MM3 force field for hydrocarbons. 1. *J. Am. Chem. Soc.* **1989**, *111*, 8551-8566.
- (161) Lii, J. H.; Allinger, N. L. Molecular mechanics. The MM3 force field for hydrocarbons. 2. Vibrational frequencies and thermodynamics. *J. Am. Chem. Soc.* **1989**, *111*, 8566-8575.
- (162) Lii, J. H.; Allinger, N. L. Molecular mechanics. The MM3 force field for hydrocarbons. 3. The van der Waals' potentials and crystal data for aliphatic and aromatic hydrocarbons. *J. Am. Chem. Soc.* **1989**, *111*, 8576-8582.

- (163) Nagy, J.; Smith, V. H.; Weaver, D. F. Critical Evaluation of Benzene Analytical Nonbonded Force Fields. Reparametrization of the MM3 Potential. *J. Phys. Chem.* **1995**, *99*, 13868-13875.
- (164) Bilic, A.; Reimers, J. R.; Hush, N. S. The structure, energetics, and nature of the chemical bonding of phenylthiol adsorbed on the Au(111) surface: Implications for density-functional calculations of molecular-electronic conduction. *The Journal of Chemical Physics* **2005**, *122*, 094708.
- (165) Ponder, J. W.; 4.2 ed.; Washington University School of Medicine: 2004.
- (166) Andrews, D. Q.; Cohen, R.; Duyne, R. P. V.; Ratner, M. A. Single molecule electron transport junctions: Charging and geometric effects on conductance. *The Journal of Chemical Physics* **2006**, *125*, 174718.
- (167) Krüger, D.; Fuchs, H.; Rousseau, R.; Marx, D.; Parrinello, M. Pulling Monatomic Gold Wires with Single Molecules: An Ab Initio Simulation. *Physical Review Letters* **2002**, *89*, 186402.
- (168) Zhenyu, L.; Kosov, D. S. Nature of well-defined conductance of amine-anchored molecular junctions: Density functional calculations. *Physical Review B (Condensed Matter and Materials Physics)* **2007**, *76*, 035415.
- (169) García-Suárez, V. M.; Kostyrko, T.; Bailey, S.; Lambert, C.; Bulka, B. R. Study of the transport properties of a molecular junction as a function of the distance between the leads. *physica status solidi (b)* **2007**, *244*, 2443-2447.
- (170) Romaner, L.; Heimel, G.; Gruber, M.; Brédas, J.-L.; Zojer, E. Stretching and Breaking of a Molecular Junction. *Small* **2006**, *2*, 1468-1475.
- (171) Foley, E. 2008.
- (172) Y Hasegawa et al... Retrieved 06/05/08, [http://www.rhk-tech.com/results/Low-Temperature-STM-image-of-Si\(100\).php](http://www.rhk-tech.com/results/Low-Temperature-STM-image-of-Si(100).php).
- (173) Jens, S.; Bruno, P. High-resolution microscope for tip-enhanced optical processes in ultrahigh vacuum. *Review of Scientific Instruments* **2007**, *78*, 103104.
- (174) Tian, J. H.; Liu, B.; Li, X. L.; Yang, Z. L.; Ren, B.; Wu, S. T.; Tao, N. J.; Tian, Z. Q. Study of Molecular Junctions with a Combined Surface-Enhanced Raman and Mechanically Controllable Break Junction Method. *J. Am. Chem. Soc.* **2006**, *128*, 14748-14749.
- (175) Encai, H.; George, C. S. Electromagnetic fields around silver nanoparticles and dimers. *The Journal of Chemical Physics* **2004**, *120*, 357-366.

- (176) Ward, D. R.; Grady, N. K.; Levin, C. S.; Halas, N. J.; Wu, Y.; Nordlander, P.; Natelson, D. Electromigrated Nanoscale Gaps for Surface-Enhanced Raman Spectroscopy. *Nano Lett.* **2007**, *7*, 1396-1400.
- (177) Ward, D. R.; Halas, N. J.; Ciszek, J. W.; Tour, J. M.; Wu, Y.; Nordlander, P.; Natelson, D. Simultaneous Measurements of Electronic Conduction and Raman Response in Molecular Junctions. *Nano Lett.* **2008**, *8*, 919-924.
- (178) Akkerman, H. B.; Naber, R. C. G.; Jongbloed, B.; van Hal, P. A.; Blom, P. W. M.; de Leeuw, D. M.; de Boer, B. Electron tunneling through alkanedithiol self-assembled monolayers in large-area molecular junctions. *Proceedings of the National Academy of Sciences* **2007**, *104*, 11161-11166.
- (179) Nitzan, A. Electron Transmission Through Molecules and Molecular Interfaces. *Annual Review of Physical Chemistry* **2001**, *52*, 681-750.
- (180) Emberly, E. G.; George, K. Antiresonances in molecular wires. *Journal of Physics: Condensed Matter* **1999**, 6911.
- (181) Mayor, M.; Weber, H. B.; Reichert, J.; Elbing, M.; Hänisch, C. v.; Beckmann, D.; Fischer, M. Electric Current through a Molecular Rod - Relevance of the Position of the Anchor Groups. *Angewandte Chemie International Edition* **2003**, *42*, 5834-5838.
- (182) Hush, N. S. Retrieved 5/01/08, <http://www.physics.uq.edu.au/cmp-workshop/Forms/hush.ppt>.
- (183) Marcus, R. A.; Sutin, N. *Biochimica et Biophysica Acta* **1985**, *811*, 265.
- (184) Reimers, J. R.; Hall, L. E.; Crossley, M. J.; Hush, N. S. Rigid Fused Oligoporphyrins as Potential Versatile Molecular Wires. 2. B3LYP and SCF Calculated Geometric and Electronic Properties of 98 Oligoporphyrin and Related Molecules. *J. Phys. Chem. A* **1999**, *103*, 4385-4397.
- (185) Moser, C. C.; Keske, J. M.; Warncke, K.; Farid, R. S.; Dutton, P. L. Nature of biological electron transfer. *Nature* **1992**, *355*, 796-802.
- (186) Tombros, N.; Jozsa, C.; Popinciuc, M.; Jonkman, H. T.; van Wees, B. J. Electronic spin transport and spin precession in single graphene layers at room temperature. *Nature* **2007**, *448*, 571-574.
- (187) Liljeroth, P.; Repp, J.; Meyer, G. Current-Induced Hydrogen Tautomerization and Conductance Switching of Naphthalocyanine Molecules. *Science* **2007**, *317*, 1203-1206.
- (188) Metzger, R. M.; Chen, B., et al. Unimolecular Electrical Rectification in Hexadecylquinolinium Tricyanoquinodimethanide. *J. Am. Chem. Soc.* **1997**, *119*, 10455-10466.

- (189) Metzger, R. M. Unimolecular Electrical Rectifiers. *Chem. Rev.* **2003**, *103*, 3803-3834.
- (190) Elbing, M.; Ochs, R.; Koentopp, M.; Fischer, M.; von Hanisch, C.; Weigend, F.; Evers, F.; Weber, H. B.; Mayor, M. Molecular Electronics Special Feature: A single-molecule diode. *Proceedings of the National Academy of Sciences* **2005**, *102*, 8815-8820.
- (191) Guisinger, N. P.; Greene, M. E.; Basu, R.; Baluch, A. S.; Hersam, M. C. Room Temperature Negative Differential Resistance through Individual Organic Molecules on Silicon Surfaces. *Nano Letters* **2004**, *4*, 55-59.
- (192) Flood, A. H.; Stoddart, J. F.; Steuerman, D. W.; Heath, J. R. CHEMISTRY: Enhanced: Whence Molecular Electronics? *Science* **2004**, *306*, 2055-2056.
- (193) Kubatkin, S.; Danilov, A.; Hjort, M.; Cornil, J.; Bredas, J.-L.; Stuhr-Hansen, N.; Hedegard, P.; Bjornholm, T. Single-electron transistor of a single organic molecule with access to several redox states. *Nature* **2003**, *425*, 698-701.
- (194) Danilov, A. V.; Kubatkin, S. E.; Kafanov, S. G.; Bjornholm, T. Strong electronic coupling between single C60 molecules and gold electrodes prepared by quench condensation at 4 K. A single molecule three terminal device study. *Faraday Discussions* **2006**, *131*, 337-345.
- (195) Yu, L. H.; Natelson, D. Transport in single-molecule transistors: Kondo physics and negative differential resistance. *Nanotechnology* **2004**, S517.
- (196) Zant, H. S. J. v. d.; Kervennic, Y.-V., et al. Molecular three-terminal devices: fabrication and measurements. *Faraday Discussions* **2006**, *131*, 347-356.
- (197) Albrecht, T.; Albrecht, T.; Guckian, A.; Ulstrup, J.; Vos, J. G. A. V. J. G. Transistor effects and in situ STM of redox molecules at room temperature
Transistor effects and in situ STM of redox molecules at room temperature. *Nanotechnology, IEEE Transactions on* **2005**, *4*, 430-434.
- (198) Tao, N. Measurement and control of single molecule conductance. *Journal of Materials Chemistry* **2005**, *15*, 3260-3263.
- (199) Li, X.; He, J.; Hihath, J.; Xu, B.; Lindsay, S. M.; Tao, N. Conductance of Single Alkanedithiols: Conduction Mechanism and Effect of Molecule-Electrode Contacts. *J. Am. Chem. Soc.* **2006**, *128*, 2135-2141.
- (200) Hais, W.; vanZalinge, H.; Higgins, S. J.; Bethell, D.; Hobenreich, H.; Schiffrin, D. J.; Nichols, R. J. Redox State Dependence of Single Molecule Conductivity. *J. Am. Chem. Soc.* **2003**, *125*, 15294-15295.
- (201) Chen, F.; He, J.; Nuckolls, C.; Roberts, T.; Klare, J. E.; Lindsay, S. A Molecular Switch Based on Potential-Induced Changes of Oxidation State. *Nano Lett.* **2005**, *5*, 503-506.

- (202) Zhang, C.; He, Y.; Cheng, H.-P.; Xue, Y.; Ratner, M. A.; Zhang, X. G.; Krstic, P. Current-voltage characteristics through a single light-sensitive molecule. *Physical Review B (Condensed Matter and Materials Physics)* **2006**, *73*, 125445.
- (203) Troisi, A.; Ratner, M. A. Conformational Molecular Rectifiers. *Nano Letters* **2004**, *4*, 591-595.
- (204) He, J.; Chen, F., et al. Switching of a photochromic molecule on gold electrodes: single-molecule measurements. *Nanotechnology* **2005**, *16*, 695.
- (205) Galperin, M.; Ratner, M. A.; Nitzan, A.; Troisi, A. Nuclear Coupling and Polarization in Molecular Transport Junctions: Beyond Tunneling to Function. *Science* **2008**, *319*, 1056-1060.
- (206) Collier, C. P.; Mattersteig, G.; Wong, E. W.; Luo, Y.; Beverly, K.; Sampaio, J.; Raymo, F. M.; Stoddart, J. F.; Heath, J. R. A [2]Catenane-Based Solid State Electronically Reconfigurable Switch. *Science* **2000**, *289*, 1172-1175.
- (207) Moresco, F.; Meyer, G.; Rieder, K.-H.; Tang, H.; Gourdon, A.; Joachim, C. Conformational Changes of Single Molecules Induced by Scanning Tunneling Microscopy Manipulation: A Route to Molecular Switching. *Physical Review Letters* **2001**, *86*, 672.
- (208) Armstrong, N.; Hoft, R. C.; McDonagh, A.; Cortie, M. B.; Ford, M. J. Exploring the Performance of Molecular Rectifiers: Limitations and Factors Affecting Molecular Rectification. *Nano Lett.* **2007**, *7*, 3018-3022.
- (209) Zahid, F.; Paulsson, M.; Polizzi, E.; Ghosh, A. W.; Siddiqui, L.; Datta, S. A self-consistent transport model for molecular conduction based on extended Huckel theory with full three-dimensional electrostatics. *The Journal of Chemical Physics* **2005**, *123*, 064707.
- (210) Sautet, P.; Joachim, C. Electronic interference produced by a benzene embedded in a polyacetylene chain. *Chemical Physics Letters* **1988**, *153*, 511-516.
- (211) Simmons, J. G. Generalized Formula for the Electric Tunnel Effect between Similar Electrodes Separated by a Thin Insulating Film. *Journal of Applied Physics* **1963**, *34*, 1793-1803.
- (212) Simmons, J. G. Low-Voltage Current-Voltage Relationship of Tunnel Junctions. *Journal of Applied Physics* **1963**, *34*, 238-239.
- (213) Grave, C.; Risko, C.; Shaporenko, A.; Wang, Y.; Nuckolls, C.; Ratner, M. A.; Rampi, M. A.; Zharnikov, M. Charge Transport through Oligoarylene Self-assembled Monolayers: Interplay of Molecular Organization, Metal-Molecule Interactions, and Electronic Structure. *Advanced Functional Materials* **2007**, *17*, 3816-3828.

- (214) Solomon, G. C.; Andrews, D. Q.; Goldsmith, R. H.; Hansen, T.; Wasielewski, M. R.; Duynes, R. P. V.; Ratner, M. A. Understanding quantum interference in molecular conduction. *submitted* **2008**.
- (215) Yacoby, A.; Helblum, M.; Mahalu, D.; Shtrikman, H. Coherence and phase sensitive measurements in a quantum dot. *Solid-State Electronics* **1996**, *40*, 225-231.
- (216) Aihara, K.; Yamamoto, M.; Mizutani, T. Three-terminal conductance modulation of a quantum interference device using a quantum wire with a stub structure. *Applied Physics Letters* **1993**, *63*, 3595-3597.
- (217) Debray, P.; Raichev, O. E.; Vasilopoulos, P.; Rahman, M.; Perrin, R.; Mitchell, W. C. Ballistic electron transport in stubbed quantum waveguides: Experiment and theory. *Physical Review B* **2000**, *61*, 10950.
- (218) Datta, S. Quantum devices. *Superlattices and Microstructures* **1989**, *6*, 83-93.
- (219) Schuster, R.; Buks, E.; Heiblum, M.; Mahalu, D.; Umansky, V.; Shtrikman, H. Phase measurement in a quantum dot via a double-slit interference experiment. *Nature* **1997**, *385*, 417-420.
- (220) Lee, H. W. Generic Transmission Zeros and In-Phase Resonances in Time-Reversal Symmetric Single Channel Transport. *Physical Review Letters* **1999**, *82*, 2358.
- (221) Sols, F.; Macucci, M.; Ravaioli, U.; Hess, K. On the possibility of transistor action based on quantum interference phenomena. *Applied Physics Letters* **1989**, *54*, 350-352.
- (222) Kobayashi, K.; Aikawa, H.; Sano, A.; Katsumoto, S.; Iye, Y. Fano resonance in a quantum wire with a side-coupled quantum dot. *Physical Review B* **2004**, *70*, 035319.
- (223) Mitin, V. V.; Kochelap, V. A.; Stroscio, M. A. *Introduction to Nanoelectronics*; 1 ed.; Cambridge University Press: Cambridge, 2008.
- (224) Walter, D.; Neuhauser, D.; Baer, R. Quantum interference in polycyclic hydrocarbon molecular wires. *Chemical Physics* **2004**, *299*, 139-145.
- (225) Goyer, F.; Ernzerhof, M.; Zhuang, M. Source and sink potentials for the description of open systems with a stationary current passing through. *Journal of Chemical Physics* **2007**, *126*, 144104-8.
- (226) Kalyanaraman, C.; Evans, D. G. Molecular Conductance of Dendritic Wires. *Nano Lett.* **2002**, *2*, 437-441.

- (227) Collepardo-Guevara, R.; Walter, D.; Neuhauser, D.; Baer, R. A Hückel study of the effect of a molecular resonance cavity on the quantum conductance of an alkene wire. *Chemical Physics Letters* **2004**, *393*, 367-371.
- (228) Lindsay, S. M.; Ratner, M. A. Molecular Transport Junctions: Clearing Mists. *Advanced Materials* **2007**, *19*, 23-31.
- (229) Solomon, G. C.; Andrews, D. Q.; Goldsmith, R. H.; Hansen, T.; Wasielewski, M. R.; Duyne, R. P. V.; Ratner, M. A. Quantum interference in acyclic systems: The unexpected conductance of cross-conjugated molecules. *submitted* **2008**.
- (230) Itakura, K.; Yuki, K.; Kurokawa, S.; Yasuda, H.; Sakai, A. Bias dependence of the conductance of Au nanocontacts. *Physical Review B* **1999**, *60*, 11163.
- (231) Zheng, T.; Jia, H.; Wallace, R. M.; Gnade, B. E. Characterization of conductance under finite bias for a self-assembled monolayer coated Au quantized point contact. *Applied Surface Science* **2006**, *253*, 1265-1268.
- (232) Yasuda, H.; Sakai, A. Conductance of atomic-scale gold contacts under high-bias voltages. *Physical Review B* **1997**, *56*, 1069.
- (233) Landauer, R. Electrical resistance of disordered one-dimensional lattices. *Philosophical Magazine* **1970**, *21*, 863 - 867.
- (234) Lee, C.; Yang, W.; Parr, R. G. Development of the Colce-Salvetti correlation-energy formula into a functional of the electron density. *Phys. Rev. B* **1988**, *37*, 785.
- (235) Becke, A. D. Density-functional thermochemistry. III. The role of exact exchange. *J. Chem. Phys.* **1993**, *98*, 5648-52.
- (236) Shao, Y.; Molnar, L. F., et al. Advances in methods and algorithms in a modern quantum chemistry program package. *Physical Chemistry Chemical Physics* **2006**, *8*, 3172-3191.
- (237) Andrews, D. Q.; Duyne, R. P. V.; Ratner, M. A. Stochastic modulation in molecular electronic transport Junctions: Molecular dynamics coupled with charge transport calculations. *submitted* **2008**.
- (238) Solomon, G. C.; Gagliardi, A.; Pecchia, A.; Frauenheim, T.; Carlo, A. D.; Reimers, J. R.; Hush, N. S. The symmetry of single-molecule conduction. *The Journal of Chemical Physics* **2006**, *125*, 184702.
- (239) Tykwinski, R.; Zhao, Y. Cross-Conjugated Oligo(enynes). *Synlett* **2002**, 1939-1953.
- (240) Gholami, M.; Tykwinski, R. R. Oligomeric and Polymeric Systems with a Cross-conjugated π -Framework. *Chem. Rev.* **2006**, *106*, 4997-5027.

- (241) Papadopoulos, T. A.; Grace, I. M.; Lambert, C. J. Control of electron transport through Fano resonances in molecular wires. *Physical Review B: Condensed Matter* **2006**, *74*, 193306.
- (242) Cardamone, D. M.; Stafford, C. A.; Mazumdar, S. Controlling Quantum Transport through a Single Molecule. *Nano Lett.* **2006**, *6*, 2422-2426.
- (243) Cross Conjugation. Retrieved 8/12/2007, <http://en.wikipedia.org/wiki/Cross-conjugation>.
- (244) Phelan, N. F.; Orchin, M. Cross Conjugation. *Journal of Chemical Education* **1968**, *45*, 633-637.
- (245) Bruschi, M.; Giuffreda, M. G.; Lüthi, H. P. Through versus Cross Electron Delocalization in Polytriacetylene Oligomers: A Computational Analysis. *ChemPhysChem* **2005**, *6*, 511-519.
- (246) Bruschi, M.; Giuffreda, M. G.; Lüthi, H. P. trans versus geminal Electron Delocalization in Tetra- and Diethynylethenes: A New Method of Analysis. *Chemistry - A European Journal* **2002**, *8*, 4216-4227.
- (247) van der Veen, M. H.; Rispens, M. T.; Jonkman, H. T.; Hummelen, J. C. Molecules with Linear pi - Conjugated Pathways between All Substituents: Omniconjugation. *Advanced Functional Materials* **2004**, *14*, 215-223.
- (248) Moonen, N. N. P.; Pomerantz, W. C., et al. Donor-substituted cyanoethynylethenes: pi-Conjugation and band-gap tuning in strong charge-transfer chromophores. *Chemistry-a European Journal* **2005**, *11*, 3325-3341.
- (249) Walree, Cornelis A. v.; Kaats-Richters, Veronica E. M.; Veen, Sandra J.; Wieczorek, B.; Wiel, Johanna H. van d.; Wiel, Bas C. van d. Charge-Transfer Interactions in 4-Donor 4'-Acceptor Substituted 1,1-Diphenylethenes. *European Journal of Organic Chemistry* **2004**, *2004*, 3046-3056.
- (250) Kuznetsov, A. M.; Ulstrup, J. *Electron Transfer in Chemistry and Biology*; Wiley: Chichester, UK, 1999.
- (251) Hoffmann, R. Interaction of orbitals through space and through bonds. *Acc. Chem. Res.* **1971**, *4*, 1-9.
- (252) Giuffreda, M. G.; Bruschi, M.; Lüthi, H. P. Electron Delocalization in Linearly -Conjugated Systems: A Concept for Quantitative Analysis. *Chemistry - A European Journal* **2004**, *10*, 5671-5680.
- (253) Soler, J. M.; Artacho, E.; Gale, J. D.; García, A.; Junquera, J.; Ordejón, P.; Sánchez-Portal, D. The SIESTA method for ab initio order-N materials simulation. *Journal of Physics: Condensed Matter* **2002**, *14*, 2745-2779.

- (254) Hush, N. S. Homogeneous and heterogeneous optical and thermal electron transfer. *Electrochimica Acta* **1968**, *13*, 1005.
- (255) Nitzan, A. A Relationship between Electron-Transfer Rates and Molecular Conduction. *J. Phys. Chem. A* **2001**, *105*, 2677-2679.
- (256) Skinner, J. L.; Hsu, D. Pure dephasing of a two-level system. *J. Phys. Chem.* **1986**, *90*, 4931-4938.
- (257) Segal, D.; Nitzan, A. Steady-state quantum mechanics of thermally relaxing systems. *Chemical Physics* **2001**, *268*, 315-335.
- (258) Leggett, A. J.; Chakravarty, S.; Dorsey, A. T.; Fisher, M. P. A.; Garg, A.; Zwirger, W. Dynamics of the dissipative two-state system. *Reviews of Modern Physics* **1987**, *59*, 1.
- (259) Goldsmith, R. H.; Wasielewski, M. R.; Ratner, M. A. Scaling Laws for Charge Transfer in Multiply Bridged Donor/Acceptor Molecules in a Dissipative Environment. *J. Am. Chem. Soc.* **2007**, *129*, 13066-13071.
- (260) Goldsmith, R. H.; Wasielewski, M. R.; Ratner, M. A. Electron Transfer in Multiply Bridged Donor-Acceptor Molecules: Dephasing and Quantum Coherence. *Journal of Physical Chemistry B* **2006**, *110*, 20258-20262.
- (261) Davis, W. B.; Wasielewski, M. R.; Ratner, M. A.; Mujica, V.; Nitzan, A. Electron Transfer Rates in Bridged Molecular Systems: A Phenomenological Approach to Relaxation. *J. Phys. Chem. A* **1997**, *101*, 6158-6164.
- (262) Cherepy, N. J.; Shreve, A. P.; Moore, L. J.; Boxer, S. G.; Mathies, R. A. Electronic and Nuclear Dynamics of the Accessory Bacteriochlorophylls in Bacterial Photosynthetic Reaction Centers from Resonance Raman Intensities. *J. Phys. Chem. B* **1997**, *101*, 3250-3260.
- (263) Kennedy, S. P.; Garro, N.; Phillips, R. T. Coherent Control of Optical Emission from a Conjugated Polymer. *Physical Review Letters* **2001**, *86*, 4148.
- (264) Milota, F.; Sperling, J.; Szocs, V.; Tortschanoff, A.; Kauffmann, H. F. Correlation of femtosecond wave packets and fluorescence interference in a conjugated polymer: Towards the measurement of site homogeneous dephasing. *The Journal of Chemical Physics* **2004**, *120*, 9870-9885.
- (265) Myers, A. B. Molecular Electronic Spectral Broadening in Liquids and Glasses. *Annual Review of Physical Chemistry* **1998**, *49*, 267-295.
- (266) Mohamad, T.; Gerald, J. S.; Shaul, M. Nonlinear optical response functions for a chromophore with linear and quadratic electron--vibration coupling. *The Journal of Chemical Physics* **1999**, *110*, 1017-1024.

- (267) Sension, R. J. Biophysics: Quantum path to photosynthesis. *Nature* **2007**, *446*, 740-741.
- (268) Lee, H.; Cheng, Y.-C.; Fleming, G. R. Coherence Dynamics in Photosynthesis: Protein Protection of Excitonic Coherence. *Science* **2007**, *316*, 1462-1465.
- (269) Li, C.; Pobelov, I.; Wandlowski, T.; Bagrets, A.; Arnold, A.; Evers, F. Charge Transport in Single Au | Alkanedithiol | Au Junctions: Coordination Geometries and Conformational Degrees of Freedom. *J. Am. Chem. Soc.* **2008**, *130*, 318-326.
- (270) Patoux, C.; Coudret, C.; Launay, J. P.; Joachim, C.; Gourdon, A. Topological Effects on Intramolecular Electron Transfer via Quantum Interference. *Inorg. Chem.* **1997**, *36*, 5037-5049.
- (271) Yaliraki, S. N.; Ratner, M. A. Interplay of Topology and Chemical Stability on the Electronic Transport of Molecular Junctions. *Ann NY Acad Sci* **2002**, *960*, 153-162.
- (272) Reddy, P.; Jang, S.-Y.; Segalman, R. A.; Majumdar, A. Thermoelectricity in Molecular Junctions. *Science* **2007**, *315*, 1568-1571.
- (273) Zhitenev, N. B.; Meng, H.; Bao, Z. Conductance of Small Molecular Junctions. *Physical Review Letters* **2002**, *88*, 226801.
- (274) Dadosh, T.; Gordin, Y.; Krahne, R.; Khivrich, I.; Mahalu, D.; Frydman, V.; Sperling, J.; Yacoby, A.; Bar-Joseph, I. Measurement of the conductance of single conjugated molecules. *Nature* **2005**, *436*, 677-680.
- (275) Cho, J.; Zhao, Y.; Tykwinski, R. R. Synthesis and characterization of cross-conjugated oligo(phenylene enynylene)s. *ARKIVOC* **2005**, (iv), 142-150.
- (276) Miller, O. D.; Muralidharan, B.; Kapur, N.; Ghosh, A. W. Rectification by charging: Contact-induced current asymmetry in molecular conductors. *Physical Review B (Condensed Matter and Materials Physics)* **2008**, *77*, 125427-10.
- (277) Scott, G. D.; Chichak, K. S.; Peters, A. J.; Cantrill, S. J.; Stoddart, J. F.; Jiang, H. W. Mechanism of enhanced rectification in unimolecular Borromean ring devices. *Physical Review B (Condensed Matter and Materials Physics)* **2006**, *74*, 113404-4.
- (278) Reichert, J.; Ochs, R.; Beckmann, D.; Weber, H. B.; Mayor, M.; Löhneysen, H. v. Driving Current through Single Organic Molecules. *Physical Review Letters* **2002**, *88*, 176804.
- (279) Meinhard, J. E. Organic Rectifying Junction. *Journal of Applied Physics* **1964**, *35*, 3059-3060.
- (280) Zhou, C.; Deshpande, M. R.; Reed, M. A.; L. Jones, I.; Tour, J. M. Nanoscale metal/self-assembled monolayer/metal heterostructures. *Applied Physics Letters* **1997**, *71*, 611-613.

- (281) Ashwell, G. J.; Urasinska, B.; Tyrrell, W. D. Molecules that mimic Schottky diodes. *Physical Chemistry Chemical Physics* **2006**, *8*, 3314-3319.
- (282) Metzger, R. M. Unimolecular rectifiers: Present status. *Chemical Physics* **2006**, *326*, 176-187.
- (283) Stokbro, K.; Taylor, J.; Brandbyge, M. Do Aviram-Ratner Diodes Rectify? *J. Am. Chem. Soc.* **2003**, *125*, 3674-3675.
- (284) Ashwell, G. J.; Urasinska, B.; Wang, C.; Bryce, M. R.; Grace, I.; Lambert, C. J. Single-molecule electrical studies on a 7 nm long molecular wire. *Chemical Communications* **2006**, 4706-4708.
- (285) Guisinger, N. P.; Basu, R.; Greene, M. E.; Baluch, A. S.; Hersam, M. C. Observed suppression of room temperature negative differential resistance in organic monolayers on Si(100). *Nanotechnology* **2004**, S452.
- (286) Yablonovitch, E. The Chemistry of Solid-State Electronics. *Science* **1989**, *246*, 347-351.
- (287) Guo, X.; Whalley, A.; Klare, J. E.; Huang, L.; O'Brien, S.; Steigerwald, M.; Nuckolls, C. Single-Molecule Devices as Scaffolding for Multicomponent Nanostructure Assembly. *Nano Lett.* **2007**, *7*, 1119-1122.
- (288) Dobson, C. M. Chemical space and biology. *Nature* **2004**, *432*, 824-828.

Appendix A. Computer code

This code optimizes the fit of an input dataset to a system meant to model the behavior of our pseudo logarithmic current to voltage amplifier. The amplifier is design with the feedback loop containing a resistor in parallel with a set of back to back diodes. At low current the behavior of the current to voltage converter is linear and dominated by the 10×10^9 resistor. At high current values the current to voltage behavior is dominated by the logarithmic behavior of the diodes. To fit the behavior we need only to include a resistor (Rlin) and an exponential function ($e^{(\text{expvar} * V)}$, with $V = \text{voltage}$) and two offsets (Voffset and expoffset). The program varies the four variables until the R-squared fit is minimized.

$$\text{FittedCurve (ydata)} = (\text{xdata}/\text{Rlin} + \text{Voffset}/\text{Rlin}) + \text{expoffset} * e^{(\text{expvar} * V)}$$

The input is an (x,y) file, with x = to the current input and y = output voltage. This calibration data set was created by using a resistor and calculating $V = I/R$ the current over the desired range was measured, in this case from 1×10^{-10} to 1×10^{-4} amps. The molecular imaging software does not have any way to utilize a logarithmic preamplifier so the output from the preamp is utilized by setting within the software that 1V output from the preamplifier = 1nA. Doing this means that we will only be using 1/3 of the range of the preamplifier because the maximum voltage output from the log preamp board is $\approx 3.4\text{V}$. While we are currently limiting the dynamic range we simplify the math for calibration purposes. The output of the fitting program gives an R-squared, a plot with the data points and fit line for verification, and then a plot of the residuals. Then 4 fit parameters are then output and can used in converting the voltage output from the logarithmic amplifier to get the tunneling current. It would be ideal if

this was built into the STM software. This would allow setting the tunneling current and viewing the results in real time, something that is not possible currently.

```
function fitcurvedemo(xdata, ydata)
format long
% Call fminsearch with a chosen start point.
start_point = [1.2 9.049 5e-15 1e9];
model = @expfun;
options = optimset('MaxFunEvals',10000, 'MaxIter', 10000);
estimates = fminsearch(model, start_point, options);
% expfun accepts curve parameters as inputs, and outputs sse,
% the sum of squares error for A * exp(-lambda * xdata) - ydata,
% and the FittedCurve. FMINSEARCH only needs sse, but we want to
% plot the FittedCurve at the end.
function [sse, FittedCurve] = expfun(params)
    Voffset = params(1);
    expvar = params(2);
    expoffset = params(3);
    Rlin = params(4);

    Ilog = (expoffset * exp(expvar * xdata));
    Rlog = (xdata ./ Ilog);

    rT = 1./Rlog; %
    rT3 = 1/Rlin + rT; %
    rT2 = 1./rT3; %
    fit = (Rlin - rT2) / Rlin ; % this checks out ok

    FittedCurve = (xdata/Rlin + Voffset/Rlin) + Ilog;
    ErrorVector = (ydata - FittedCurve) ./ ydata;
    sse = sum(ErrorVector .^ 2)
    R12 =corrcoef(ydata, FittedCurve);
    r12 = R12(1,2);
    r12sq = r12^2
end

h = plot(ydata, xdata, '*')
hold on
[sse, FittedCurve] = model(estimates);
plot(FittedCurve, xdata, 'r')
set(gca, 'xscale', 'log')
xlabel('xdata')
ylabel('f(estimates,xdata)')
title(['Fitting to function ', func2str(model)]);
legend('calibration data', 'fit line')
saveas(h, 'Logfit.jpg')
hold off
h = plot(ydata(:,1), ErrorVector(:,1), 'or')
set(gca, 'xscale', 'log')
saveas(h, 'Residuals.jpg')
```

```
Voffset,   expvar,   expoffset,   Rlin  
end
```

Provided is my latest test calibration file with current input in the first column and voltage output in the second column.

Current input / Voltage output

```
0.0000000010000 0.00600000000000  
0.0000000015000 0.05100000000000  
0.0000000020000 0.10600000000000  
0.0000000025000 0.14700000000000  
0.0000000030000 0.20100000000000  
0.0000000035000 0.26000000000000  
0.0000000035000 0.25500000000000  
0.0000000040000 0.30000000000000  
0.0000000045000 0.36000000000000  
0.0000000070000 0.60000000000000  
0.0000000070000 0.56500000000000  
0.0000000100000 0.90000000000000  
0.0000000140000 1.16300000000000  
0.0000000150000 1.22000000000000  
0.0000000170000 1.27700000000000  
0.0000000200000 1.34600000000000  
0.0000000250000 1.40400000000000  
0.0000000270000 1.41800000000000  
0.0000000300000 1.44600000000000  
0.0000000350000 1.47300000000000  
0.0000000400000 1.49700000000000  
0.0000000450000 1.51500000000000  
0.0000000470000 1.52200000000000  
0.0000000515000 1.52400000000000  
0.0000000700000 1.57000000000000  
0.0000000700000 1.56800000000000  
0.0000000970000 1.62100000000000  
0.0000001000000 1.62000000000000  
0.0000001030000 1.61800000000000  
0.0000001741290 1.68100000000000  
0.0000001970000 1.70300000000000  
0.0000002000000 1.70200000000000  
0.0000002060000 1.70000000000000  
0.0000003181820 1.74900000000000  
0.0000004000000 1.77800000000000  
0.0000004700000 1.80100000000000  
0.0000007000000 1.83200000000000  
0.0000007000000 1.83300000000000  
0.0000009700000 1.87900000000000
```

```
0.00000010300000 1.8730000000000000
0.00000019700000 1.9530000000000000
0.00000020000000 1.9470000000000000
0.00000025621900 1.9680000000000000
0.00000046818200 2.0310000000000000
0.00000047000000 2.0420000000000000
0.00000049751200 2.0410000000000000
0.00000070000000 2.0720000000000000
0.00000090909100 2.1040000000000000
0.00000097000000 2.1180000000000000
0.00000103000000 2.1120000000000000
0.00000197000000 2.1920000000000000
0.00000200000000 2.1870000000000000
0.00000700000000 2.3180000000000000
0.00001030000000 2.3610000000000000
```

Setting the sample calibration as a two column data set. The program is run as
fitlogamp_loglin_offset (lgdata(:,2),lgdata(:,1))

The output fit for the four parameters is given below, with an R-squared value of the fit as
0.99967.

```
r12sq = 0.99967585708088
Voffset = 0.09524544123407
expvar = 9.65082357076096
expoffset = 1.352837103378484e-015
Rlin = 9.953083416797543e+008
```

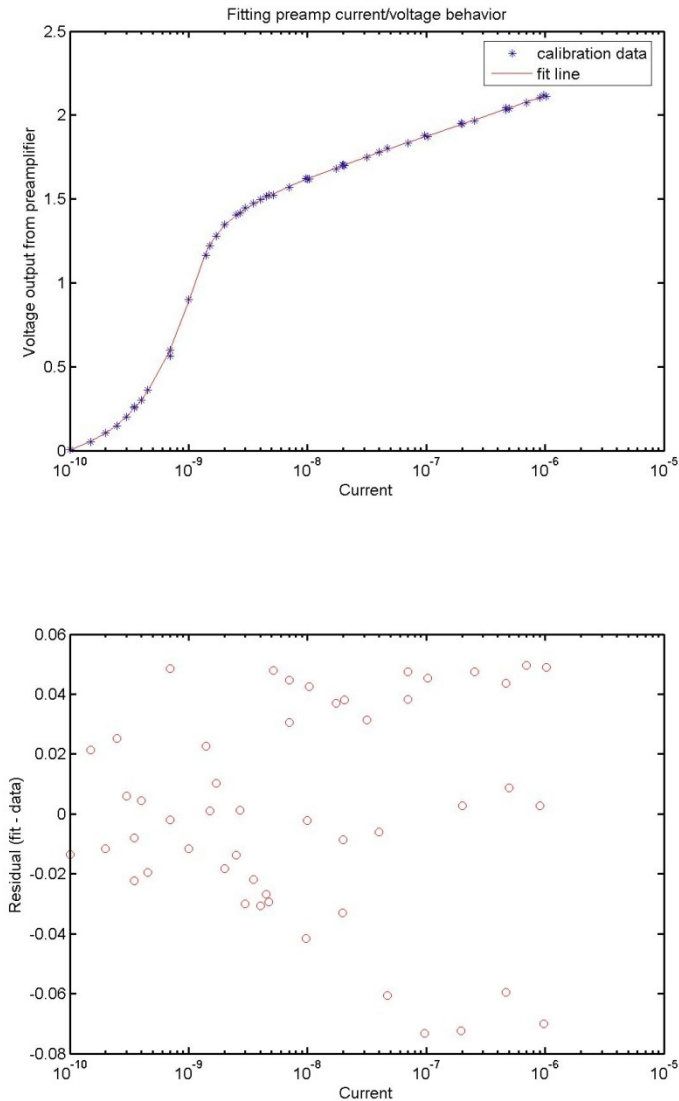


Figure Appendix 1-1. The output from the Matlab fitting function shows the calibration data plotted with the current data as well as the residuals in the bottom plot. By looking at the residuals this is a good fit with no correlation between the fitting errors as a function of input current. The error does slightly increase as the current increases.

Appendix B. Transmission plots calculated in Hückel-IV 3.0

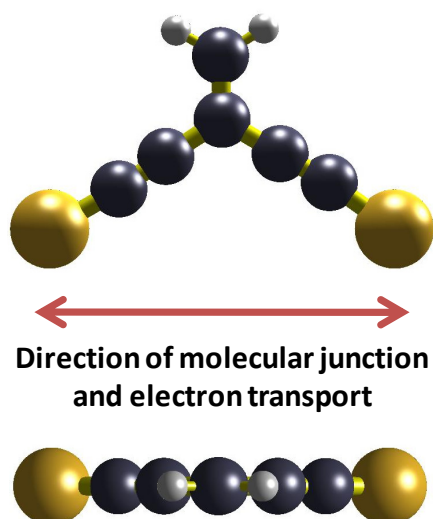
This appendix includes most of the molecular transmission plots that I have calculated using Hückel-IV 3.0. While the transmission spectrum is not an experimental observable it provides more information than a plot of conductance versus voltage. Each transmission plot is accompanied by two images of the molecular device showing the view from two angles separated by a 90° rotation. The input structures in most cases were optimized to the AM1 level of theory. The molecular structures utilized to generate publication quality calculations were optimized using QChem 3.0 at the B3LYP 6-311G** level. The transmission features generally show small variations with different geometry optimization unless there is a very large change in the optimized structure. This appendix is meant to serve as a general guide and no indication of the geometry optimization is provided. The molecular images were generated by taking the Hückel-IV 3.0 generated device file and plotting the structure in matlab.

These plots are here to serve as a reference in designing molecular electronic systems with specific characteristics such as the position of the frontier molecular orbitals, or possibly the position of an interference feature. The correlation between the Hückel-IV 3.0 calculations and the density function codes gDFTB and ATK 2.0 is quite reasonable. In nearly all tested cases the qualitative features are quite similar. In general the Fermi level in ATK 2.0 is slightly closer to the highest occupied molecular orbital. In longer molecules, on the order of 17 carbon atoms in the backbone separating the electrodes, there is also an increase in the transmission probability between the HOMO and LUMO orbitals of 1-2 orders of magnitude within the DFT codes

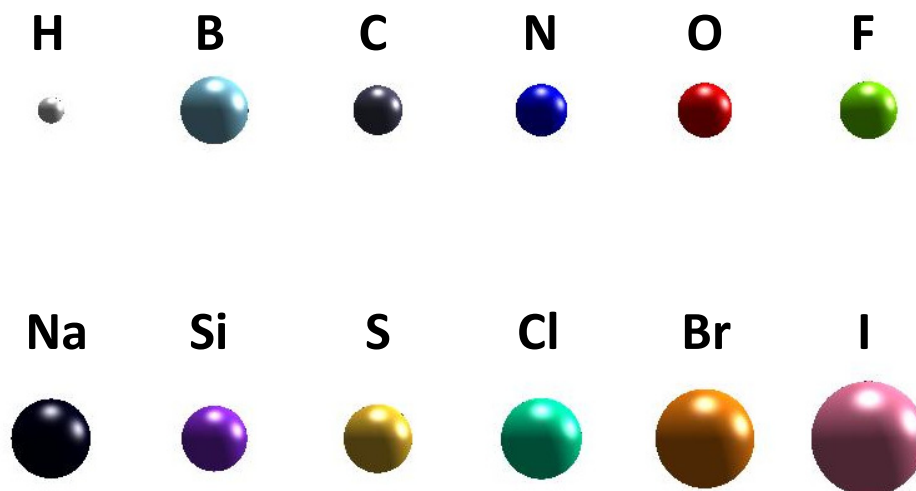
relative to Hückel-IV. This was the case in both the calculations of an alkane and alkene molecules.

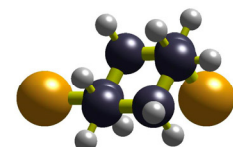
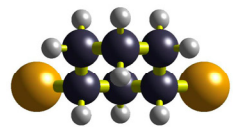
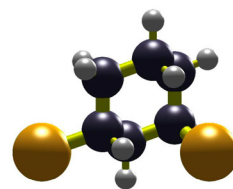
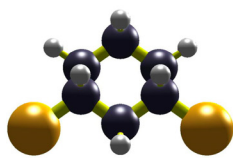
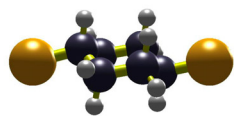
There are two other differences between the calculation results that have been observed. In Hückel-IV the sigma molecular orbital contribution to conductance is located only 1eV from the Fermi level. This is a discrepancy of 1-2eV's in comparison with both DFT methods. The only other case where a difference between the calculations was noticed was in the design of molecular diodes with a localized resonance between two interference features. In the Hückel-IV 3.0 calculations an oxygen group on the molecules created a resonance just slightly above the Fermi energy in the range of 0.15-0.5eV. In the ATK and gDFTB the localized resonance feature from the oxygen atoms occurs at $\approx 0.5\text{eV}$ higher energy. In most cases this might not have a large effect on the transmission properties of a molecule. In diode design the position of every molecular resonance and interference feature is critical to device performance. When designing and testing molecular devices that rely on interference effects alignment of the Fermi level will be critical and must be experimentally verified.

Key for Appendix B. Transmission calculations made using Hückel-IV 3.0

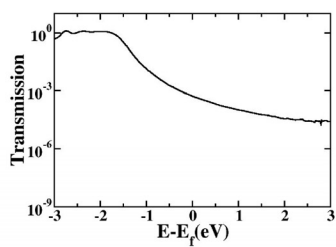


Note: The Au electrode atoms have
been removed for clarity. The top and
bottom view are rotated 90 degrees.

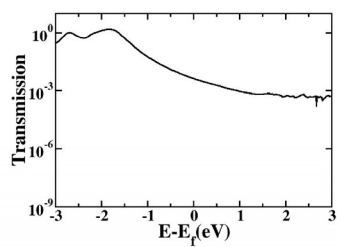




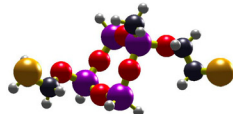
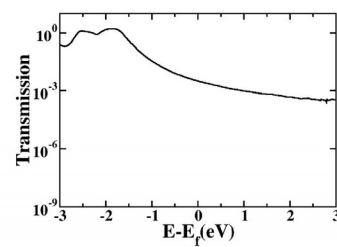
Molecule 1



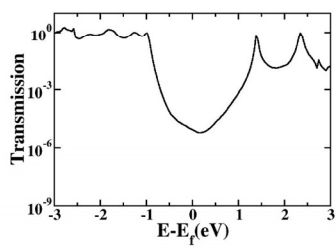
Molecule 2



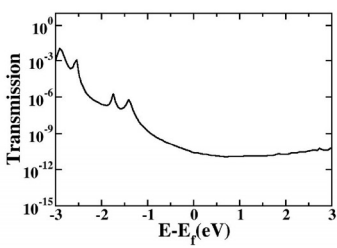
Molecule 3



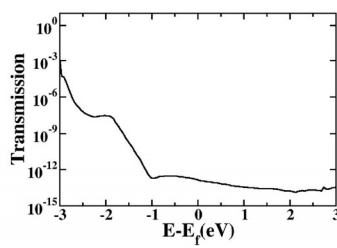
Molecule 4

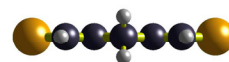
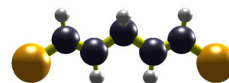


Molecule 5

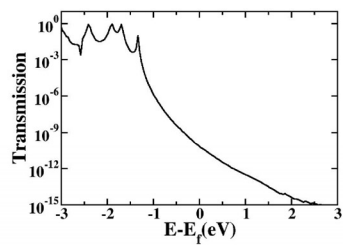


Molecule 6

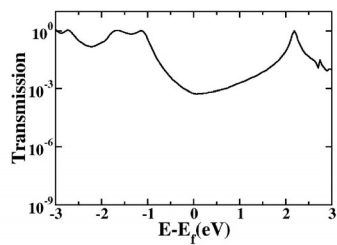




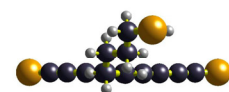
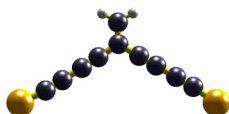
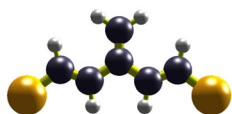
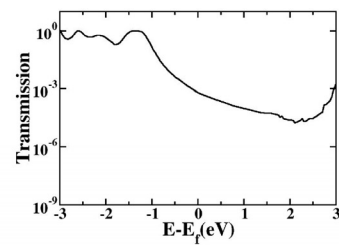
Molecule 8



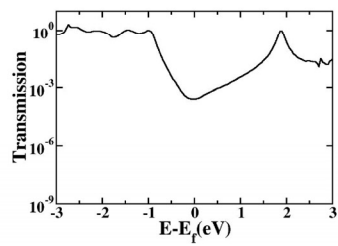
Molecule 9



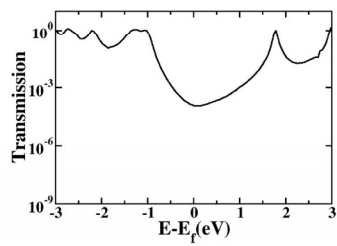
Molecule 10



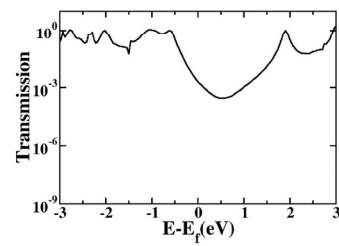
Molecule 11

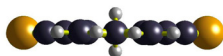
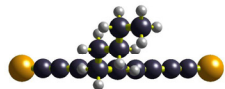
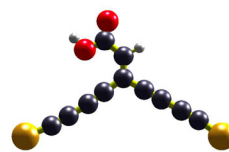


Molecule 12

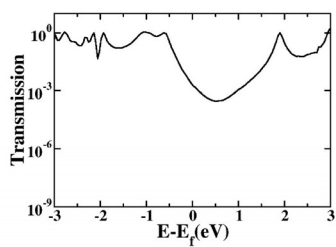


Molecule 13

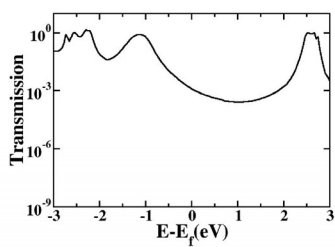




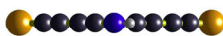
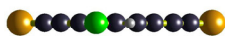
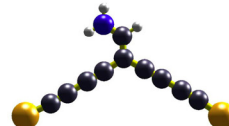
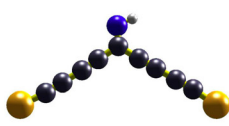
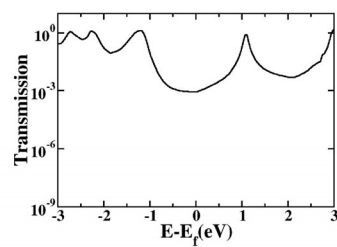
Molecule 14



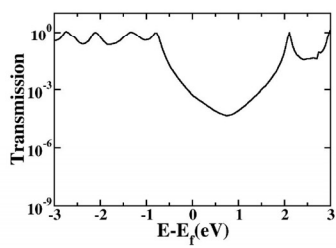
Molecule 15



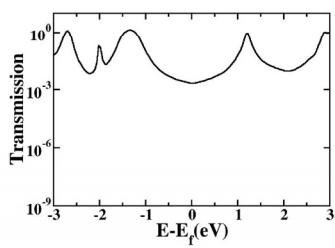
Molecule 16



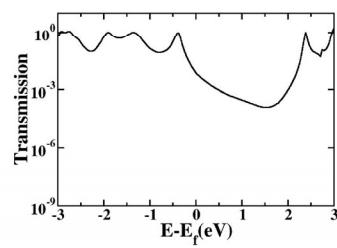
Molecule 17

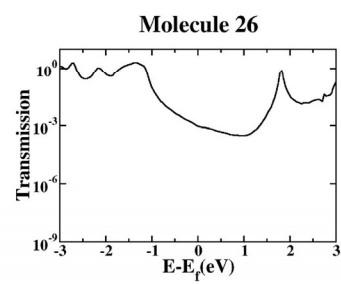
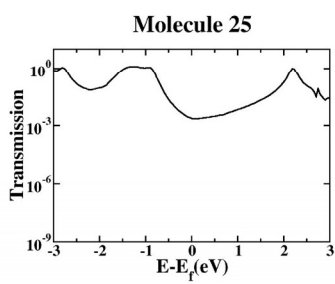
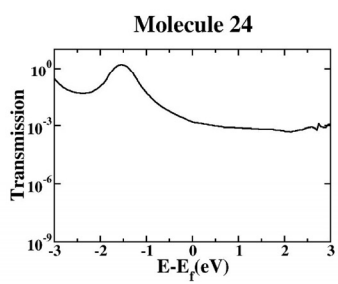
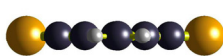
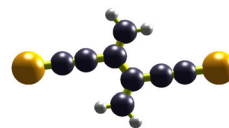
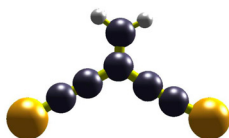
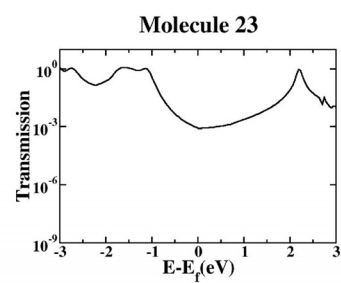
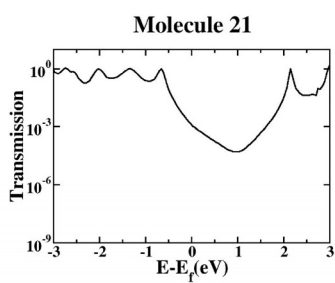
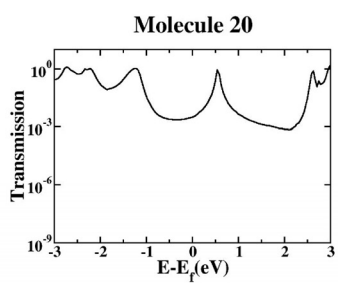
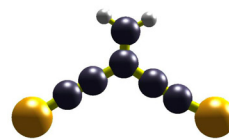
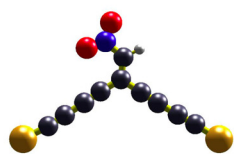


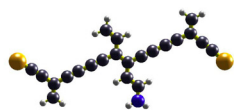
Molecule 18



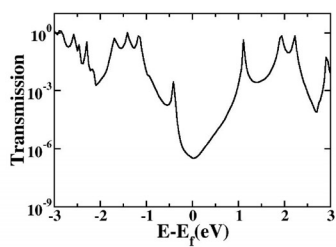
Molecule 19



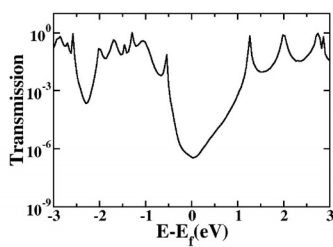




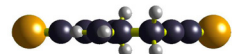
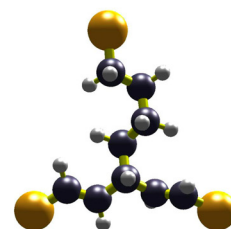
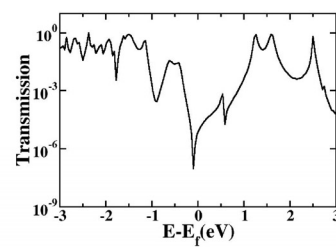
Molecule 27



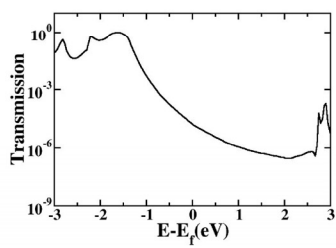
Molecule 28



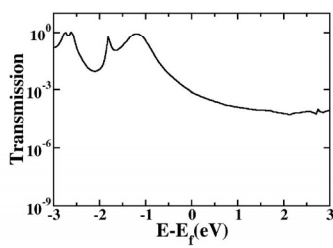
Molecule 29



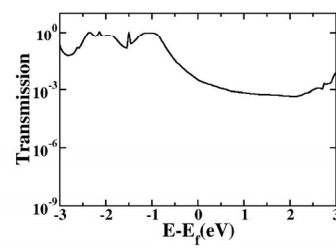
Molecule 30

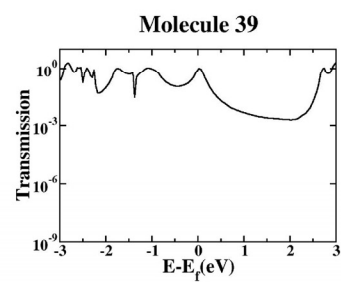
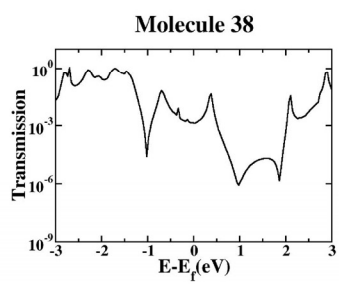
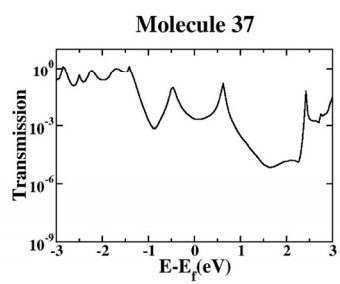
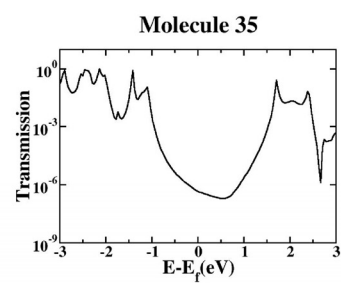
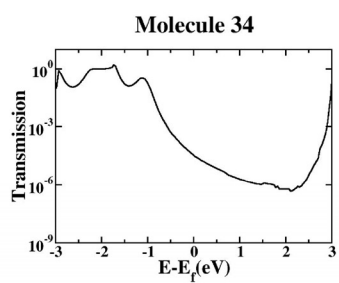
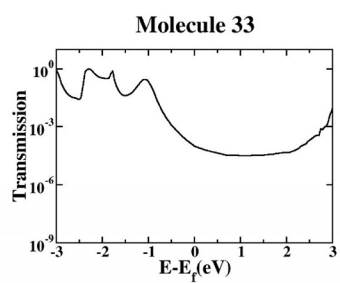
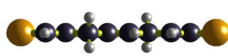
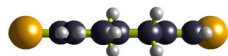


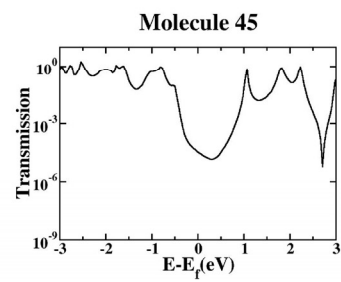
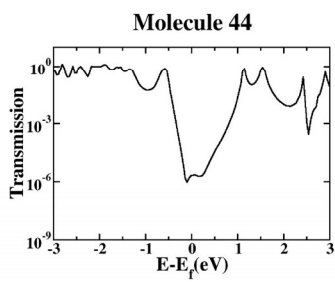
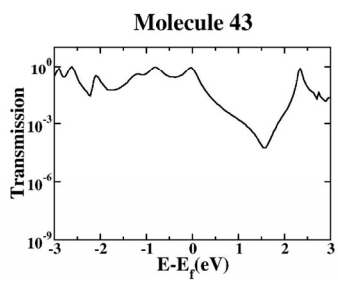
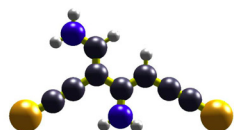
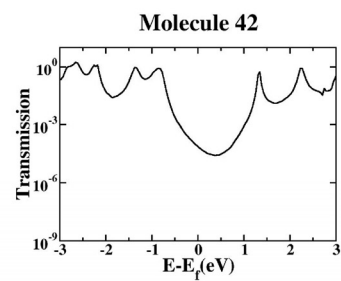
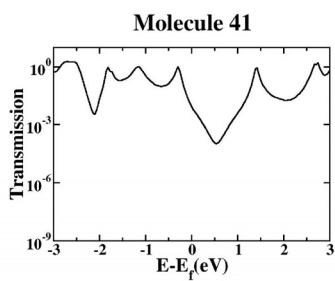
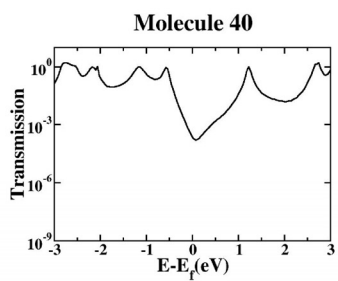
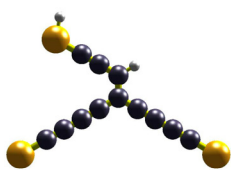
Molecule 31

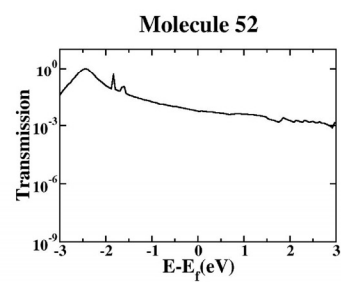
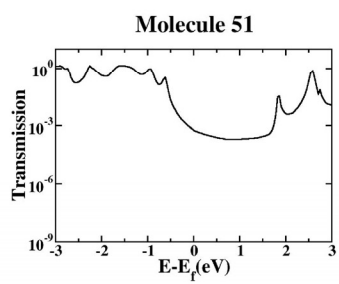
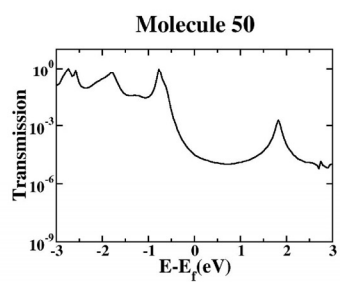
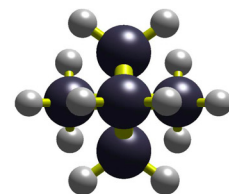
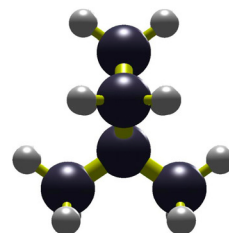
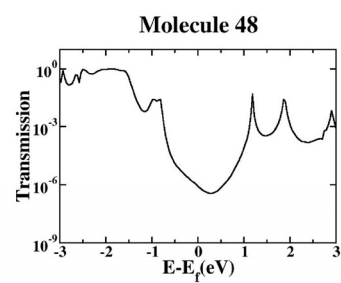
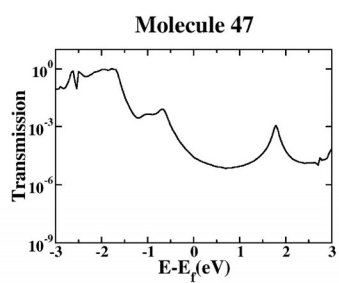
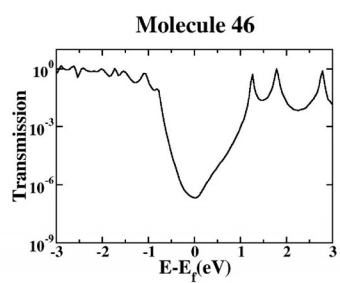
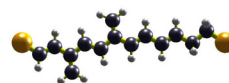


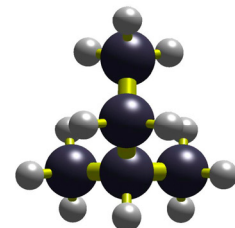
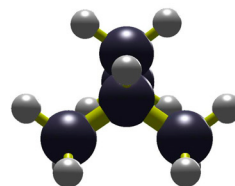
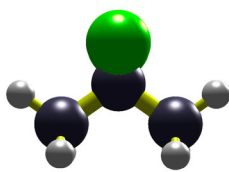
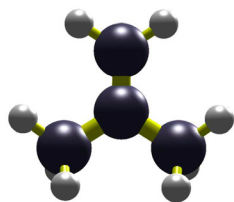
Molecule 32



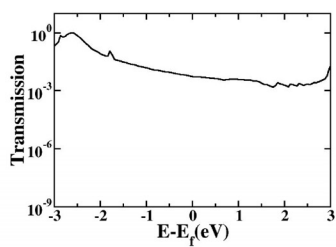




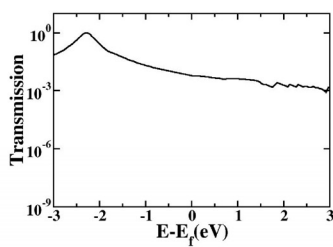




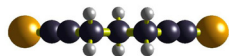
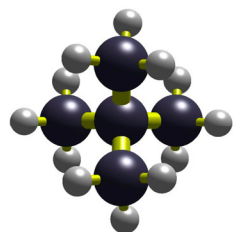
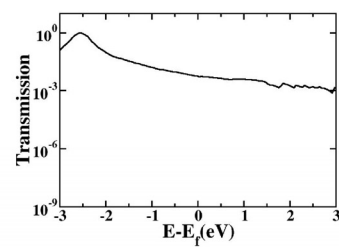
Molecule 53



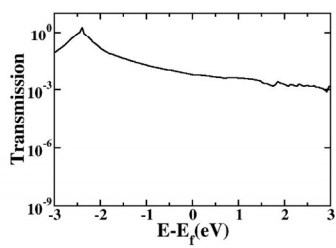
Molecule 54



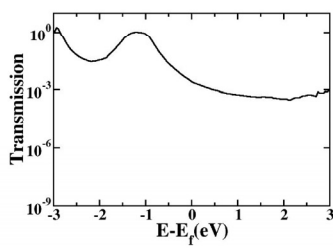
Molecule 55



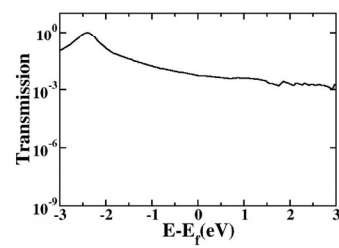
Molecule 56

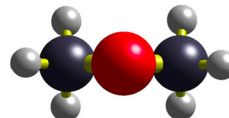
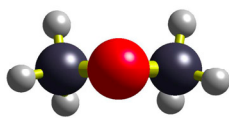
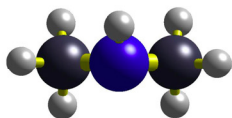
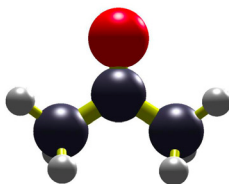
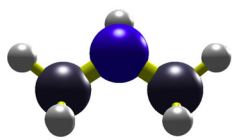


Molecule 57

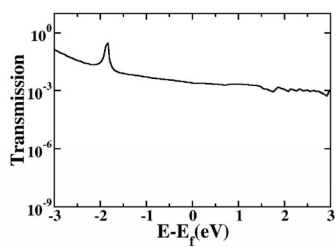


Molecule 58

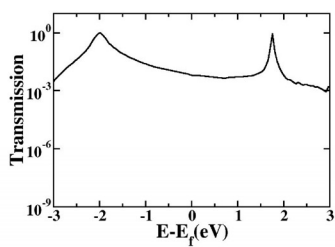




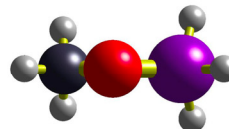
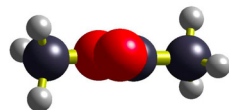
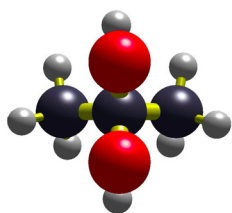
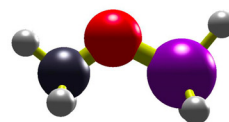
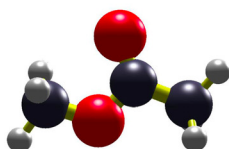
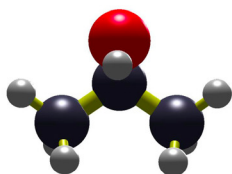
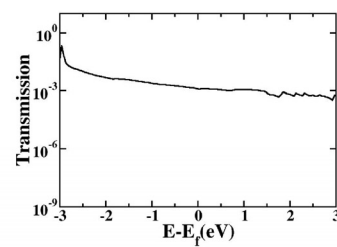
Molecule 59



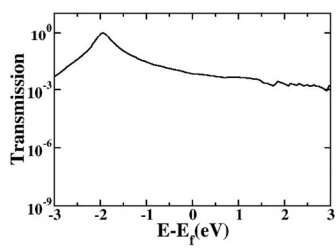
Molecule 60



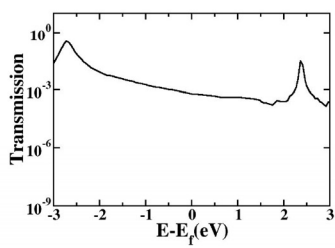
Molecule 61



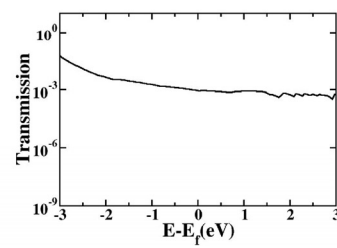
Molecule 62



Molecule 63

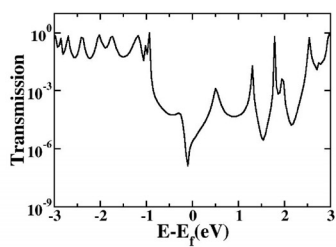


Molecule 64

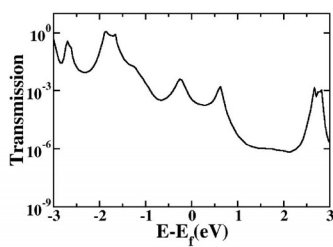




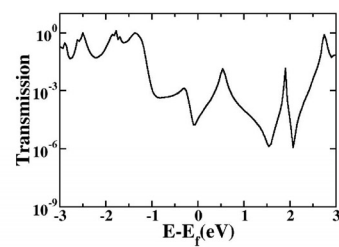
Molecule 65



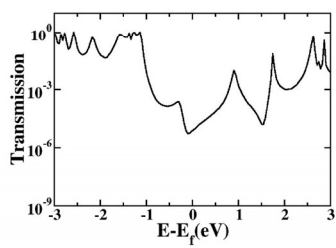
Molecule 66



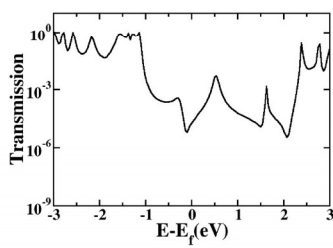
Molecule 67



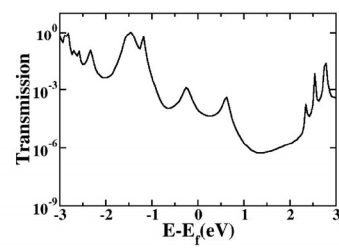
Molecule 68

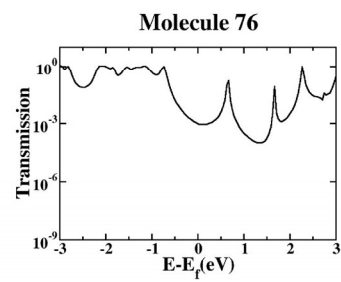
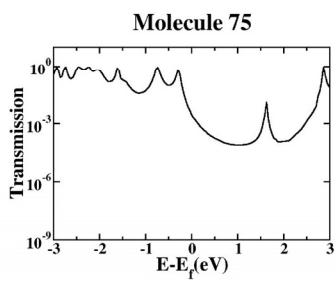
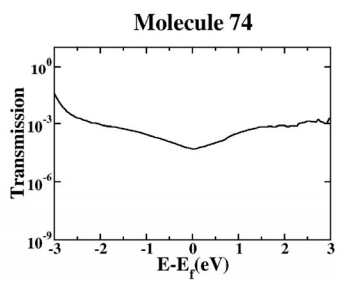
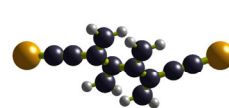
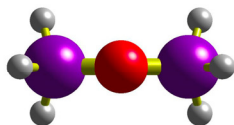
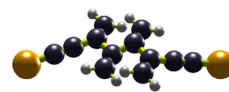
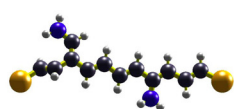
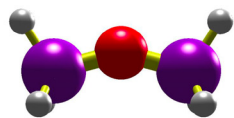
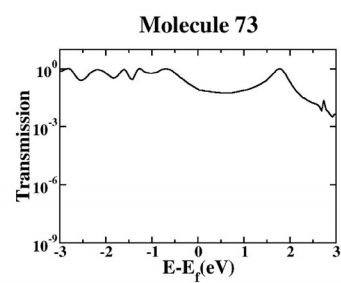
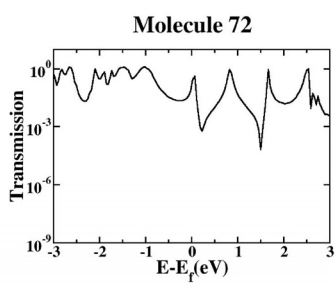
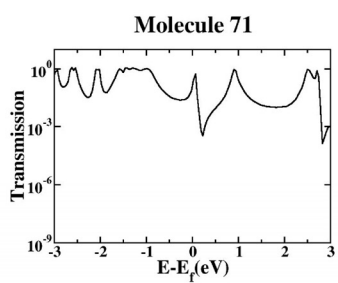
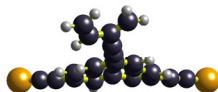
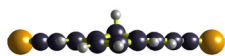


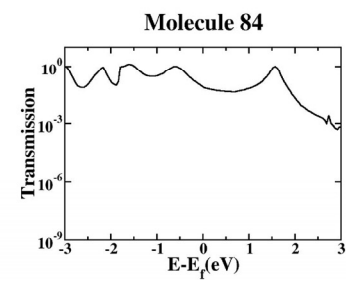
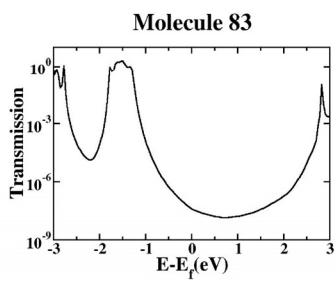
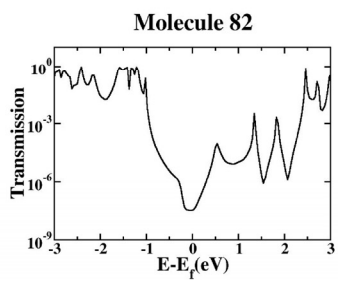
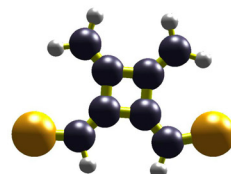
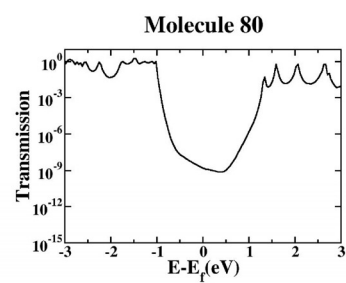
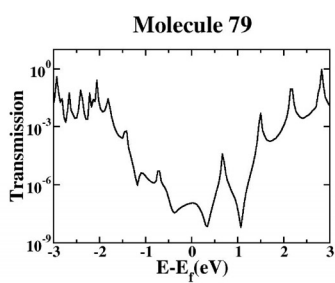
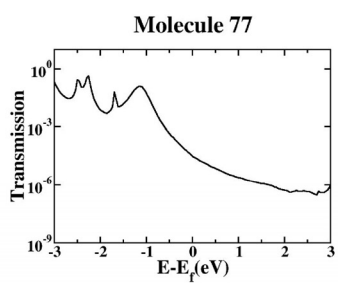
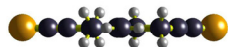
Molecule 69

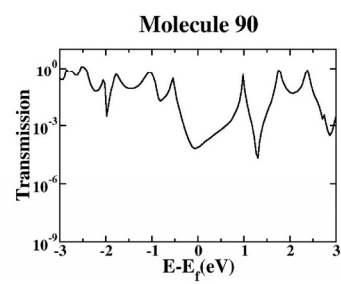
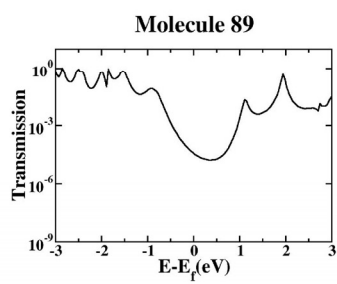
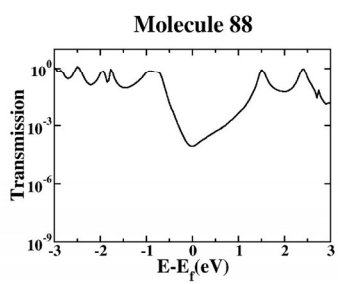
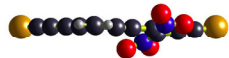
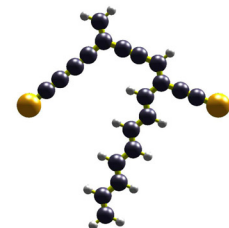
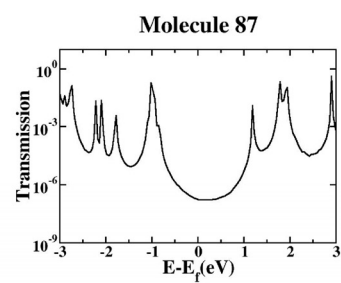
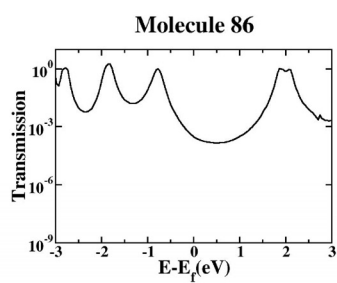
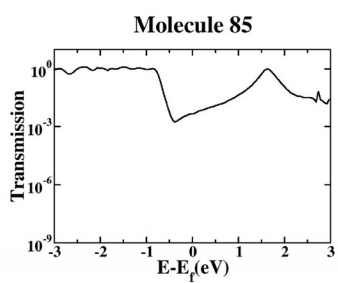


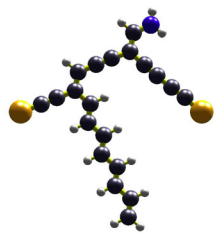
Molecule 70



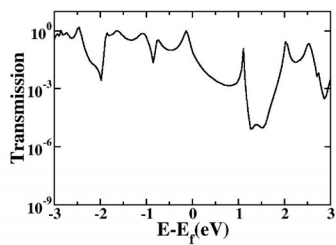




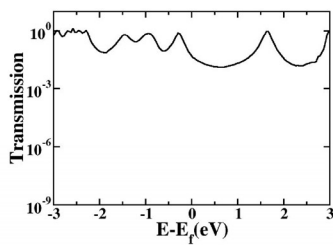




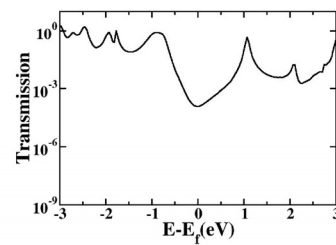
Molecule 92



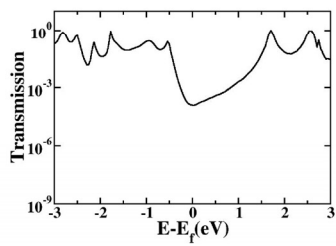
Molecule 93



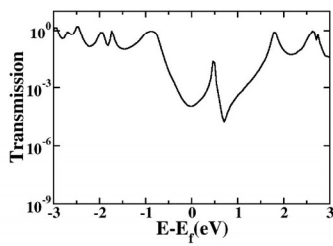
Molecule 94



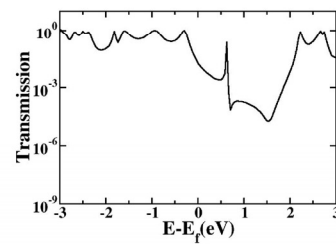
Molecule 95

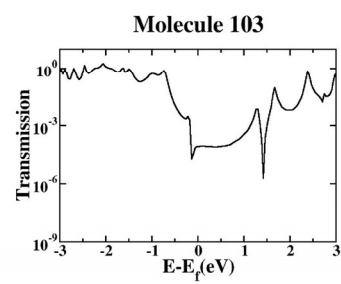
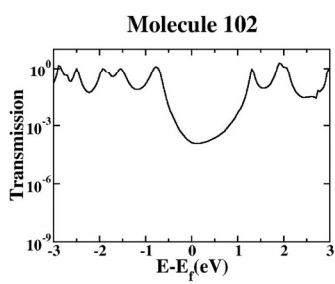
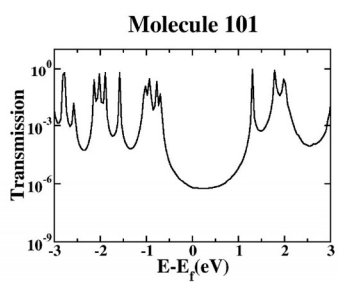
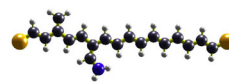
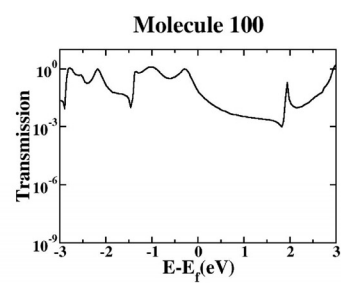
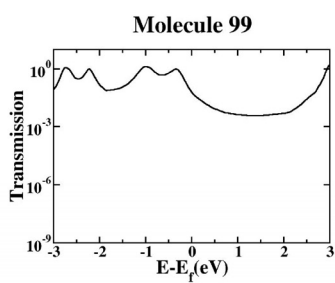
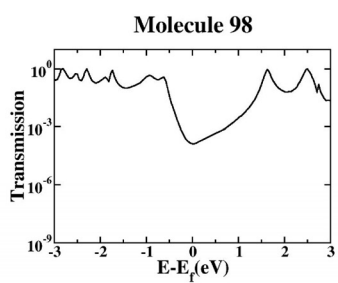


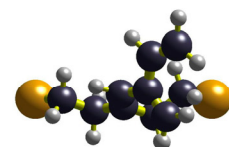
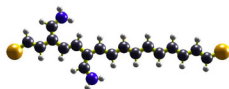
Molecule 96



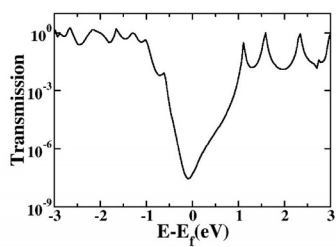
Molecule 97



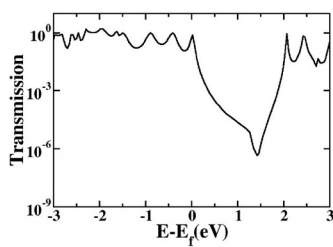




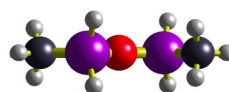
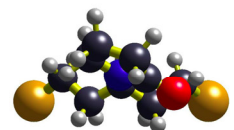
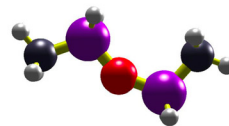
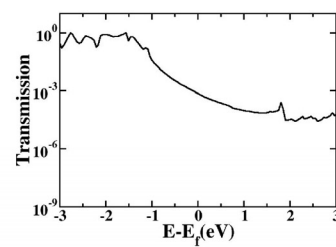
Molecule 104



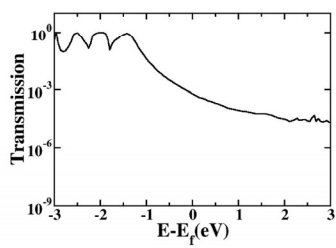
Molecule 105



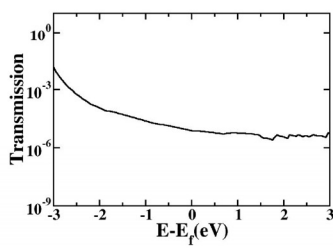
Molecule 106



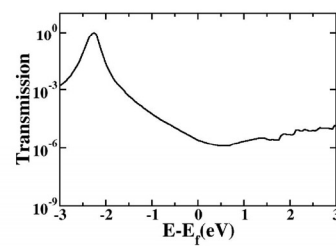
Molecule 107

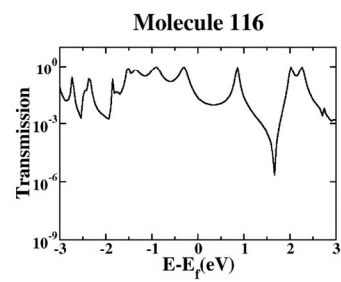
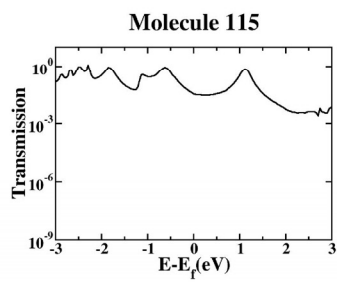
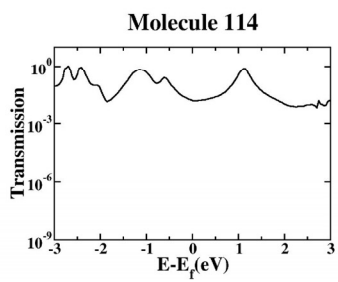
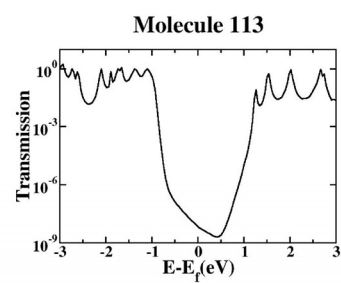
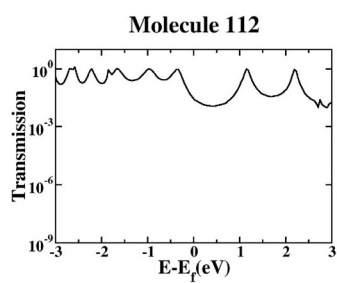
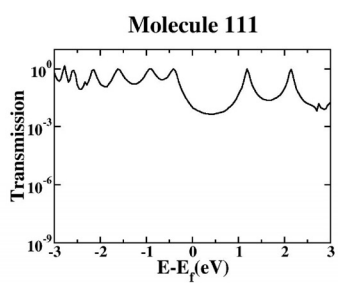
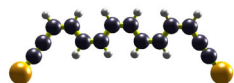


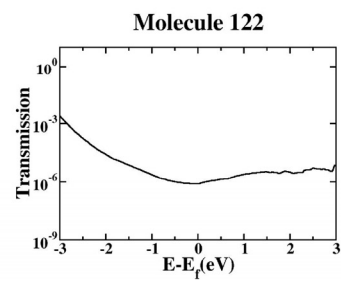
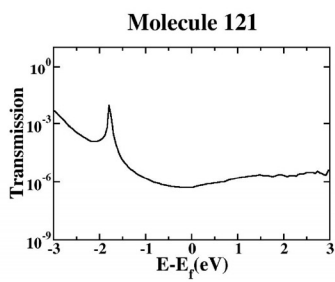
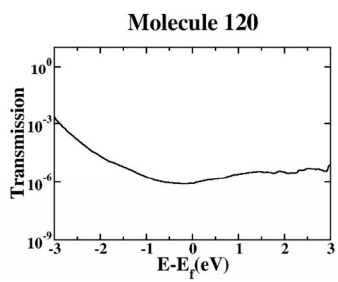
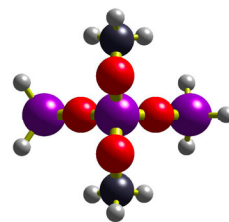
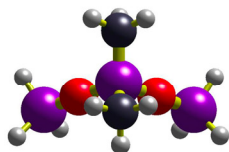
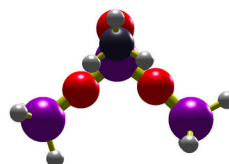
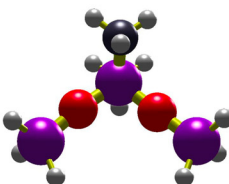
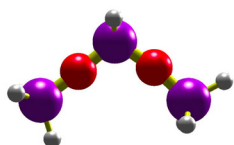
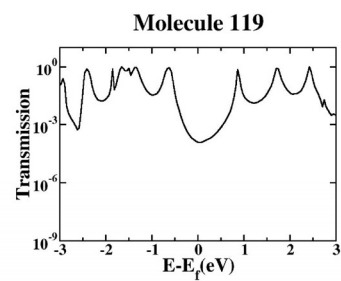
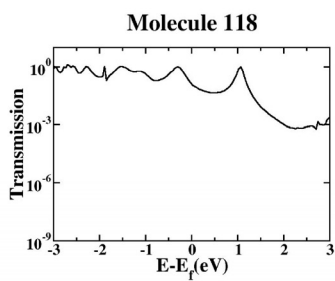
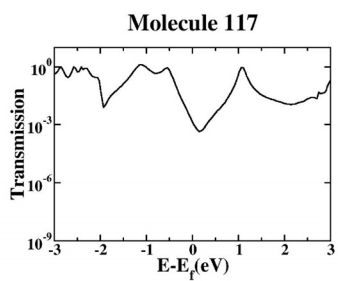
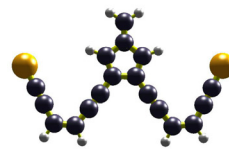
Molecule 108

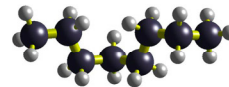
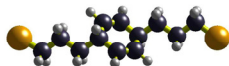
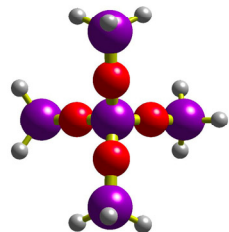
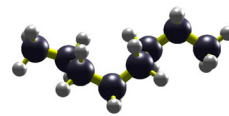
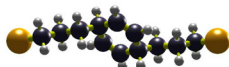
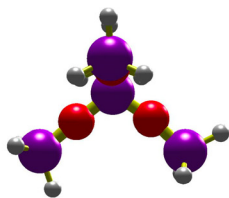


Molecule 110

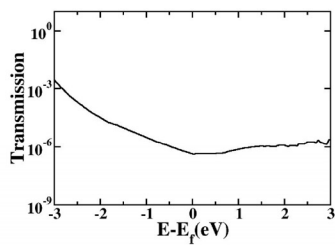




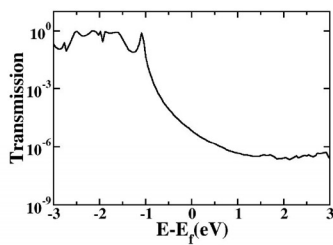




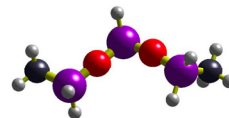
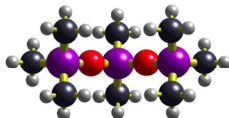
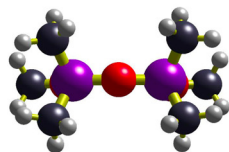
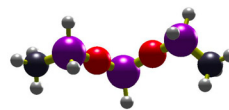
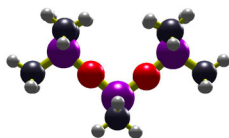
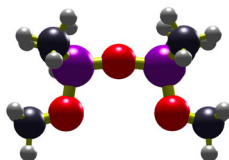
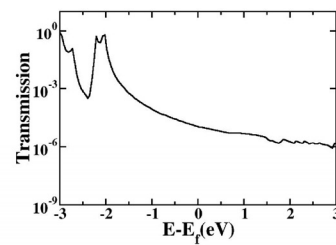
Molecule 123



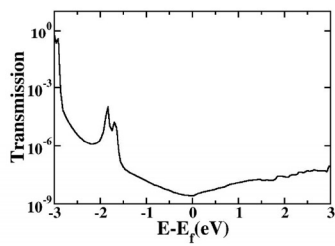
Molecule 124



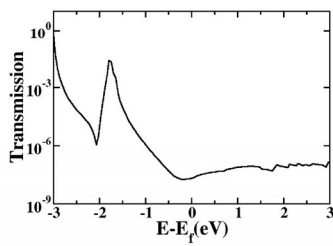
Molecule 126



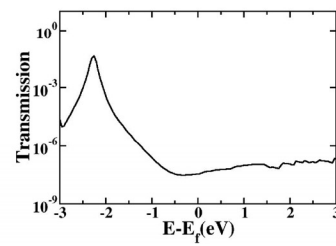
Molecule 127

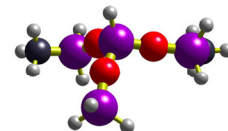
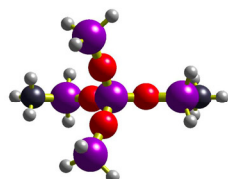
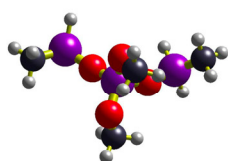
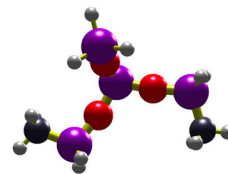
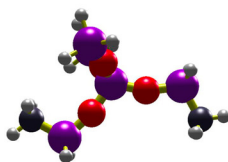
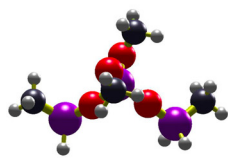


Molecule 128

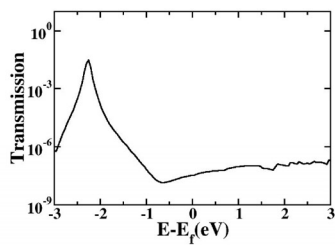


Molecule 129

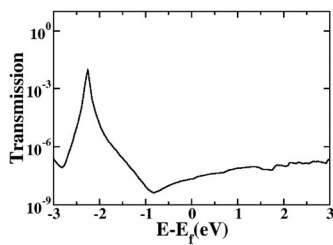




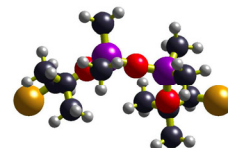
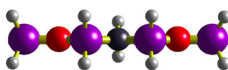
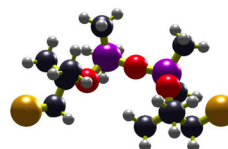
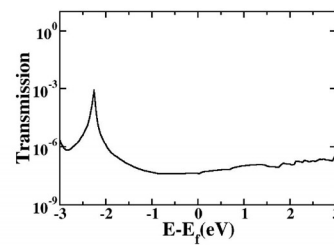
Molecule 130



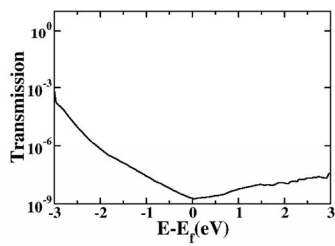
Molecule 131



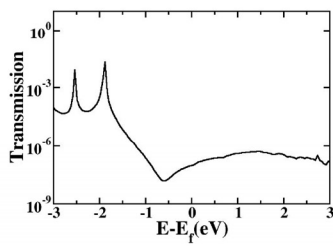
Molecule 132



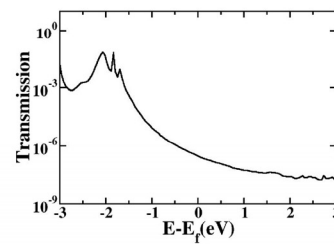
Molecule 133

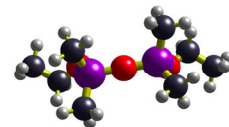
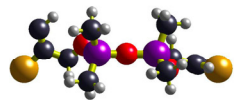
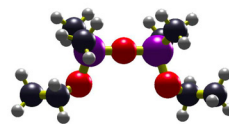
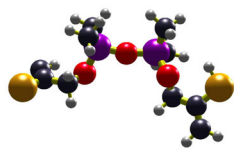


Molecule 134

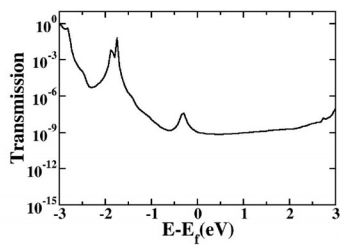


Molecule 141

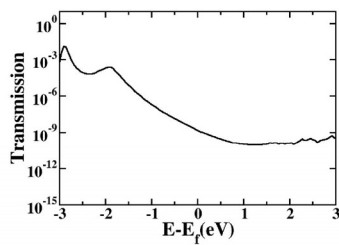




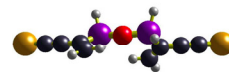
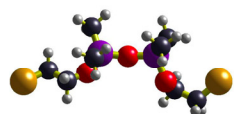
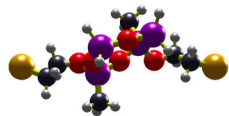
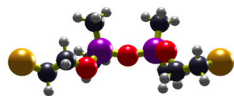
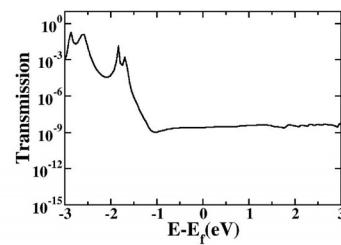
Molecule 142



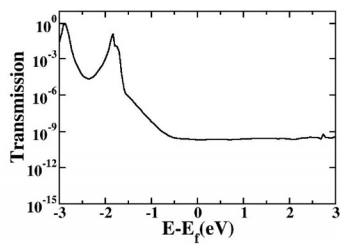
Molecule 143



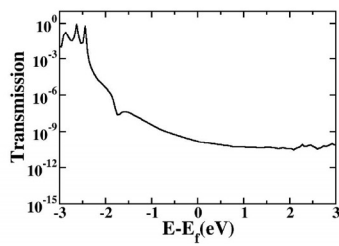
Molecule 144



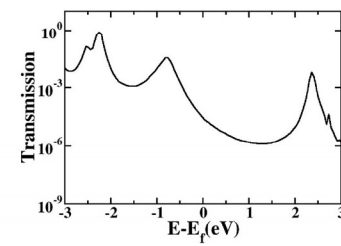
Molecule 145

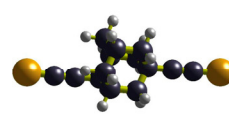
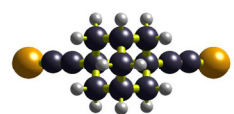
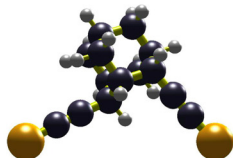
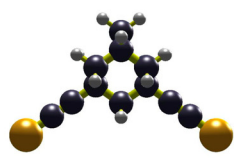


Molecule 146

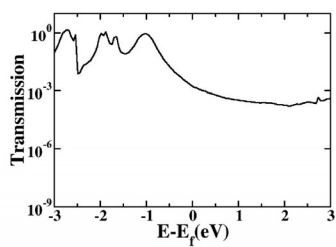


Molecule 147

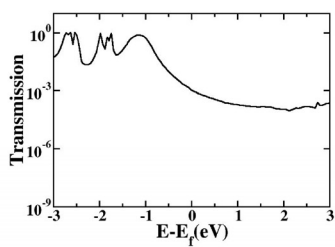




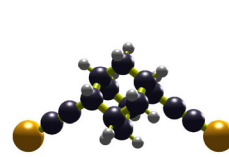
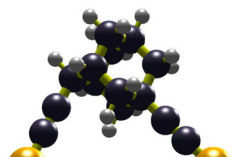
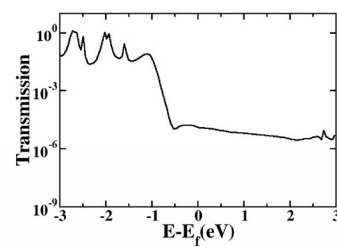
Molecule 148



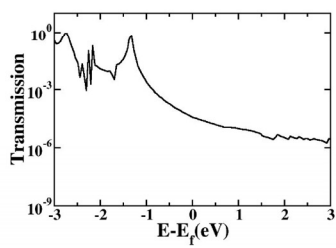
Molecule 149



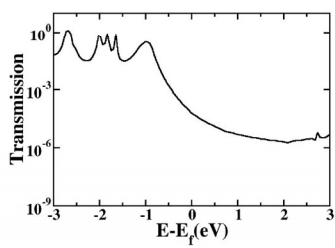
Molecule 150



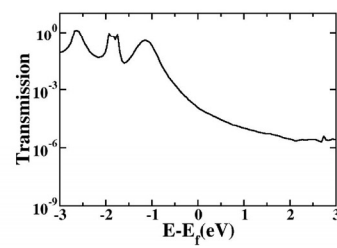
Molecule 151

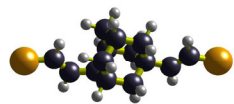
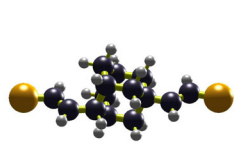


Molecule 152

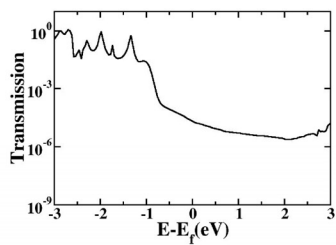


Molecule 153

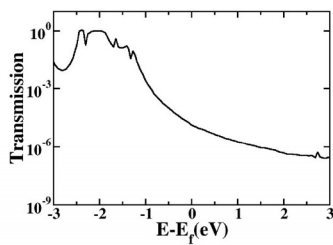




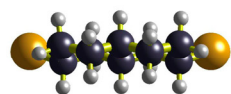
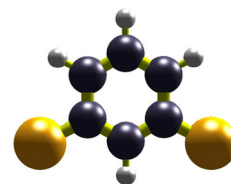
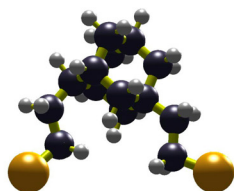
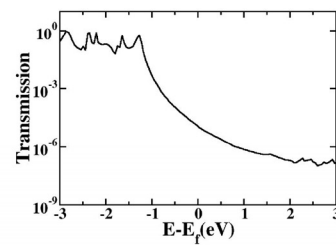
Molecule 154



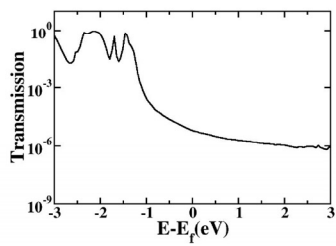
Molecule 155



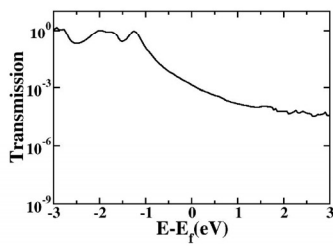
Molecule 156



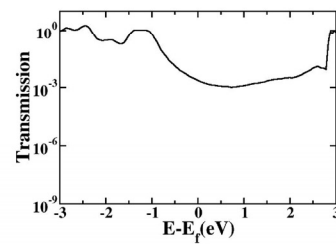
Molecule 157

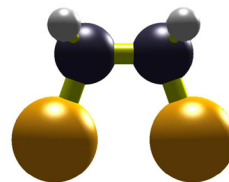
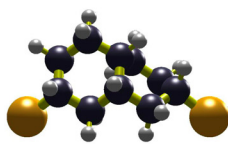
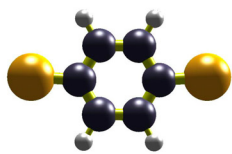


Molecule 159

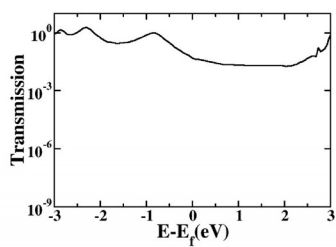


Molecule 160

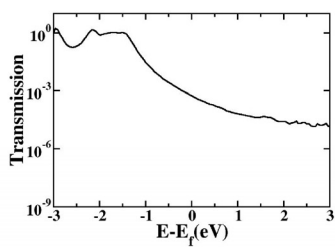




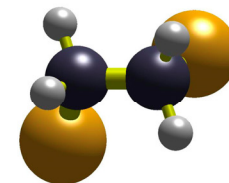
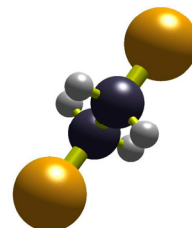
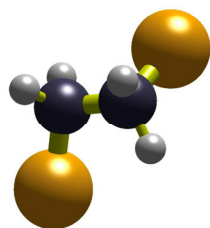
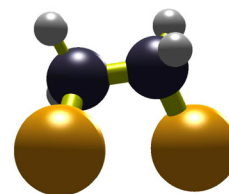
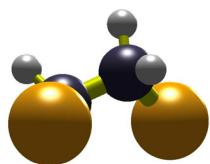
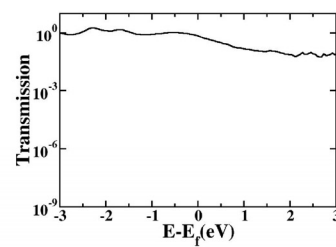
Molecule 161



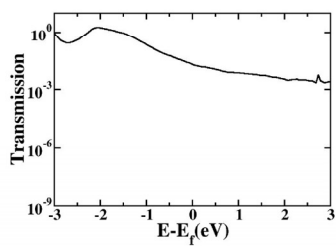
Molecule 162



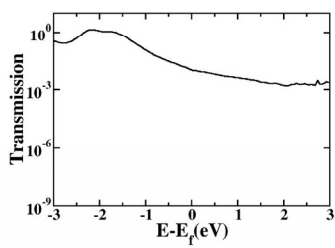
Molecule 163



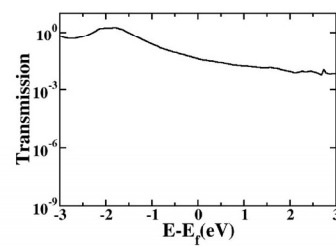
Molecule 164

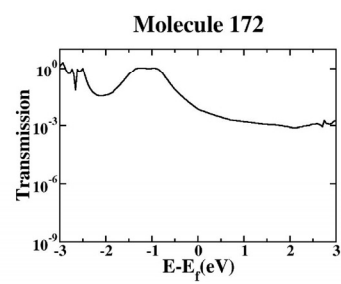
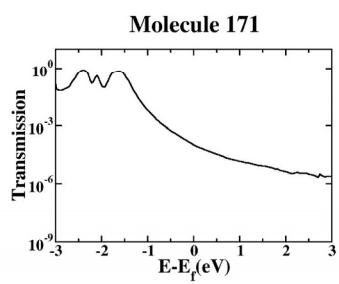
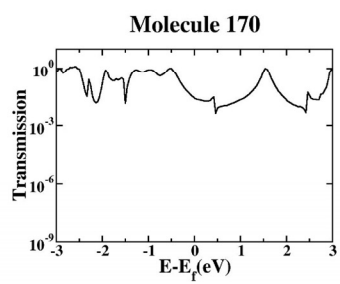
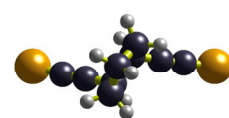
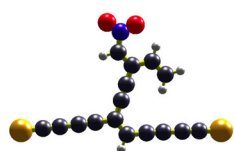
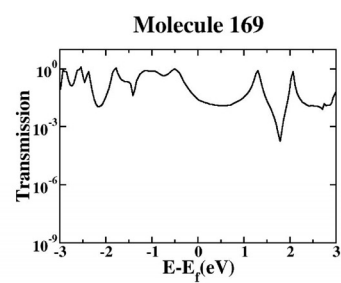
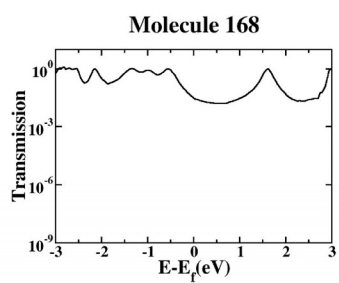
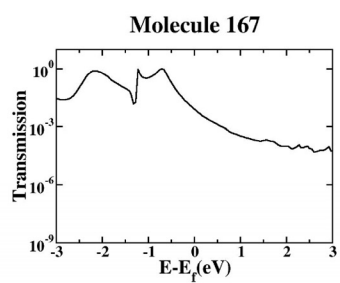
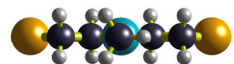


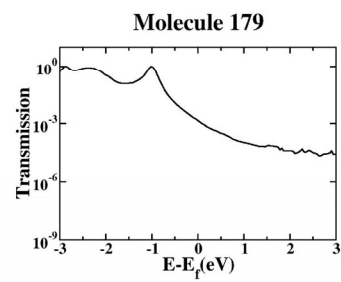
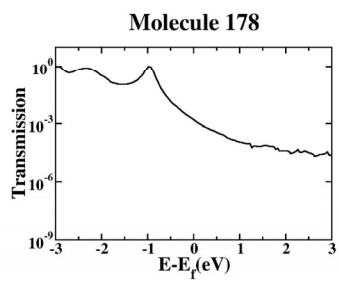
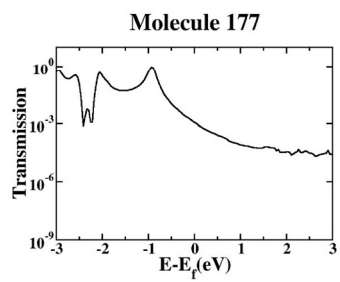
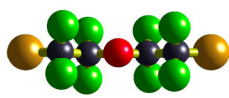
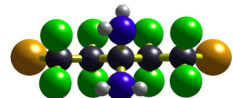
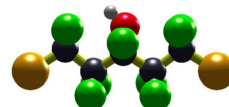
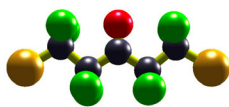
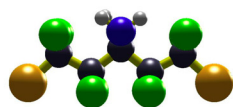
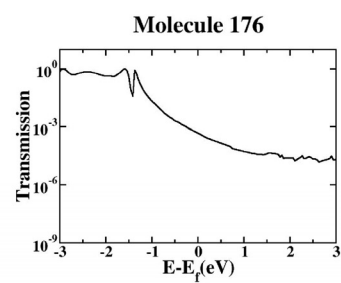
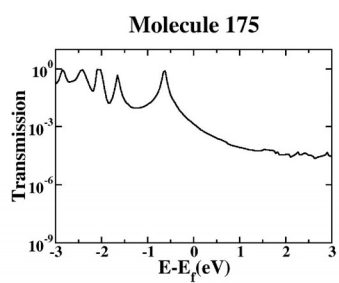
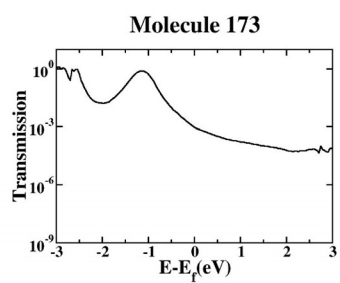
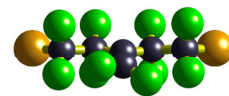
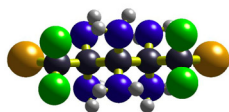
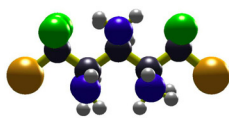
Molecule 165

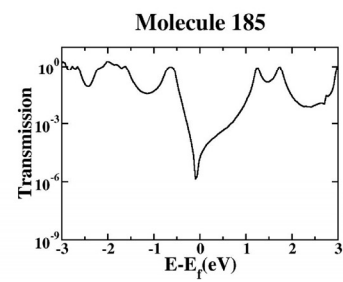
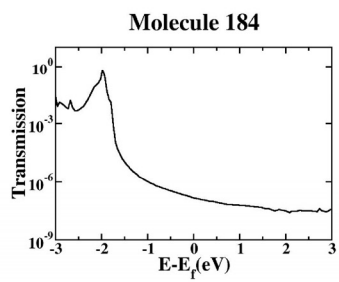
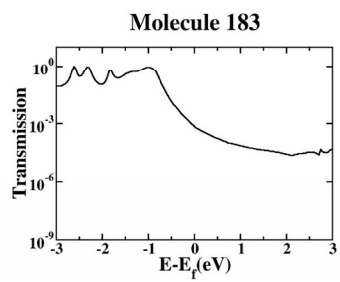
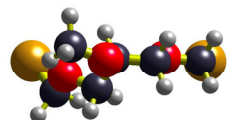
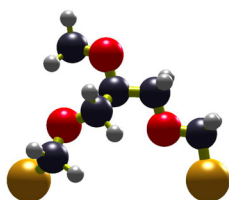
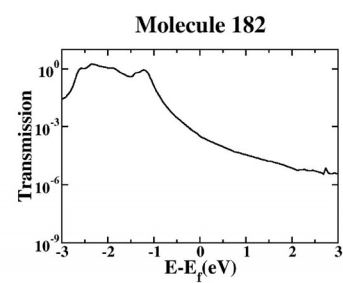
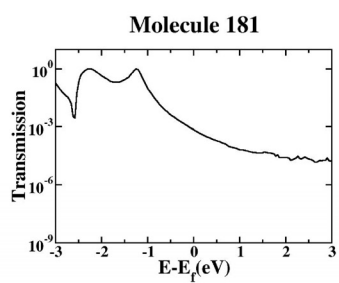
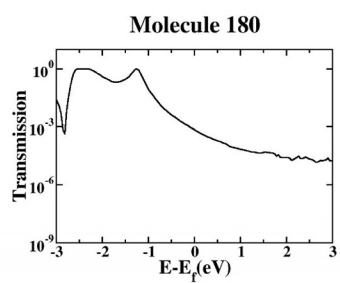
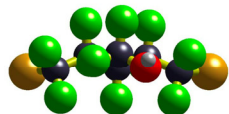
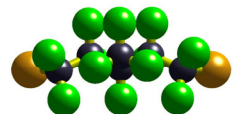
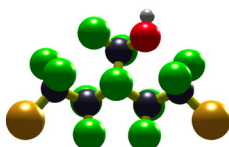
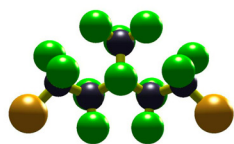


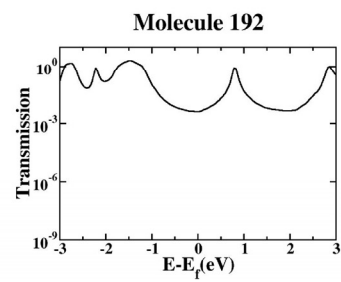
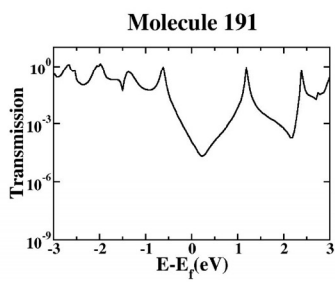
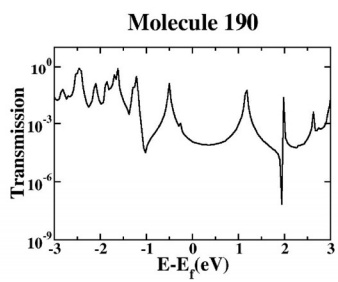
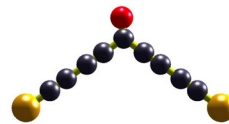
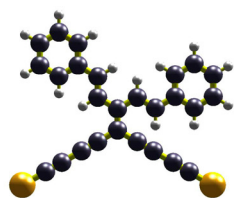
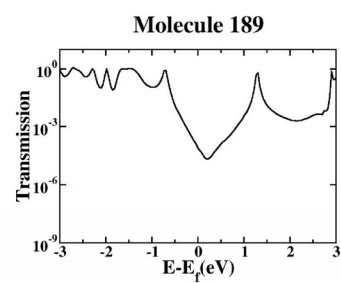
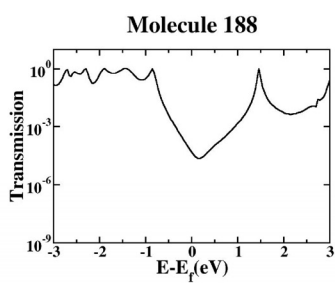
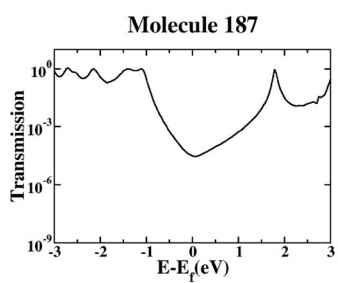
Molecule 166

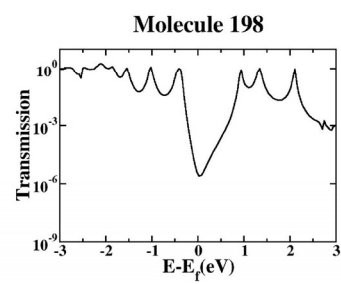
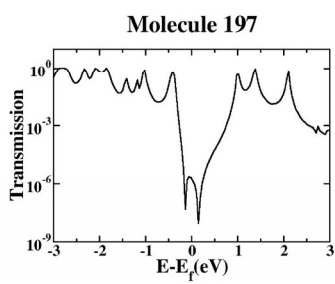
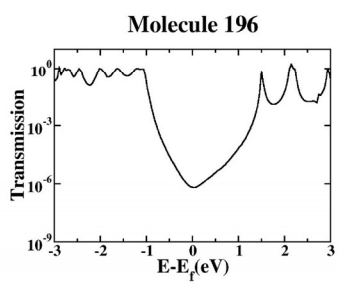
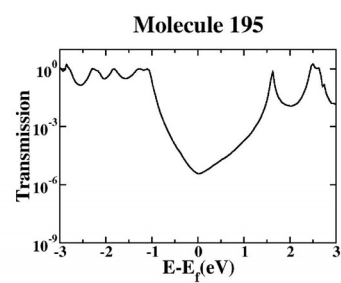
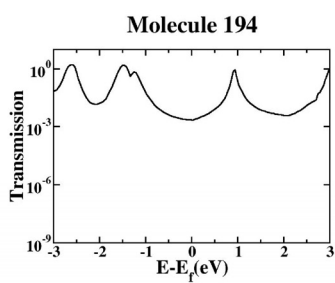
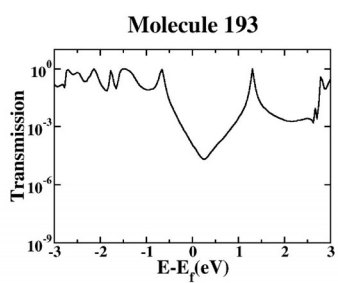


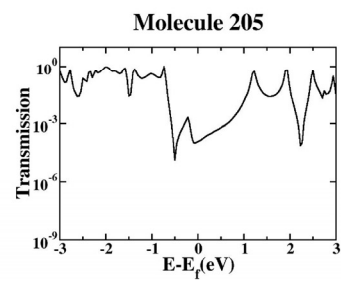
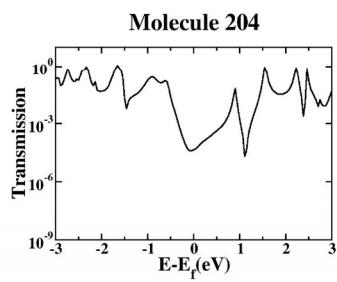
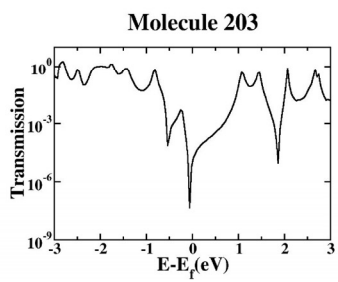
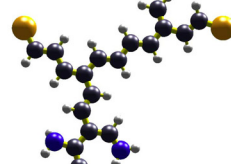
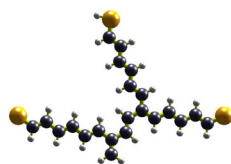
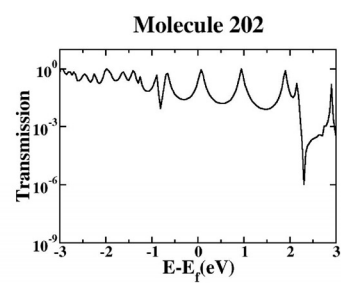
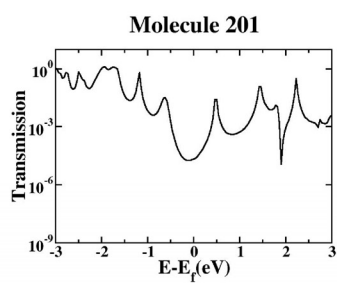
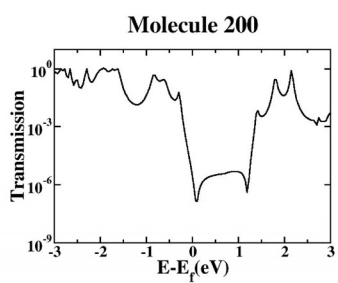
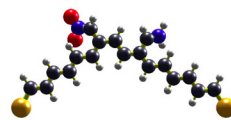


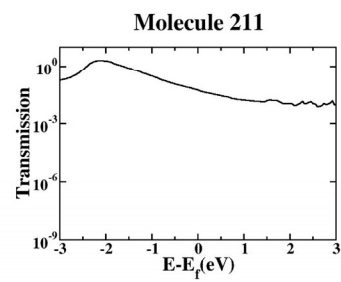
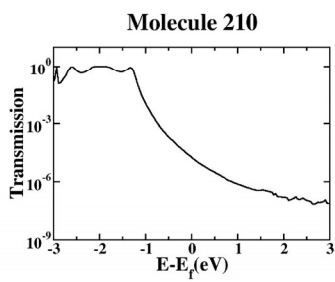
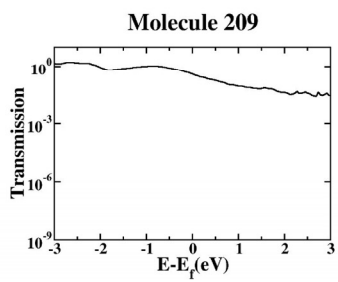
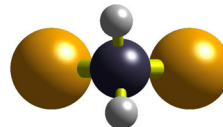
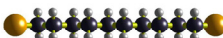
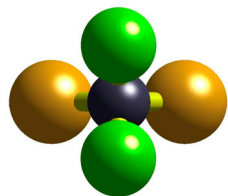
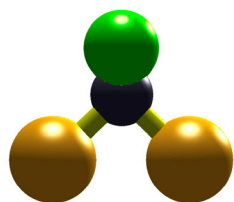
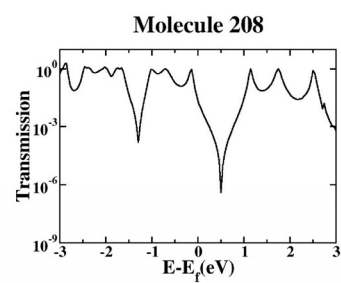
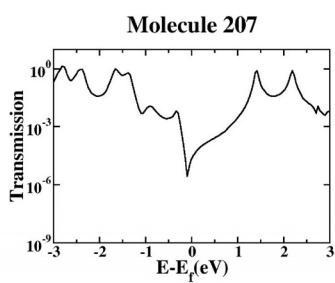
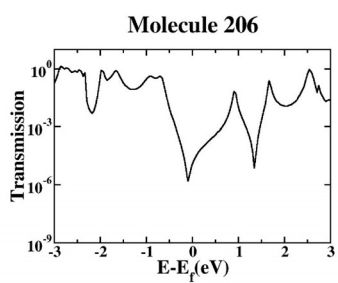
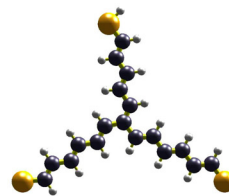
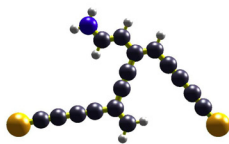


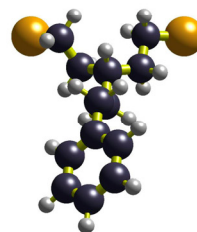
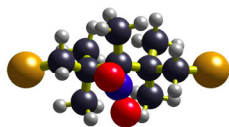




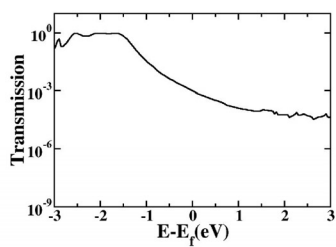




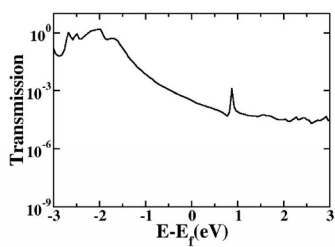




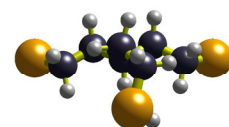
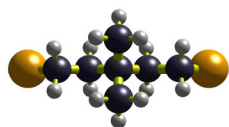
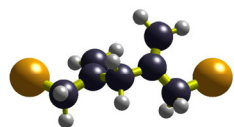
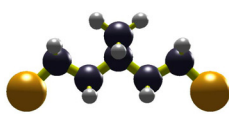
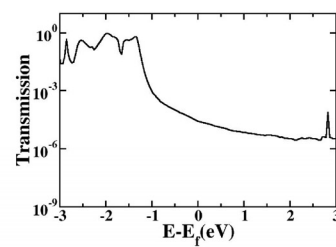
Molecule 212



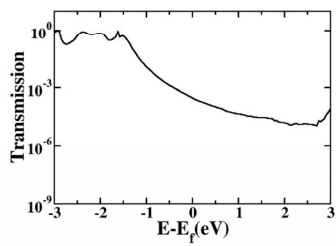
Molecule 213



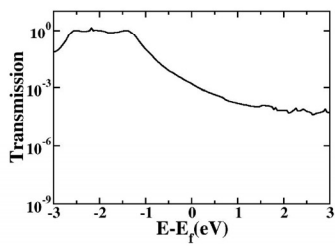
Molecule 214



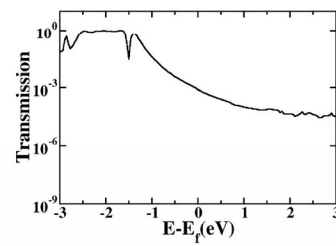
Molecule 215

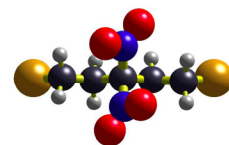
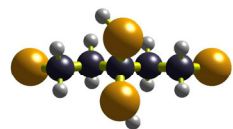
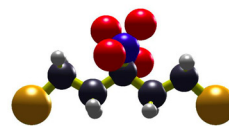
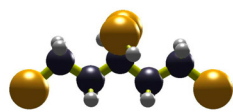


Molecule 216

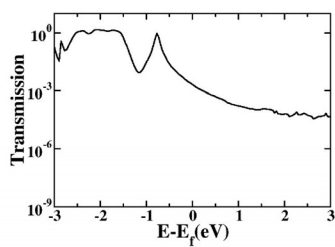


Molecule 217

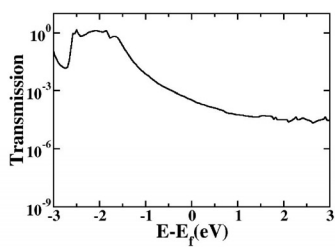




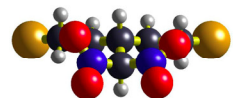
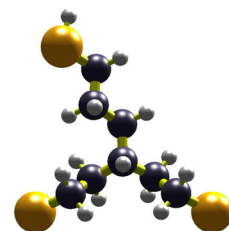
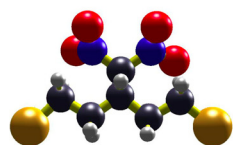
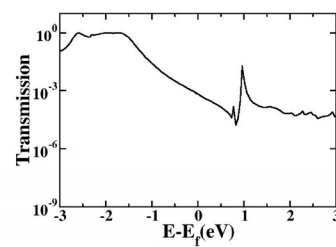
Molecule 218



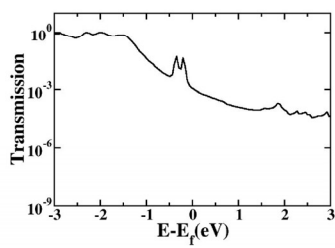
Molecule 219



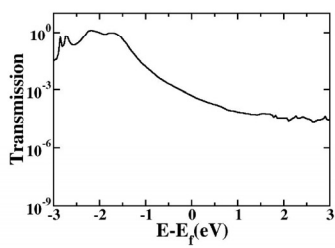
Molecule 220



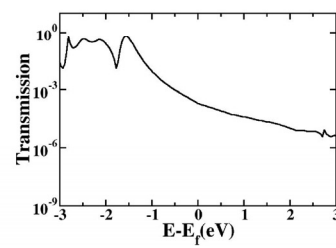
Molecule 221

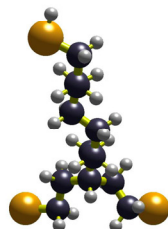
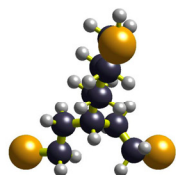
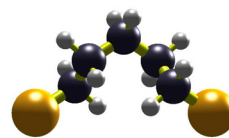
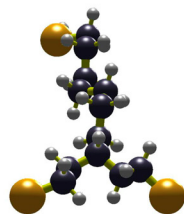
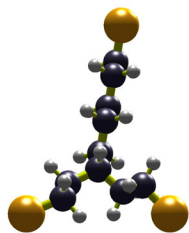


Molecule 222

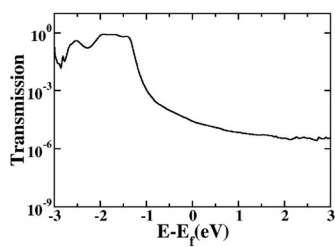


Molecule 223

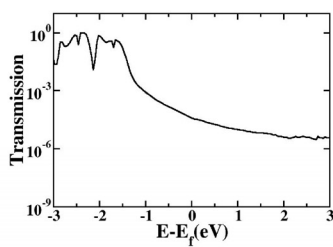




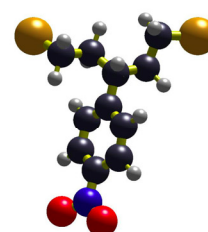
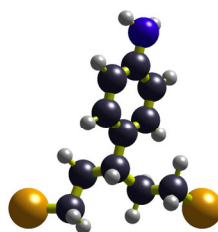
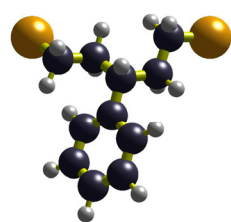
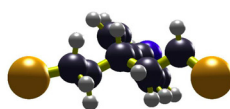
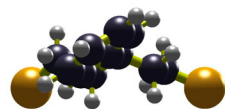
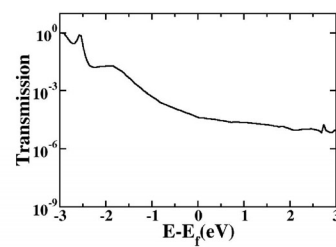
Molecule 224



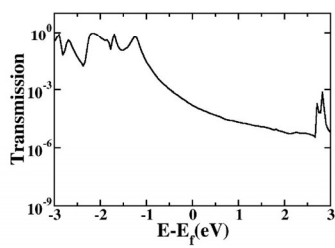
Molecule 225



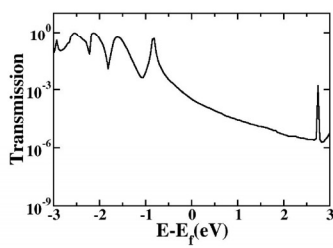
Molecule 226



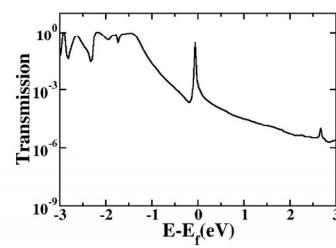
Molecule 227

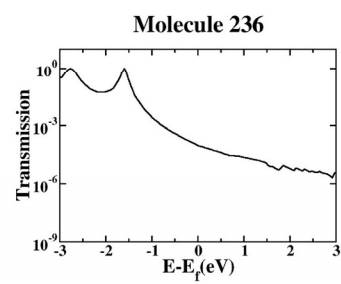
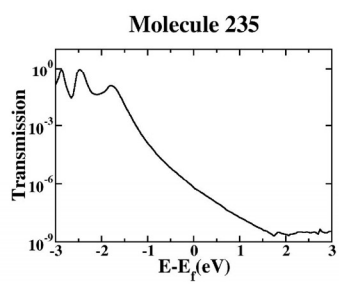
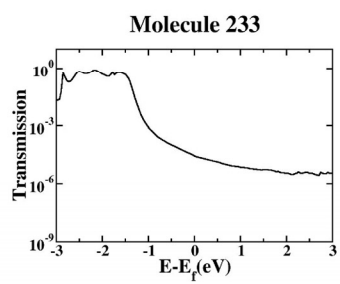
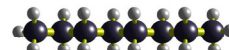
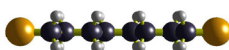
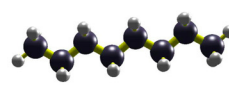
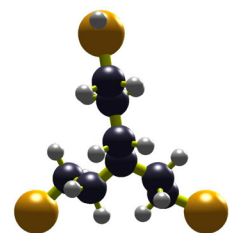
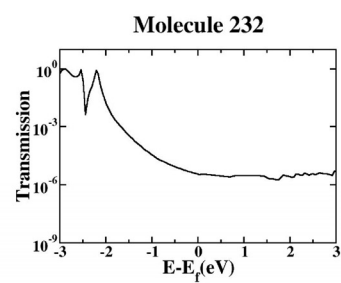
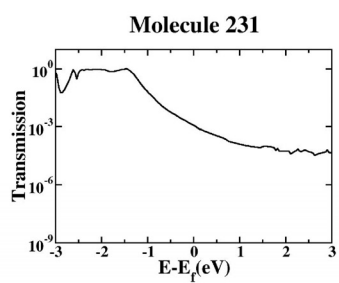
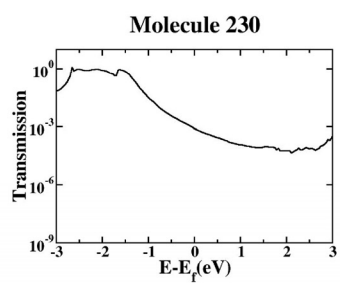
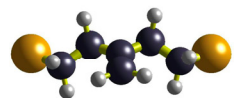


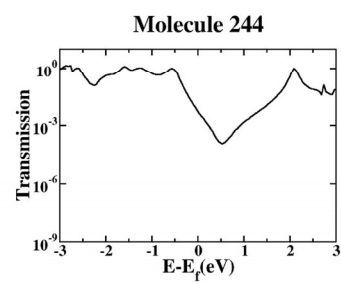
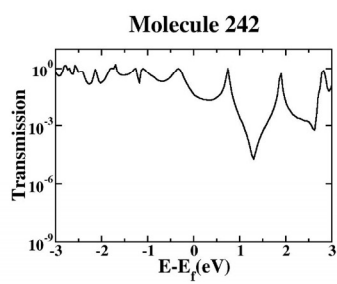
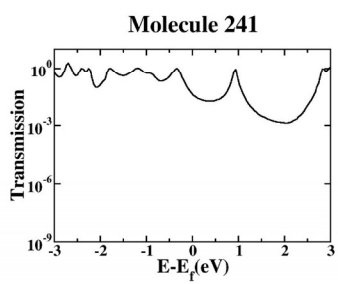
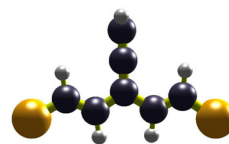
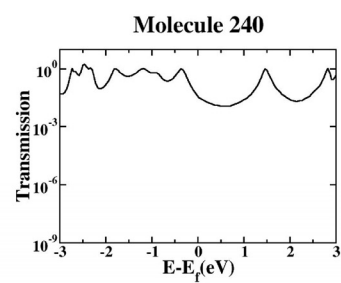
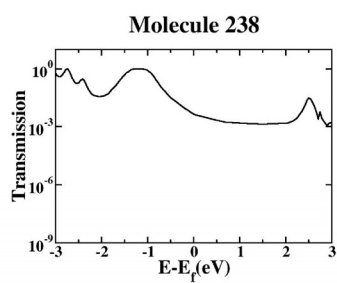
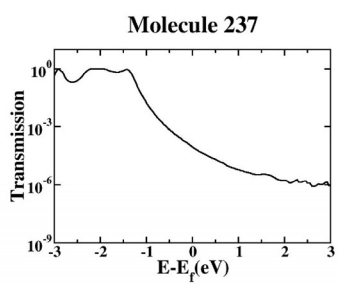
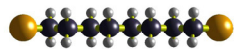
Molecule 228

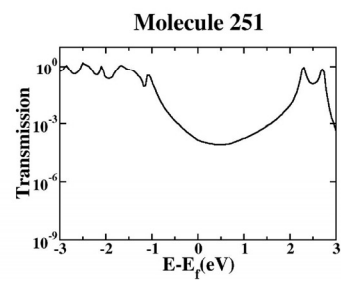
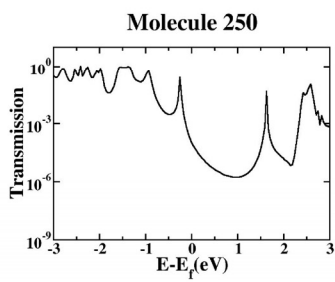
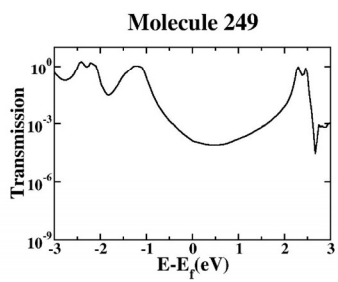
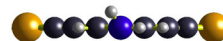
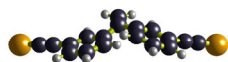
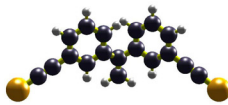
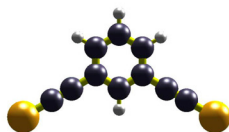
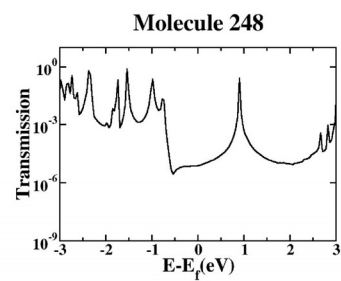
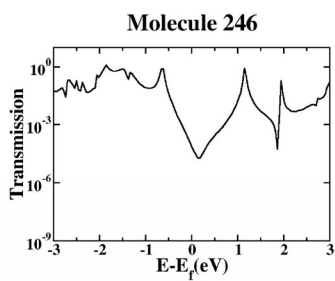
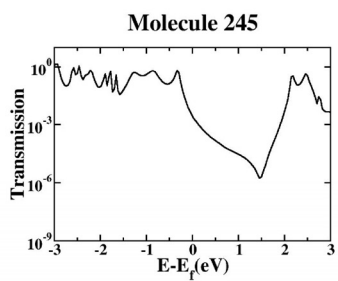
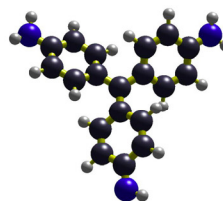
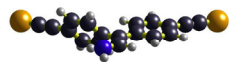
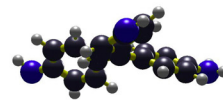


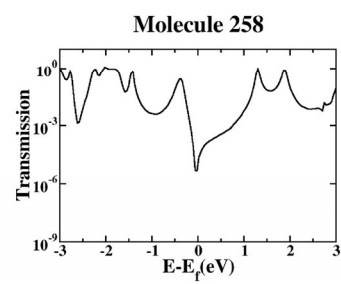
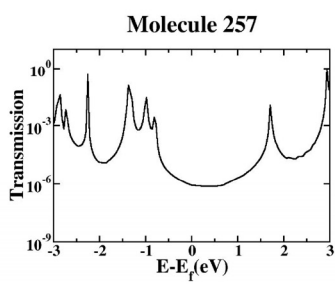
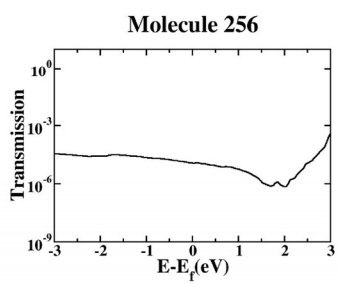
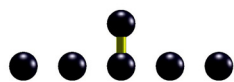
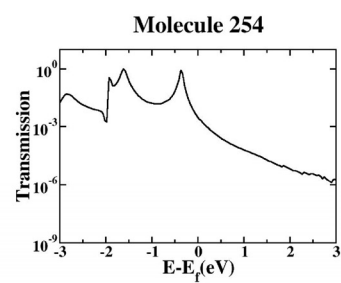
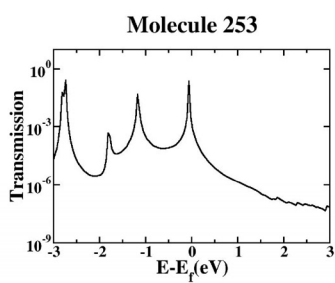
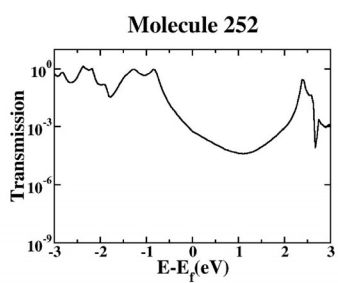
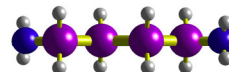
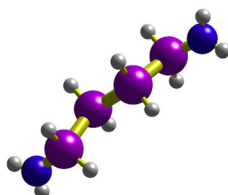
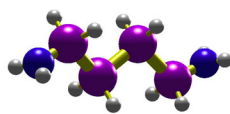
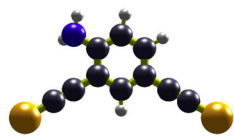
Molecule 229

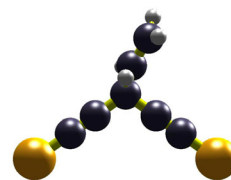




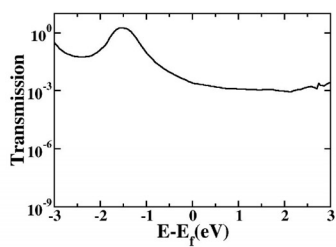




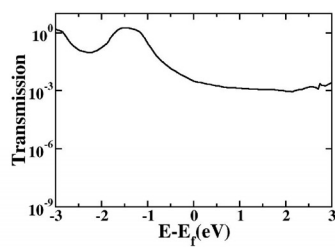




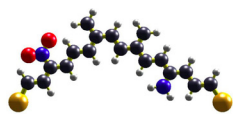
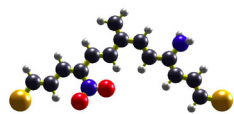
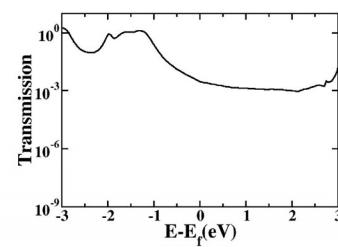
Molecule 259



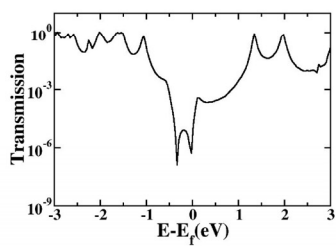
Molecule 260



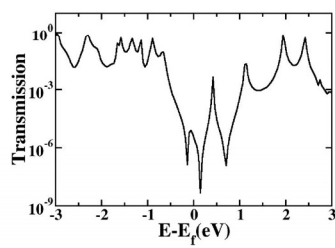
Molecule 261



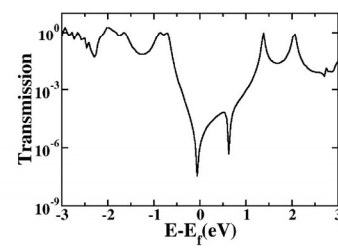
Molecule 262

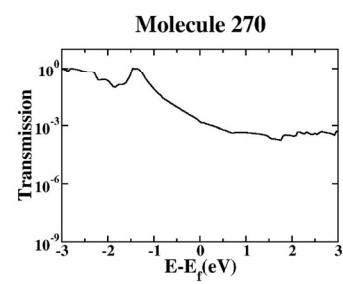
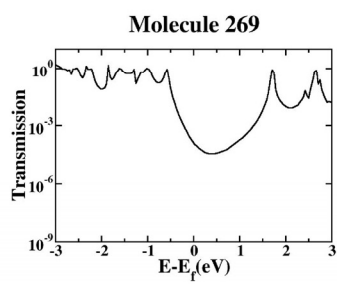
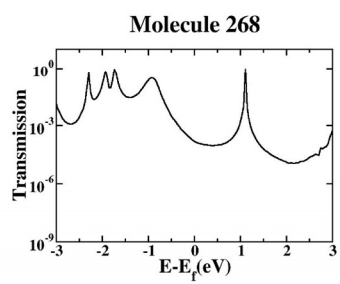
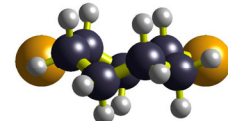
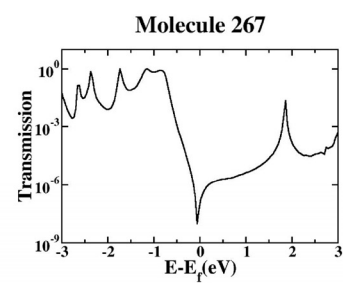
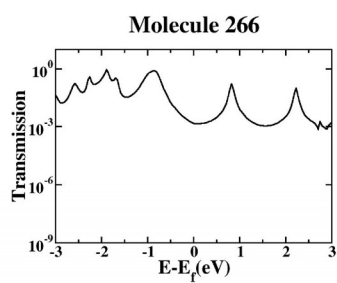
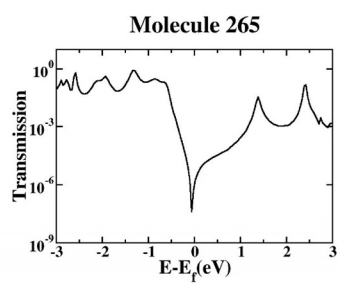
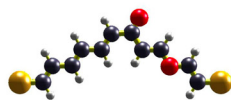


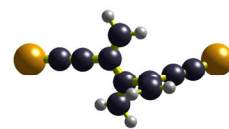
Molecule 263



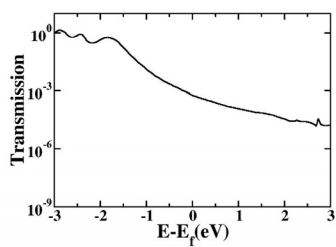
Molecule 264



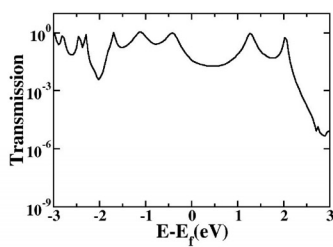




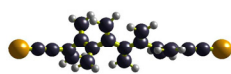
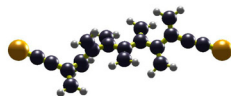
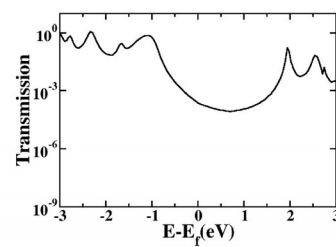
Molecule 271



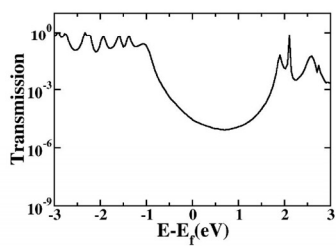
Molecule 272



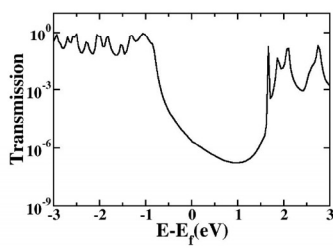
Molecule 275



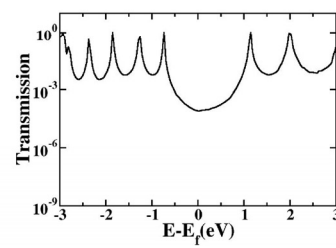
Molecule 276

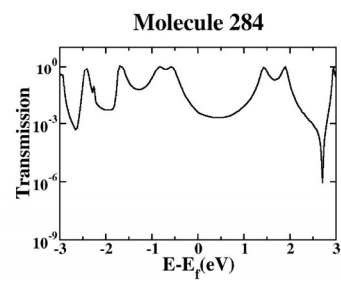
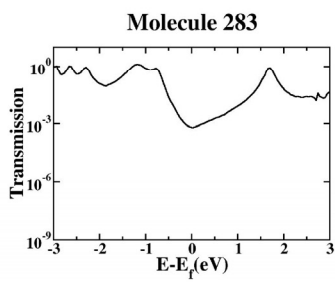
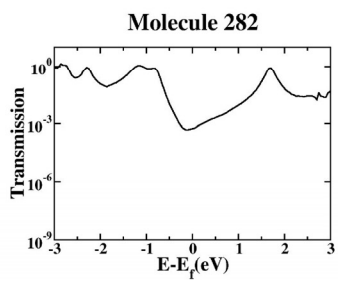
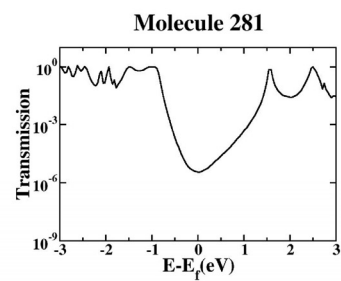
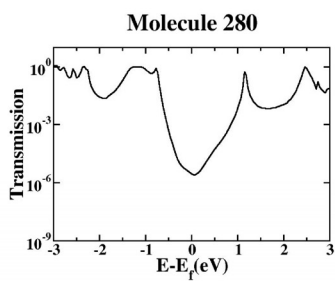
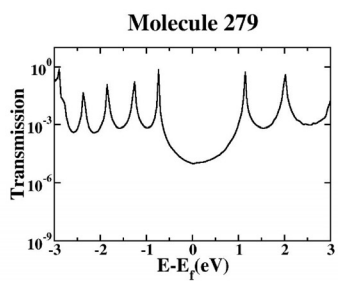
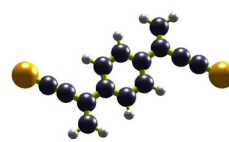


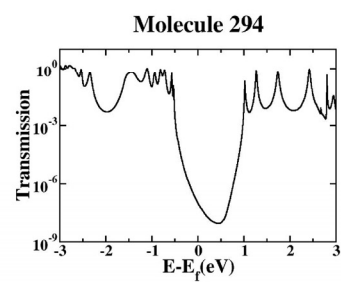
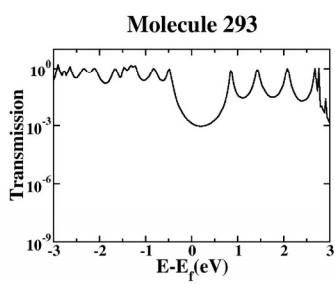
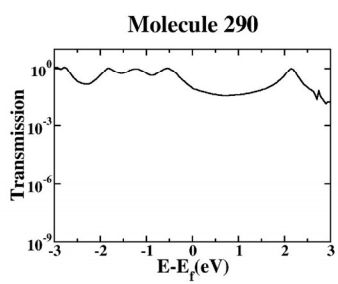
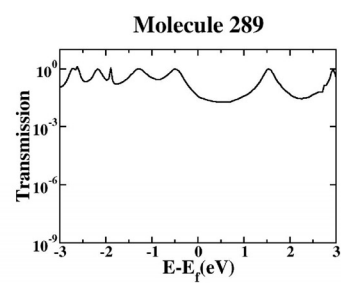
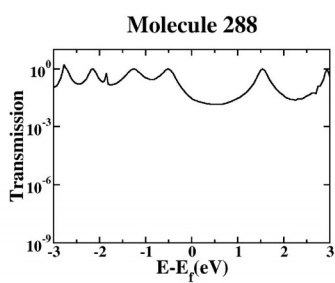
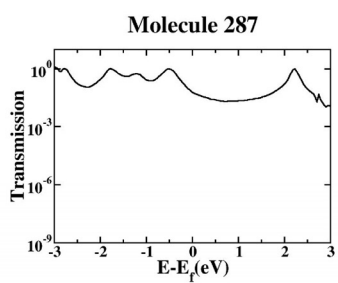
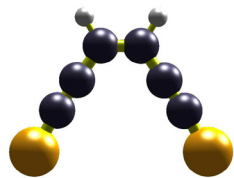
Molecule 277

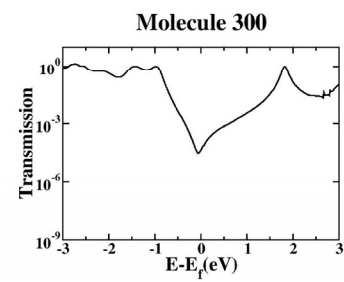
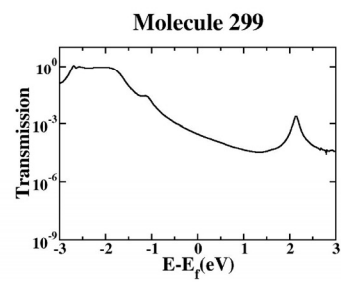
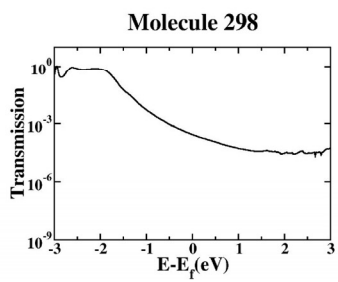
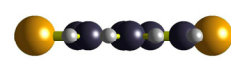
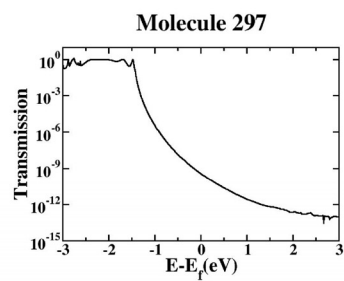
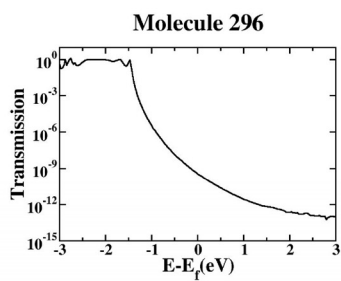
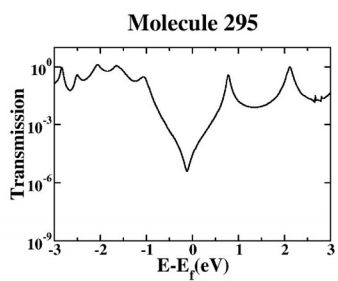
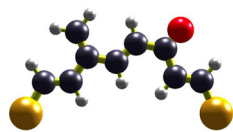


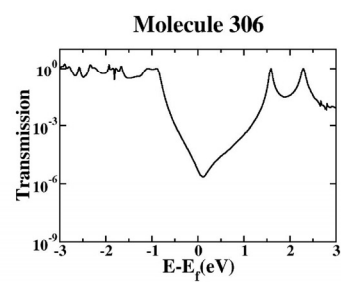
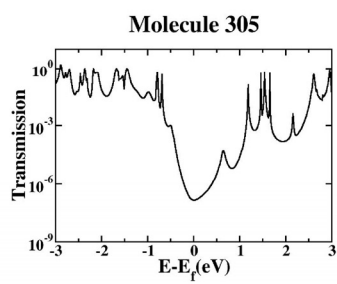
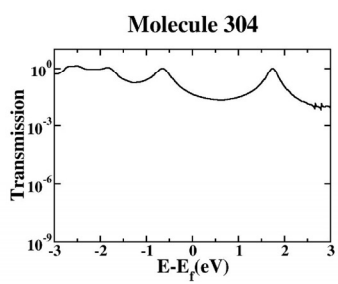
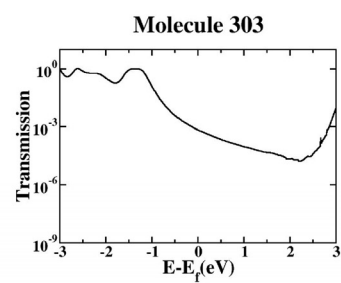
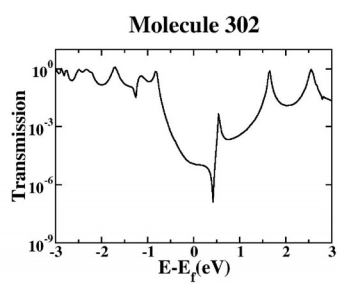
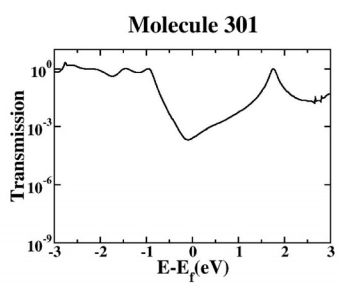
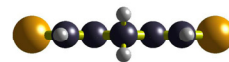
Molecule 278

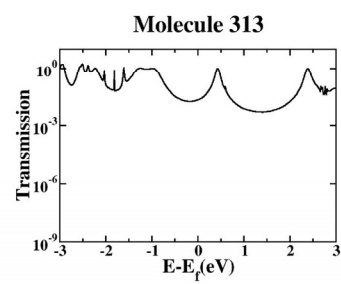
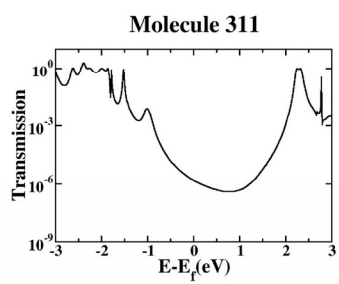
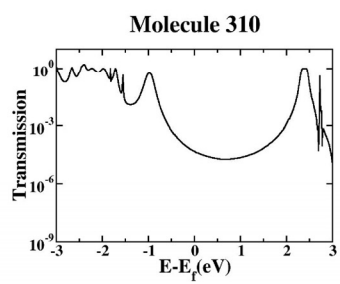
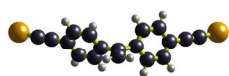
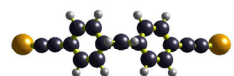
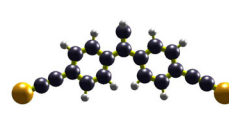
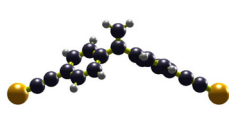
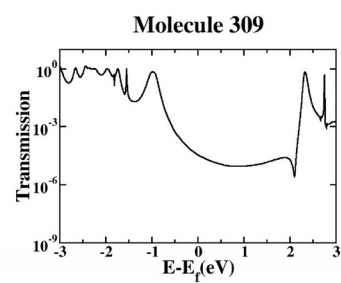
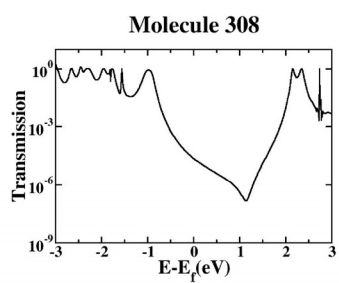
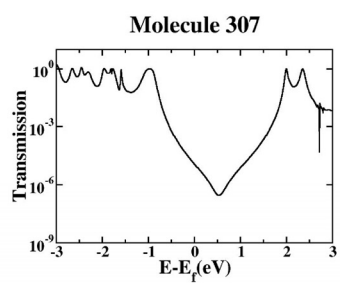
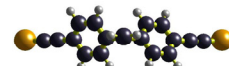
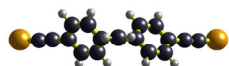
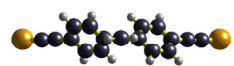


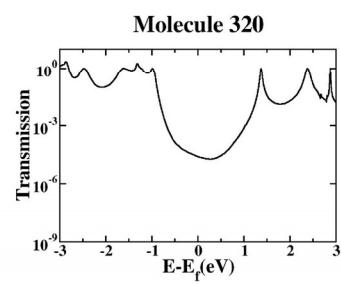
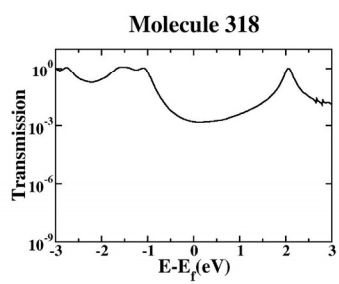
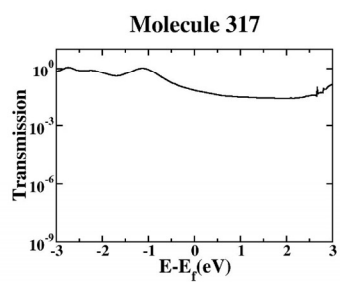
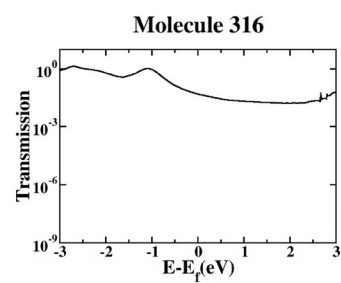
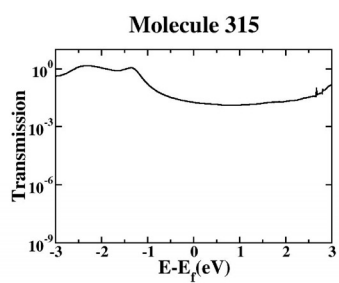
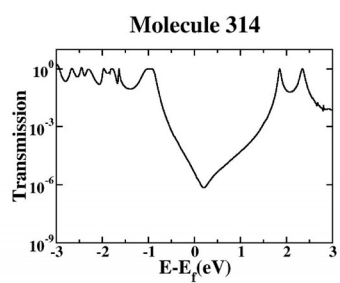
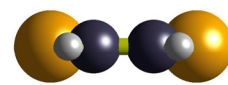
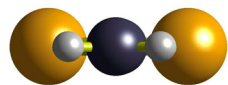
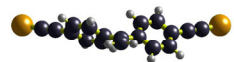
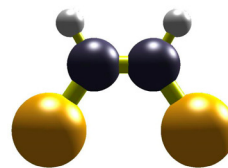
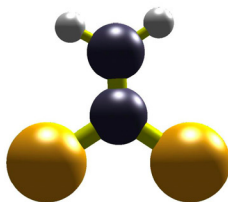


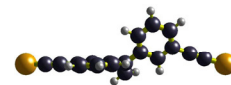




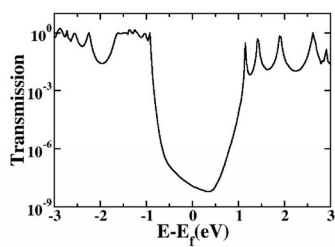




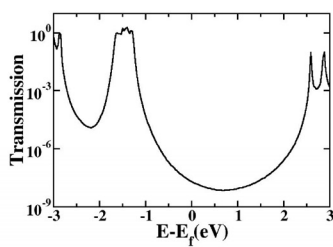




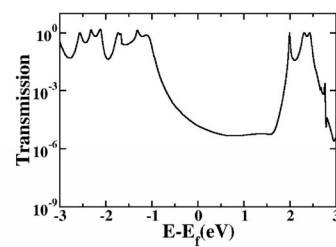
Molecule 321



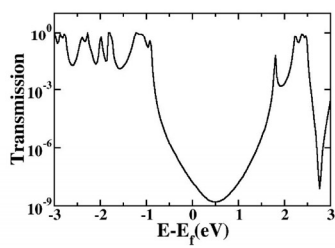
Molecule 322



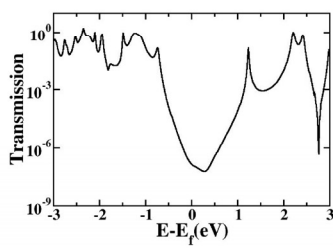
Molecule 323



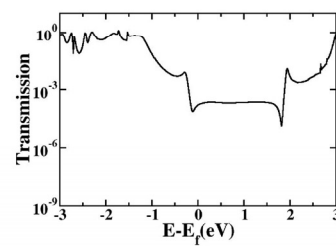
Molecule 324

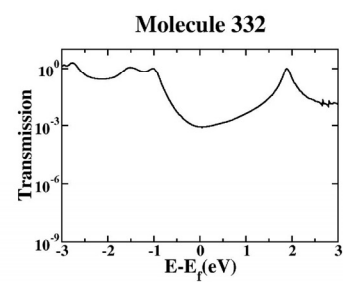
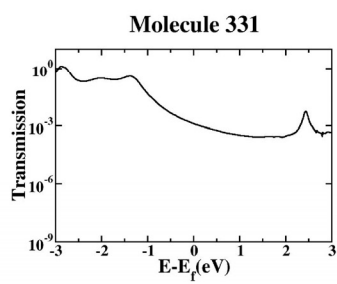
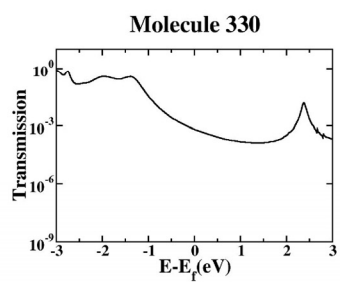
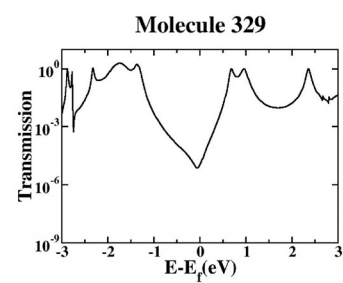
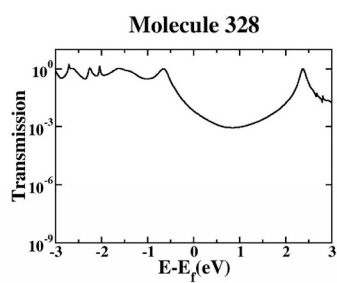
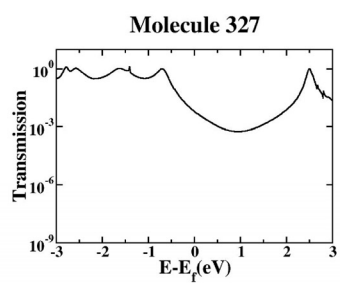
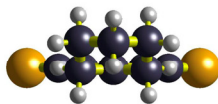
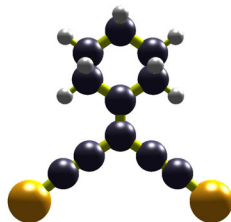
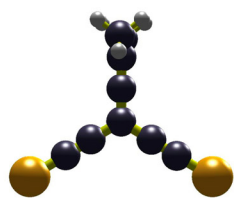


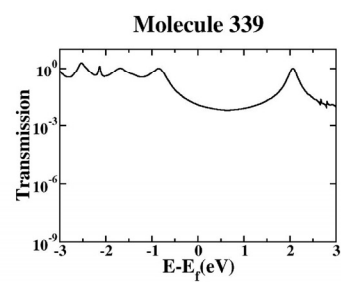
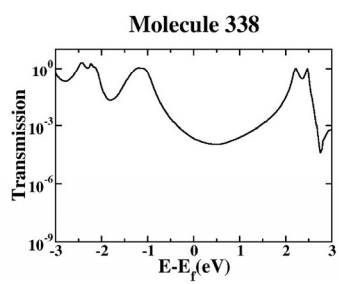
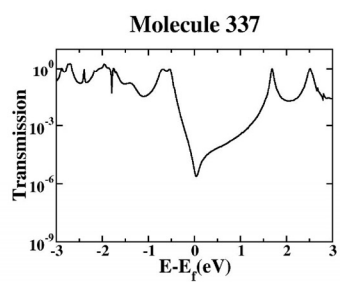
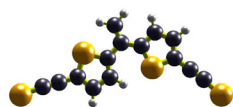
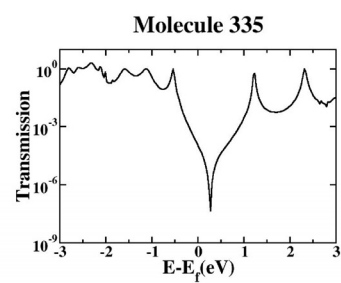
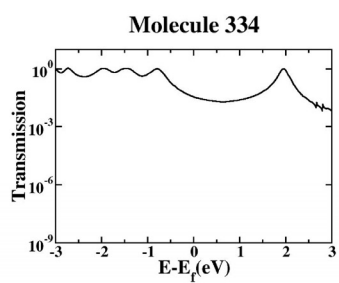
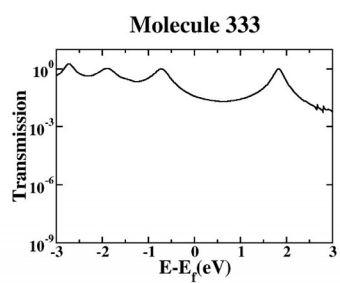
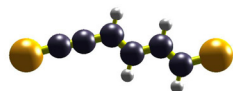
Molecule 325

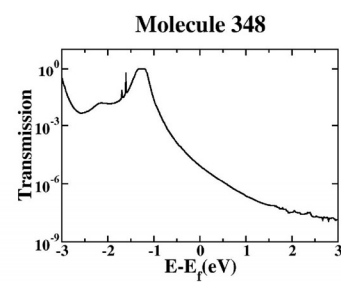
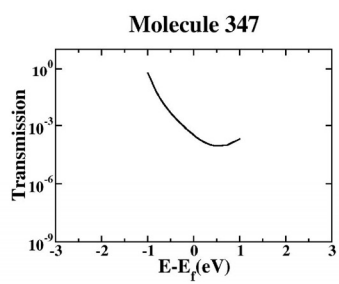
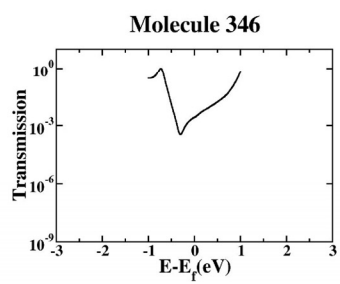
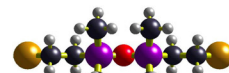
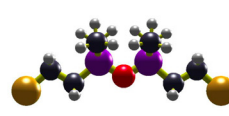
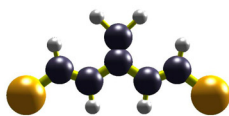
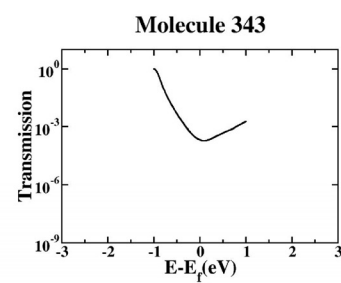
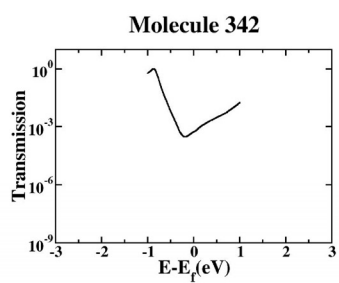
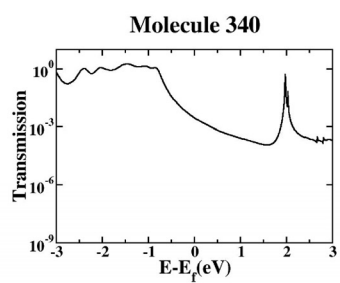
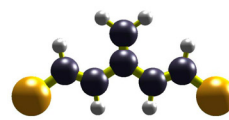
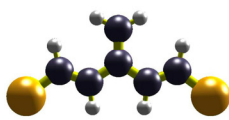
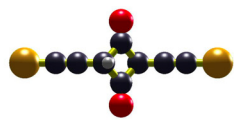


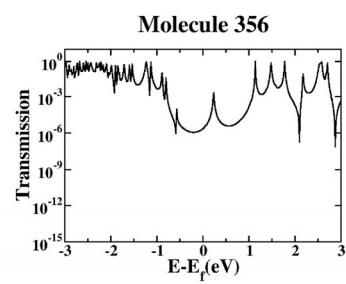
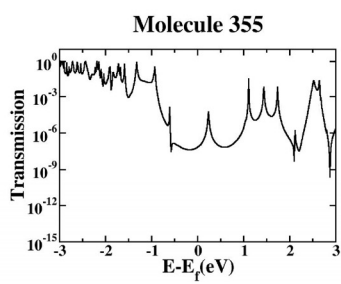
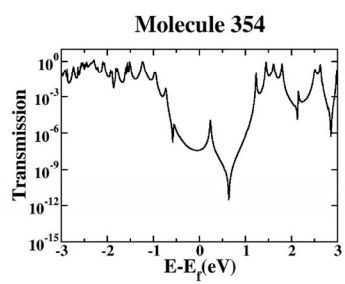
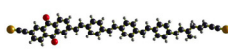
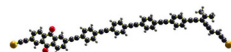
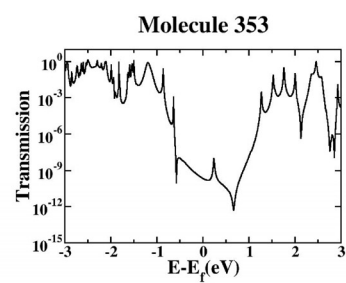
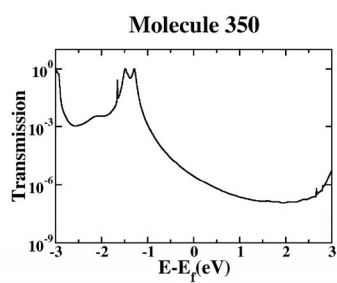
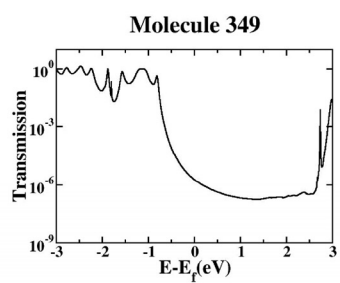
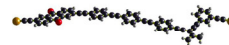
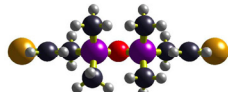
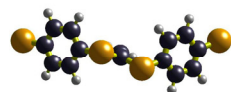
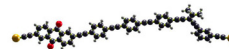
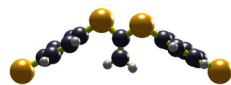
Molecule 326

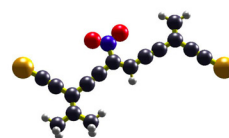
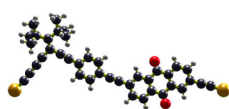




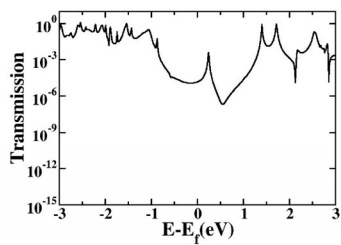




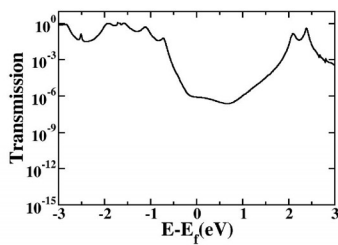




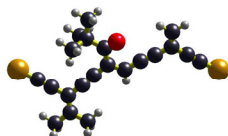
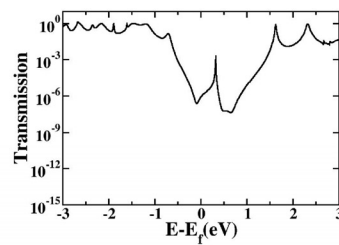
Molecule 361



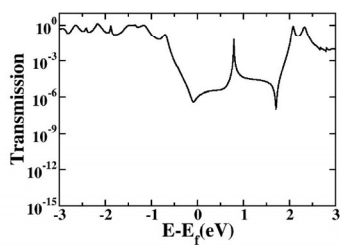
Molecule 362



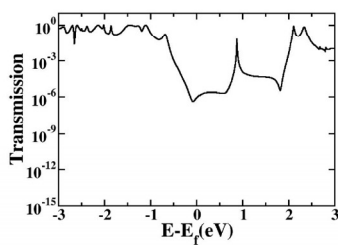
Molecule 363



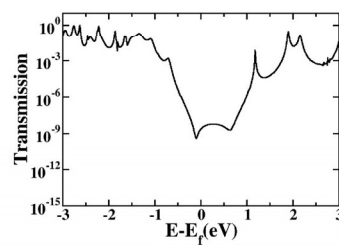
Molecule 364

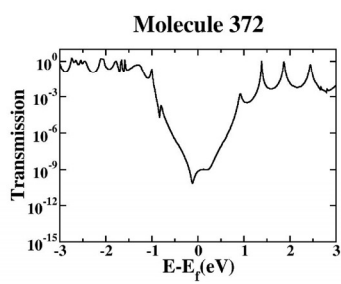
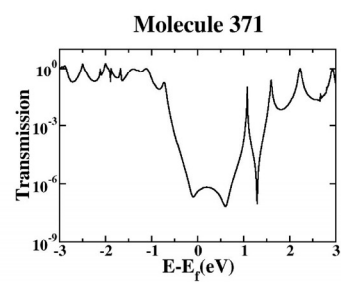
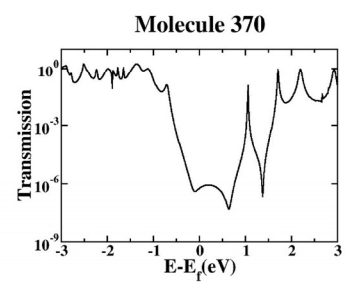
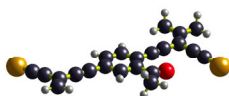
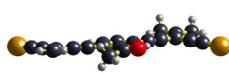
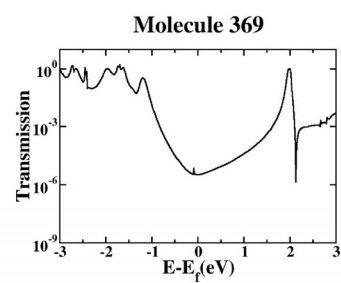
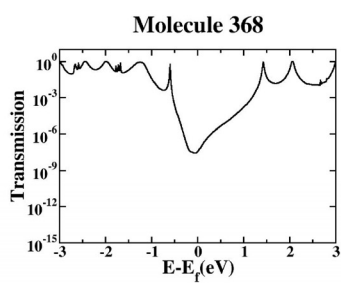
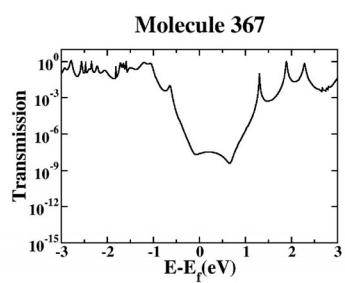
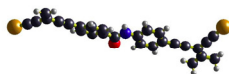
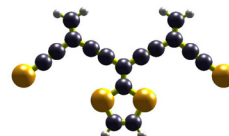
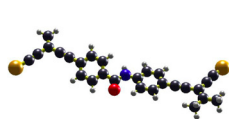


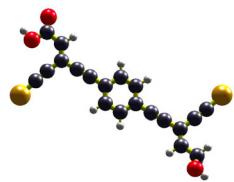
Molecule 365



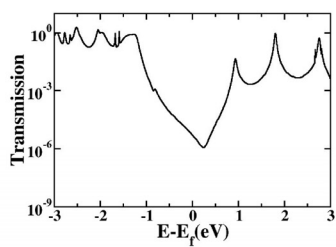
Molecule 366



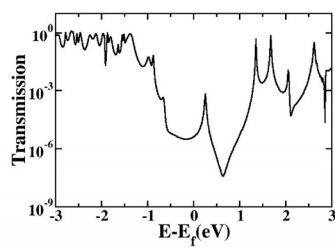




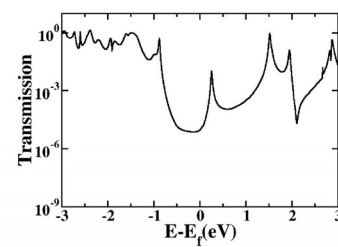
Molecule 373



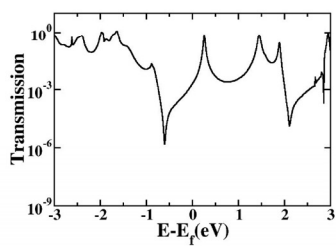
Molecule 374



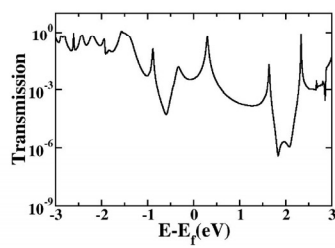
Molecule 375



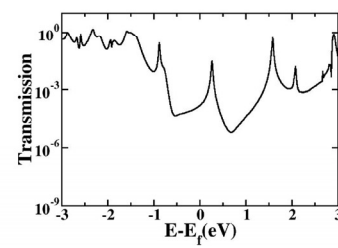
Molecule 376

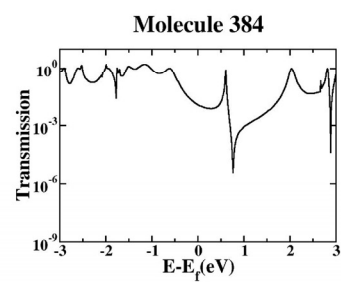
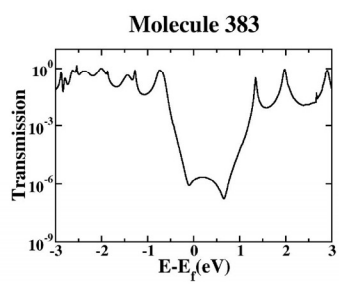
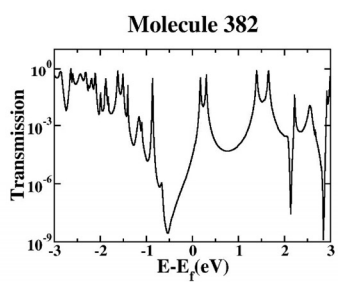
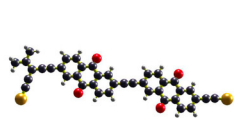
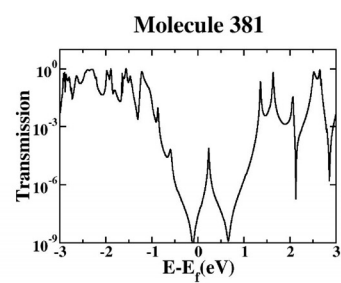
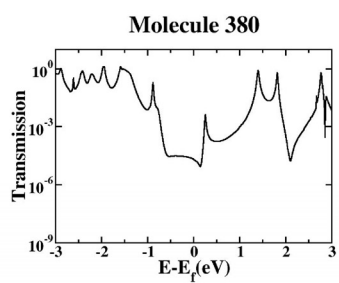
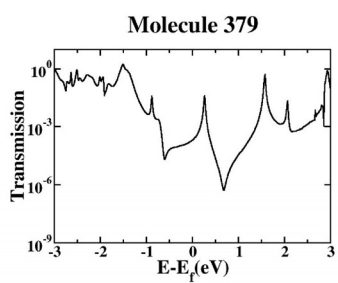
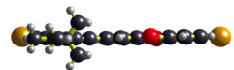


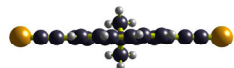
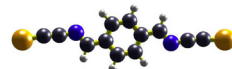
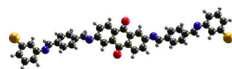
Molecule 377



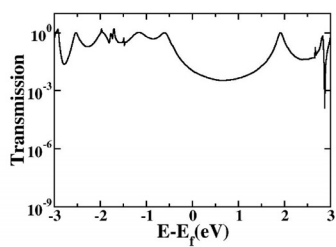
Molecule 378



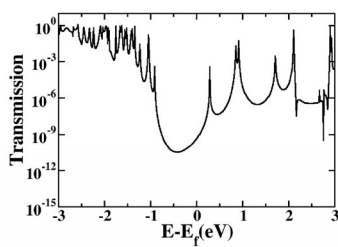




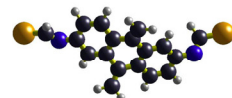
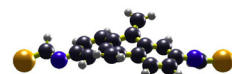
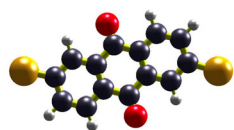
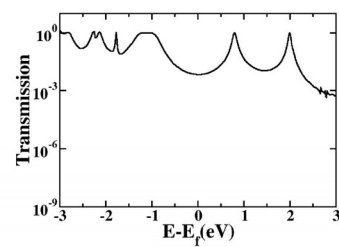
Molecule 385



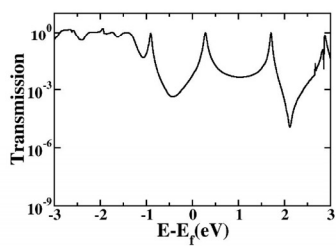
Molecule 386



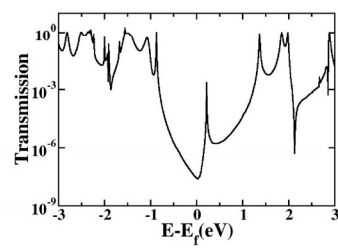
Molecule 387



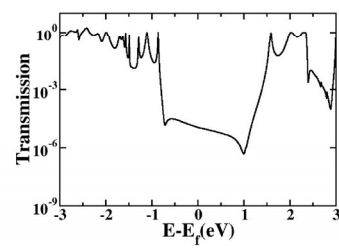
Molecule 388



Molecule 389

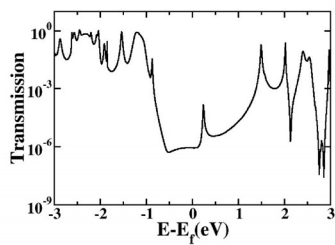


Molecule 390

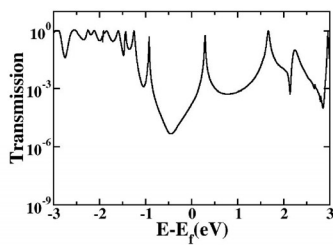




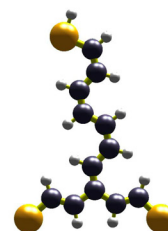
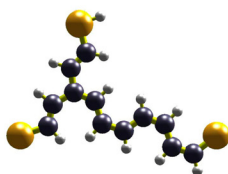
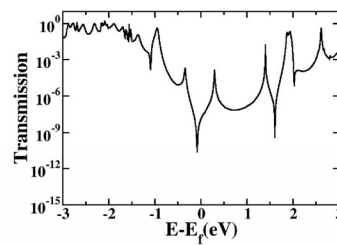
Molecule 391



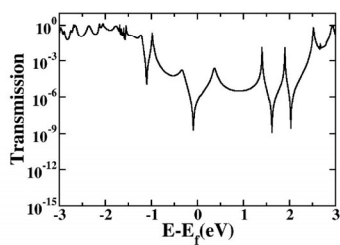
Molecule 392



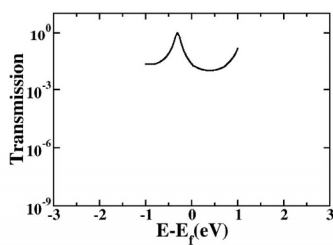
Molecule 393



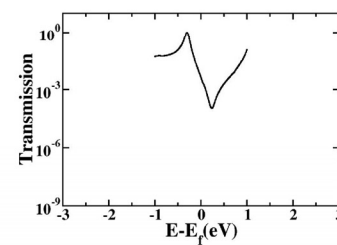
Molecule 394

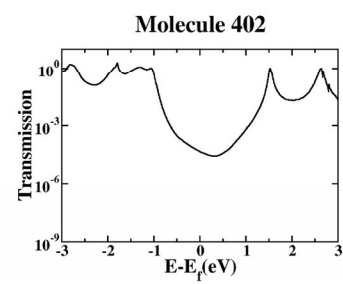
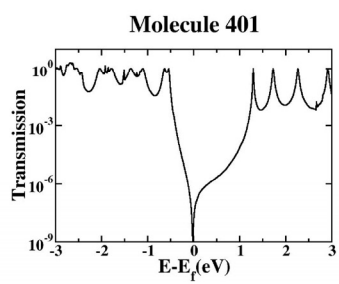
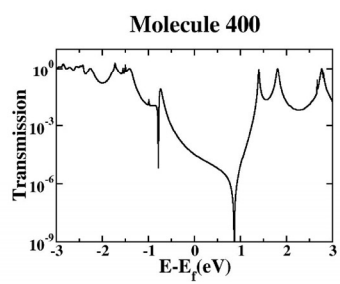
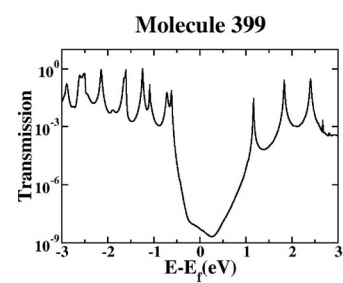
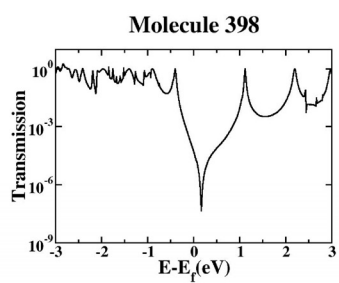
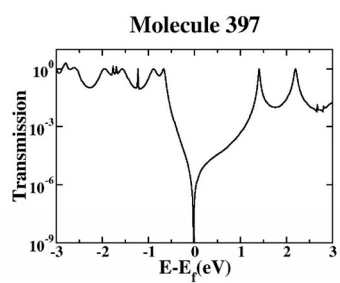
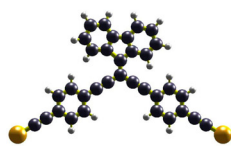


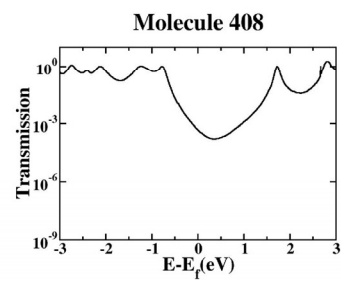
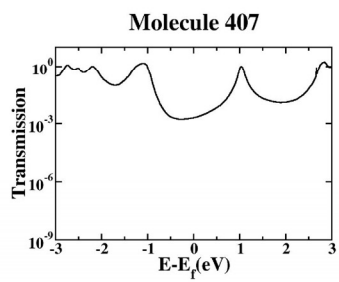
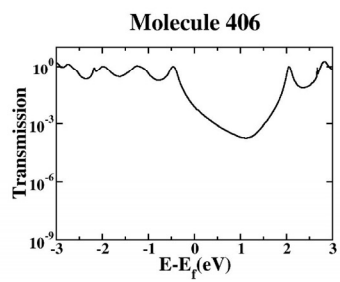
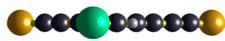
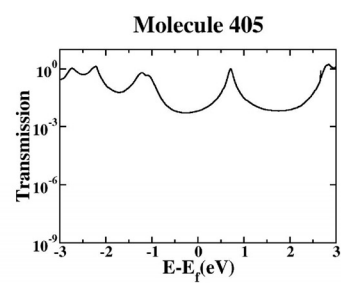
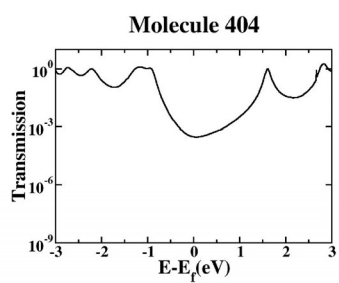
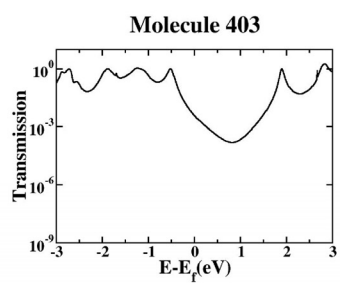
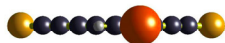
Molecule 395

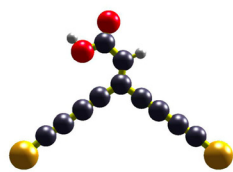


Molecule 396

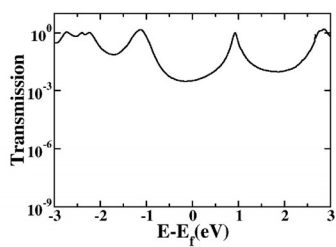




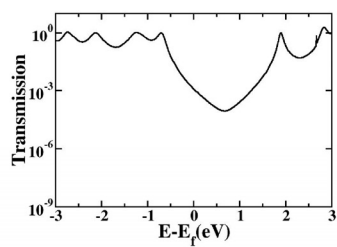




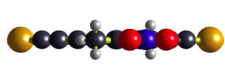
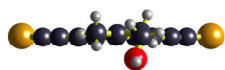
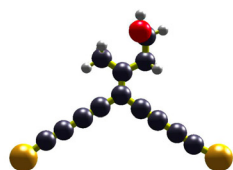
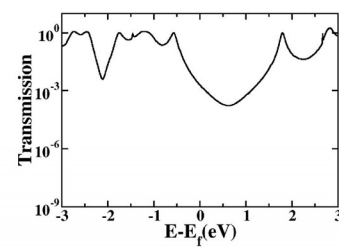
Molecule 409



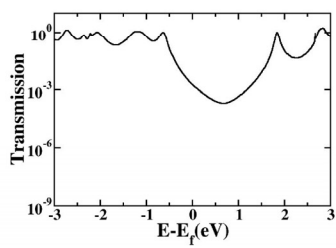
Molecule 410



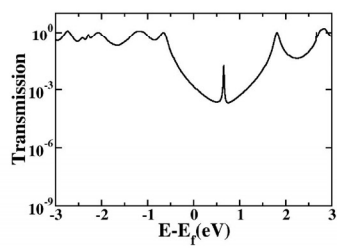
Molecule 411



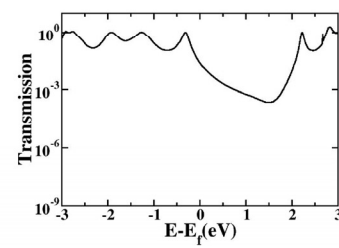
Molecule 412

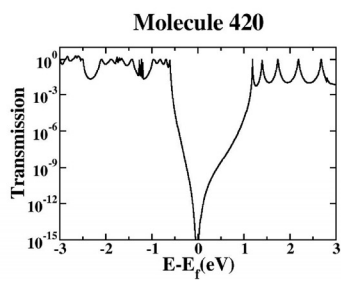
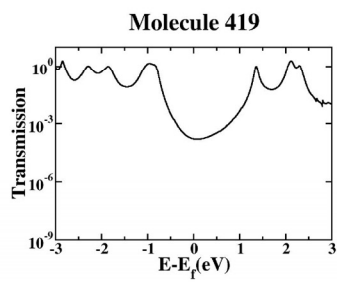
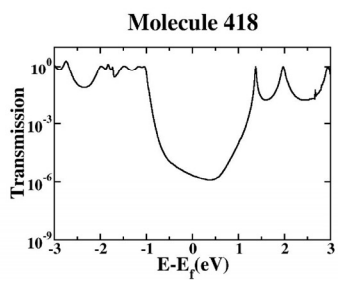
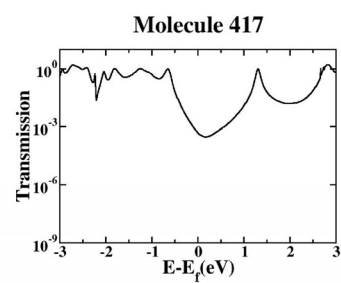
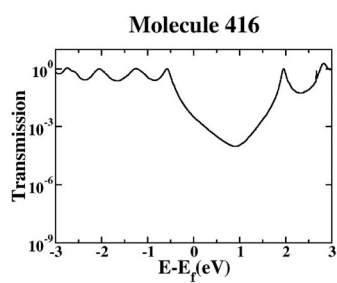
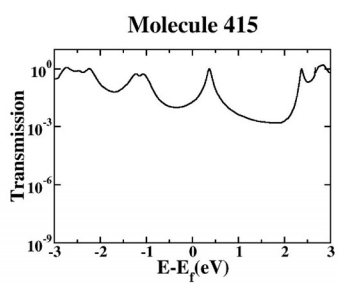


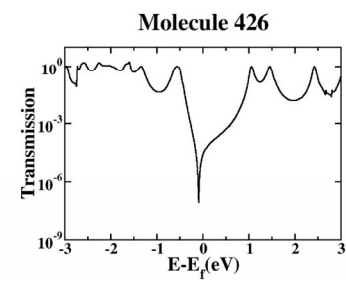
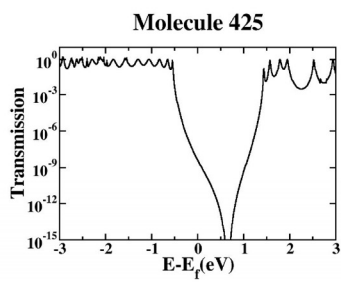
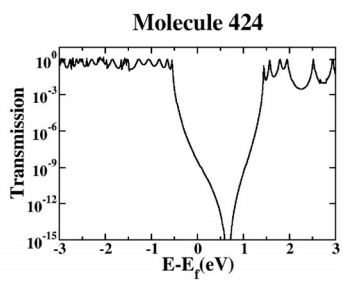
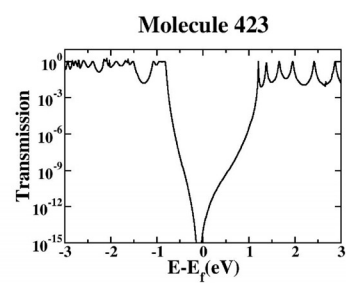
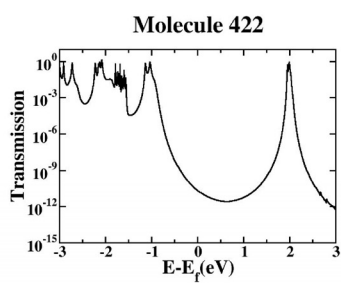
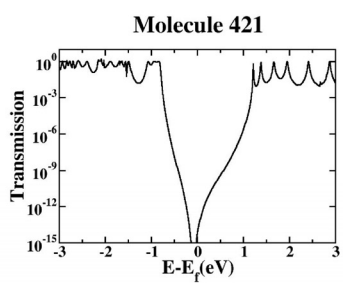
Molecule 413

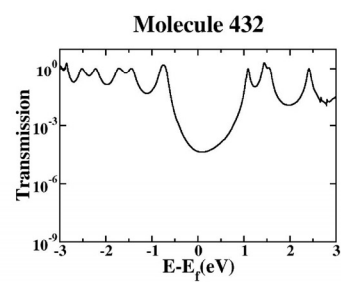
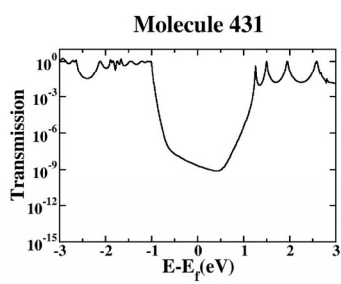
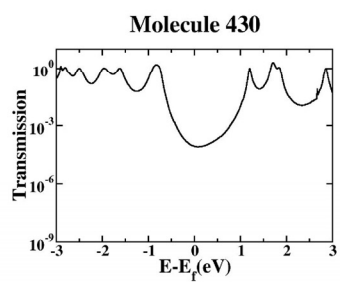
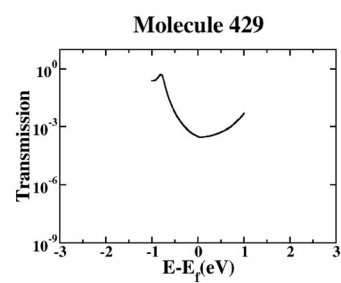
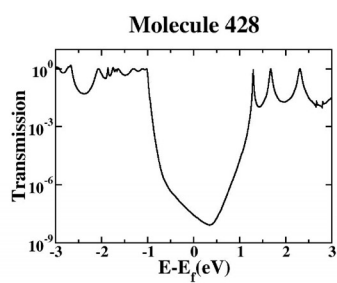
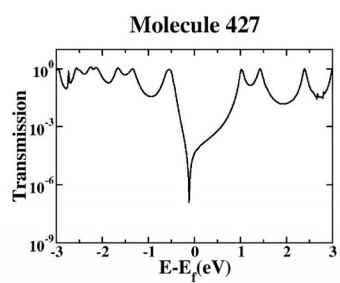
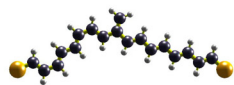


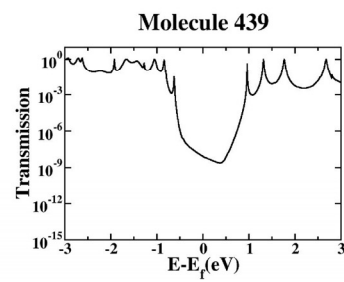
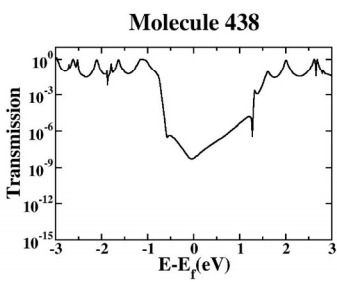
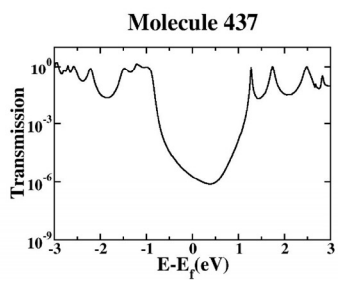
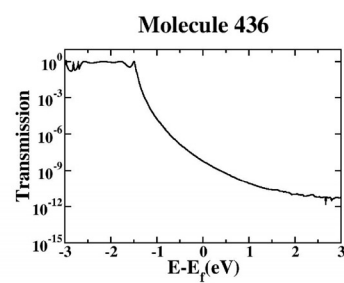
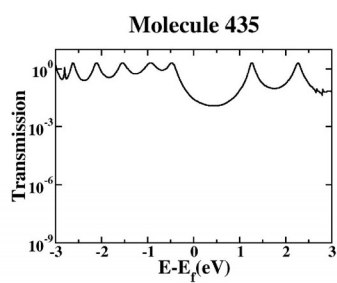
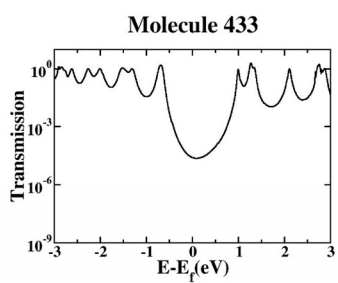
Molecule 414

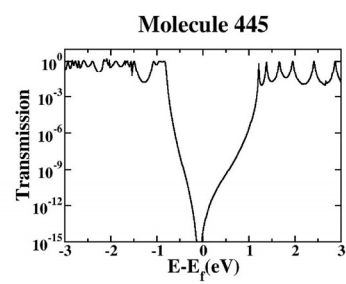
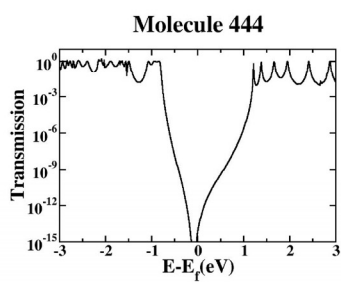
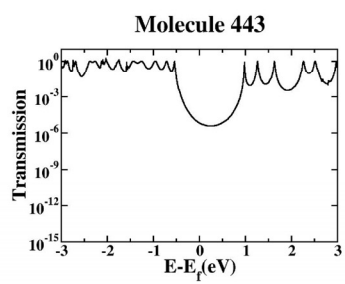
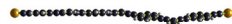
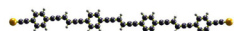
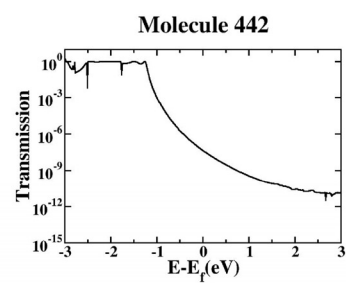
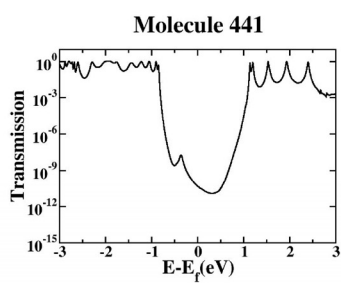
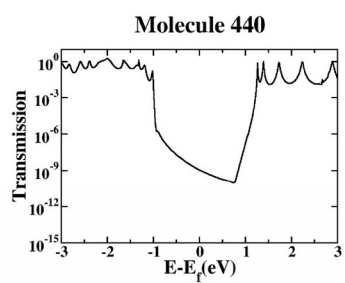


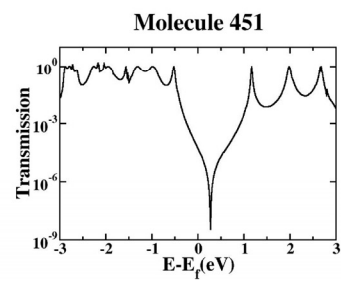
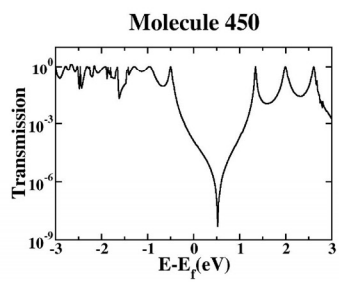
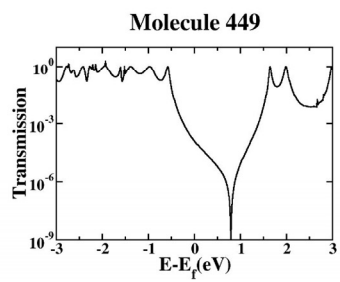
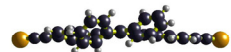
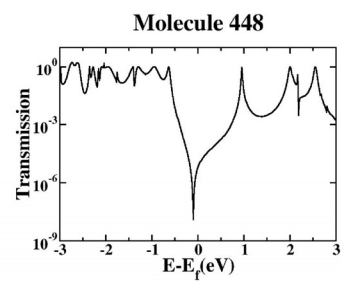
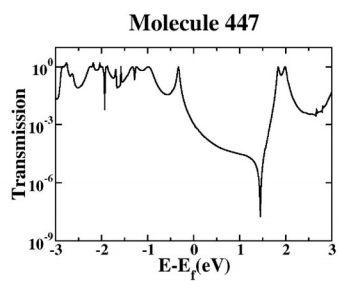
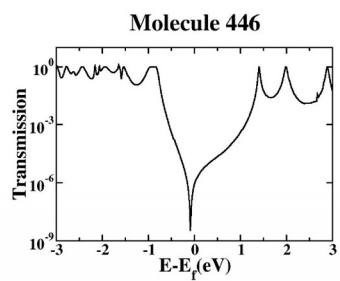
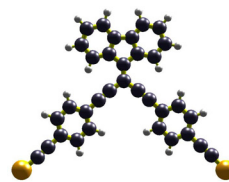


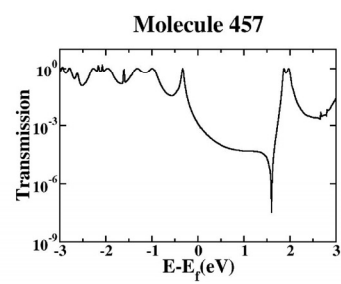
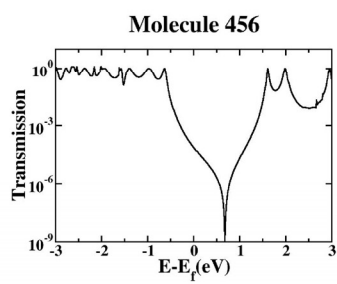
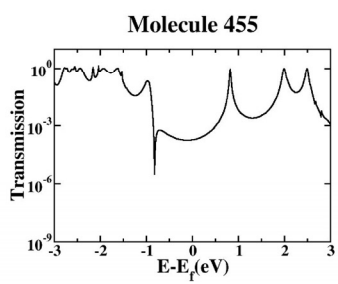
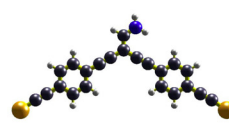
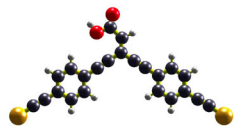
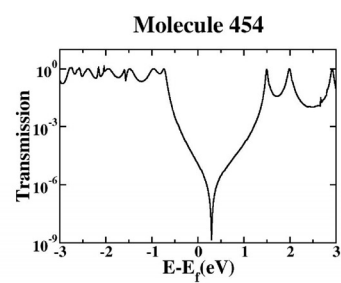
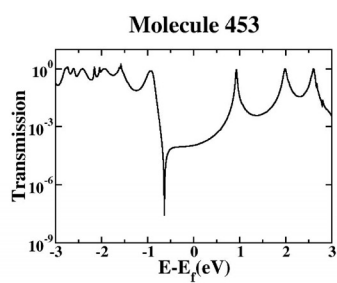
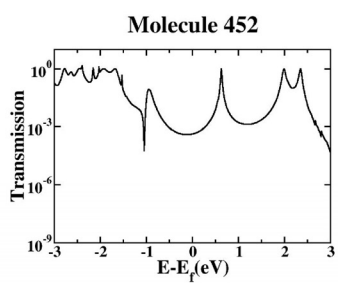
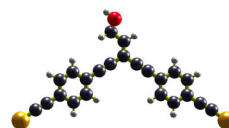
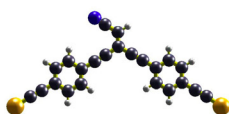
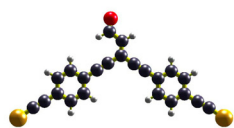


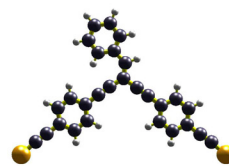
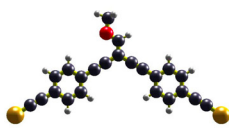
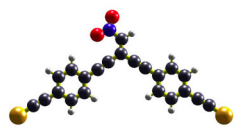




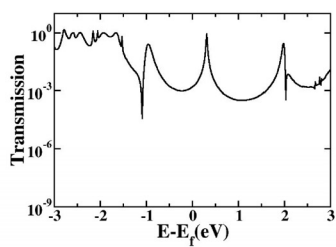




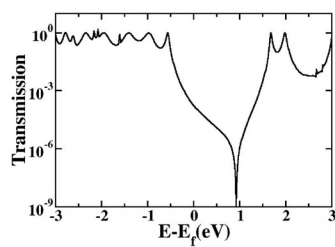




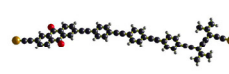
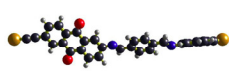
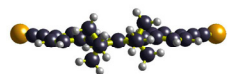
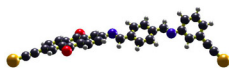
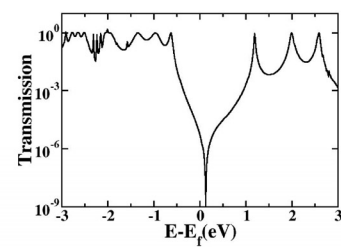
Molecule 458



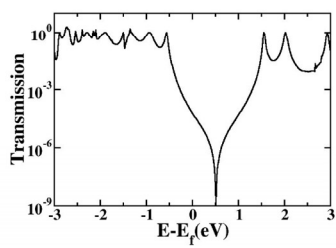
Molecule 459



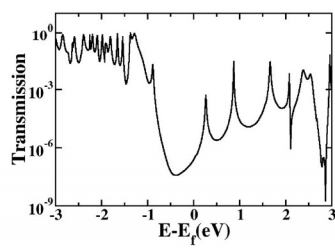
Molecule 460



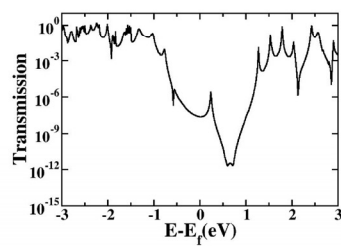
Molecule 461

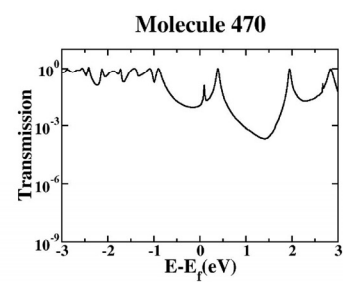
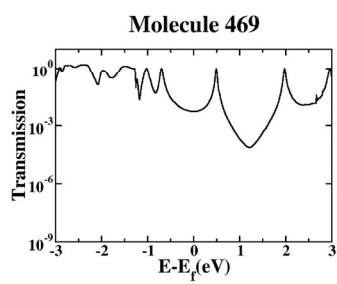
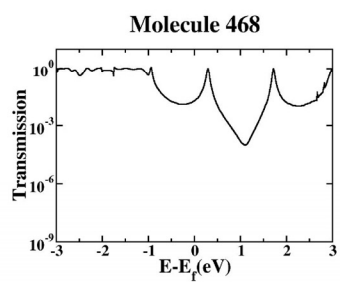
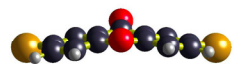
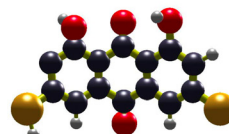
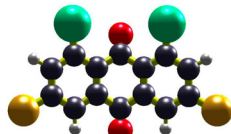
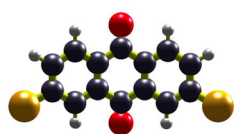
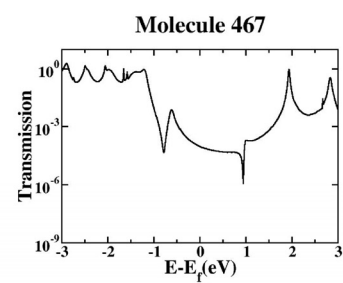
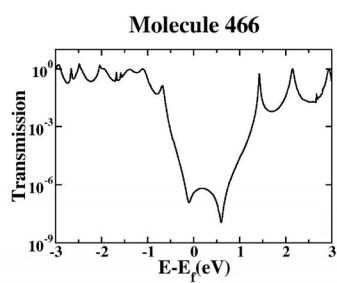
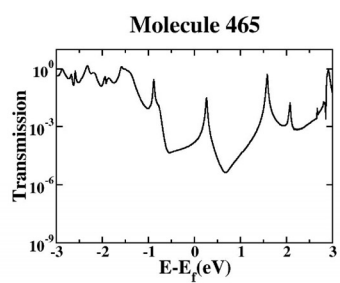
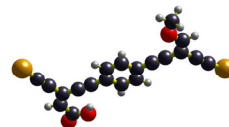
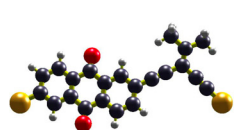


Molecule 462



Molecule 464





Appendix C. VITA

Education

- PhD** Chemistry, 2008, Northwestern University, Evanston, Illinois
BA Chemistry, 2002, Wesleyan University, Middletown, Connecticut

Research Experience

- Northwestern University, Evanston, IL, 2003-2008
Dissertation: "Molecular junctions: Control and dynamics at the single molecule limit"
Advisors: Professor Richard P. Van Duyne, Professor Mark A. Ratner
- Wesleyan University, Middletown, Connecticut, 2000-2002
High Honors Thesis: "Calculating entropy from molecular dynamics simulations using covariance matrices"
Advisor: Professor David L. Beveridge
- National Institutes of Health, Bethesda, Maryland, 1996-1997, 2000
Research: Mutation detection in patients with Gaucher disease using DNA sequencing techniques in an effort towards understanding genotype-phenotype correlation.
Mentor: Dr. Ellen Sidransky

Summary of Qualifications

- Authored four scientific manuscripts, co-authored two scientific manuscripts, five poster presentations
- Reviewed over 10 scientific manuscripts submitted for publication
- Established use of ambient scanning tunneling microscope instrument, resulting in published image
- Oversaw ordering of equipment ~\$400K
- Software: Mathematica, Maple, Matlab, Dreamweaver, Fortran, Labview, ATK, Huckel IV, Qchem, Gamess, Tinker MD, Chemdraw
- Wrote program to control optical filters for multiple users
- Designed and maintained research group website
- Analyzed extremely large datasets

Collaborations

Northwestern University, Hersam Research Group, Material Science and Engineering, 2004-2008

Purdue University, Indiana, Network for Computational Nanotechnology, student representative, 2003-2007

University of California, Irvine, Chemistry at the Space Time Limit, student representative, 2008

University of Prague, Prague, Czech Republic, visiting researcher, 2007

Molecular Imaging Corporation, Tempe, Arizona, troubleshoot instrument design, 2005

University of Copenhagen, Denmark, Niels Bohr summer school on molecular electronics, international grant recipient, 2004

Professional Societies

American Chemical Society

American Physical Society

Phi Lambda Upsilon, Graduate Chemistry Honor Society

Community Outreach

Science in the Classroom, taught monthly sciences lessons in 3rd-4th grade classes in Chicago Public Schools, 2005-2008

South Region High School Science/Math Fair Science Fair Judge, 2005-2007

“Nanoscience Day” for local Boy Scouts at Northwestern University, 2004-2008

Iracambi Atlantic Rainforest Research and Conservation Center, Brazil, 2003

Himanchal High School, Nepal, 2001

National Forest Service, Alaska, 1998

Habitat for Humanity, South Dakota, 1997

Publications

Andrews, D. Q.; Solomon, G. C.; Van Duyne, R. P.; Ratner, M. A., Single Molecule Electronics: Increasing dynamic range and switching speed to rival solid state devices. Submitted, 2008.

Andrews, D. Q.; Solomon, G. C.; Goldsmith, R. H.; Hansen, T.; Wasielewski, M. R.; Van Duyne, R. P.; Ratner, M. A. Quantum interference: The orientation dependence of electron transmission through model systems and cross-conjugated molecules. In preparation, 2008.

Solomon, G. C.; Andrews, D. Q.; Goldsmith, R. H.; Hansen, T.; Wasielewski, M. R.; Van Duyne, R. P.; Ratner, M. A. Understanding quantum interference in molecular conduction. Submitted, 2008.

Solomon, G. C.; Andrews, D. Q.; Goldsmith, R. H.; Hansen, T.; Wasielewski, M. R.; Van Duyne, R. P.; Ratner, M. A. Quantum interference in acyclic systems: The unexpected conductance of cross-conjugated molecules. Submitted, 2008.

Solomon, G. C.; Andrews, D. Q.; Van Duyne, R. P.; Ratner, M. A. When things are not as they seem: Quantum interference turns molecular electron transfer "rules" upside down, *J. Am. Chem. Soc.* Web Release Date: 03-Jun-2008; DOI: [10.1021/ja801379b](https://doi.org/10.1021/ja801379b).

Andrews, D. Q.; Van Duyne, R. P.; Ratner, M. A. Stochastic modulation in molecular electronic transport junctions: Molecular dynamics coupled with charge transport calculations, *Nano Letters*, 8 (4), 1120–1126, 2008.

Andrews, D. Q.; Cohen, R.; Van Duyne, R. P.; Ratner, M. A. Single molecule electron transport junctions: Charging and geometric effects on conductance, *J. Chem. Phys.*, 125, 174718, 2006.

Dixit, S. B.; Andrews, D. Q.; **Beveridge, D. L.** Induced fit and the entropy of structural adaptation in the complexation of CAP and λ -repressor with cognate DNA sequences. *Biophysical Journal*, 88,3147-3157, 2005.

Tayebi, N.; Andrews, D.Q.; Park, J.K.; Orvisky, E.; McReynolds, J.; Sidransky, E. ; Krasnewich, D. M. A deletion-insertion mutation in the phosphomannomutase 2 gene in an African American patient with congenital disorders of glycosylation-Ia, *American Journal of Medical Genetics*, 108 (3), 241-246, 2002.

Park, J.K.; Koprivica, V. ; Andrews, D.Q.; Madike, V.; Tayebi, N.; Stone, D.L.; Sidransky, E. M.D. Glucocerebrosidase mutations among African-American patients with type 1 Gaucher disease, *American Journal of Medical Genetics Part A*, 99 (2), 147-151, 2001.